IS-T--1515

DE91 001107

Application of Ultrasonic Guided Waves to the Characterization of Texture in Metal Sheets of Cubic and Hexagonal Crystallites

by

Li, Yan

PHD Thesis submitted to Iowa State University

Ames Laboratory, U.S. DOE

Iowa State University

Ames, Iowa 50011

Date Transmitted: October 8, 1990

PREPARED FOR THE U.S. DEPARTMENT OF ENERGY

UNDER CONTRACT NO. W-7405-Eng-82.

DISCLAIMER

Application of ultrasonic guided waves to the characterization of texture in metal sheets of cubic and hexagonal crystallites

Yan Li

Under the supervision of R. Bruce Thompson
From the Department of Aerospace Engineering
and Engineering Mechanics
Iowa State University

Texture (preferred grain orientation) of polycrystalline metal sheets is an important material property which influences the process of making products such as aluminum cans and automobile and aircraft components. Traditionally, the texture is determined by X-ray or neutron diffraction techniques which are often destructive and time-consuming in nature. Over the last decade, ultrasonics has been found to provide an alternative way to characterize texture nondestructively and quickly. This dissertation makes an in-depth study of the fundamental physical principles of ultrasonic characterization of texture in metal sheets of cubic and hexagonal crystallites. The fundation is laid by investigations of wave propagation in anisotropic plates. This is then used to evaluate the accuaracy of previously developed, conventional ultrasonic techniques for texture characterization. Through these studies, improvement of the conventional techniques has been made and new ultrasonic techniques have been proposed and applied to some Al samples. This dissertation also presents the extension of these techniques to characterization of the texture of hexagonal polycrystallites such as Ti and Zr. Discussions of ultrasonic velocity measurement methods and errors are also included.

TABLE OF CONTENTS

GENERAL INTRODUCTION

Texture, or preferred orientation of grains, is the consequence of nonrandom orientation of the crystallites of polycrystalline aggregates. This nonrandom orientation is developed during manufacturing and fabricating processes such as annealing, rolling and drawing. Virtually all polycrystalline materials have some degrees of texture, and this texture introduces anisotropy in the physical and mechanical properties of the material. It is often very important to know the texture when making products like aluminum cans, automobile and aircraft components.

Traditionally, texture is determined by X-ray or neutron diffraction methods. The textures measured by these methods are local textures, and these methods are generally destructive in nature and often very time-consuming. In its most common implementation, the X-ray measurement senses only a near surface texture. Neutron measurements sense bulk textures, but can only be performed at specialized facilities.

Recent advances in ultrasonics have made it possible to determine texture nondestructively and quickly on bulk samples. This dissertation analyzes the accuracy of those techniques and lays the foundation for correcting for various systematic errors. Until now, most of the research in ultrasonic characterization of texture has been concentrated on polycrystals of cubic crystallites such as Al, Cu, and Fe. This dissertation also extends the ultrasonic techniques to polycrystals of hexagonal crystallites.

The determination of the texture of a thick piece of material is typically very simple once the relations between the elastic constants and the texture parameters are established. Hence, most of the recent studies appearing in the literature deal with characterization of texture in plates or sheets. This is because the ultrasonic waves propagating in plates are much more complicated when compared to the bulk waves, and those complications

must be taken into account in quantitative texture characterization. This dissertation also places emphasis on texture characterization in a plate geometry, and includes the most rigorous discussion of many of the wave propagation features that have appeared to date. Some discussions may be equally applied to other geometries.

Literature Review

Texture is mathematically described by the crystallite orientation distribution function (CODF), W (ξ, ψ, ϕ), according to Roe [1, 2],

$$W(\xi,\psi,\phi) = \sum_{l=0}^{\infty} \sum_{m=-l}^{l} \sum_{n=-l}^{l} W_{lmn} Z_{lmn}(\xi)\, e^{-im\psi}\, e^{-in\phi} \qquad (1)$$

where $\xi = \cos\theta$, and ψ, θ, and ϕ are Euler angles specifying the orientation of a crystallite with respect to the sample reference frame, $Z_{lmn}(\xi)$ is the generalization of the associated Legendre functions. The dimensionless coefficients W_{lmn} are called "orientation distribution coefficients (ODCs)". The CODF $W(\xi,\psi,\phi)$ is, in essence, a statistical distribution function of the single crystals within the polycrystalline aggregates. Once the W_{lmn} are obtained, $W(\xi, \psi, \phi)$ is fully determined.

In addition to the notation described above (Roe's notation), there are other notations available in the literature [3, 4] that are also used to describe the CODF and the ODCs. Detailed information on the similarities and differences among these different descriptions of texture can be found in Refs. 1-4. In this dissertation, only Roe's notation will be employed.

Although the complete specification of texture requires knowledge of all W_{lmn} for $l \geq 0$, in practice, W_{lmn} are often determined for l up to 20 or 30 from X-ray or neutron diffraction measurements. Ultrasonic techniques, on the other hand, can only determine W_{lmn} for $l \leq 4$ [5]. Within this limit, there are only three independent and nonzero ODCs for cubic crystallites, W_{400}, W_{420}, and W_{440}. For hexagonal materials, there are two extra ODCs, W_{200} and W_{220}. Typical values of these ODCs are on the order of 10^{-3} to 10^{-2}.

The presence of texture in a polycrystalline material gives rise to weak anisotropy which can be described in terms of the ODCs. This weak anisotropy can be sensed through precise ultrasonic measurements. The foundation of application of ultrasonic techniques to the characterization of texture in polycrystalline aggregates lies in the relations between the elastic constants of the aggregates, which can be inferred from ultrasonic velocity measurements, and the ODCs. For the cubic crystallites, these relations were recently discussed in detail by Sayers [6] and Hirao et al. [7]. The development of these relations involves an averaging procedure that takes into account the anisotropy within the single crystals. Depending on the details of the averaging procedure, three different averaging methods can be obtained: the Voigt, Reuss, and Hill averaging methods [6~8]. The commonly used one in texture analysis is the Hill averaging method [9]. For the hexagonal crystallites, the relations between the ODCs and the elastic constants have been established by Sayers [10,11], Li and Thompson [12] and Li et al. [13].

Once the relations between the ODCs and the elastic constants are developed, texture of thick materials can be readily determined ultrasonically [6]. Texture in plates or sheets, however, is much more difficult to determine because the stress free boundary conditions at the plate surfaces cause the wave propagation to be dispersive. There have been many studies in this area [14~20]. Basically, there are two conventional ultrasonic techniques, one uses the SH_0 mode and the other uses the long wavelength limit of the S_0 mode, where SH_0 and S_0 refer to the fundamental horizontally polarized shear and symmetric Lamb modes of the sheet or plate respectively. The SH_0 mode technique alone cannot determine all three W_{4m0} while the dispersion of the S_0 mode must be treated carefully in order to reliably predict ODCs. Recently, a new technique using Lamé mode properties has been proposed. This technique has certain advantages over the conventional techniques

[21,22]. However, more work needs to be done before it can be applied widely.

There have been many publications which compare nondestructive ultrasonic techniques and X-ray or neutron diffraction measurements [20,23~26]. In general, the predictions for W_{420} and W_{440} from ultrasonic techniques are in good agreement with the results from diffraction techniques. In some cases, the ultrasonic estimates for W_{400} correlate well with diffraction results while in other cases, particularly on Al alloys, they do not.

One important application of texture characterization is in the formability analysis of steel sheets. The correlation between texture parameters and formability parameters has been realized for some years [27,28]. The underlying physical principles have been studied and discussed by Stickels and Mould [29] and Davis et al. [30]. Studies in which ultrasonic texture characterization is used in formability analysis can be found in the literature [31~33].

Up until recently, there have been no ultrasonic applications in the characterization of texture in hexagonal crystallites. Due to the increased interests and needs in aerospace and nuclear industries [34,35], the ultrasonic techniques for cubic materials have been extended to the hexagonal materials [36]. These techniques alone, however, do not provide sufficient equations to determine all five ODCs; new or different techniques must be employed or developed [37,38]. Recent studies in this area have shown some promise in the ultrasonic determination of texture using higher order plate modes [38].

Objectives of This Study

The commonly used configuration of ultrasonic characterization of texture utilizes the velocities of the long wavelength limit of the S_0 plate mode. The theory underlying this technique is, strictly speaking, valid only for plates of zero thickness (infinitely thin). Under this theory, the propagating

wave is nondispersive and the velocities of a textured plate or sheet cam be easily measured. However, true plates are never infinitely thin. The waves propagating in a plate of finite thickness are plate modes, and these plate modes, including the S_0 mode, are virtually always dispersive. To determine texture using the S_0 mode, the dispersion must be considered. One of the objectives of this study is to develop, analyze, and understand the exact dispersion relations for wave propagation in anisotropic plates. These dispersion relations are the foundations for the rest of this study. Another objective of this study is to use these dispersion relations to evaluate two available approximate methods that make the dispersion corrections on the measured S_0 velocities so that the dispersion corrected velocities can be used in the equations that were developed for the nondispersive long wavelength limit of the S_0 mode.

In the ultrasonic measurement of texture, the waves are always applied in the form of pulses. The propagation of pulses of a dispersive wave is significantly different from that of a nondispersive wave. Two objectives of this study are to develop a pulse propagation model that is suitable for the ultrasonic characterization of texture and to use this model to estimate the measurement errors involved in the velocity measurement where the dispersive S_0 waves are treated as nondispersive waves.

In the estimation of one of the three texture parameters, W_{400}, there is sometimes a disagreement between ultrasonically predicted W_{400} and the independent neutron diffraction measurement. This disagreement is partially due to the limitation of the conventional S_0 mode technique. Developing a different ultrasonic technique to predict W_{400} and evaluating this technique experimentally are additional objectives of this study.

As the demand for nondestructive characterization of texture in Ti and Zr (hexagonal crystallites) increases in aerospace and nuclear industries, it is natural to develop ultrasonic techniques to measure texture of polycrystalline aggregates of hexagonal crystals. One of the objectives is to

extend the available techniques developed for the cubic materials to the hexagonal materials. These technique are, however, not sufficient for the hexagonal materials since two more texture parameters need to be determined. Another objective of this study is, therefore, to develop other techniques so that all five $W_{l\,mn}$ for l up to 4 can be determined.

Explanation of Dissertation Format

This dissertation follows the guidelines for the alternate dissertation format specified in the Graduate College Thesis Manual at Iowa State University. The dissertation consists of, in addition to the general introduction at the beginning of the dissertation, eight parts, a general summary, a reference list, acknowledgements, and an appendix.

The eight parts describe the work completed during the Ph. D. program. Each part is an independent entity that either has been or will be submitted for publication. Part I presents a set of relations between the elastic constants and texture parameters for polycrystalline materials of hexagonal crystallites. These relations are the key to the ultrasonic characterization of texture in hexagonal polycrystalline materials. This part has been published in the Journal of Applied Physics [13]. Part II contains a paper which investigates the characteristics of elastic wave propagation in anisotropic plates. This is the fundamental physics of ultrasonic determination of material anisotropy (including texture) in plate structures. This part has also been published in the Journal of the Acoustical Society of America [39]. Part III studies two pulse propagation models for dispersive waves. It provides a tool for the analysis to be presented in Part V. This part is to be submitted to the Journal of the Acoustical Society of America. Part IV discusses one aspect of the effects of dispersion on texture determination using one of the conventional ultrasonic techniques. It makes a theoretical evaluation of the conventional S_0 mode technique using the formulae and results presented in Part II. This part has been submitted to the Journal of

the Acoustical Society of America. Part V uses one of the models evaluated in Part III to model and analyze the measurement aspect of the effects of dispersion on the texture determination. This part is to be submitted to the IEEE Transactions on Ultrasonics, Ferroelectricity, and Frequency Control. Part VI contains the principles of a newly proposed ultrasonic technique for texture determination. This part has been published in the Review of Progress in Quantitative Nondestructive Evaluation, Vol. 8B [40]. Part VII concentrates on hexagonal crystallites, with emphasis on the newly proposed technique. Included are theories and experimental results obtained on two samples of hexagonal crystallites. This part has been submitted for publication in Nondestructive Characterization of Materials, Vol. 4 [33]. Part VIII reports and compares experimental results for the texture measurement on ten Al plates. This part is to be published in the Review of Progress in Quantitative Nondestructive Evaluation, Vol. 10.

This dissertation concludes with a summary, a list of references cited, acknowledgements, and an appendix that describes a useful signal processing method to determine ultrasonic velocity or wave number information for the dispersive S_0 waves. This method has been implemented in an ultrasonic texture/stress measurement system that has just been built at Iowa State University, and the method has been found to produce highly accurate results [41,42].

PART I.

RELATIONS BETWEEN ELASTIC CONSTANTS C_{ij} AND TEXTURE PARAMETERS FOR HEXAGONAL MATERIALS

ABSTRACT

Ultrasonic techniques have recently been applied to the texture characterization in polycrystalline aggregates of hexagonal crystals. The basis of this application lies in the relations between the elastic constants $\bar{C}_{ij}$ of the aggregates, which can be inferred from ultrasonic wave velocity measurements, and the orientation distribution coefficients. This communication presents such relations for aggregates which possess orthotropic material symmetry and hexagonal crystal symmetry for Voigt, Reuss, and Hill averaging methods in a unified and concise representation.

INTRODUCTION

There has been increasing interest in characterization of texture in hexagonal materials in recent years [1,2]. Texture, or preferred orientation of grains, is often quantitatively described by the orientation distribution coefficients (ODCs) or W_{lmn} in Roe's notation [3,4]. These are, in essence, the coefficients of an expansion of the crystallite orientation distribution function in terms of a series of generalized spherical harmonics. Now, ultrasonic techniques are being applied to texture measurement of hexagonal materials because of their nondestructive nature [5,6]. The foundation of application of ultrasonic techniques to the determination of texture in polycrystalline aggregates of hexagonal crystals lies in the relations between the elastic constants $\bar{C}_{ij}$ of the aggregates, which can be inferred from velocity measurements , and the ODCs. This note presents such relations for aggregates which possess orthotropic material symmetry and hexagonal crystal symmetry.

DEVELOPMENT OF THE RELATIONS

In general, the elastic constants $\bar{C}_{ij}$ and the elastic compliances $\bar{S}_{ij}$ of textured materials can be formally expressed as

$$\bar{C}_{ij} = C^{o}_{ij} + \Delta C_{ij} \tag{1}$$

$$\bar{S}_{ij} = S^{o}_{ij} + \Delta S_{ij} \tag{2}$$

where C^{o}_{ij} and S^{o}_{ij} are elastic constants and compliances of the corresponding isotropic (texture-free) polycrystalline aggregates satisfying the $C^{o}_{11}-C^{o}_{12}=2C^{o}_{44}$ and $S^{o}_{11}-S^{o}_{12}=\frac{1}{2}S^{o}_{44}$ isotropy conditions. ΔC_{ij} and ΔS_{ij} are the differences due to the presence of texture; they are functions of W_{lmn} for $0 < l \leq 4$. For aggregates of hexagonal crystallites, W_{200}, W_{220}, W_{400}, W_{420}, and W_{440} are the only five independent members of these ODCs which are nonzero.

The explicit relations described by Eqs. (1) and (2) depend on the averaging procedures. Voigt, Reuss, and Hill averaging methods are the three commonly employed in texture studies owing to their simplicity. The relations between the elastic constants $\bar{C}_{ij}$ and W_{lmn} for the Voigt averaging method were developed by Sayers [7]. These relations, although explicit in principle, rely on the equations given in the appendix of the paper by Smith and Dahlen [8]. We also independently developed the $\bar{C}_{ij}$ -- W_{lmn} relations using the method described by Morris [9]. A comparison with the results by Sayers reveals that Sayers' expressions can be further simplified to ours if a print error in the expression for γ_{1111} in the appendix of Smith and Dahlen's paper is corrected[1]. To many users of these relations, this error might not be obvious, and further errors might be introduced as a consequence of

[1] The correct expression for γ_{1111} is
$\gamma_{1111}=3\gamma_s^{00c}+6\gamma_s^{20c}+6\gamma_s^{22c}+3\gamma_s^{40c}+\gamma_s^{42c}+\gamma_s^{44c}$.

applying these relations. One of the primary purposes of this communication is to correct that error by explicitly presenting the resulting relations in a form believed to be particularly convenient.

The relations between elastic compliances $\bar{S}_{ij}$ and W_{lmn} for the Reuss averaging method were also derived and published by Sayers [10], following the procedures outlined by Morris [9]. Practically speaking, ultrasonic velocities are more easily expressed in terms of elastic stiffnesses rather than elastic compliances; and the Hill averaging method, which is the arithmetic mean of the Voigt and Reuss averaging methods[2], is found to give the most acceptable accuracy among the three. For this reason, it is often more convenient to invert the $\bar{S}_{ij}$ -- W_{lmn} relations in Eq. (2) for the Reuss averaging method to the $\bar{C}_{ij}$ -- W_{lmn} relations. This can be mathematically described as

$$\bar{\mathbf{C}} = \bar{\mathbf{S}}^{-1} = (\mathbf{S}^0 + \Delta\mathbf{S})^{-1} = [\, \mathbf{S}^0 \,(\, \mathbf{I} + \mathbf{S}^{0\,-1}\Delta\mathbf{S}\,)]^{-1}. \qquad (3)$$

In the application of ultrasonics to texture characterization, the anisotropy of the polycrystalline aggregates is sometimes small. Under this weak anisotropy assumption, $\| \mathbf{S}^{0\,-1}\Delta\mathbf{S} \| << 1.0$. Therefore, the inversion process in Eq. (3) can be carried out analytically, arriving at expressions that resemble Eq. (1) in form. Similar work was done for the cubic materials by Hirao et al. [12]. At the end of this note, a comparison table will be given to show the results of the analytical inversion for a given set of W_{lmn}.

In the following, explicit expressions for both $\bar{\mathbf{C}}_{Voigt}$ and $\bar{\mathbf{C}}_{Reuss}$ are summarized in a unified and concise representation where the contributions of W_{2m0} and W_{4m0} can be readily observed:

---

[2]Hill [11] did not explicitly propose such an averaging method for aggregates of hexagonal crystallites. The definition for Hill's averaging method here is a natural extension from that for aggregates of cubic crystallites, which was proposed by Hill.

$$
\begin{aligned}
\bar{C}_{11} &= C^{o}_{11} + 4\pi^2 \, | \, 4A_1\alpha_1 + B\beta_1 | \\
\bar{C}_{22} &= C^{o}_{11} + 4\pi^2 \, | \, 4A_1\alpha_2 + B\beta_2 | \\
\bar{C}_{33} &= C^{o}_{11} + 4\pi^2 \, | \, 4A_1\alpha_3 + B\beta_3 | \\
\bar{C}_{23} &= C^{o}_{12} + 4\pi^2 \, | \, 2A_2\alpha_1 + B\beta_4 | \\
\bar{C}_{13} &= C^{o}_{12} + 4\pi^2 \, | \, 2A_2\alpha_2 + B\beta_5 | \\
\bar{C}_{12} &= C^{o}_{12} + 4\pi^2 \, | \, 2A_2\alpha_3 + B\beta_6 | \\
\bar{C}_{44} &= C^{o}_{44} + 4\pi^2 \, | \, A_3\,\alpha_1 + B\beta_4 | \\
\bar{C}_{55} &= C^{o}_{44} + 4\pi^2 \, | \, A_3\,\alpha_2 + B\beta_5 | \\
\bar{C}_{66} &= C^{o}_{44} + 4\pi^2 \, | \, A_3\,\alpha_3 + B\beta_6 |
\end{aligned}
\qquad (4)
$$

with
$$
\begin{aligned}
\alpha_1 &= \frac{1}{210}\left(\sqrt{10}\, W_{200} - 2\sqrt{15}\, W_{220} \right) \\
\alpha_2 &= \frac{1}{210}\left(\sqrt{10}\, W_{200} + 2\sqrt{15}\, W_{220} \right) \\
\alpha_3 &= -\frac{1}{105}\sqrt{10}\, W_{200}
\end{aligned}
\qquad (4a)
$$

and
$$
\begin{aligned}
\beta_1 &= \frac{1}{105}\left(3\sqrt{2}\, W_{400} - 4\sqrt{5}\, W_{420} + 2\sqrt{35}\, W_{440} \right) \\
\beta_2 &= \frac{1}{105}\left(3\sqrt{2}\, W_{400} + 4\sqrt{5}\, W_{420} + 2\sqrt{35}\, W_{440} \right) \\
\beta_3 &= \frac{8}{105}\sqrt{2}\, W_{400} \\
\beta_4 &= -\frac{4}{105}\left(\sqrt{2}\, W_{400} + \sqrt{5}\, W_{420} \right) \\
\beta_5 &= -\frac{4}{105}\left(\sqrt{2}\, W_{400} - \sqrt{5}\, W_{420} \right) \\
\beta_6 &= \frac{1}{105}\left(\sqrt{2}\, W_{400} - 2\sqrt{35}\, W_{440} \right)
\end{aligned}
\qquad (4b)
$$

where $\bar{C}_{ij}$ and C^{o}_{ij} are averaging method dependent; A_1, A_2, A_3, and B, which are elastic anisotropy constants, are also averaging method dependent. For the Voigt averaging method

$$C^o_{11} = \frac{1}{15}\,(\,8c_{11} + 3c_{33} + 4c_{13} + 8c_{44})$$

$$C^o_{12} = \frac{1}{15}\,(\,c_{11} + 5c_{12} + c_{33} + 8c_{13} - 4c_{44})$$

$$C^o_{44} = \frac{1}{30}\,(\,7c_{11} - 5c_{12} + 2c_{33} - 4c_{13} + 12c_{44})$$

$$A_1 = a^c_1 = 4c_{11} - 3c_{33} - c_{13} - 2c_{44} \qquad (4c)$$

$$A_2 = a^c_2 = c_{11} - 7c_{12} + c_{33} + 5c_{13} - 4c_{44}$$

$$A_3 = a^c_3 = -\,5c_{11} + 7c_{12} + 2c_{33} - 4c_{13} + 6c_{44}$$

$$B = a^c_4 = c_{11} + c_{33} - 2c_{13} - 4c_{44}$$

and for the Reuss averaging method

$$C^o_{11} = (\,S^o_{11} + S^o_{12}\,) \,/\, |(\,S^o_{11} - S^o_{12})(\,S^o_{11} + 2S^o_{12})|$$

$$C^o_{11} = -\,S^o_{12} \,/\, |(\,S^o_{11} - S^o_{12})(\,S^o_{11} + 2S^o_{12})|$$

$$C^o_{44} = 1 \,/\, S^o_{44}$$

$$S^o_{11} = \frac{1}{15}\,(\,8s_{11} + 3s_{33} + 4s_{13} + 2s_{44}) \qquad (4d)'$$

$$S^o_{12} = \frac{1}{15}\,(\,s_{11} + 5s_{12} + s_{33} + 8s_{13} - s_{44})$$

$$S^o_{44} = \frac{2}{15}\,(\,7s_{11} - 5s_{12} + 2s_{33} - 4s_{13} + 3s_{44})$$

$$A_1 = -\,4\,C^{o2}_{44}\,a^s_1 - 14\,C^o_{12}\,C^o_{44}\,a^s_0$$

$$A_2 = -\,4\,C^{o2}_{44}\,a^s_2 + 14\,C^o_{12}\,C^o_{44}\,a^s_0$$

$$A_3 = -\,4\,C^{o2}_{44}\,a^s_3$$

$$B = -\,4\,C^{o2}_{44}\,a^s_4$$

$$a^s_0 = s_{11} + s_{12} - s_{33} - s_{13} \qquad (4d)''$$

$$a^s_1 = 4s_{11} - 3s_{33} - s_{13} - \frac{1}{2}s_{44}$$

$$a^s_2 = s_{11} - 7s_{12} + s_{33} + 5s_{13} - s_{44}$$

$$a^s_3 = -\,5s_{11} + 7s_{12} + 2s_{33} - 4s_{13} + \frac{3}{2}s_{44}$$

$$a^s_4 = s_{11} + s_{33} - 2s_{13} - s_{44}$$

where c_{ij} and s_{ij} are elastic constants and compliances of single hexagonal

crystals and are related by

$$s_{11} = \frac{1}{2}\left(\frac{c_{33}}{c_0} + \frac{1}{c_{11} - c_{12}}\right), \qquad s_{12} = \frac{1}{2}\left(\frac{c_{33}}{c_0} - \frac{1}{c_{11} - c_{12}}\right), \qquad s_{33} = \frac{c_{11} + c_{12}}{c_0},$$

$$s_{13} = -c_{13}/c_0, \qquad s_{44} = 1/c_{44}, \qquad c_0 = c_{33}(c_{11} + c_{12}) - 2c_{13}^2.$$

Once the $\bar{C}_{Voigt}$ and $\bar{C}_{Reuss}$ are determined, $\bar{C}_{Hill} = (\bar{C}_{Voigt} + \bar{C}_{Reuss})/2$ can be readily calculated. Notice that, regardless of averaging methods, the relation $A_1+A_2+A_3=0$ always exists. In addition, there are the following relations for α_i and β_i:

$$\alpha_1 + \alpha_2 + \alpha_3 = 0,$$

$$\beta_1 + \beta_2 + \beta_3 + 2(\beta_4 + \beta_5 + \beta_6) = 0,$$

$$\beta_1 + \beta_5 + \beta_6 = \beta_2 + \beta_4 + \beta_6 = \beta_3 + \beta_4 + \beta_5 = 0.$$

Table I lists the elastic isotropy and anisotropy constants for Voigt, Reuss, and Hill averaging methods for three common hexagonal materials. The single crystal elastic constants of these materials used in the computations are from [13]. Table II lists the elastic constants $\bar{C}_{ij}$ for a given set of W_{lmn} of a Ti plate sample. The rolling history and chemical composition of this Ti sample are unkown since it was purchased directly from a local vender. The W_{lmn} of this sample were obtained from neutron diffraction [14]. In this table, $\bar{C}_V$ and $\bar{C}_{R_1}$ are the elastic constants $\bar{C}_{ij}$ computed from Eqs. (4), $\bar{C}_{R_2}$ are the elastic constants $\bar{C}_{ij}$ obtained by numerically inverting $\bar{S}_{ij}$. $\bar{C}_{H_1}$ and $\bar{C}_{H_2}$ are the mean values of $\bar{C}_V$ -- $\bar{C}_{R_1}$ and $\bar{C}_V$ -- $\bar{C}_{R_2}$ respectively. One can see that $\bar{C}_{R_1}$ and $\bar{C}_{R_2}$ are reasonably close; consequently, so are $\bar{C}_{H_1}$ and $\bar{C}_{H_2}$.

One of the distinguished advantages for the representations in Eqs. (4) is the apparent resemblance to the $\bar{C}_{ij}$ -- W_{lmn} relations for the cubic

materials which were published in [12] and applied widely. In particular, realizing $W_{200}=W_{220}=0$ for cubic materials, we can obtain the $\bar{C}_{ij}$ -- W_{lmn} relations for the cubic materials by multiplying β_i in Eqs. (4b) by 3/2. The factor 3/2 is the consequence of lower order symmetry for cubic crystallites.

ACKNOWLEDGEMENT

Ames Laboratory is operated for the U. S. Department of Energy by the Iowa State University under contract No. W-7405-Eng-82. This work was supported by the Director for Energy Research, Office of Basic Energy Sciences.

REFERENCES:

1. M. J. Philippe, F. Wagner, and C. Esling. "Textures, Deformation Mechanisms and Mechanical Properties of Hexagonal Materials." Proc. 8th International Conference on Textures of Materials. Eds. J. S. Kallend and G. Gottstein. Warrendale, PA: The Metallurgical Society, 1988. 837-42.

2. T. M. Holden, R. R. Hosbons, J. H. Root, and E. F. Ibrahim. "Neutron Diffraction Measurements of Strain and Texture in Welded Zr 2.5 Nb Tube." Nondestructive Monitoring of Material Properties. Eds. J. Holbrook and J. Bussiere. Pittsburgh, PA: MRS, 1988. 59-64.

3. R. -J. Roe. "Description of Crystallite Orientation in Polycrystalline Materials. III. General Solution to Pole Figure Inversion." J. Appl. Phys. 36 (1965): 2024-31.

4. R. -J. Roe. "Inversion of Pole Figures for Materials Having Cubic Crystal Symmetry." J. Appl. Phys. 37 (1966): 2069-72.

5. Y. Li and R. B. Thompson. "Ultrasonic Characterization of Texture." Nondestructive Monitoring of Material Properties. Eds. J. Holbrook and J. Bussiere. Pittsburgh, PA: MRS, 1988. 83-88.

6. Y. Li, R. B. Thompson, and S. S. Lee. "Ultrasonic Measurement of Texture of Cubic and Hexagonal Materials." In Review of Progress in Quantitative Nondestructive Evaluation. Vol. 9B. Eds. D. O. Thompson and D. E. Chimenti. New York: Plenum Press, 1990. 1781-88.

7. C. M. Sayers. "Angular Dependent Ultrasonic Wave Velocities in Aggregates of Hexagonal Crystals." Ultrasonics 24 (1986): 289-91.

8. M. L. Smith and F. A. Dahlen. "The Azimuthal Dependence of Love and Rayleigh Wave Propagation in a Slightly Anisotropic Medium." J. Geophys. Res. 78 (1973): 3321-33.

9. P. R. Morris. "Averaging Four-Rank Tensors with Weight Functions." J. Appl. Phys. 40 (1969): 447-48.

10. C. M. Sayers. "The Elastic Anisotropy of Polycrystalline Aggregates of Zirconium and its Alloys." J. Nuclear Materials 144 (1987): 211-13.

11. R. Hill. "The Elastic Behaviour of A Crystalline Aggregate." Proc. Phys. Soc. A65 (1952): 349-354.

12. M. Hirao, K. Aoki, and H. Fukuoka. "Texture of Polycrystalline Metals Characterized by Ultrasonic Velocity Measurements." J. Acoust. Soc. Am. 81 (1987): 1434-40.

13. R. F. S. Hearmon. In Landolt - Börnstein: Numerical Data and Functional Relationships in Science and Technology. Vol. III/1. Berlin/Heidelberg: Springer-Verlag, 1966. 12.

14. C. M. Sayers, Harwell Laboratories, AERE, private communication, 1986.

Table I. Elastic isotropy and anisotropy constants (in GPa)

Mat'l	method	C^o_{11}	C^o_{12}	C^o_{44}	A_1	A_2	A_3	B
Ti	Voigt	163.93	75.53	44.20	-62.00	-145.00	207.00	23.00
	Hill	162.86	76.07	43.40	-61.80	-141.81	203.61	16.69
	Reuss	161.78	76.60	42.59	-61.60	-138.61	200.21	10.38
Zr	Voigt	145.68	72.16	36.76	-55.80	-6.60	62.40	42.40
	Hill	145.18	72.28	36.45	-49.05	-5.22	54.27	38.99
	Reuss	144.68	72.39	36.14	-42.30	-3.85	46.14	35.59
Zn	Voigt	134.81	41.59	46.61	345.40	100.70	-446.10	-31.60
	Hill	120.68	38.77	40.96	417.33	17.46	-434.79	-76.66
	Reuss	106.55	35.94	35.31	489.25	-65.78	-423.47	-121.73

Table II. Elastic constants $\bar{C}_{ij}$ for a given set of W_{lmn} (in GPa)
(W_{200} = 0.014328, W_{220} = -0.004532, W_{400} = 0.003117,
W_{440} = -0.003411, and W_{410} = 0.002361)

$\bar{C}$	11	22	33	23	13	12	44	55	66
$\bar{C}_V$	160.80	163.55	168.46	71.26	74.56	80.27	47.44	44.18	40.47
$\bar{C}_{R_1}$	158.34	161.35	166.12	72.46	75.88	81.23	45.67	42.79	39.09
$\bar{C}_{R_2}$	158.71	161.81	166.58	72.20	75.64	81.09	45.91	42.79	39.35
$\bar{C}_{H_1}$	159.57	162.45	167.29	71.86	75.22	80.75	46.55	43.48	39.78
$\bar{C}_{H_2}$	159.76	162.68	167.52	71.73	75.10	80.68	46.67	43.48	39.91

PART II.

INFLUENCE OF ANISOTROPY ON THE DISPERSION CHARACTERISTICS OF GUIDED ULTRASONIC PLATE MODES

ABSTRACT

Dispersion curves are developed for elastic wave propagation in an anisotropic plate of monoclinic or higher symmetry. Emphasis is placed on analytic expressions for various features. Generalization of the isotropic Rayleigh-Lamb dispersion relations are derived for the cases of a) propagation along a material symmetry axis and b) propagation in a general direction. Examination of the high frequency limit of the lowest symmetric and antisymmetric mode dispersion curves yields expressions for the half space surface or Rayleigh wave velocity. It is shown that the dispersion curves for these modes can exhibit multiple crossings in approaching this limit, and an analytic solution is presented for the constant crossing interval that occurs for propagation along symmetry directions. The analytic results are illustrated by extensive numerical calculations for a variety of degrees of anisotropy with emphasis placed on the relationship between the slowness curves governing partial wave propagation and various features of the dispersion curves.

INTRODUCTION

In recent years, interest in elastic wave propagation in anisotropic media has been growing rapidly. Historically, most of the work has been concerned with plane waves in unbounded media [1]; relatively little attention has been given to elastic wave propagation in anisotropic plates. This is an important gap, for in the study of polycrystalline metals or composite materials, plate structures with various degrees of macroscopic anisotropy are often encountered. Understanding of wave propagation becomes very critical in the nondestructive evaluation of these plates or in the analysis of their dynamic vibrations. Similar problems are found to have relevance in seismology. This paper is intended to explore in detail a number of features of elastic wave propagation in anisotropic plates that are substantially different from the corresponding behavior in isotropic plates. Primary emphasis is placed on the case of plates with macroscopic orthotropic symmetry, although other cases are also considered. Extensive use is made of both the development of analytic formulae for special cases and the use of numerical examples to illustrate the richness of behavior possible.

Although investigations of wave propagation in free isotropic plates were first reported in 1917 [2] and followed by extensive investigations [3~5], the pioneering work on propagation of elastic waves in free anisotropic plates was conducted and published more than 50 years later by Solie and Auld [6]. In their paper, a general formalism for computing dispersion relations for plates of arbitrary symmetry was derived. Using an interactive program, which carried out all the computational steps numerically, dispersion curves were computed for wave propagation in a (001) cut cubic Cu plate at angles of 0, 5, 30, 40, and 45 degrees from the [100] direction. These dispersion curves demonstrated the great differences between the anisotropic and isotropic

cases. Many of the features were interpreted in terms of the dispersion that would be exhibited by uncoupled SV and L modes, a concept which had first been introduced by Mindlin for the isotropic case [7]. The uncoupled mode behavior was found in turn to be strongly influenced by the slowness curves for plane waves propagating in unbounded media. Other observations of Solie and Auld included the coupling of SH waves with quasi-L and quasi-SV waves for mode propagation in nonsymmetry directions. For mode propagation along symmetry axes, it was observed that a solution consisting of disturbances bound to the two surfaces of the plate existed as the high frequency asymptotic limit of the lowest symmetric S_0 and antisymmetric A_0 modes. The wave speed in this limit could either be less (Rayleigh wave) or greater (pseudo-surface wave) than that of an SH wave propagating in the same direction, the latter being a case explored in detail by Lim and Farnell [8] in their study of acoustic surface waves. Solie and Auld also noted the oscillatory fashion in which the S_0 and A_0 modes approached this limit in certain cases, in contrast to their monotonically decreasing separation in the isotropic case. The oscillations were attributed to the concavity of the quasi-shear slowness curves in the direction of propagation. New results presented in this paper show other possible causes which produce similar phenomena.

In the last few years, an increased interest in the problem of guided wave propagation in anisotropic plates has developed. Kosevich and Syrkin derived analytical dispersion relations for hexagonal plates of special orientations and studied some particular features of these dispersion curves [9]. Markus et al. analyzed wave propagation in an orthotropic plate with concentration on wave propagation in symmetry directions [10]. They also noticed that S_0 and A_0 dispersion curves sometimes approach their asymptotic limit in an oscillatory manner. A spectrum of related works have also been reported in the literature [11~18]. At a recent conference, Nayfeh and Chimenti [19] presented studies of wave propagation in anisotropic

plates with monoclinic symmetry, including analytical expressions for dispersion equations. At the same time, the present authors [20] presented dispersion relations for orthotropic plates. The computations differed in detail (coordinate system either transformed to the propagation direction or aligned with material symmetry axes) and motivation (characterization of composites as opposed to textured metal polycrystals), but as would be expected, equivalent expressions for the dispersion curves were obtained.

In this paper, we report in detail and expand on our results [20], including their extension to monoclinic symmetry as motivated by the work of Nayfeh and Chimenti [19]. In addition to the dispersion equations, analytical expressions are presented for the associated features of the oscillations of the S_0 and A_0 modes. These analytical results are supported by detailed numerical studies of the dispersion curves of several materials having different degrees of anisotropy. To provide physical motivation, these have been chosen to correspond to copper polycrystals with different degrees of preferred grain orientation. Following the observations of Solie and Auld [6], extensive use is made of plane wave slowness surfaces to interpret the data. The paper concludes with a short summary of the results.

METHOD OF SOLUTION

The most frequently used method for analysis of wave propagation in an anisotropic medium is based on the "superposition of partial waves", wherein the final displacement solution is obtained through summation of plane wave solutions having common sinusoidal variations in the direction of propagation. The procedure for this method, which has been used in much of the prior work cited in the previous section, is outlined in the remainder of this section. The detailed mathematics of equation derivations can be found in Appendix A.

Consider a homogeneous free plate possessing a symmetry plane which is parallel to its surfaces. In other words, the material is assumed to have at least monoclinic symmetry with the symmetry plane lying in the plane of the plate. If the plate normal direction is labeled as x_3 and a Cartesian coordinate system is chosen as shown in Fig. 1, then the wave displacement field must satisfy the governing equations for an elastic, homogeneous, anisotropic, and nonpiezoelectric medium:

$$\rho \ddot{u}_i = C_{ijkl}\, u_{k,lj} \qquad (i,j,k,l=1,2,3), \qquad (1)$$

provided that body forces are negligible. In Eqs. (1), C_{ijkl} are the elastic constants, u_i are the components of the particle displacement vector and ρ is the material density. The usual summation over all repeated indices is implied.

For a harmonic disturbance of frequency ω, the displacement field for a plane wave solution with no attenuation is of form

$$\bar{u} = U n_j \bar{e}_j \exp[i(\omega t - k_l x_l)] \qquad (2)$$

for wave propagation in an arbitrary direction. In Eq. (2), $\bar{e}_j$ is a unit vector along the "j" axis, $n_j \bar{e}_j$ is the particle displacement vector (not necessarily a unit vector) and k is the wave propagation vector. U is the displacement

amplitude and n_j is the direction cosine of the displacement when $n_j \bar{e}_j$ is a unit vector.

A. Mode Propagation In an Arbitrary Direction

Substituting Eq. (2) into Eqs. (1) and employing the abbreviated notation for elastic constants leads to the Christoffel equations,

$$\begin{bmatrix} A_{11} & A_{12} & A_{13} \\ A_{12} & A_{22} & A_{23} \\ A_{13} & A_{23} & A_{33} \end{bmatrix} \begin{Bmatrix} n_1 \\ n_2 \\ n_3 \end{Bmatrix} = 0 \qquad (3)$$

where A_{ij} are functions of k_1, k_2, and k_3 and ω given in Appendix A. The solutions for plate modes may then be expressed as the superposition of all partial plane wave solutions of Eqs. (3) sharing common values of ω, k_1, and k_2. One may view the possible values of k_3 as the eigenvalues of Eqs. (3), which may be obtained by setting the determinant of the coefficient matrix to be zero. The resulting algebraic equation for k_3^2 is of cubic form in terms of k_1^2, k_2^2 and ω^2. It is this very character that makes analytical expressions presented later possible. This is in general not true for triclinic materials which do not have any symmetry planes. Let us define the roots for k_3 as $\pm\sqrt{r_1}$, $\pm\sqrt{r_2}$, and $\pm\sqrt{r_3}$ for later reference. The eigenvectors for Eqs. (3) can then be obtained in terms of these roots. The eigenvectors are partial wave displacement vectors, and for each eigenvalue of k_3, there exists one eigenvector which is uniquely determined to within a scalar multiplier.

For wave propagation in a free plate, the wave displacement field must satisfy the stress free boundary conditions: i.e.,

$$\sigma_{13} = \sigma_{23} = \sigma_{33} = 0 \qquad @\ x_3 = \pm\, b/2 \qquad (4)$$

where b is the thickness of the plate.

From Hooke's law, the total stress field can be expressed in terms of the partial wave displacement amplitudes U_p, p=1~6, which are scalar

multipliers for the eigenvectors of the partial waves. Forcing the total stress field to satisfy Eq. (4) leads to six linear equations with a 6x6 coefficient matrix for U_p.

For nontrivial solutions, the determinant of the coefficient matrix for U_p must vanish. Because the plate material possesses a symmetry plane normal to the x_3 direction, the solutions can always be separated into symmetric and antisymmetric types. By setting $U_1=\pm U_2$, $U_3=\pm U_4$, and $U_5=\pm U_6$ as needed to achieve these symmetries, the six linear equations for U_p can be reduced to a pair of three equations in U_1, U_3 and U_5. The condition for a nontrivial solution is then that the determinant of the coefficient matrix of the vector $(U_1, U_3, U_5)'$ vanishes. This leads to an analytical generalization of the Rayleigh-Lamb dispersion equations for the anisotropic case:

$$P_1\left[\tan\left(\sqrt{R_1}\frac{\pi}{2}\right)\right]^{\pm 1} + P_2\left[\tan\left(\sqrt{R_2}\frac{\pi}{2}\right)\right]^{\pm 1} + P_3\left[\tan\left(\sqrt{R_3}\frac{\pi}{2}\right)\right]^{\pm 1} = 0 \qquad (5)$$

where $P_1 = P(R_1, R_2, R_3)$, $P_2 = P(R_2, R_3, R_1)$, $P_3 = P(R_3, R_1, R_2)$, and $R_i = r_i(b/\pi)^2$. The detailed definition of the function P is provided in Eq. (A.6) of Appendix A.

Because of the existence of discontinuities in tangent functions, Eqs. (5) are not ideal for computation. To avoid these discontinuities in computations, it is advantageous to use the following expressions.

$$P_1S_1C_2C_3 + P_2S_2C_3C_1 + P_3S_3C_1C_2 = 0\,, \qquad \text{(antisymmetric)} \qquad (6)$$

$$P_1C_1S_2S_3 + P_2C_2S_3S_1 + P_3C_3S_1S_2 = 0\,, \qquad \text{(symmetric)} \qquad (7)$$

where $S_i \equiv \sin\left(\sqrt{R_i}\frac{\pi}{2}\right)$ and $C_i \equiv \cos\left(\sqrt{R_i}\frac{\pi}{2}\right)$.

Once a root to Eq. (6) or (7) is found, the stress fields and displacement fields can be computed easily. Note that Eqs. (6) and (7) are either real or purely imaginary equations. They are continuous except at a few isolated singularity points.

B. Mode Propagation in a Symmetry Direction

When the plate possesses additional symmetry, e.g., orthotropic, cubic or transversely isotropic, one can take advantage of some simplifications in the definitions of the A_{ij} in Eqs. (3) due to the vanishing or interrelationship of some of the elastic constants. Moreover, when the wave propagates in a direction coinciding with a symmetry plane, further simplifications occur which deserve some special attention. In particular, partial waves whose polarizations lie in the plane containing the propagation direction and the plate normal (sagittal plane) become decoupled from the orthogonally polarized SH (horizontally polarized shear) waves. For small anisotropy, the partial waves polarized in the sagittal plane can be identified as quasi-L and quasi-SV (vertically polarized shear) waves.

Although the analysis procedure is the same as outlined in the previous section, the final dispersion equations are in similar but simpler forms. Suppose the plate has at least orthotropic symmetry, and that x_1-x_3 and x_2-x_3 are the additional two symmetry planes. Then when propagating in the x_1 or x_2 direction, SH modes are decoupled from Rayleigh-Lamb modes, the latter being polarized in the sagittal plane.

There are two extra symmetry axes for cubic symmetry materials. In these situations, it will be advantageous to make elastic constant transformation first, then use equations presented in this section rather than those developed in the previous section. These results will not be explicitly presented in this paper.

Let $\pm\sqrt{r_1}$ correspond to the eigenvalues for SH waves. Then, the dispersion equations for Rayleigh-Lamb waves are

$$Q_1\left[\tan\left(\sqrt{R_2}\,\frac{\pi}{2}\right)\right]^{\pm 1} - Q_2\left[\tan\left(\sqrt{R_3}\,\frac{\pi}{2}\right)\right]^{\pm 1} = 0 \qquad (8)$$

(+ for antisymmetric solutions and - for symmetric solutions),

where $Q_1 = Q(R_2, R_3)$, $Q_2 = Q(R_3, R_2)$ and the function Q is defined at the end

of Appendix A. The associated computational forms are

$$Q_1 S_2 C_3 - Q_2 S_3 C_2 = 0 \qquad \text{(antisymmetric)} \qquad (9)$$

$$Q_1 C_2 S_3 - Q_2 C_3 S_2 = 0 \qquad \text{(symmetric)} \qquad (10)$$

where S_i and C_i are defined in the previous section. Eqs. (8) can be further expressed as

$$\frac{\tan\left(\sqrt{R_2}\,\frac{\pi}{2}\right)}{\tan\left(\sqrt{R_3}\,\frac{\pi}{2}\right)} = \left(\frac{Q_2}{Q_3}\right)^{\pm 1} \qquad \begin{pmatrix} + & \text{antisymmetric} \\ - & \text{symmetric} \end{pmatrix} \qquad (11)$$

This form resembles, and for an isotropic medium reduces to, the well known Rayleigh-Lamb wave dispersion equations.

C. Surface Wave Determination

The numerical studies that follow in the next section illustrate a number of interesting similarities and differences in the isotropic and anisotropic cases. Two of these have led to additional analytical studies. Appendix B considers in detail solutions that are bound near surfaces in the limit b -->∞. As noted by Solie and Auld [6], these must be closely related to the surface waves studied by Lim and Farnell [8]. The general conclusion is an analytic expression for the surface wave velocity: $P_1+P_2\pm P_3=0$, where the rule for the selection of the ± sign is given in Appendix B. For propagation along a symmetry direction, a simple expression for the Rayleigh wave velocity or the pseudo surface wave velocity can also be obtained which is equivalent to the result from Royer and Dieulesaint [16].

D. Crossing of S_0 and A_0 Modes for Propagation in Symmetry Directions

In the isotropic case, the lowest order symmetric and antisymmetric Lamb wave dispersion curves asymptotically approach one another in the high frequency limit, with the slope being the Rayleigh wave velocity. In anisotropic media, the modes may exhibit multiple crossings as they approach the surface wave limit. Appendix C shows that when the Rayleigh

wave solution occurs under the conditions for which R_2 and R_3 are complex conjugates, the S_0 and A_0 modes will have multiple crossings with the velocity of crossing points being the Rayleigh wave velocity. Also proved in Appendix C is that the spacing of these crossings is a constant, with the crossings occurring at $k = n\frac{\pi}{b}\sqrt{g(Z)}$, n=1,2,... ,where g(Z) is defined in Eq. (C.6).

NUMERICAL RESULTS

The equations of the last section have been used to numerically study a number of the features of the dispersion curves of anisotropic, free plates. As a basis of comparison, the well known behavior of guided modes in an isotropic medium is briefly reviewed. Throughout this section, the dispersion curve plots will be given in terms of the dimensionless wave vector, $\frac{b}{\pi}k$, and frequency $\frac{b}{\pi}\frac{\omega}{\sqrt{C_{66}/\rho}}$. Here k is defined to be the magnitude of the in-plane wave vector, $k=\sqrt{k_1^2 + k_2^2}$; the slowness curve plots will be given in dimensionless slownesses $\frac{k}{\omega}\sqrt{\frac{C_{66}}{\rho}}$ and $\frac{k_3}{\omega}\sqrt{\frac{C_{66}}{\rho}}$. In all plots, V_R, V_{SW}, and V_{PSW} stand for Rayleigh wave, surface wave, and pseudo surface wave velocities respectively. V_R and V_{PSW} are used to describe propagation in symmetry directions with the term pseudo surface wave used to denote the case in which the velocity is greater than that of the lowest SH mode. V_{SW} is used to describe propagation in nonsymmetry directions.

A. Isotropic Plates

Fig. 2a presents the dispersion curves for an isotropic polycrystalline plate of copper, characterized by elastic constants given in Table I. The SH partial waves, which are decoupled from the SV and L partial waves because of the isotropy, combine to form SH guided modes. The SV and L partial waves, which are coupled, combine to form Lamb guided modes. The SH and Lamb modes can be further subdivided into symmetric and antisymmetric modes, depending on the symmetry of the displacement field with respect to the mid-plane of the plate. In this paper, the Lamb modes will be identified as follows: S_0, S_1,...for the symmetric modes and A_0, A_1,...for the antisymmetric modes. The enumeration starts with the lowest ω for a fixed

k. The SH modes can also be subdivided according to their symmetry, and we will introduce the notation HS_0, HS_1...for the symmetric modes and HA_1, HA_2,...for the antisymmetric modes. In this convention, the index "0" is only used for a mode which propagates at all frequencies, i.e., has no cutoff frequency. Hence there is no mode designated HA_0.

The partial waves making up the guided mode solutions must satisfy the Christoffel equations, whose solutions are graphically illustrated by the slowness surfaces, shown in Fig. 2b. For this case of isotropy, the slowness surfaces take the form of spheres (distorted into ellipses in the figure by the choice of different scales for the ordinate and abscissa) and are indicated by solid lines. Only two slowness curves are shown, since the behaviors of the SH and SV partial waves are identical in isotropic solids. In addition to the solid slowness surfaces, Fig. 2b includes a pair of dashed hyperbole. These represent the magnitude of the purely imaginary component of k_3 that is found when $(\omega/k) < V$ where V is the velocity of the corresponding wave type (compressional or shear).

The importance of the partial wave solutions in determining the behavior of the dispersion curves was first noted by Mindlin [7] and reviewed by Meeker and Meitzler [3] and Auld [5]. At this point, it is worth recalling a few simple aspects of those discussions. Consider the case in which ω is fixed and k increases from zero. The value of k_3 will generally decrease from a finite real value to zero and will then increase with a purely imaginary value. This sequence corresponds to the partial plane wave propagating in a direction which rotates from the x_3 axis to the x_1 axis, followed by the development of an inhomogeneous (evanescent) partial wave solution in which the fields decay exponentially along the x_3 axis. As this change in character of the partial wave solution from propagating to inhomogeneous has important consequences on the dispersion curves, Figs. 2a and 2b have been divided into three regions. As the boundaries are defined by particular values of k/ω, they appear as vertical lines on the slowness plots and as lines

emanating from the origin with different slopes on the dispersion curves.

In region 1, all partial waves are freely propagating. In region 2, the L waves become inhomogeneous with an exponentially decay in the thickness direction. In region 3, both L and S solutions are inhomogeneous.

Four classes of special behavior, intimately related to the different wave propagation characteristics in these regions, are found for the isotropic media. These special behaviors are discussed in the following paragraphs. The changes induced by anisotropy will then be the topic of the remainder of the paper.

Three Mode Crossing Points in Region 1

In region 1, a series of points are found at which three modes, a symmetric Lamb, an antisymmetric Lamb, and a horizontally polarized shear mode, mutually intersect. The reason for these triple crossings may be understood from a review of Lamb wave phenomena by Meeker and Meitzler [3], who made heavy use of an earlier analysis by Mindlin [7]. While seeking analytical guidance for the construction of dispersion curves, Mindlin considered the behavior of longitudinal and vertically polarized shear partial waves under the assumption that they were not coupled at the stress free surfaces. The result was a set of hyperbolic dispersion curves characterized by ordering parameters p (longitudinal) and q (shear). Mindlin observed that, if these hypothetical dispersion curves crossed for both p and q even or both p and q odd, then the true dispersion curves would pass through the same point. It is a trivial extension to note that, since the dispersion curves of SH modes are the same as those for uncoupled SV modes, three modes will cross at each intersection.

Two Mode Crossings at Region 1-2 Boundary

Along the boundary between regions 1 and 2, $\omega/k = V_L$, the modes S_n and HS_n always cross. The reason for this crossing is as follows. Consider first

the S_n mode. In general, it will be the sum of two partial longitudinal waves inclined at angles $\pm\sin^{-1}\sqrt{1-(kV_L/\omega)^2}$ with respect to the mode propagation direction and two partial shear waves inclined at angles $\pm\sin^{-1}\sqrt{1-(kV_S/\omega)^2}$. The relative amplitudes of these partial waves are determined by first forming a symmetric combination of the two sets of partial waves and then requiring that $\sigma_{33}=\sigma_{13}=0$ at $x_3=\pm b/2$. When the S_n mode crosses the boundary line $\omega/k = V_L$, then the symmetric L solution is simply $u_1 = \exp[i(\omega t-\omega x/V_L)]$. Since this has no associated σ_{13} component of stress, the condition that $\sigma_{13}=0$ at $x_3=\pm b/2$ must be satisfied entirely by the symmetric combination of shear waves. Simple analysis shows that this leads to the condition $\sin(k_3 b/2) = 0$, equivalent to the dispersion curve for the HS_n modes. Hence the crossing at the S_n and HS_n modes on the boundary line.

Mode Tangency in Region 2

The decoupled L modes do not occur in region 2. Hence none of the three mode crossings are expected. However, it is found that the Lamb modes are tangent to the SH modes when they cross the line $\omega/k=\sqrt{2}V_S$ at the points $k=(\pi/b)p$, $p = 1, 2, \ldots$ The tangencies of the modes (S_n, HA_{n+1}; $n=0,1,\ldots$) are interleaved between the tangencies of the modes (A_n, HS_n; $n=1,2,\ldots$). At these points, known as Lamé points, the partial mode decompositions of both the Lamb and SH modes reduce to a pair of shear waves propagating at $\pm 45^0$ with respect to the plate normal. The displacements are, of course, orthogonal. In particular, the Lamé modes contain no longitudinal partial waves. At each intersection point, the modes exhibit the common group velocity $V_S/\sqrt{2}$.

Asymptotic Limit in Region 3

Only two modes are found in region 3. The A_0 mode lies in this region for all frequencies while the S_0 mode passes into this region. Because both partial waves are inhomogeneous in region 3, the modes take the form of symmetric and antisymmetric combinations of solutions localized near the plate surface. The S_0 and A_0 mode dispersion curves do not cross each other. Instead, ω/k asymptotically approaches the Raleigh velocity, V_R, for each. The displacement fields approach symmetric or antisymmetric combinations of Rayleigh waves on the two plate surfaces in this high frequency limit.

B. Anisotropic Plates

In order to better understand the effects of anisotropy on these and other features of guided wave propagation, we have computed the dispersion curves and corresponding slowness surfaces for a variety of materials and propagation directions. The materials chosen for study were modeled as copper polycrystals. The elastic constants used, as shown in Table I, were computed based on a procedure in which Hill's averaging scheme [21] is combined with an analytical representation of the effect of preferred grain orientation (texture) [22,23]. The latter is parametized by a set of orientation distribution coefficients (ODC's) [24,25], whose values are given in Table II. The ODC's were not selected because of the likelihood of finding these particular orientations in commonly encountered materials, but rather to illustrate various interesting influences of anisotropy on plate wave behavior. Even more dramatic effects would be expected for such strongly anisotropic materials as fiber reinforced composites. Here "ISO" refers to the previously discussed isotropic example, "WA" is an example with relatively weak anisotropy, and "SA", "SB", and "SC" are three examples with relatively strong anisotropy. The case of "AL" corresponding to a single crystal of aluminum rather than polycrystalline copper, was added to illustrate weak anisotropy with cubic symmetry.

Table III lists the numerical examples and the associated figures to be discussed in the following subsections. In each figure, the dispersion curves shown in part a) is accompanied by slowness curves in part b). The latter provide important information needed to interpret the former, as has already been seen for the isotropic case.

Propagation Along a Symmetry Direction

For propagation along a symmetry axis ($\theta = 0^0$ or 90^0 in orthotropic plates; $\theta = 0^0, 45^0$, or 90^0 in cubic plates), the guided modes decouple in a fashion that is similar to the isotropic plate response. Again, Lamb mode solutions are polarized in the sagittal plane and SH mode solutions are polarized in the plane of the plate perpendicular to the propagation direction. Each of these can be subdivided into symmetric and antisymmetric modes using the previously introduced notations.

As can be seen from the slowness curves, shown in part b of each figure for propagation along a symmetry direction (Figs. 3, 4, 5, 7, 10, 11, 13, 14, and 16), the SH partial waves have a behavior that is quite similar to that found in the isotropic case, with the slowness surfaces becoming ellipses rather than circles. The slowness curve in the inhomogeneous wave region is again a hyperbola. The dispersion curves $\omega(k)$ formed for the SH plate modes, obtained through the superposition of these SH partial waves, are also hyperbole, asymptotically approaching the velocity of a plane shear wave, $\sqrt{C_{66}/\rho}$ for $\theta = 0^0$ or 90^0 and $\sqrt{(C_{11}-C_{12})/2\rho}$ for $\theta = 45^0$ in the "AL" case, as frequency increases.

The other four partial waves do not generally have polarizations which are purely parallel or purely perpendicular to the propagation direction. For modest degrees of anisotropy, they can be identified as quasi-longitudinal (QL) or quasi-shear vertical (QSV) waves. We have found that the QL and QSV slowness curves can be divided into three classes of behavior which produce significantly different dispersion curves. These behaviors are

influenced by the following underlying analytic behavior. As noted before, solution of the Christoffel equations leads to a cubic equation with real coefficients for k_3^2. Along symmetry directions, the solution for k_3 is either purely real or purely imaginary for SH partial waves. After removing that response, k_3^2 for the QL and QSV partial waves is governed by a quadratic equation with real coefficients. It follows from the quadratic theorem that the solutions for k_3^2 must be both real or a complex conjugate pair. After evaluating the square root, k_3 can have a pair of real values (RR), a real and a purely imaginary value (RI), a pair of imaginary values (II), or a pair of complex conjugate values (CC).

We have found that for a fixed ω, the sequence through which the pair of roots passes as k increases falls in three classes of response, and that each class of slowness response produces quite different dispersion curves. The class I response is a distortion of the isotropic case (Figs. 14 and 16). As k increases, the solutions for k_3 pass through the sequence RR-RI-II as first the QL and then the QSV solutions become inhomogeneous. In class II response, the pair of imaginary solutions meet. The sequence then becomes RR-RI-II-CC (Figs. 3. 4, 5, 7, and 13), with the imaginary portion of the complex pair of roots emanating from the II intersection and the real part growing from the abscissa in a fashion that has the qualitative appearance of a hyperbola. Class III responses occurs when the real part of the k_3 solution for the QSV partial wave is a multivalued function of k, as often occurs in strongly anisotropic media (Figs. 10 and 11). This forces the initial portion of the sequence to be RR-RI-RR, with the inhomogeneous extension of the QL partial wave slowness (purely imaginary) returning to the axis to merge with the QSV partial wave slowness. Under such conditions, we have found that the full sequence is RR-RI-RR-CC. In distinction to Class II, the real portion of the complex conjugate pair emanates for the turning point on the

QT slowness while the imaginary part grows from the abscissa in a fashion that again has the qualitative appearance of a hyperbola.

The numerical examples illustrate the influence of each of these slowness responses on the guided mode dispersion curves. For each case studied, the slowness curves are divided into regions according to the character of solutions for k_3/ω. When the corresponding behavior for the SH wave is excluded, one finds 3 distinct regions in class I and 4 regions in classes II and III responses. The boundaries between these regions are indicated on the dispersion curves by lines of the appropriate slope. Note that, when SH waves are included in the slowness and dispersion curves, extra regions may appear depending on the details of anisotropy. The total numbers of regions for the examples presented here are listed in Table IV. For orthotropic plates, there are generally four regions in class I response and five regions in class II and III responses. Due to the smallness of the II region in Fig. 3, the boundary lines for this region become extremely close on the figure. Also note that, for propagation in symmetry directions, the boundary lines for the SH waves are always identical to the HS_0 mode dispersion curves. To avoid overlaying of the lines for the boundaries and HS_0 modes and display both of them clearly, we plotted the HS_0 modes for the range of $kb/\pi=1\sim5$ and the boundary lines of SH waves for the range of $kb/\pi=5\sim6$.

In all cases, regions 1 and 2 have a similar character to that exhibited in isotropic media. However, examination of the dispersion curves show that the three mode crossing points in region 1, the two mode crossing points on the region 1-2 boundary, and the mode tangencies in region 2 no longer occur. This is not surprising since the analytical arguments that were previously presented supporting the existence of these special points depended in detail on the isotropy of the material. As in the isotropic case, crossings of the S_n and A_n modes are generally not observed in region 2. As noted by Solie and Auld [6], this would appear to be the anisotropic

generalization of Mindlin's arguments [7]. If one wrote the anisotropic generalization of the dispersion curves for decoupled QL and QSV partial waves it would be found that the crossings of the decoupled dispersion curves correspond to those of the S_n and A_n modes. However, all these must occur in region 1 where the QL partial waves are freely propagating. One exception associated with the multivalued regions of the QSV partial waves, will be discussed later. In distinction to the tangency of the isotropic case, the SH modes generally cross the Lamb modes in region 2.

Class I response is observed in both weakly and strongly anisotropic materials (Figs. 14 and 16). As in the isotropic case, there are no crossings of the S_n and A_n modes beyond region 1. The S_0 and A_0 modes asymptotically approach one another in the high frequency limit, each consisting of combinations of surface wave solutions on the two plate surfaces. The velocity in this surface wave limit may be either greater (Fig. 16) or less (Fig. 14) than the lowest SH modes. The strong influence of the slowness curves is particularly noticeable in Fig. 14. Note the near vertical segment of the QL slowness curve, which implies that partial waves will have group velocities nearly parallel to the x_1 axis and of magnitude close to the reciprocal of the projected intercept of the slowness curve with the abscissa [5]. Recalling that the group velocity of a guided mode is given by $V_g = d\omega/dk$ the tendency of the S_n and A_n modes to be tangent to the line dividing regions 1 and 2 is consistent with the notion that the Lamb mode group velocities are also close to this value.

Class III response is only observed in some strongly anisotropic materials (Figs. 10 and 11). The multivalued QSV slowness curves and associated complexities lead to dramatic changes in the dispersion curves. In contrast to the class I response, crossings between the S_n and A_n modes appear in many regions. Note in particular the behavior of the S_0 and A_0 modes, which cross one another at multiple points as k increases. As shown in Appendix C, these crossings all fall on a line passing through the origin

and having a slope equal to the Rayleigh or pseudo-surface wave velocity. Furthermore, they are equally spaced with the interval given in that appendix. This intertwining of the modes is a consequence of the complex conjugate relationship between the solutions for k_3. Intertwining of other modes is also observed. It qualitatively appears that the degree of intertwining is related to the extent of the multivalued region of the QSV mode slowness.

Solie and Auld [6] noted that the intertwining of the S_0 and A_0 dispersion curves was related to the multivalued QSV slowness curve. We have found a second condition that produces this same consequence. The class II response corresponds to the sequence RR-RI-II-CC, (Figs. 3, 4, 5, 7, and 13), which is generally found in materials with weak anisotropy but possibly with strong anisotropy (Fig. 13). Fig. 13 is a special case which can be viewed as having the II region in class II or the second RR region in class III shrunk to zero. As in class I, but distinct from class III, crossings of the S_n and the A_n modes in class II generally do not occur beyond region 1. A qualitative examination of the printed figures might suggest that the S_0 and the A_0 modes asymptotically approach one another at high frequencies. However, examination of the numerical data, as well as the analysis presented in Appendix C, shows that they cross at equally spaced intervals in all the cases presented except Fig. 5. This exception is discussed below.

These observations lead to a generalized interpretation of the S_0 and A_0 mode crossing phenomenon. Solie and Auld noted that multivalued QSV slowness curves produce crossing, as confirmed by our class III results. Observation of the same phenomena in class II suggests that a more general cause is responsible. Examination of the analysis in Appendix C suggests that the controlling factor is the existence of a pair of complex conjugate roots for k_3 when k is equal to the Rayleigh wave vector. This is confirmed by referring to the above figures, on which the Rayleigh or pseudo-surface wave vector has also been marked. With the exception of Fig. 5, the Rayleigh or

pseudo-surface wave vector falls in the CC region of the slowness for all members of Classes II and III; hence, the S_0 and A_0 mode crossings are expected. This interpretation is consistent with the alternate explanation of Solie and Auld in which the oscillatory behavior was associated with a finite real part of the transverse partial wave vector.

A generalization of this observation appears to govern other mode crossings. It was reported above that extensive S_n and A_n mode crossing were found in class III. Comparison of the dispersion and slowness regions reveals that these only occur in regions in which both the QL and QSV partial wave solution for k_3 have real components (Figs. 10 and 11). In fact, all the figures presented support the generalization that S_n and A_n mode crossings are only found in regions in which both the QL and QSV slowness have real parts. This statement can be validated by analyzing Eqs. (11) as follows.

In order for S_n and A_n to cross, the following equation must be satisfied:

$$\tan^2\left(\sqrt{R_2}\,\frac{\pi}{2}\right) = \tan^2\left(\sqrt{R_3}\,\frac{\pi}{2}\right). \qquad (12)$$

In the RR region where both R_2 and R_3 are positive, the solutions to Eq. (12) are $\sqrt{R_2} + \sqrt{R_3} = 2n$, where n is an integer; thus, there are infinitely many crossings in the RR region. In the RI region where either R_2 or R_3 is negative (say $R2 < 0$); then $\tan\left(\sqrt{R_2}\,\frac{\pi}{2}\right) = i\tanh\left(\sqrt{|R_2|}\,\frac{\pi}{2}\right)$. Plugging this expression into Eq. (12) leads to the conclusion that no crossing can be found in the RI region. In the II region where both R_2 and R_3 are negative, Eq. (12) can be rewritten as

$$\left(\tanh\left(\sqrt{|R_2|}\,\frac{\pi}{2}\right) - \tanh\left(\sqrt{|R_3|}\,\frac{\pi}{2}\right)\right)\left(\tanh\left(\sqrt{|R_2|}\,\frac{\pi}{2}\right) + \tanh\left(\sqrt{|R_3|}\,\frac{\pi}{2}\right)\right) = 0.$$

Except the root R_2=R_3, which is the boundary lines of the II and the CC regions, no meaningful solution exists for the above equation; hence S and A do not cross in the II region. The crossing phenomenon in the CC region, as mentioned before, is discussed in details in Appendix C.

In isotropic media and many cases of anisotropy, the Rayleigh velocity is less than the lowest SH velocity, which is approached by other modes. However, the Rayleigh velocity can be greater than that of the slowest SH waves, in which case the Rayleigh waves are known as pseudo surface waves. This phenomenon has been observed for both strongly and weakly anisotropic plates in all three classes (Figs. 4, 11, 13, and 16).

Table IV summarizes the characteristics of the examples discussed above.

Propagation in a General Direction

When considering propagation in a general direction, pure SH solutions do not generally exist. None of the partial waves have pure polarizations (parallel or perpendicular to the propagation direction) and all are coupled by the boundary conditions. If one imagines propagation at an angle slightly removed from a symmetry axis, the S_n and HS_n become coupled to form a set of symmetric modes while the A_n and HA_n modes become coupled to form a set of antisymmetric modes. When the anisotropy is small or propagation is near a symmetry direction, the plate modes can be identified as having quasi-SH or Lamb character. In other cases, This identification is often not possible.

The slowness plots can again be characterized according to the sequence of roots, with strong implications on the form of dispersion curves. However, now the behavior of all three roots must be considered in the analysis. In class NI, the general form of the isotropic response is followed with the sequence RRR-RRI-RII-III. Here, the prefix N has been added to the previous classification to indicate propagation along a nonsymmetry direction. In one deviation, two of the imaginary segments will intercept, leading to class NII, which has region sequence RRR-RRI-RII-III-ICC. In another deviation (class NIII) multivalued slowness surfaces enter. Numerous possible subsequences can occur which will not be enumerated in

detail. The numerical results presented illustrate some, but not all, of the possible cases.

The class NI response (Fig. 15) is again a variant of the isotropic behavior. However, there are now only two sets of modes, the symmetric S_n modes can be thought of as the combination of quasi-S_n and Quasi-HS_n modes while the antisymmetric A_n modes can be thought of as the combination of quasi-A_n and quasi-HA_n modes. Along symmetry directions, the S_n and HS_n modes were decoupled (as were the A_n and HA_n) and could cross. This is not so for propagation in nonsymmetry directions, and a number of cases of mode repulsion are observed. Near these repulsions, a mode may change rapidly from quasi-Lamb to quasi-SH character or vice versa. The quasi-transverse slowness curves, which crossed at 0^0, are now coupled and hence repel. Thus the partial wave polarization rapidly changes in this region.

Class NII behavior is exhibited in Fig. 6 for the case of propagation at 45^0 in weakly anisotropic material WA. The response is essentially the same as that observed in Figs. 5 and 7, with the addition of certain mode repulsions and rapid changes in polarization as discussed above. The mode repulsions in Fig. 6 are not obvious due to the weak anisotropy, but close examinations of numerical data unquestionably confirmed all the repulsions at all the seemingly crossing points for modes of same symmetry.

A wide variety of phenomena can be observed in class NIII, as illustrated by Figs. 8, 9, and 12. Figs. 8 and 9 present results at 30^0 and 60^0 for strongly anisotropic material SA. These are characterized by a multivalued region of the inner quasi-transverse mode. Fig. 8 shows a case where the surface wave velocity is about the same as that of the SH plane wave solution. In this case, the surface wave is of SH type because the wave motion has large SH component. When this occurs, a solution known as the quasi surface wave (V_{QSW}), where the wave motion has a large component in the saggital plane, often exists in the RCC region [8]. A close examination of Fig. 8a confirms this conclusion. Fig. 12 presents results at 20^0 in strongly

anisotropic material SB. Here both inner and outer quasi-transverse curves are multivalued.

Because the coupling of the three partial waves in each plate mode makes it impossible to differentiate SH and Lamb modes, mode crossings may be found throughout the dispersion curves in the general propagation direction in any of these classes. As for propagation along symmetry directions, special features depending on isotropy no longer exist. The surface wave solution is always found in a region in which all roots have an imaginary component. In class NI, the A_0 and S_0 modes asymptotically approach this limit. In the class NII response shown in Fig. 6, the surface wave solution fell in a region with purely imaging solutions for k_3 and no mode crossing was observed. In class NIII response, mode crossings are observed as the surface wave limit is approached, which is in a region with ICC roots. However, the interval between crossings is not equal, and crossings do not fall on a straight line.

Because of these complexities, explicit formulae for surface wave velocity computations have not been obtained. However, the implicit analytic formulae given in Appendix B are still valid and the solution for the surface wave can be found in the ICC region. Although sometimes difficult to see, particularly for strong anisotropy, the surface wave velocity is still the asymptotic limit of the A_0 and S_0 modes.

Table V lists the characteristics of the examples discussed in this section.

IV. CONCLUSIONS

We have developed a set of dispersion equations for elastic wave propagation in a general monoclinic free plate. These equations are consistent with and, when the anisotropy vanishes, reducible to the well known Rayleigh-Lamb dispersion equations. As a by-product, we have also derived equations for the computation of the surface wave speed. Through some representative numerical examples having different degrees of anisotropy, we have demonstrated the deviation of dispersion behavior for general orthotropic free plates from the isotropic one. We have predicted that, for wave propagating in a symmetry direction, S_0 and A_0 will cross each other infinitely many times if the Rayleigh wave occurs in the all-complex-eigenvalue region. Furthermore, we have proved that, for wave propagating in a symmetry direction, when S_0 and A_0 cross each other, the crossing points are equally spaced, and the phase velocities of all crossing points are identical to that of the Rayleigh wave. Needless to say, the dispersion relations for anisotropic plates are significantly more complicated than those for isotropic plates. Further study is inevitable to fully comprehend the nature of the wave propagation.

ACKNOWLEDGEMENT

Ames Laboratory is operated for the U. S. Department of Energy by the Iowa State University under contract No. W-7405-Eng-82. This work was supported by the Director for Energy Research, Office of Basic Energy Sciences.

REFERENCES

1. M. J. P. Musgrave. Crystal Acoustics. San Francisco: Holden-Day, 1970.

2. H. Lamb. "On Waves in An Elastic Plate" Proc. Roy. Soc. London. A 93 (1917): 114-28.

3. T. R. Meeker and A. H. Meitzler. "Guided Wave Propagation in Elongated Cylinders and Plates." In Physical Acoustics. Ed. W. P. Mason. New York: Academic, 1965. 112-119.

4. I. A. Viktorov. Rayleigh and Lamb Waves. New York: Plenum Press, 1967.

5. B.A. Auld. Acoustic Fields and Waves in Solids. Vol. II. New York: Wiley, 1973.

6. L. P. Solie and B. A. Auld. "Elastic Waves in Free Anisotropic Plates." J. Acoust. Soc. Am. 54 (1973): 50-65.

7. R. D. Mindlin. "Waves and Vibrations in Isotropic, Elastic Plates." in Structural Mechanics. New York: Pergamon, 1960. 199-232.

8. T. C. Lim and G. W. Farnell. "Character of Pseudo Surface Waves on Anisotropic Crystals." J. Acoust. Soc. Am. 45 (1969): 845-51.

9. Y. A. Kosevich and E. S. Syrkin. "Elastic Waves in Plates of Highly Anisotropic Crystal." Sov. Phys. Acoust. 31 (1985): 365-67.

10. S. A. Markus, M. D. Kaplan, and S. V. Veremeenko. "Propagation of Natural Waves in Orthotropic Plates" Sov. J. Nondestr. Test 21 (1985): 739-44.

11. C. R. Reuter. "On the Plate Velocity of a Generally Orthotropic Plate." J. Comp. Mat. 4 (1970): 129-32.

12. D. E. Munson and K. W. Schuler. "Steady Wave Analysis of Wave Propagation in Laminates and Mechanical Mixtures." J. Comp. Mat. 5 (1971): 286-304.

13. T. S. Chow. "On the Propagation of Flexural Waves in an Orthotropic Laminated Plate and Its Response to an Impulsive Load." J. Comp. Mat. 5 (1971): 30619.

14. J. Lothe and D. M. Barnett. "On the Existence of Surface-wave Solutions for Anisotropic Elastic Half-spaces with Free Surface." J. Appl. Phys. 47 (1976): 428-33.

15. D. M. Barnett and J. Lothe. "Free Surface (Rayleigh) waves in Anisotropic Elastic Half-spaces: the Surface Impedance Method." Proc. R. Soc. Lond. A402 (1985): 135-152.

16. D. Royer and E. Dieulesaint. "Rayleigh Wave Velocity and Displacement in Orthorhombic, Tetragonal, Hexagonal, and Cubic Crystals." J. Acoust. Soc. Am. 76 (1984): 1438-44.

17. E. R. Baylis and W. A. Green. "Flexural Waves in Fibre-Reinforced Laminated Plates." J. Sound and Vib. 110 (1986): 1-26.

18. G. T. Mase and G. C. Johnson. "An Acoustoelastic Theory for Surface Waves in Anisotropic Media." J. Appl. Mech. 54 (1987): 127-35.

19. A. H. Nayfeh and D. E. Chimenti. "Free Wave Propagation in Plates of General Anisotropic Media." In Review of Progress in Quantitative Nondestructive Evaluation. Vol. 8A. Eds. D. O. Thompson and D. E. Chimenti. New York: Plenum Press, 1989. 181-88.

20. Y. Li and R. B. Thompson. "Propagation of Guided Elastic Waves in Orthotropic Plates." In Review of Progress in Quantitative Nondestructive Evaluation. Vol. 8A. Eds. D. O. Thompson and D. E. Chimenti. New York: Plenum Press, 1989. 189-96.

21. M. Hirao, K. Aoki, and H. Fukuoka. "Texture of Polycrystalline Metals Characterized by Ultrasonic Velocity Measurements." J. Acoust. Soc. Am. 81 (1987):1434-40.

22. R. B. Thompson, J. F. Smith, S. S. Lee, and G. C. Johnson. "A Comparison of Ultrasonic and X-ray Determinations of Texture in Thin Cu amd Al Plates." Met. Trans. 20A (1989): 2431-2447.

23. C. M. Sayers. "Ultrasonic Velocities in Anisotropic Polycrystalline Aggregates" J. Phys. D: Appl. Phys. 15 (1982): 2157-67.

24. R. -J. Roe. "Description of Crystallite Orientation in Polycrystalline Materials. III. General Solution to Pole Figure Inversion." J. Appl. Phys. 36 (1965): 2024-31.

25. R. -J. Roe. "Inversion of Pole Figures for Materials Having Cubic Crystal Symmetry." J. Appl. Phys. 37 (1966): 2069-72.

26. J. F. Nye. Physical Properties of Crystals. Oxford: Claredon Press, 1957.

Table I. Elastic Constants (in GPa)

Case	C_{11}	C_{22}	C_{33}	C_{23}	C_{13}	C_{12}	C_{44}	C_{55}	C_{66}
AL	108.0	108.0	108.0	62.0	62.0	62.0	28.3	28.3	28.3
ISO	200.7	200.7	200.7	106.1	106.1	106.1	47.3	47.3	47.3
WA	200.0	197.1	198.3	108.8	105.9	107.1	50.1	47.1	48.3
SA	182.1	167.7	174.9	126.2	111.8	119.1	92.1	53.5	67.6
SB	210.3	231.3	170.0	111.0	132.0	70.7	58.2	109.4	24.2
SC	284.3	228.7	245.3	111.6	56.1	72.6	44.7	28.5	32.9

Table II. Orientation Distribution Coefficients

Case	W_{400}	W_{420}	W_{440}
WA	0.002	0.0015	0.001
SA	0.025	0.01	0.015
SB	0.031	-0.010	-0.018
SC	-0.020	0.010	-0.015

Table III. Numerical Examples And Associated Figures

Fig.	2	3	4	5	6	7	8	9	10	11	12	13	14	15	16
Case	ISO	AL	AL	WA	WA	WA	SA	SA	SA	SB	SB	SB	SC	SC	SC
Dir.	all	0^0	45^0	0^0	45^0	90^0	30^0	60^0	90^0	0^0	20^0	90^0	0^0	60^0	90^0

Table IV. Characteristics of Examples for Propagation in Symmetry Directions

Figure	Number of Regions	Class	Region Sequence[a]	Surface Wave Type	S_0 and A_0 Crossing	First Crossing[b]
2	3	I	RR-RI-II	R	N	∞
3	4	II	RR-RI-II-CC	R	Y	3.2745
4	5	II	RR-RI-II-CC	PSW	Y	4.4512
5	5	II	RR-RI-II-CC	R	N	∞
7	5	II	RR-RI-II-CC	R	Y	5.9917
10	5	III	RR-RI-RR-CC	R	Y	1.2493
11	5	III	RR-RI-RR-CC	PSW	Y	1.2054
13[c]	4	II	RR-RI-CC	PSW	Y	2.6450
14	4	I	RR-RI-II	R	N	∞
16	4	I	RR-RI-II	PSW	N	∞

[a] Excluding SH modes.

[b] The value of the dimensionless wave number bk/π at the first mode crossing point of the S_0 and A_0 modes; i.e., $\sqrt{g(Z)}$ in Eq. (C.6).

[c] Degenerate case.

Table V. Characteristics of Examples for Propagation in Nonsymmetry Directions

Figure	Number of Regions	Class	Region Sequence	Surface Wave Region
6	5	NII	RRR-RRI-RII-III-ICC	III
8	5	NIII	RRR-RRI-RRR-RCC-ICC	ICC
9	5	NIII	RRR-RRI-RRR-RCC-ICC	ICC
12	7	NIII	RRR-RRI-RRR-RCC-RRR-RCC-ICC	ICC
15	4	NI	RRR-RRI-RII-III	III

APPENDIX A: DERIVATION OF DISPERSION EQUATIONS

For a material of monoclinic symmetry with symmetry plane parallel to x_1-x_2 plane (see Fig. 1), there are in general 13 nonzero elastic constants in the elastic tensor [26]. If we make the following definitions,

$$\begin{aligned}
\alpha_{11} &= C_{11}\cos^2\alpha + 2C_{16}\sin\alpha\cos\alpha + C_{66}\sin^2\alpha \\
\alpha_{22} &= C_{66}\cos^2\alpha + 2C_{26}\sin\alpha\cos\alpha + C_{22}\sin^2\alpha \\
\alpha_{33} &= C_{55}\cos^2\alpha + 2C_{45}\sin\alpha\cos\alpha + C_{44}\sin^2\alpha \\
\alpha_{23} &= (C_{44} + C_{23})\sin\alpha + (C_{45} + C_{36})\cos\alpha \\
\alpha_{13} &= (C_{45} + C_{36})\sin\alpha + (C_{13} + C_{55})\cos\alpha \\
\alpha_{12} &= C_{16}\cos^2\alpha + (C_{12} + C_{66})\sin\alpha\cos\alpha + C_{26}\sin^2\alpha
\end{aligned} \tag{A.1}$$

$$K = \left(\frac{b}{\pi}k\right)^2, \quad W = \left(\frac{b}{\pi}\right)^2\frac{\rho\omega^2}{C_{66}}, \quad K_3 = \left(\frac{b}{\pi}k_3\right)^2$$

where k is the wave number in the propagation direction and α is the angle of propagation direction with respect to x_1 direction, then the elements of Christoffel matrix in Eqs. (3) can be expressed as

$$\begin{aligned}
A_{11} &= (\alpha_{11}K + C_{55}K_3 - C_{66}W)\left(\frac{\pi}{b}\right)^2, \quad A_{23} = \alpha_{23}\sqrt{KK_3}\left(\frac{\pi}{b}\right)^2, \\
A_{22} &= (\alpha_{22}K + C_{44}K_3 - C_{66}W)\left(\frac{\pi}{b}\right)^2, \quad A_{13} = \alpha_{13}\sqrt{KK_3}\left(\frac{\pi}{b}\right)^2, \\
A_{33} &= (\alpha_{33}K + C_{33}K_3 - C_{66}W)\left(\frac{\pi}{b}\right)^2, \quad A_{12} = (\alpha_{12}K + C_{45}K_3)\left(\frac{\pi}{b}\right)^2.
\end{aligned} \tag{A.2}$$

By setting the determinant of Christoffel matrix to zero, we have an equation of cubic form for K_3 in terms of K and W which can be easily solved. By defining the roots for K_3 as $(K_3)_i = R_i$, the eigenvector (or displacement vector) for each partial wave can be obtained through the first two equations of Eqs. (3) as

$$\begin{Bmatrix} n_1 \\ n_2 \\ n_3 \end{Bmatrix}_{p,\,p+1} = \begin{Bmatrix} \pm\sqrt{KR_r}\,N_x(R_r) \\ \pm\sqrt{KR_r}\,N_y(R_r) \\ N_z(R_r) \end{Bmatrix} \qquad p=1,3,5;\ r = \begin{Bmatrix} 1 \text{ for } p=1 \\ 2 \text{ for } p=3 \\ 3 \text{ for } p=5 \end{Bmatrix} \qquad (A.3)$$

where $N_x(R) = (\alpha_{12}K + C_{45}R)\alpha_{23} - (\alpha_{22}K + C_{44}R - C_{66}W)\,\alpha_{13}$

$N_y(R) = (\alpha_{12}K + C_{45}R)\alpha_{13} - (\alpha_{11}K + C_{55}R - C_{66}W)\,\alpha_{23}$

$N_z(R)=(\alpha_{11}K+C_{55}R-C_{66}W)(\alpha_{22}K+C_{44}R-C_{66}W)-(\alpha_{12}K+C_{45}R)^2$

and the first and second subscripts on the left side of Eqs. (A.3) correspond to, respectively, the upper and lower signs on the right side of the equations.

The stress field, based on Hooke's law $\sigma_{ij} = C_{ijkl}\,u_{k,l}$ can be obtained as

$$\{\sigma_{i3})_{p,p+1} = U_{p,p+1}\,f_i(R_r)\,e^{\mp i\sqrt{R_r}\frac{\pi}{b}x_3}\exp\left|i(\omega t - k_1x_1 - k_2x_2)\right| \qquad (A.4)$$

where $f_1(R_r) = \sqrt{K}G_1(R_r)$, $f_2(R_r) = \sqrt{K}G_2(R_r)$, and $f_3(R_r) = \pm\sqrt{R_r}G_3(R_r)$

$G_1(R) = C_{55}RN_x(R) + C_{45}RN_y(R) + (C_{45}\sin\alpha + C_{55}\cos\alpha)N_z(R)$

$G_2(R) = C_{45}RN_x(R) + C_{44}RN_y(R) + (C_{44}\sin\alpha + C_{45}\cos\alpha)N_z(R)$

$G_3(R) = K(C_{13}\cos\alpha+C_{36}\sin\alpha)N_x(R)+K(C_{23}\sin\alpha+C_{36}\cos\alpha)N_y(R)+C_{33}N_z(R).$

The relation between r and p is the same as that in Eqs. (A.3). The total stress field is then $(\sigma_{i3})_{Total} = \sum_{p=1}^{6}(\sigma_{i3})_p$.

By imposing the stress free boundary conditions (Eq. (4)) and separating the symmetric and antisymmetric solutions, we have, for antisymmetric solutions,

$$\begin{bmatrix} \sqrt{K}G_1(R_1)\,C_1 & \sqrt{K}G_1(R_2)\,C_2 & \sqrt{K}G_1(R_3)\,C_3 \\ \sqrt{K}G_2(R_1)\,C_1 & \sqrt{K}G_2(R_2)\,C_2 & \sqrt{K}G_2(R_3)\,C_3 \\ \sqrt{R_1}G_3(R_1)\,S_1 & \sqrt{R_2}G_3(R_2)\,S_2 & \sqrt{R_3}G_3(R_3)\,S_3 \end{bmatrix} \begin{Bmatrix} U_1 \\ U_2 \\ U_3 \end{Bmatrix} = 0 \qquad (A.5)$$

where S_i and C_i are as defined in Eqs. (9) and (10). Symmetric solutions can be obtained by making C_i <--> S_i substitutions to Eqs. (A.5). For nontrivial solutions, the determinant of the coefficient matrix must vanish. This leads to Eqs. (6) and (7), which can be more concisely expressed as Eqs. (5) with the

definition of P as,

$$P(X,Y,Z) = \sqrt{X}\, G_3(X)|G_1(Y)\, G_2(Z) - G_1(Z)\, G_2(Y)| \qquad (A.6)$$

If the plate material possesses another symmetry plane which is perpendicular to the plate surfaces, then when wave propagates in a direction parallel to this plane, SH waves are decoupled from L and SV waves, which means the displacement vectors due to SH waves are perpendicular to those of L and SV waves. If the added symmetry plane is aligned with x_1-x_3 plane, then significant simplifications can be made on the dispersion equations. In such a case, $C_{16}=C_{26}=C_{36}=C_{45}=0$ and Eqs. (A.2) become $\alpha_{11} = C_{11}$, $\alpha_{22} = C_{66}$, $\alpha_{33} = C_{55}$, $\alpha_{13} = C_{13} + C_{15}$, $\alpha_{12} = \alpha_{23} = 0$, and the roots for K_3 can be solved explicitly as

$$(K_3)_1 = R_1 = -\frac{C_{66}}{C_{44}}(K-W) \qquad \text{(SH waves)} \qquad (A.7)$$

and $$(K_3)_{2,3} = R_{2,3} = \frac{-b\pm\sqrt{b^2-4ac}}{2a} \qquad \text{(L and SV waves)} \qquad (A.8)$$

where $a = C_{33}C_{55}$

$$b = (C_{13}C_{33}-2C_{13}C_{55}-C_{13}^2)K - C_{66}(C_{33}+C_{55})W$$

$$c = C_{11}C_{55}K^2 - (C_{11}+C_{55})C_{66}KW + C_{66}^2 W^2$$

For isotropic media, Eqs. (A.8) give $R_{2,3} = -K + \frac{C_{44}}{C_{11}, C_{44}}W$.

From the boundary conditions for SH waves, we can readily get the dispersion equations for the SH waves as (for both antisymmetric and symmetric modes):

$$\sin\left(\pi\sqrt{R_1}\right) = 0 \qquad \text{or} \quad W = K + \frac{C_{44}}{C_{66}}n^2 \qquad \text{(n—integer)} \qquad (A.9)$$

For quasi-L and quasi-SV waves, on the other hand, the eigenvectors can be obtained from the first equation of Eqs. (3). After applying boundary conditions $\sigma_{13}=\sigma_{33}=0$ @ $x_3=\pm b/2$ and separating symmetric and antisymmetric solutions, the dispersion equations become Eqs. (8) with

$$Q(X,Y) = \sqrt{X}\ (A_1X+A_2)\ (B_1Y-B_2)$$

$$A_1 = C_{33}C_{55}\ ,\ A_2 = K|C_{11}C_{33}-C_{13}(C_{13}+C_{55})| - C_{33}C_{66}W \qquad (A.10)$$

$$B_1 = C_{13}\ ,\qquad B_2 = C_{66}W - C_{11}K.$$

One can also use the third equation of Eqs. (3) to get the eigenvectors. The resulting dispersion relations, given by Markus et al. [10], are equivalent but in different form.

APPENDIX B: SURFACE WAVE SPEED DETERMINATION

B.1. Wave Propagates in An Arbitrary Direction of A Monoclinic Material

In order to have a surface wave, the R_i must be either negative (so the square roots are pure imaginary) or complex numbers; this ensures that the superposition of partial waves has the property of "exponential decay". There are two cases: 1) R_1, R_2, and R_3 are all negative; and 2) R_1 is negative and $R_2=R_3^*$ are complex conjugates.

For case 1, as $b\to\infty$, $\left[\tan\left(\sqrt{R_r}\frac{\pi}{2}\right)\right]^{\pm 1}\to \pm i$, so, we have from Eqs. (5):

$$P_1 + P_2 + P_3 = 0 \qquad \text{(B.1)}$$

For case 2, $b\to\infty$, $\left[\tan\left(\sqrt{R_1}\frac{\pi}{2}\right)\right]^{\pm 1}\to \pm i$ and if $R_2=a+id$, $R_3=a-id$, $(d>0)$ then $\left[\tan\left(\sqrt{R_2}\frac{\pi}{2}\right)\right]^{\pm 1}\to \pm i$ and $\left[\tan\left(\sqrt{R_3}\frac{\pi}{2}\right)\right]^{\pm 1}\to +i$ thus, Eqs. (5) become

$$P_1 + P_2 - P_3 = 0 \qquad \text{(B.2)}$$

Although Eqs. (B.1) and (B.2) are functions of K and W, the surface wave velocity can be obtained by solving for the ratio W/K; then ρV_{sw}^2, with V_{SW} being the surface wave velocity, equals $C_{66}W/K$.

B.2 Wave Propagates in Principal Direction (Say X_1 Direction)

Similar to the situation described in B.1, we have two cases: 1) R_2 and R_3 are all negative; and 2) $R_2=R_3^*$ are complex conjugates. Equations (8) become

$$Q_1 \pm Q_2 = 0 \qquad \begin{pmatrix} - \text{ for case 1} \\ + \text{ for case 2} \end{pmatrix} \qquad \text{(B.3)}$$

Equations (B.3) can be further simplifies to

$$A_3 Z^3 + A_2 Z^2 + A_1 Z + A_0 = 0 \qquad \text{(for both cases)} \qquad \text{(B.4)}$$

where $Z = \rho V_R^2$, $B = C_{11}C_{33} - C_{13}^2$, $A_0 = C_{55}B^2$, $A_1 = -B(2C_{33}C_{55} + B)$

$A_2 = C_{33}[C_{55}(C_{33} - C_{11}) + 2B]$, and $A_3 = C_{33}(C_{55} - C_{33})$.

Equation (B.4) reduces to the well known Rayleigh wave equation for isotropic media.

APPENDIX C. MULTIPLE CROSSINGS OF S_0 AND A_0 MODES FOR WAVE PROPAGATION IN SYMMETRY DIRECTIONS

When Rayleigh waves occur in the region $R_2=R_3^*$, S_0 and A_0 modes are found crossing each other with the crossing points equally spaced. This can be shown analytically.

The region boundary line of the $R_2=R_3^*$ region is dictated by $b^2-4ac=0$ in Eqs. (A.8)'. The vanishing of this discriminant gives another quadratic equation for $Z_0=\rho V^2$,

$$a_1 Z_0^2 + b_1 Z_0 + c_1 = 0 \qquad (C.1)$$

where $a_1 = (C_{33}-C_{55})^2$,

$b_1 = 2\{2C_{55}[C_{33}(C_{11}+C_{55})+C_{13}(C_{55}+C_{33})]+(C_{55}+C_{33})(C_{13}^2-C_{11}C_{33})\}$,

$c_1 = (C_{13}^2-C_{11}C_{33})[4C_{55}(C_{13}+C_{55})+C_{13}^2-C_{11}C_{33}]$.

Thus, if $Z_0 > Z$, where Z is calculable from Eq. (B.4), then the Rayleigh wave will occur in the complex region $R_2=R_3^*$.

When S_0 and A_0 cross, the crossing points must satisfy both dispersion equations, i.e.,

$$Q_1 \tan\left(\sqrt{R_3}\frac{\pi}{2}\right) - Q_2 \tan\left(\sqrt{R_2}\frac{\pi}{2}\right) = 0 \qquad (C.2)$$

and

$$Q_1 \tan\left(\sqrt{R_2}\frac{\pi}{2}\right) - Q_2 \tan\left(\sqrt{R_3}\frac{\pi}{2}\right) = 0 \qquad (C.3)$$

Since in the region $R_2=R_3^*$, $\tan\left(\sqrt{R_2}\frac{\pi}{2}\right) = -\tan\left(\sqrt{R_3}\frac{\pi}{2}\right)$, both of the above dispersion equations become $Q_1+Q_2=0$. This is identical to Eqs. (B.3) case 2, the Rayleigh wave speed computation equation. Thus, the A_0 and S_0 crossing points fall on the Rayleigh wave line.

Furthermore, the solution to $\tan\left(\sqrt{R_2}\frac{\pi}{2}\right) = -\tan\left(\sqrt{R_3}\frac{\pi}{2}\right)$ can be found as

$$\sqrt{R_2} + \sqrt{R_3} = 2n \qquad (C.4)$$

where n is an integer. This can be simplified to

$$\sqrt{4ac} - b = 4an^2 \qquad (C.5)$$

where a, b, and c are defined in Eqs. (A.8).

Since we know at the crossing points the velocity is the Rayleigh wave velocity, Eq. (C.5) can be rewritten as (recall $C_{66}W/K=\rho V_R^2=Z$):

$$K = g(Z)\, n^2 \quad \text{or} \quad k = n\frac{\pi}{b}\sqrt{g(Z)} \qquad n=1,2,... \qquad (C.6)$$

where $g(Z)=\dfrac{4C_{33}C_{55}}{\sqrt{4C_{33}C_{55}(C_{11}-Z)(C_{55}-Z)-[(C_{11}C_{33}-2C_{13}C_{55}-C_{13}^2)-(C_{33}+C_{55})Z]}}$.

For a particular material, g(Z) is a constant, therefore the crossings on dispersion curve plot will be equally spaced.

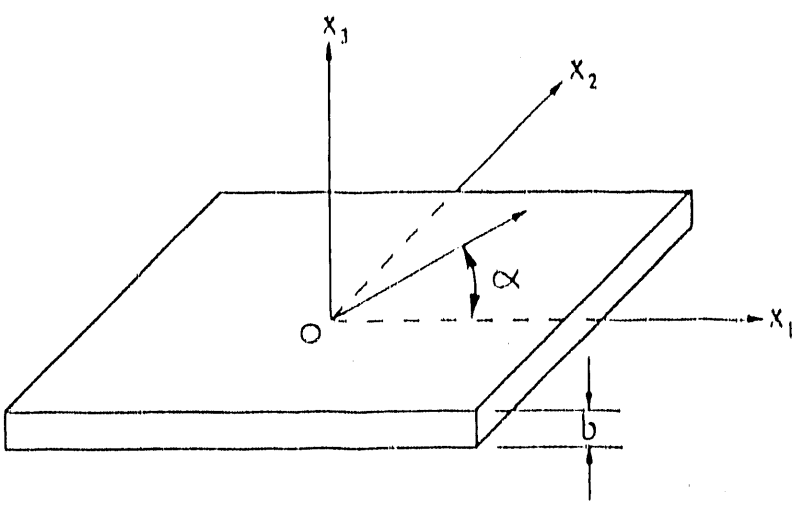

Fig. 1. Coordinates of plate

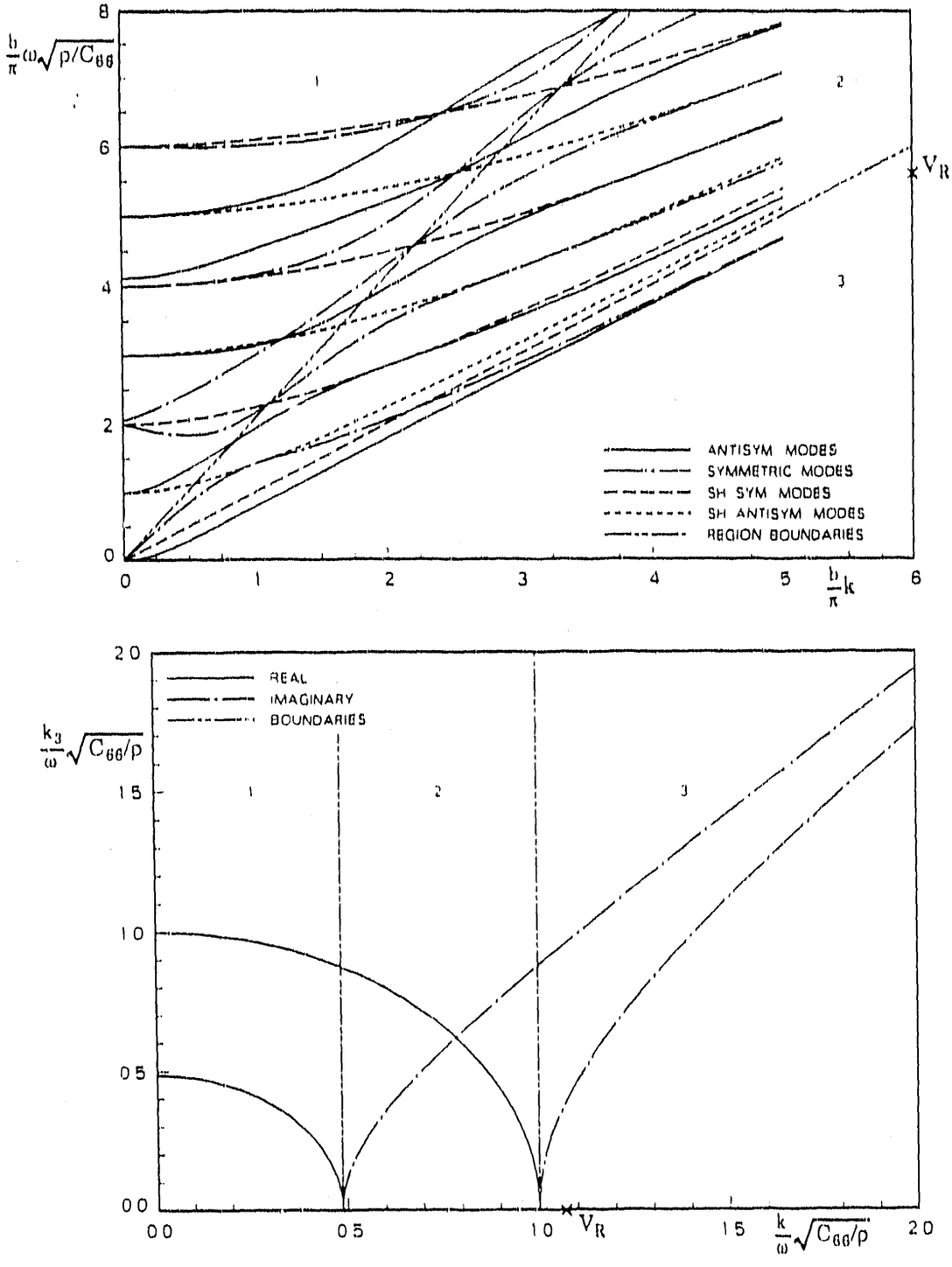

Fig. 2. Wave propagation in an isotropic copper polycrystal plate, a) dispersion curves; b) slowness curves

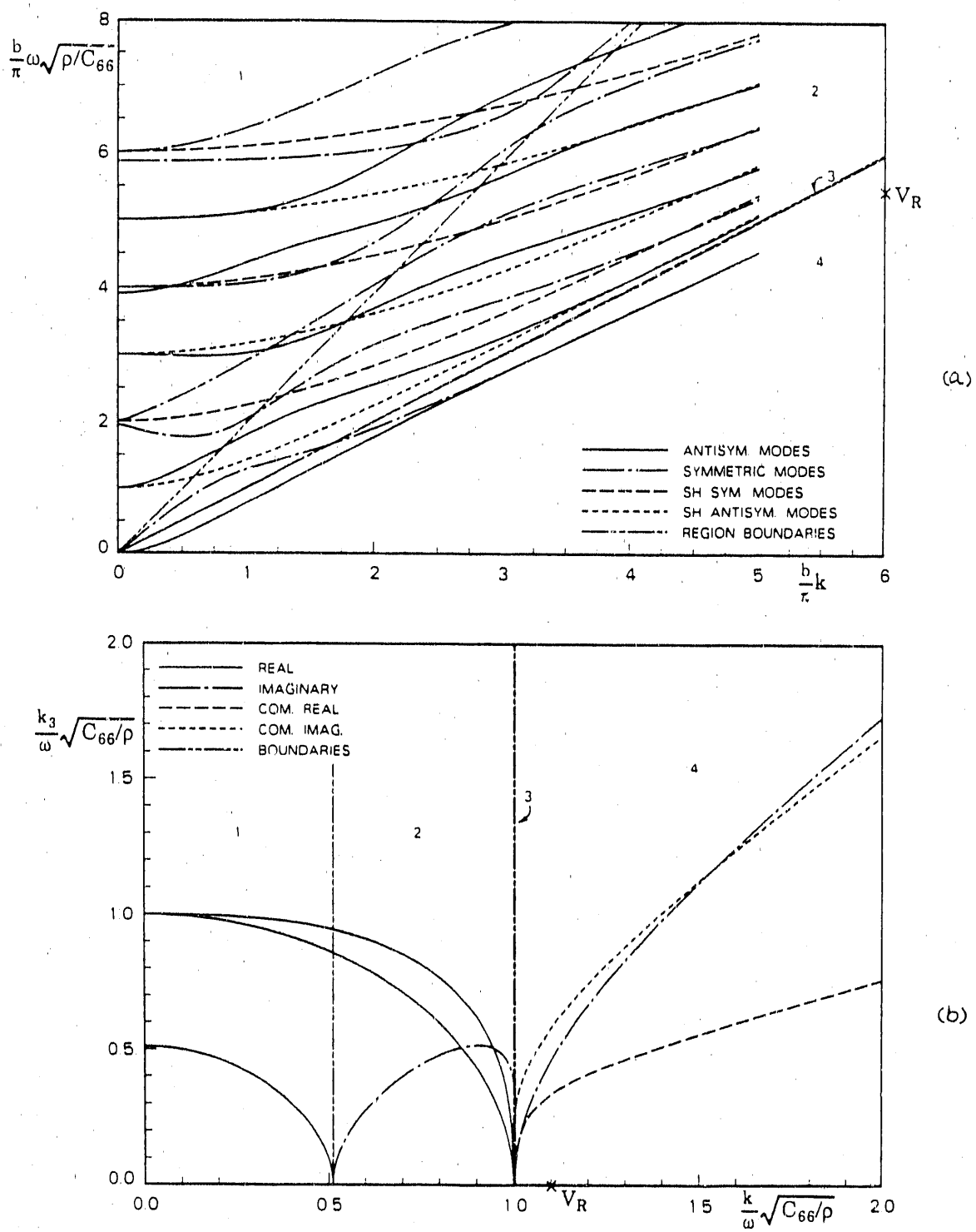

Fig. 3. Wave propagation in single crystal Al plate on {100} plane in <010> direction a) dispersion curves; b) slowness curves

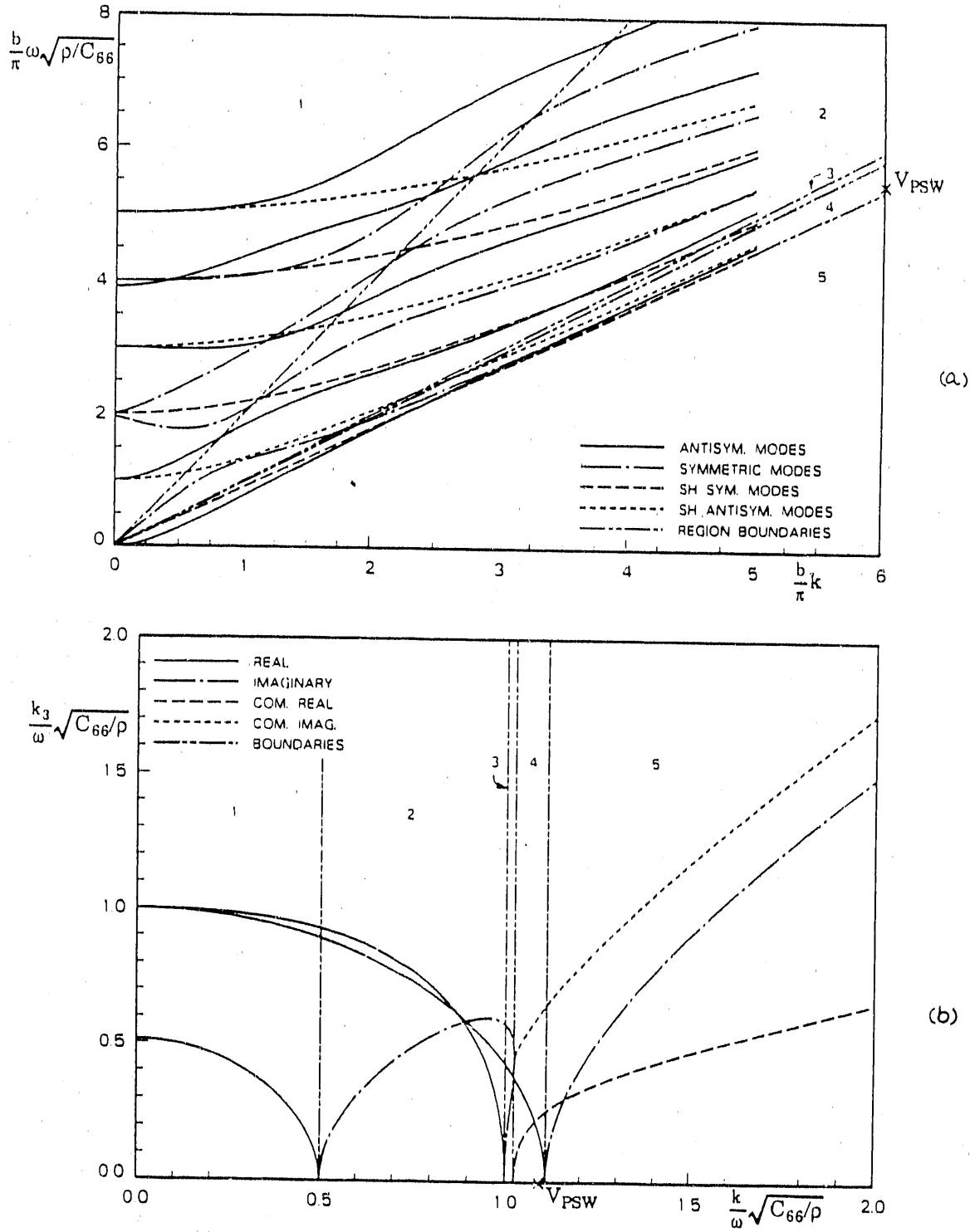

Fig. 4. Wave propagation in single crystal Al plate on {100} plane in <110> direction a) dispersion curves; b) slowness curves

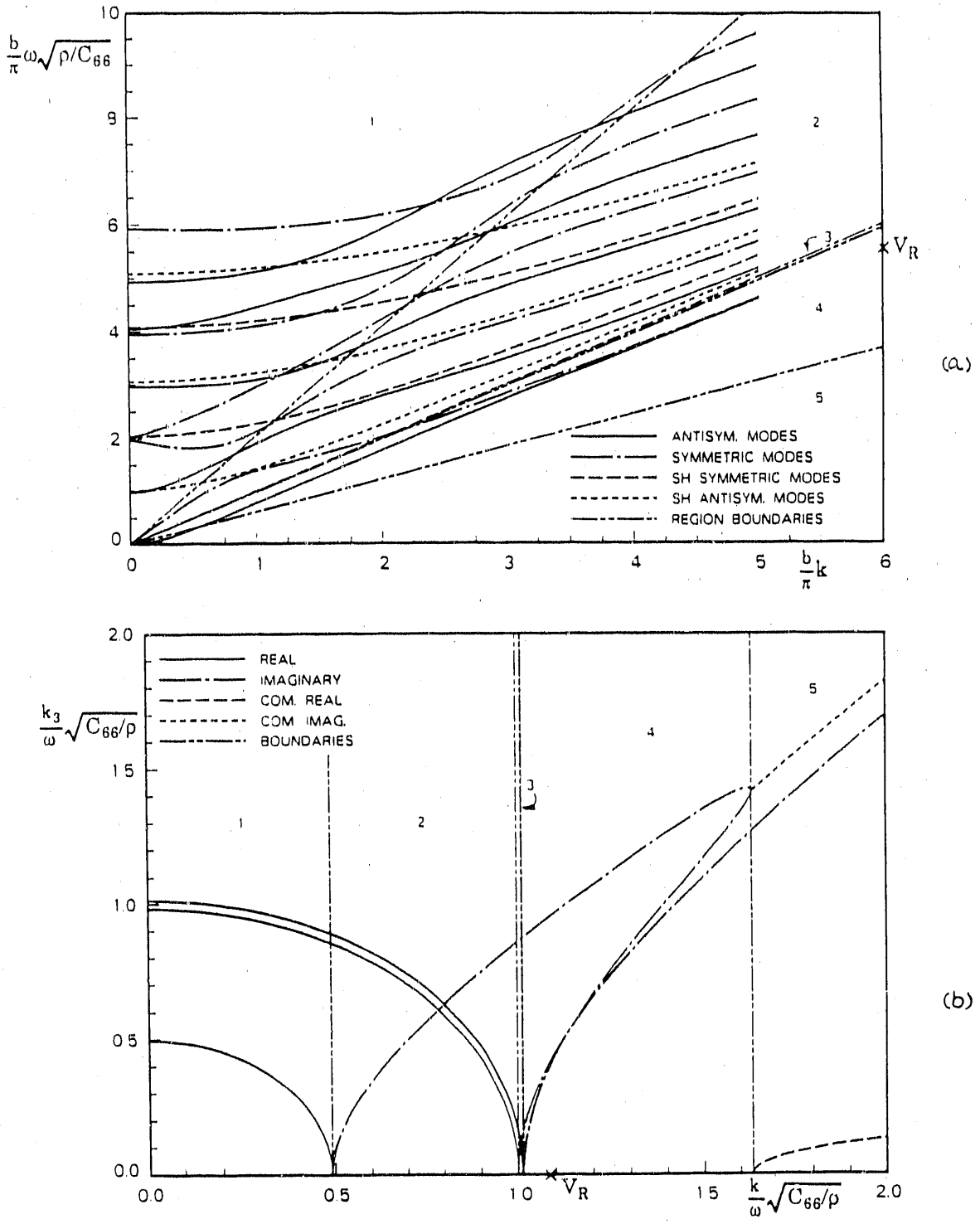

Fig. 5. Wave propagation in weakly orthotropic copper polycrystal plate (case WA), propagation angle is 0 degrees: a) dispersion curves; b) slowness curves

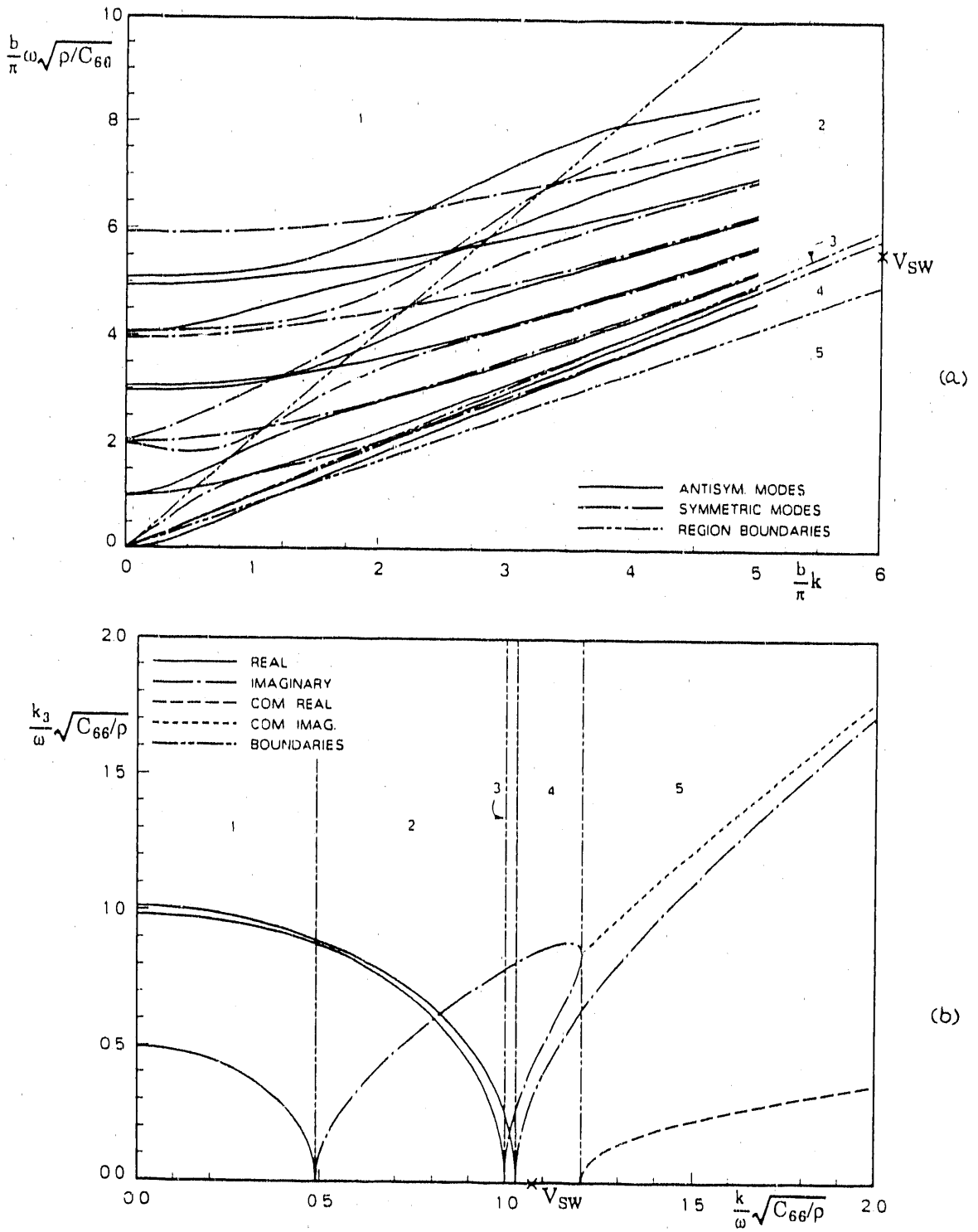

Fig. 6. Wave propagation in weakly orthotropic copper polycrystal plate (case WA), propagation angle is 45 degrees: a) dispersion curves; b) slowness curves

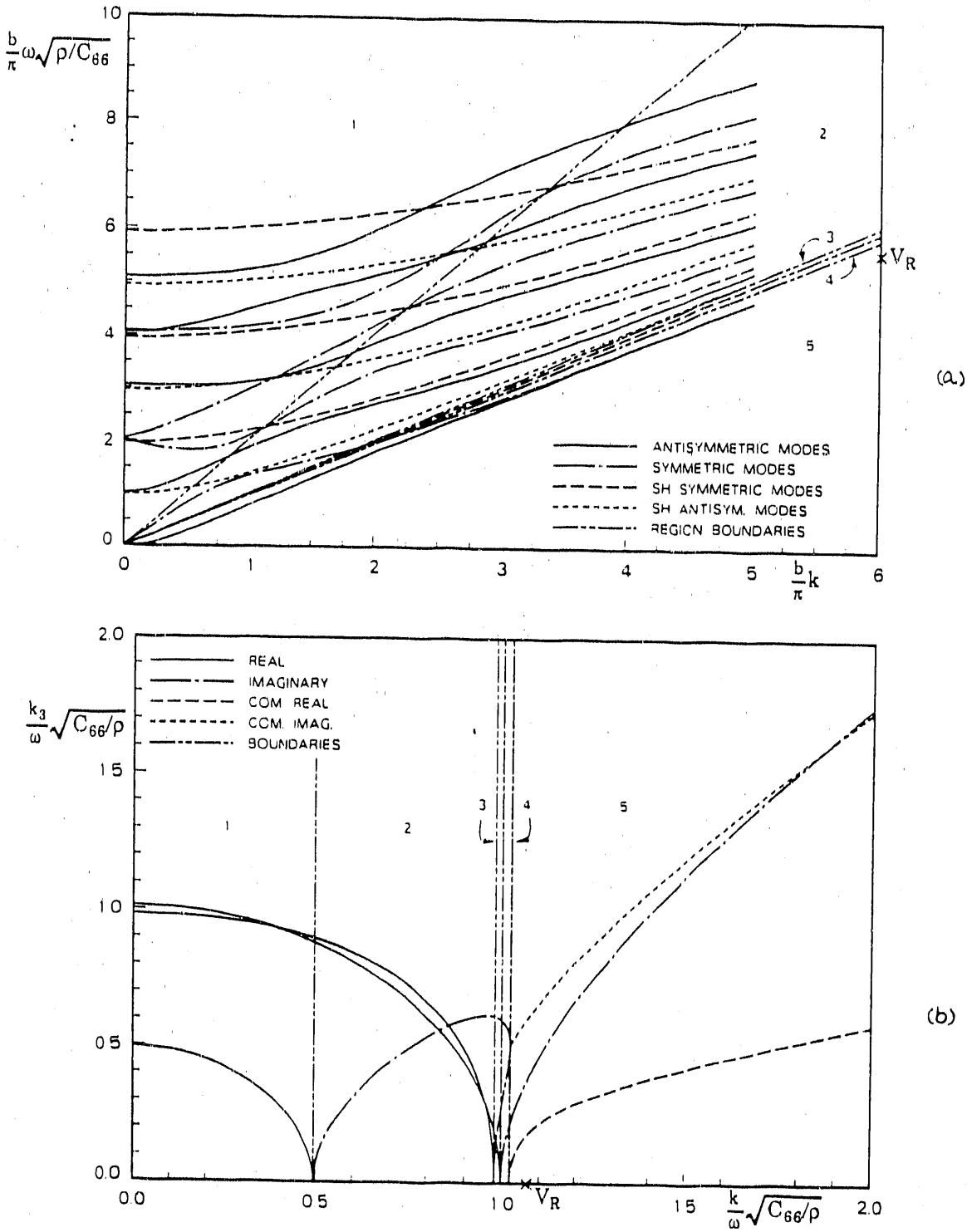

Fig. 7. Wave propagation in weakly orthotropic copper polycrystal plate (case WA), propagation angle is 90 degrees: a) dispersion curves; b) slowness curves

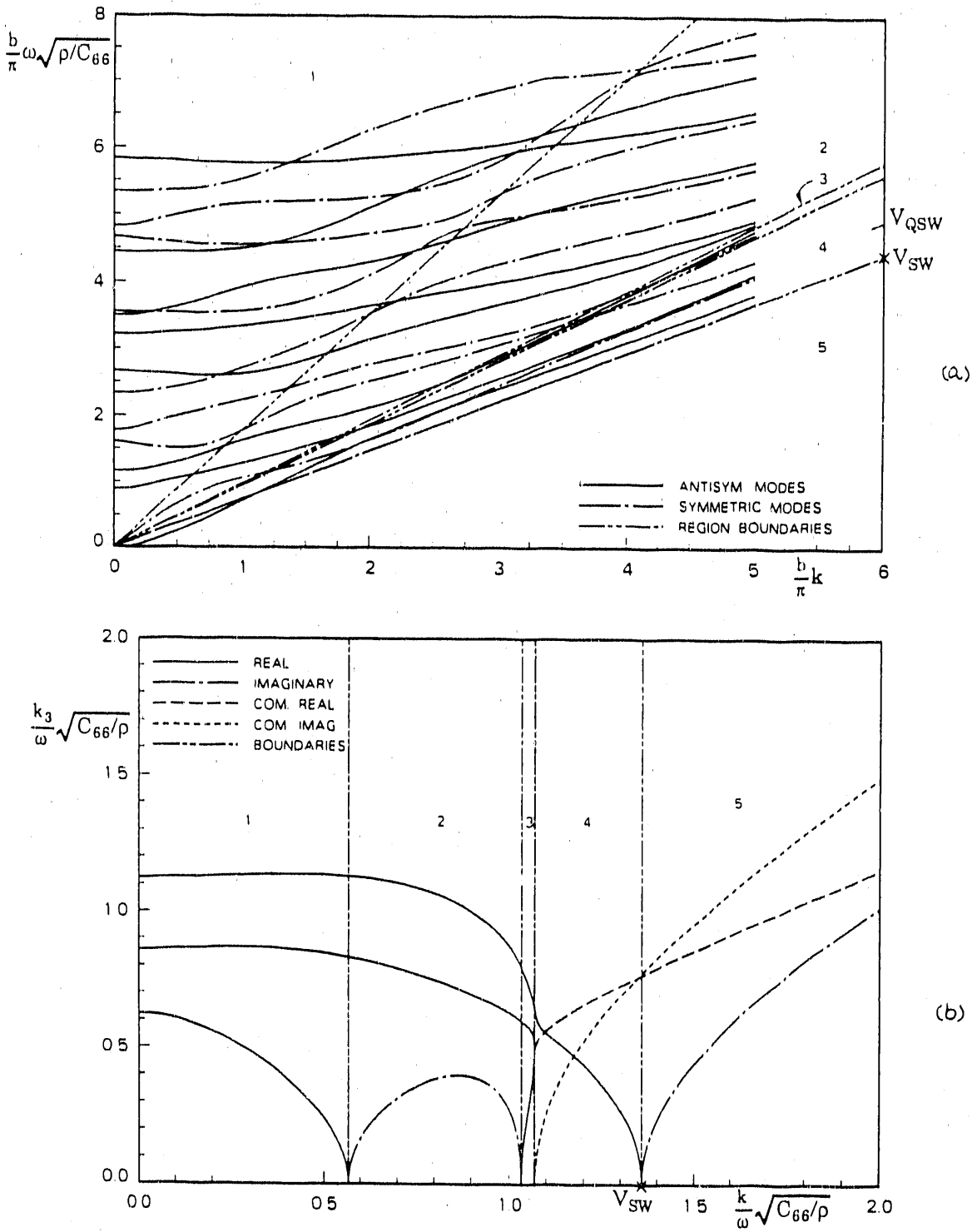

Fig. 8. Wave propagation in strongly orthotropic copper polycrystal plate (case SA), propagation angle is 30 degrees: a) dispersion curves; b) slowness curves

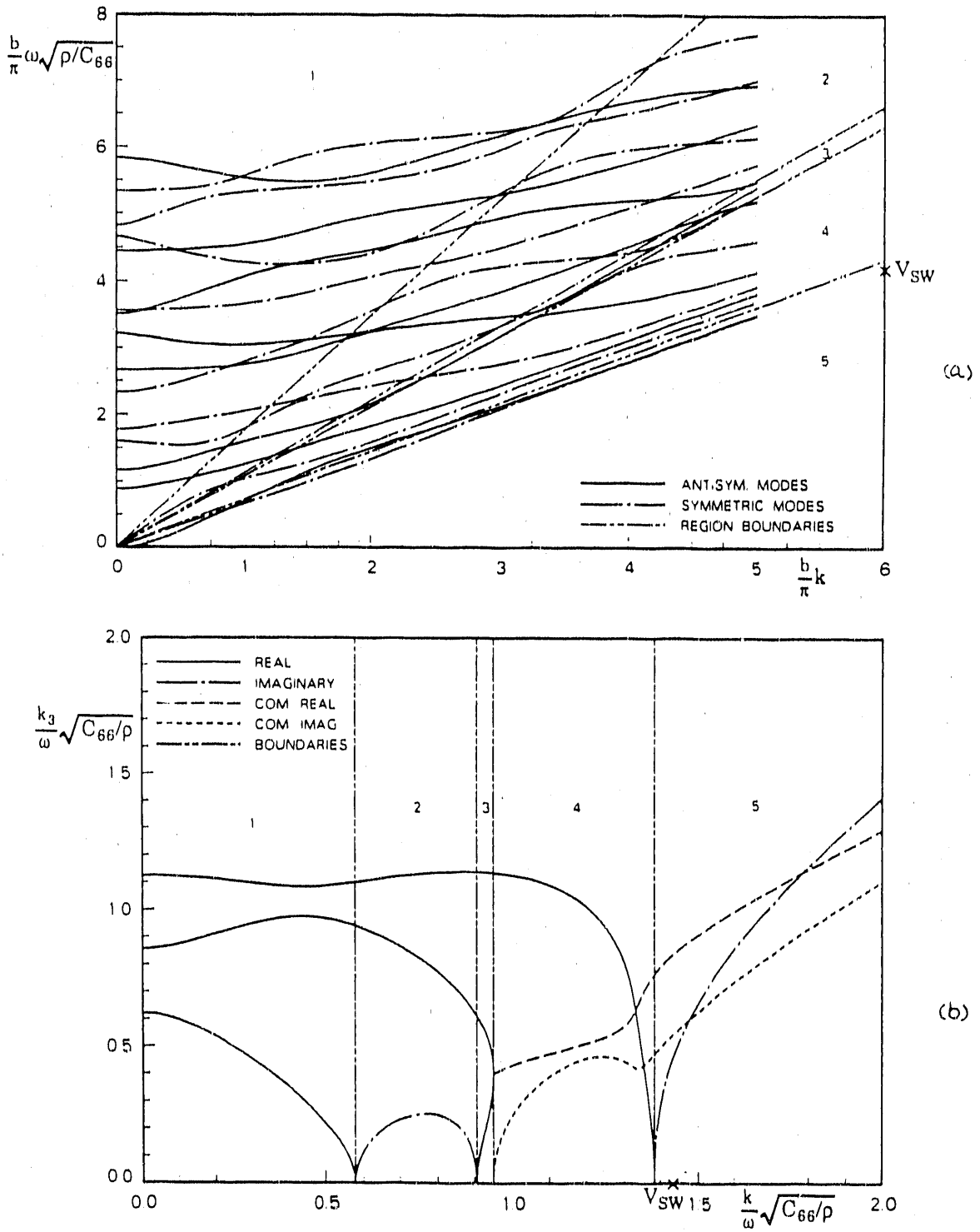

Fig. 9. Wave propagation in strongly orthotropic copper polycrystal plate (case SA), propagation angle is 60 degrees: a) dispersion curves; b) slowness curves

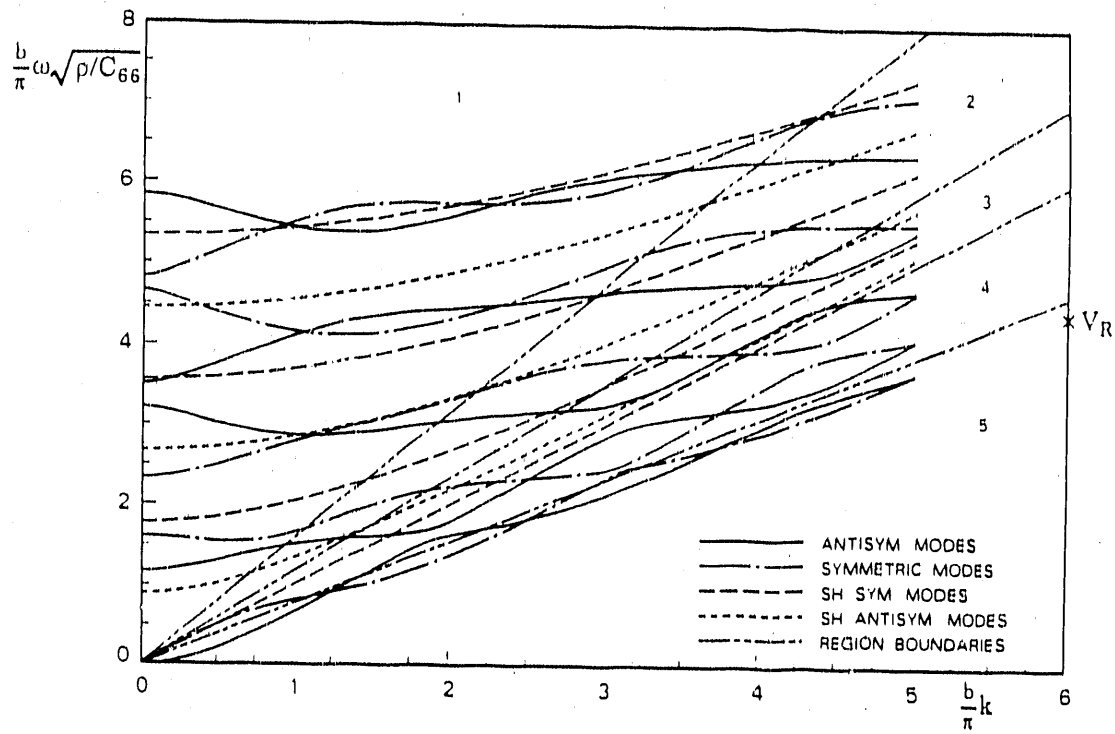

(a)

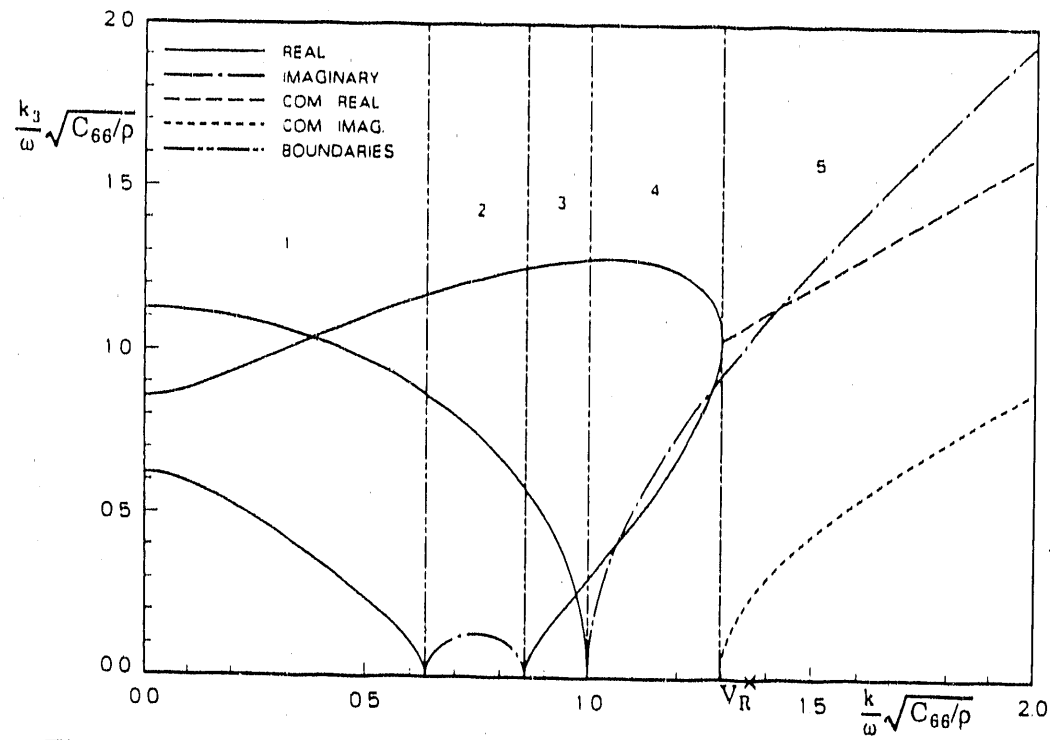

(b)

Fig. 10. Wave propagation in strongly orthotropic copper polycrystal plate (case SA), propagation angle is 90 degrees: a) dispersion curves; b) slowness curves

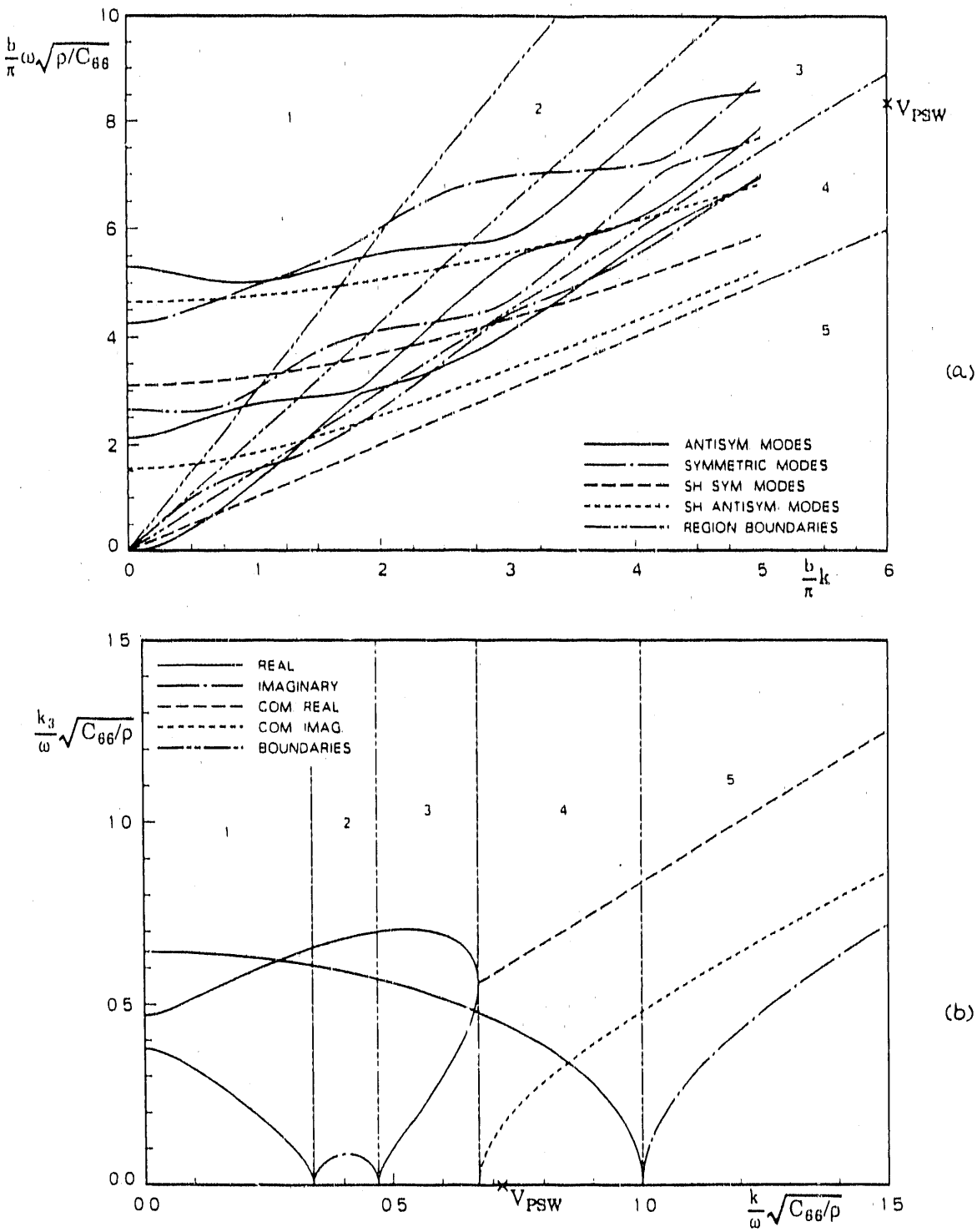

Fig. 11. Wave propagation in strongly orthotropic copper polycrystal plate (case SB), propagation angle is 0 degrees: a) dispersion curves; b) slowness curves

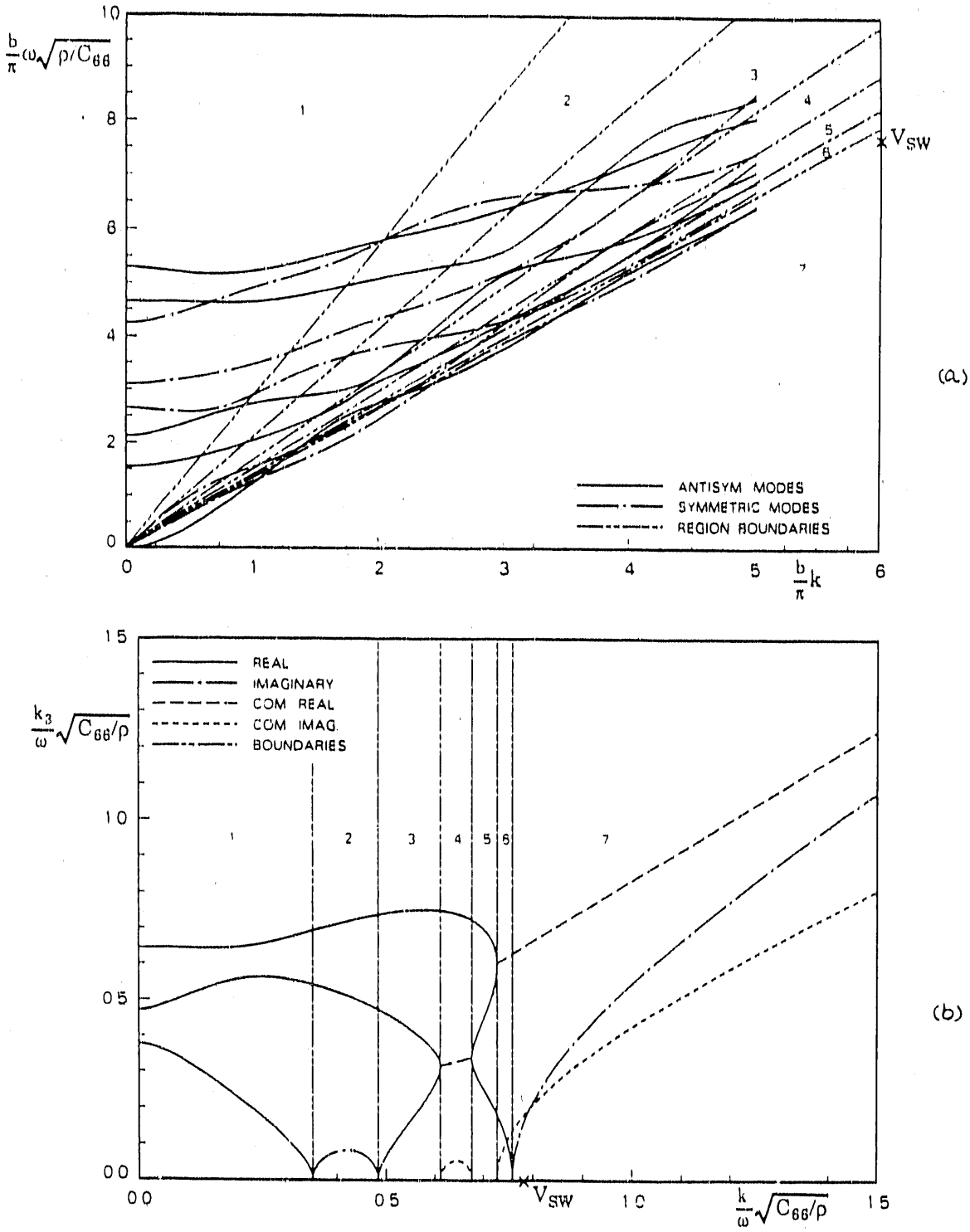

Fig. 12. Wave propagation in strongly orthotropic copper polycrystal plate (case SB), propagation angle is 20 degrees: a) dispersion curves; b) slowness curves

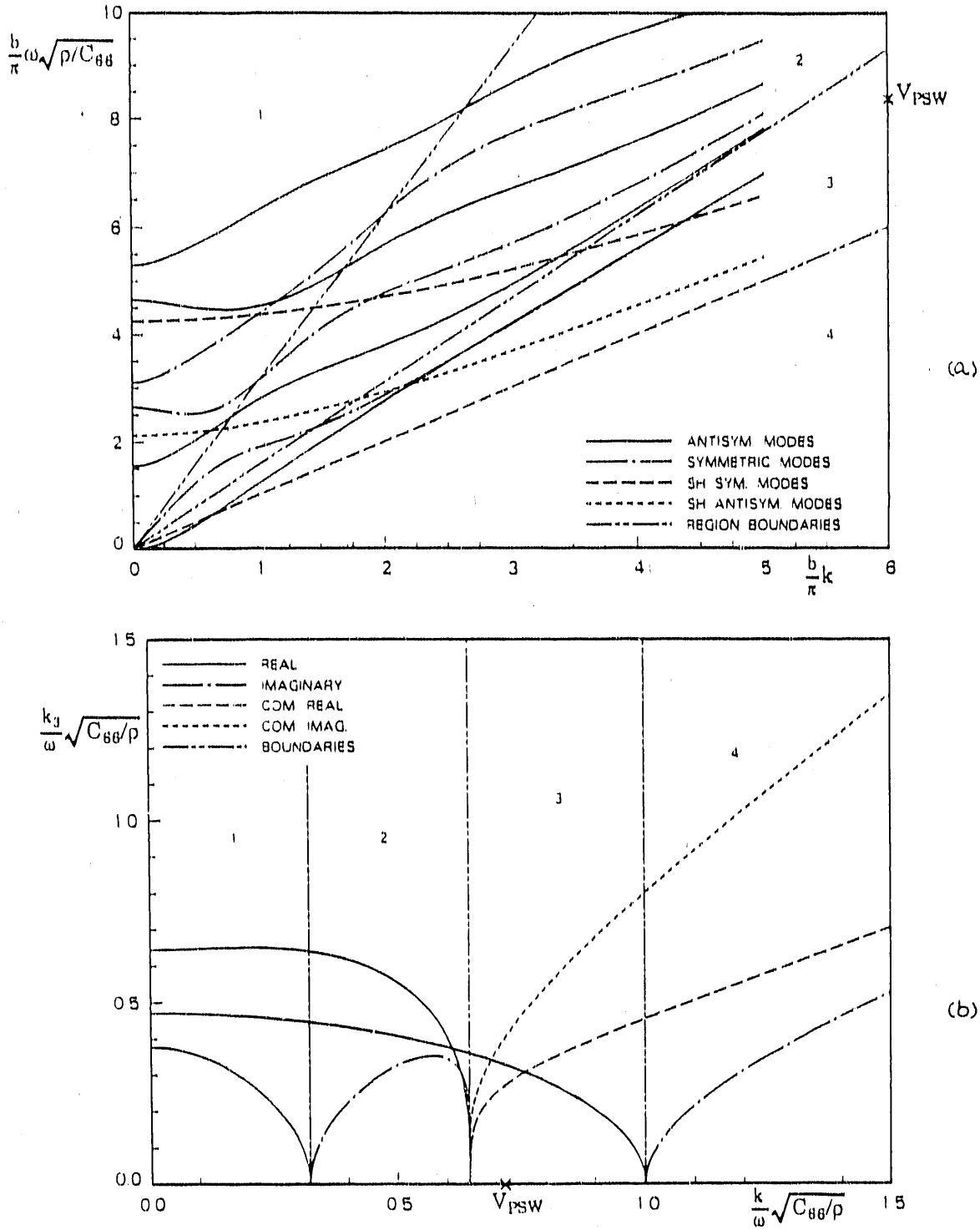

Fig. 13. Wave propagation in strongly orthotropic copper polycrystal plate (case SB), propagation angle is 90 degrees: a) dispersion curves; b) slowness curves

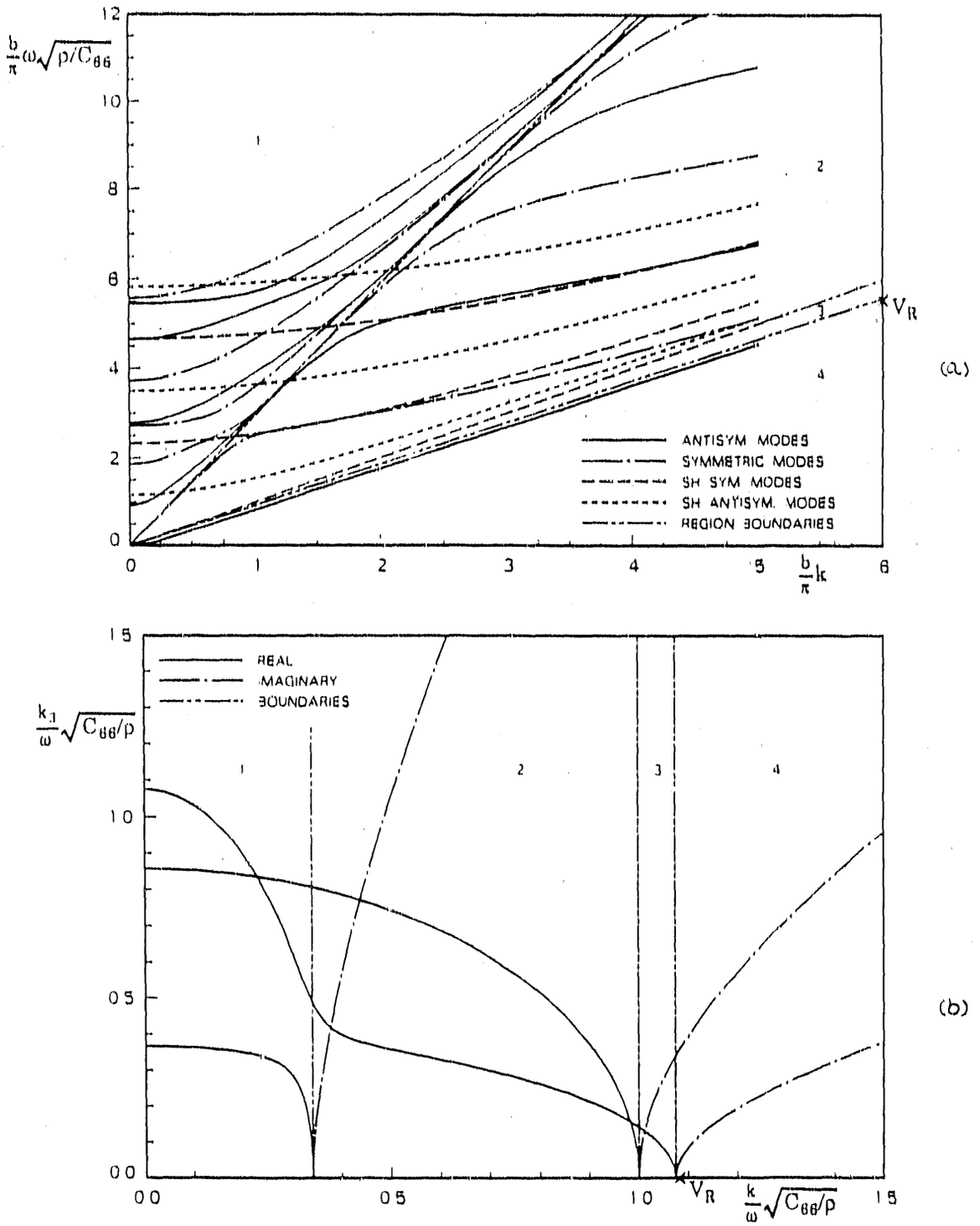

Fig. 14. Wave propagation in strongly orthotropic copper polycrystal plate (case SC), propagation angle is 0 degrees: a) dispersion curves; b) slowness curves

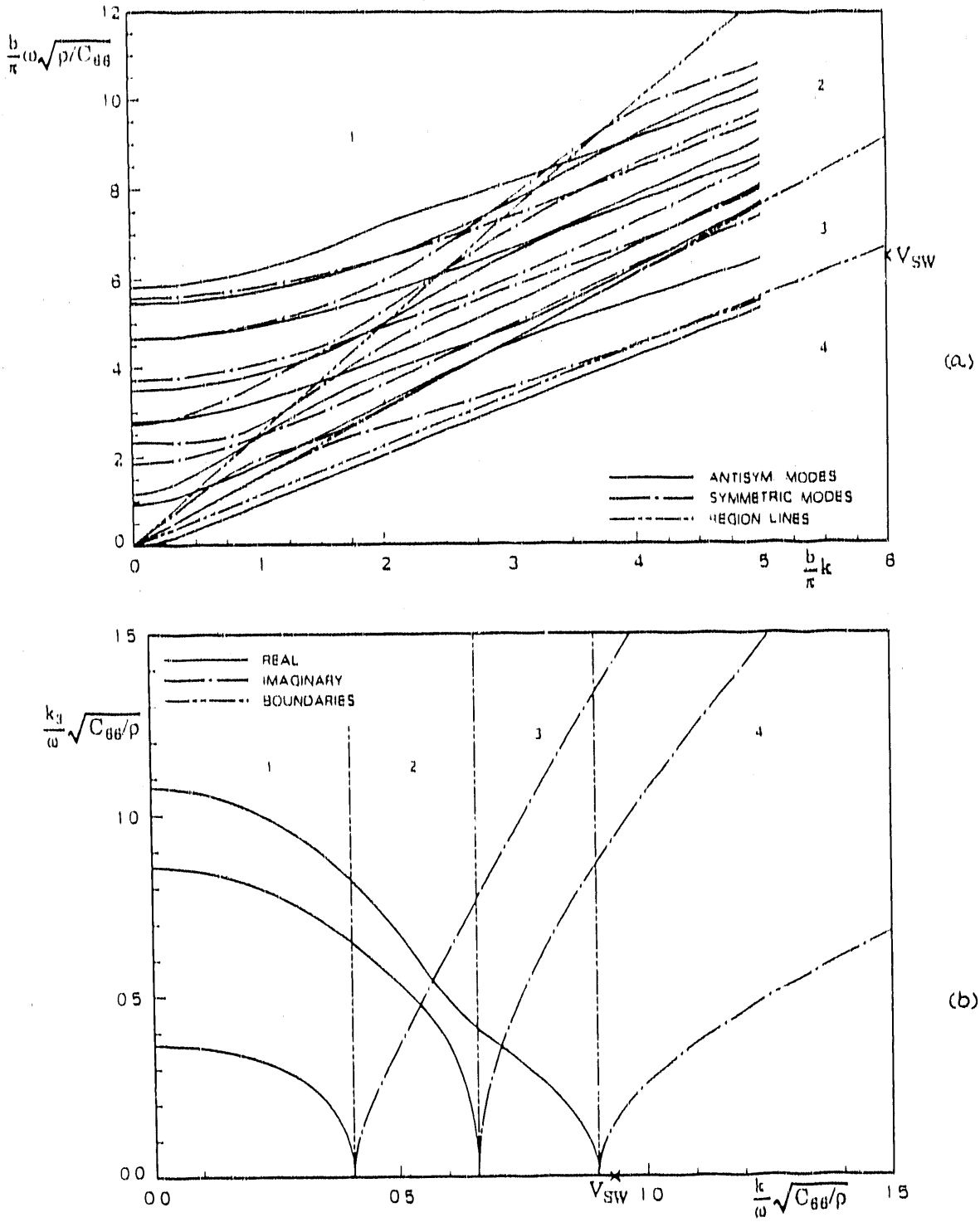

Fig. 15. Wave propagation in strongly orthotropic copper polycrystal plate (case SC), propagation angle is 60 degrees: a) dispersion curves; b) slowness curves

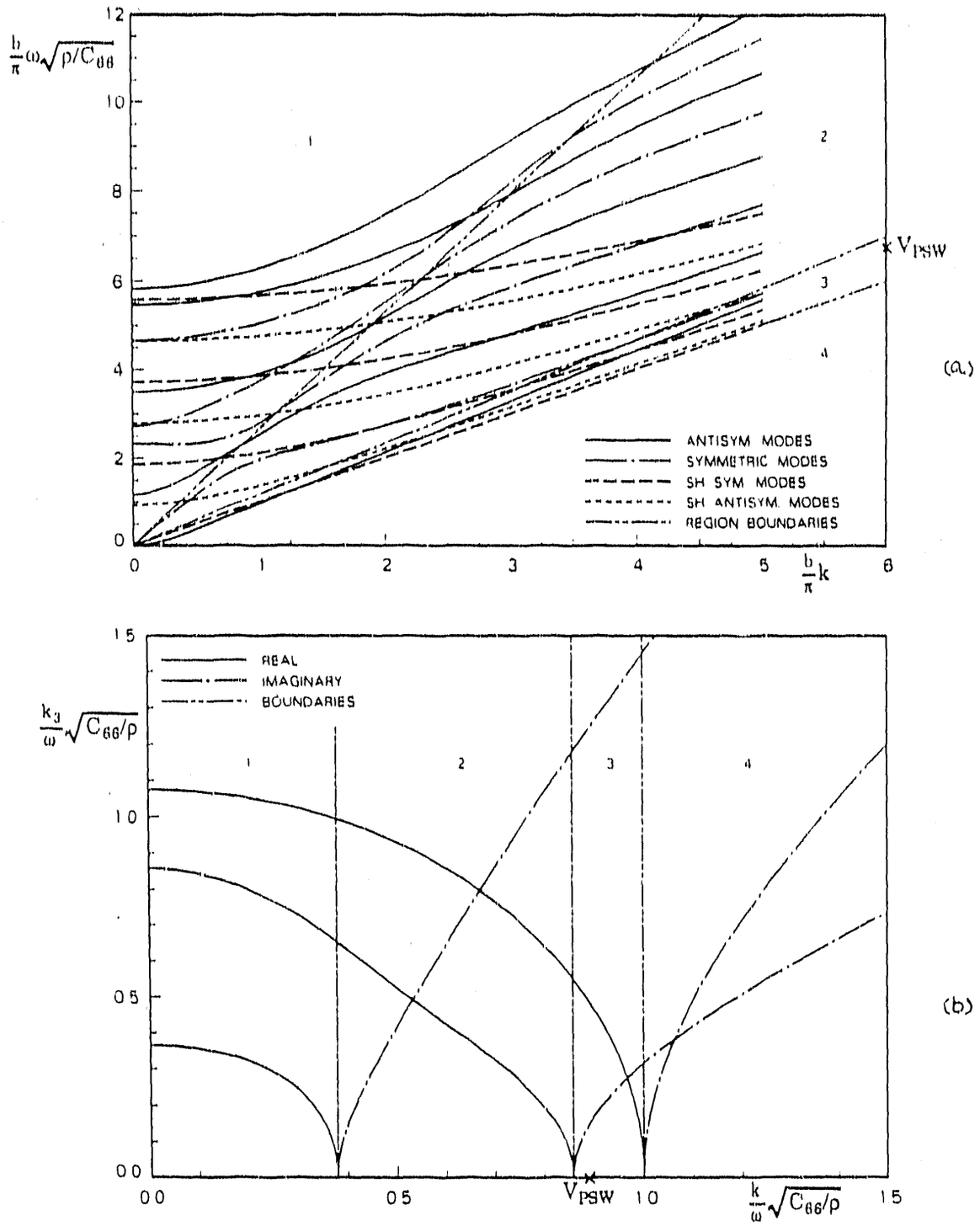

Fig. 16. Wave propagation in strongly orthotropic copper polycrystal plate (case SC), propagation angle is 90 degrees: a) dispersion curves; b) slowness curves

PART III.

PULSE PROPAGATION ANALYSIS OF DISPERSIVE WAVES

ABSTRACT

In most applications of dispersive waves, waves are applied in the form of pulses. It is well known that when a propagating wave is dispersive, a pulse changes its shape and spreads out as it propagates. Two analytical models are available in the literature that analyze the pulse propagation of dispersive waves. One was introduced by Thompson and Elsley and the other by Terina and Garrett and McCumber. The two models were proposed in studies of different types of dispersive waves. Both models were developed for Gaussian shaped pulses, one in time and one in space. This paper makes a further study of these two models and discusses their common characteristics and differences. Additional analytical solutions for various features associated with the pulse propagation and distortion are derived and presented. Some of these characteristics can be used to make interpretation of signals easy in time domain. To evaluate how these models perform, experiments with ultrasonic dispersive waves were conducted. The dispersive waves employed in this paper are plate (Lamb) waves. Comparisons are made of the experimental waveforms with the predictions by the two models. It is found that, at least in this study, the pulse propagation model proposed by Thompson and Elsley is more appropriate than the other one. Quantitative comparisons for various aspects of pulse propagation are also made between the experimental results and the simulations based on the model by Thompson and Elsley. The advantages and disadvantages of the two models are also discussed. The paper concentrates on Gaussian shaped pulses with a brief discussion for non-Gaussian shaped pulses.

INTRODUCTION

Since in most applications of dispersive waves, waves are applied in the form of pulses, successful applications of dispersive waves require a clear understanding of the characteristics of pulse propagation. When a propagating wave is dispersive, a pulse of this wave changes its shape and spreads out as it propagates. Generally speaking, when the propagating wave is dispersive, the pulse propagation is complicated in two aspects. First, the phase velocity and group velocity are different, hence the individual cycles travel at a different speed than the wave packet. Secondly, a pulse contains many frequency components and these frequency components propagate at different phase and group velocities, some fast and some slow, leading to an increase in the pulse width.

There have been several published articles in the literature in which pulse propagation of dispersive waves is studied and modeled. Most of these articles are related to the electromagnetic (optical) pulses, although the principles are applicable to general dispersive waves. In late '60s and early '70s, Terina [1,2] and Garrett and McCumber [3] independently developed analytical solutions for Gaussian shaped pulses propagating in media with absorption and dispersion. In their papers, the propagation of pulses that have a Gaussian shaped envelope in time was modeled and numerical analysis was performed to evaluate the accuracy of the model. For the convenience of discussion in this paper, we call this model "the time model" for the reason that the model was developed for pulses having Gaussian envelopes in time. The time model was not experimentally evaluated until about ten years later when Chu and Wong [4] reported some experimental confirmation of the conclusion drawn by Garrett and McCumber regarding the pulse peak propagation velocity. This confirmation, however, was argued by Katz and Alfano [5] shortly by pointing out that the experimental

resolution of their measurement does not warrant the proof. A review article with many references published by Puri and Birman [6] discussed the model by Garrett and McCumber and the application of the model.

At about the same time that the time model was introduced, Thompson and Elsley [7] proposed another model which approximates the pulse propagation of dispersive ultrasonic waves. In their report, Thompson and Elsley analyzed the propagation of pulses that have a spatial Gaussian shaped envelope. We will call this model "space model" since this model is for pulses of Gaussian shapes in space. Again, only theoretical analysis was presented in their report, no experimental evaluation of the validity of the model was supplied.

As the application of dispersive waves increases, better understanding and modeling of dispersive wave propagation becomes essential. In this paper, we will make a further study of the two pulse propagation models and discuss the similarities and differences. We will also develop some additional analytical solutions for various features associated with the pulse propagation and distortion. For the purposes of clarity and completeness, this paper will present the two models in a parallel fashion. Comparisons will be made as the models being presented. Concentration will be placed on the propagation of Gaussian shaped pulses, both in time and in space, although non-Gaussian shaped pulses will also be briefly discussed.

To evaluate the pulse propagation models, experiments using ultrasonic dispersive waves were conducted on a 2.2 mm thick Al plate. Waveforms of different types of dispersive plate modes (Lamb waves) using two different types of transducers were obtained and compared to the predictions by the two pulse propagation models. Quantitative comparisons for various aspects of pulse propagation were also made between the experimental waveforms and the simulated ones for the space model. Through the waveform examples, it is shown how the pulse propagation model can be used to determine some of the important dispersion

characteristics of dispersive waves. At the end of this paper, discussions will be made for the possible applications of this model.

Before we proceed, it is necessary to clarify the notation for propagating waves. In the ultrasonics community, a wave propagating in the positive direction is generally represented by $e^{j(\omega t-kx)}$. This is different from $e^{-j(\omega t-kx)}$, which is the one sometimes used in optics community. To be consistent, $e^{j(\omega t-kx)}$ will be used through out this paper.

PULSE PROPAGATION MODELS AND ANALYSIS

A. Pulse Propagation Models

A propagating pulse , which contains many frequency components, can be expressed by either of the following Fourier integrals:

$$u_s(t,x) = \frac{1}{2\pi}\int_{-\infty}^{\infty} A_s(k)\exp[j(\omega t - kx)]\,dk \tag{1a}$$

or

$$u_t(t,x) = \frac{1}{2\pi}\int_{-\infty}^{\infty} A_t(\omega)\exp[j(\omega t - kx)]\,d\omega \tag{1b}$$

where $u_s(t,x)$ and $u_t(t,x)$ are the displacement fields, x is the propagation distance, k is the wave number or spatial frequency, ω is the angular frequency, $A_s(k)$ and $A_t(\omega)$ are functions relating to the bandwidth of the spatial frequency k and temporal frequency ω respectively. Equation (1a) was proposed by Thompson and Elsley which corresponds to the space model and Eq. (1b) was used in most of the studies cited in the previous section which corresponds to the time model. The subscripts t and s in Eqs. (1a) and (1b) indicate this correspondence.

For dispersive wave propagation, the angular frequency ω is related to the spatial frequency k by a dispersion relation governing the wave propagation; i.e., $F(\omega,k)=0$. This relation is typically nonlinear, often implicit and multivalued (multiple modes). If we assume that only one mode of propagation is present, then the dispersion relation $F(\omega,k)=0$ can be expanded at (ω_0,k_0), where ω_0 and k_0 are the central angular and spatial frequencies and (ω_0, k_0) is the point of operation of the propagating wave packet on the dispersion curve, as Taylor series:

$$\omega(k) = \omega_0 + (k-k_0)\frac{d\omega}{dk}\Big|_{k=k_0} + \frac{1}{2}(k-k_0)^2\frac{d^2\omega}{dk^2}\Big|_{k=k_0} + \cdots \tag{2a}$$

or

$$k(\omega) = k_0 + (\omega-\omega_0)\frac{dk}{d\omega}\Big|_{\omega=\omega_0} + \frac{1}{2}(\omega-\omega_0)^2 \frac{d^2k}{d\omega^2}\Big|_{\omega=\omega_0} + \cdots \qquad (2b)$$

where $d\omega/dk|_{k=k_0} = V_g = \omega_0'$ and $d^2\omega/dk^2|_{k=k_0} = \omega_0''$ are the slope (group velocity) and the curvature for the $\omega=\omega(k)$ plot at the point of operation and $dk/d\omega|_{\omega=\omega_0} = 1/V_g = k_0'$ and $d^2k/d\omega^2|_{\omega=\omega_0} = k_0''$ are the slope (inverse of group velocity) and the curvature for the $k=k(\omega)$ plot. k_0'' and ω_0'' are related by $\omega_0''=-V_g^3 k_0''$.

Substituting Eq. (2) into Eq. (1) and dropping off the higher order terms, Eq. (1) can be written as

$$u_s(t,x) = \frac{1}{2\pi} e^{j(\omega_0 t - k_0 x)} \int_{-\infty}^{\infty} A_s(k) \exp\{j[(k-k_0)(V_g t - x) + \frac{1}{2}\omega_0''(k-k_0)^2 t]\}\, dk \qquad (3a)$$

or

$$u_t(t,x) = \frac{1}{2\pi} e^{j(\omega_0 t - k_0 x)} \int_{-\infty}^{\infty} A_t(\omega) \exp\{j[(\omega-\omega_0)(t - x/V_g) - \frac{1}{2}k_0''(\omega-\omega_0)^2 x]\}\, d\omega\,. \qquad (3b)$$

For arbitrary functions $A_s(k)$ and $A_t(\omega)$, numerical computation is usually required to evaluate the integrals in Eq. (3). When $A_s(k)$ and $A_t(\omega)$ are Gaussian functions, however, integrations in Eq. (3) can be carried out analytically, leading to useful physical insights.

Let

$$A_s(k) = \alpha_s B_s \exp[-\frac{1}{2}B_s^2(k-k_0)^2] \qquad (4a)$$

and

$$A_t(\omega) = \alpha_t B_t \exp[-\frac{1}{2}B_t^2(\omega-\omega_0)^2] \qquad (4b)$$

where α_s and α_t are normalization coefficients and B_s and B_t are half widths of initial Gaussian pulses in space and in time respectively (because, as will be seen, those are what they represent physically).

With the Gaussian functions defined in Eq. (4), analytical solutions to Eq. (3) have been obtained as:

$$u_s(t,x) = U_s(t,x) \exp\{j[\omega_0 t - k_0 x + \mathrm{Arg}_s(t,x)]\} \qquad (5a)$$

or

$$u_t(t,x) = U_t(t,x)\exp\{j[\omega_0 t - k_0 x - Arg_t(t,x)]\} \tag{5b}$$

where

$$U_s(t,x) = \frac{\alpha_s}{\sqrt{2\pi}(1+\tau_\xi^2)^{1/4}}\exp\{-\frac{(V_g t-x)^2}{2B_\xi^2(1+\tau_\xi^2)}\} \tag{6a}$$

$$U_t(t,x) = \frac{\alpha_t}{\sqrt{2\pi}(1+\tau_t^2)^{1/4}}\exp\{-\frac{(t-x/V_g)^2}{2B_t^2(1+\tau_t^2)}\} \tag{6b}$$

$$Arg_s(t,x) = \frac{1}{2}\tan^{-1}\tau_s - \frac{(V_g t-x)^2\tau_s}{2B_\xi^2(1+\tau_\xi^2)} \tag{7a}$$

$$Arg_t(t,x) = \frac{1}{2}\tan^{-1}\tau_t - \frac{(t-x/V_g)^2\tau_t}{2B_t^2(1+\tau_t^2)} \tag{7b}$$

with $\tau_s=\omega_0''t/B_\xi^2$ and $\tau_t=k_0''x/B_t^2$.

Equations (5~7) describe two pulse propagation solutions with many interesting features. These features are listed below with more quantitative analysis and discussions to be presented in the rest of this section:

(1) At t=0, $\tau_s=0$, $U_s(0,x) = \frac{\alpha_s}{\sqrt{2\pi}}\exp\{-\frac{x^2}{2B_\xi^2}\}$ and $Arg_s(0,x)=0$. This means that the pulse envelope predicted by the space model has a Gaussian shape and there is no extra phase shift in the exponent which implies the zero-crossings of individual cycles within the pulse are separated by an equal distance $2\pi/k_0$ in space. However, at t=0, $\tau_t\neq 0$, $U_t(0,x)$, the pulse shape predicted by the time model, is symmetric but not Gaussian in space. And because of $Arg_t(0,x)\neq 0$, the zero-crossings of individual cycles are no longer equally separated in space, though the spatial period variation is still symmetric about the center of the pulse.

(2) At x=0, $\tau_t=0$, $U_t(t,0) = \frac{\alpha_t}{\sqrt{2\pi}}\exp\{-\frac{t^2}{2B_t^2}\}$ and $Arg_t(t,0)=0$. This means that the pulse envelope predicted by the time model has a Gaussian shape and there is no extra phase shift in the exponent, implying a constant period $2\pi/\omega_0$ in time within the pulse envelope. However, at x=0, $\tau_s\neq 0$, $U_s(t,0)$, the pulse shape predicted by the space model, is symmetric but not Gaussian in time. The periods within the pulse envelope are no longer constant due to

$Arg_s(t,0)\neq 0$, even though the period variation is symmetric about the center of the pulse.

(3) As the pulse propagates, at any fixed time t, the space model predicts that the pulse remains as a Gaussian shape in space. The peak of the envelope moves at the group velocity in space $x(peak)=V_g t$. The peak envelope amplitude decreases as the propagating time increases, varying as $(1+\tau_\xi^2)^{-1/4}$. This loss of amplitude is accompanied by a pulse spreading with the spatial pulse length being proportional to $(1+\tau_\xi^2)^{1/2}$. On the other hand, the time model predicts, at any fixed time t, the pulse in space is not Gaussian; it becomes asymmetric and the envelope amplitude decreases with both the asymmetry and the loss of pulse envelope amplitude directly related to $(1+\tau_t^2)$. The peak of the pulse envelope in this case moves at a slightly different speed from the group velocity because of the slow varying function $(1+\tau_t^2)^{1/4}$ in the denominator in Eq. (6b). Similar to the space model, the pulse spreads out in space as it propagates. For both models, the concurrence of decrease in amplitude and increase in width is consistent with conservation of energy within the pulse.

(4) At any fixed propagation distance x, the space model shows that the pulse becomes distorted (skewed) and stretched in time. The pulse envelope is not symmetric with respect to the pulse center and the peak of the pulse decreases as the propagation distance increases. The rate of skewing and stretching is closely associated with the value of τ_s. The pulse peak travels at a speed a little different from the group velocity. The difference is also related to τ_s. With the time model, however, τ_t has nothing to do with time -- it is a constant when the propagation distance is fixed. Thus as the propagation distance increases, the pulse retains a Gaussian shape in time though the pulse amplitude decreases and the pulse width increases.

(5) At any positive fixed time, $t > 0$, the zero crossings of individual cycles within the pulse as predicted by the space model are no longer equally spaced at $2\pi/k_0$ due to the extra phase shifts described by Eq. (7a). In

particular, the quadratic dependence of the second term on $V_g t$-x (which is the varying term within the pulse envelope in space) causes the the pulse in space to have a symmetric phase shift with respect to the pulse center. The wavelengths of the pulse, therefore, increase or decrease within the pulse depending on the sign of ω_0''. The prediction of the wavelength variation by the time model, however, is a little different from the space model due to the fact that τ_t is a variable in space. Of the two terms in Eq. (7b), the first one is generally a slow varying function within the pulse envelope comparing to the second one. Within the second term of Eq. (7b), $\frac{\tau_t}{(1+\tau_t^2)}$ is a smooth function having no zeros hence the dominant part is still the quadratic component. This means that the spatial periods of the cycles within the pulse as predicted by the time model have a similar variation pattern; i.e., the increase or decrease of the wavelengths in space is controlled by the sign of k_0''.

(6) When viewed as a function of time for a fixed propagation distance, the space model predicts that, due to the presence of t in both terms of Eq. (7a), the phase shift introduced by $Arg_s(t,x)$ is not symmetric with respect to the pulse center and the zero crossings within the pulse are never equally separated in time. The situation here is very much like the one described in (5) for the time model with a fixed time. Likewise, the time model now predicts a outcome for the period variation in time that is similar to what described in the previous paragraph for the wavelength by the space model for a fixed distance; i.e., the extra phase shift $Arg_t(t,x)$ is symmetric with respect to the pulse center and the periods increase or decrease in accordance with the sign of k_0''.

(7) The phenomena of pulse spreading, skewing and frequency modulation (variation of periods or wavelengths) are all controlled by ω_0'' or k_0''. None of these occurs when ω_0'' or $k_0''=0$.

(8) The Fourier transforms of the time signal for a fixed distance are different for the two pulse models. As implied by the assumed function in Eq.

(4b), the magnitude of the Fourier transform of $u_t(t,x)$ is always a Gaussian. On the other hand, the magnitude of the Fourier transform of $u_s(t,x)$ is not a Gaussian. In fact, its shape depends on the dispersion function $k=k(\omega)$; i.e., $|F_s(\omega)|=A_s(k(\omega))/V_g(\omega)$, where $A_s(k)$ is given by Eq. (4a). For both models, and regardless of the functions in $A(\omega)$, the envelopes of Fourier transforms are identical for any propagation distance, even though there may be significant changes in pulse envelopes in time domain.

(9) When comparing the two pulse propagation models, one finds that the behavior of the time model in space is similar to that of the space model in time and the predictions of the time model in time is also similar to those of the space model in space. This is, of course, due to the similarity in the set up equations (Eqs. (1a) and (1b)) and the assumed Gaussian functions in Eq. (4).

B. Change of Periods within the Wave Packet

Typically a pulse signal is displayed in time domain on a oscilloscope for a fixed propagation distance x. Because of the extra term $Arg(t,x)$ in the exponential term in Eq. (7), the periods of the cycles within a wave packet for a dispersive wave vary from one location to another. If a particular zero-crossing corresponds to

$$\omega_0 t - k_0 x + Arg_s(t,x) = 2n\pi + \phi \qquad \text{(for the space model)} \qquad (8a)$$

or

$$\omega_0 t - k_0 x - Arg_t(t,x) = 2n\pi + \phi \qquad \text{(for the time model)} \qquad (8b)$$

where f is an arbitrary phase factor, at a fixed propagation distance $x = x_0$, the period as measured from two consecutive zero-crossings $\Delta t = t_2 - t_1$ can be expressed as

$$\omega_0 \Delta t \pm [Arg_{s,t}(t_2,x_0) - Arg_{s,t}(t_1,x_0)] = 2\pi \qquad (9)$$

where the plus sign corresponds to the subscript s for the space model and the minus sign corresponds to the subscript t for the time model. The theoretical period which corresponds to the central frequency of the pulse is

$D_0=2\pi/\omega_0$.

Because

$$\frac{Arg_{s,t}(t_2,x_0) - Arg_{s,t}(t_1,x_0)}{t_2 - t_1} \approx \frac{\partial Arg_{s,t}(t,x_0)}{\partial t} \quad (10)$$

Eq. (9) can be approximately rewritten as

$$\Delta t = \frac{D_0}{1 \pm \frac{1}{\omega_0}\frac{\partial Arg_{s,t}(t,x_0)}{\partial t}} \quad (11)$$

and the change of period Δt within the pulse envelope; i.e., $d\Delta t/dt$ can be obtained as

$$\frac{d\Delta t}{dt} = \pm \frac{D_0}{\omega_0} \frac{\frac{\partial^2 Arg_{s,t}(t,x_0)}{\partial t^2}}{\left|1 \pm \frac{1}{\omega_0}\frac{\partial Arg_{s,t}(t,x_0)}{\partial t}\right|^3} \quad (12)$$

In other words, $d\Delta t/dt$ has same sign as $\partial^2 Arg_t(t,x_0)/\partial t^2$ for the time model and opposite sign as $\partial^2 Arg_s(t,x_0)/\partial t^2$ for the space model.

To see the physical meanings of Eqs. (11) and (12) clearly, we need to know $\partial Arg/\partial t$ and $\partial^2 Arg/\partial t^2$ for the two models. For the time model, $Arg_t(t,x_0)$ is a second order polynomial in t, since τ_t is a constant for $x=x_0$. Therefore the sign of $\partial^2 Arg_t/\partial t^2$ is the opposite as k_0, which leads to a decrease for the periods from the leading edge of the pulse to the trailing edge for a positive k_0 and a increase for a negative k_0. This also means that, for a positive group velocity V_g, when $\omega_0>0$, the high frequency components of the pulse are at the leading edge of the pulse and when $\omega_0<0$, the low frequency components are at the leading edge.

For the space model, the exact expressions for the two derivatives are complicated because of the dependence of τ_s on t, but generally unnecessary. The characteristics of these derivatives can be found by analyzing $U_s(t,x)$ and $Arg_s(t,x)$ in Eqs. (6) and (7).

From Eq. (6a), we see that, because $(1+\tau_\xi^2)^{-1/4}$ is a slow varying function

in time when compared to $\exp[-\frac{(V_g(t-x)^2}{2B_\xi^2(1+\tau_\xi^2)}]$, $U_s(t,x)$ is less than 5% of $U_s(t,x)|_{max}$ for $b=\frac{(V_g(t-x)^2}{2B_\xi^2(1+\tau_\xi^2)} > 3$, where $U_s(t,x)|_{max} = \frac{\alpha_s}{\sqrt{2\pi}(1+\tau_\xi^2)^{1/4}}$. Within the pulse envelope, b varies from 3 to zero and back to 3; b becomes zero at $t=x/V_g$, near (not at) the peak of pulse envelope. In this region, $Arg_s(t,x)$ changes from $Arg_s(t,x)|_L = \frac{1}{2}\tan^{-1}\tau_s - 3\tau_s \approx -3\tau_s$ to $Arg_s(t,x)|_C = \frac{1}{2}\tan^{-1}\tau_s$ and back to $Arg_s(t,x)|_R \approx -3\tau_s$, with subscripts L, C, and R indicating left side, central, and right side of the pulse envelope. Because of this variation pattern for $Arg_s(t,x)$ within the pulse envelope, $\partial^2 Arg_s/\partial t^2>0$ when $\tau_s<0$ and $\partial^2 Arg_s/\partial t^2<0$ when $\tau_s>0$. Thus, when $\omega_0''>0$, $d\Delta t/dt>0$, the periods within the pulse increase from the leading edge to the trailing edge, and vice versa. Naturally, this approximated analysis should not be applied when the propagation distance is close to zero where $(1+\tau_\xi^2)^{-1/4}$ is not a slow varying function at all.

Note that the period variations predicted by the space model within the pulse envelope has the same trend as the those predicted by the time model, although there is a slight different in details, in the dependence on the ω_0''. This conclusion, of course, is under the condition that group velocity V_g is positive, which is often the case for ultrasonic dispersive waves; this may not always be true, however, for electromagnetic or optical waves.

The physical implication of this feature is that ω_0'' can be qualitatively determined as greater or less than zero directly from a waveform. This is depicted in Table I. The experimental results to be presented later will verify this phenomenon.

C. Two Important Time Locations

There are two important time locations within a pulse which are of interest. First one is the time t_p of the pulse peak location. For the time model where τ_t is constant for a fixed distance, the peak of the pulse envelope

travels at the group velocity V_g and the peak occurs at $t_p = x/V_g$.

For the space model where τ_s is a variable in time, the peak of the pulse envelope does not move at the group velocity in time; the peak does not occur at $t = x/V_g$ due to the dependence of the coefficient in front of the exponential function on time in Eq. (6a). In fact, by rewriting $U_s(t,x)$ as $U_s(t,x) = c\, f_1(t)\, f_2(t,x)$, where $c = \frac{\alpha_s}{\sqrt{2\pi}}$ is the constant coefficient, $f_1(t) = (1+\tau_\xi^2)^{-1/4}$, and $f_2(t,x) = \exp\{-\frac{(V_g t - x)^2}{2B_s^2(1+\tau_\xi^2)}\}$, one finds that the peak of the pulse envelope occurs when $\partial U_s(t,x)/\partial t = 0$:

$$\text{or} \qquad f_2(t,x)\frac{df_1(t)}{dt} + f_1(t)\frac{\partial f_2(t,x)}{\partial t} = 0. \tag{13}$$

Since for $t > 0$, $df_1/dt < 0$, $f_1 > 0$, and $f_2 > 0$, to satisfy Eq. (13), $\partial f_2/\partial t$ must be greater than zero. This leads to the conclusion $t_p < x/V_g$ regardless of the sign of ω_0''.

In fact, further mathematical analysis shows that

$$\frac{x}{V_g} > t_p > \frac{x}{V_g}\left[\frac{1}{1+\frac{1}{2}\left(\frac{\omega_0''}{B_s V_g}\right)^2}\right]$$

and if $\frac{1}{2}\left(\frac{\omega_0''}{B_s V_g}\right)^2 << 1$, as sometimes is the case, $t_p \approx \frac{x}{V_g}\left[1-\frac{1}{2}\left(\frac{\omega_0''}{B_s V_g}\right)^2\right]$. Thus the velocity of the pulse peak is greater than the true group velocity.

The second important time location within a wave packet is the time t_D where the measured period Δt equals the period D of center frequency f_0. From Eq. (11), one sees that $\Delta t = D_0$ when $\partial \mathrm{Arg}/\partial t = 0$.

For the time model, this occurs when $t = x/V_g = t_D$. In other words, the period of the cycle at the peak of the pulse envelope has the period corresponding to the center frequency of the pulse. For the space model, this is not true. As discussed before, $\partial \mathrm{Arg}/\partial t = 0$ occurs near $t = x/V_g$. In this vicinity, $\partial \mathrm{Arg}/\partial t$ can be approximated as

$$\frac{\partial \mathrm{Arg}_s(t,x)}{\partial t} \approx \frac{\omega_0''}{2B_\xi^2(1+\tau_\xi^2)} - \frac{V_g(V_g t - x)\,\tau_s}{B_\xi^2(1+\tau_\xi^2)}. \tag{14}$$

Setting this expression to zero leads to $t_D > x/V_g$.

D. Phase Velocity Variation within the Wave Packet

Because of the term Arg(t,x), all zero-crossings within a wave packet do not travel at the same speed. If we define V_{pm} as the zero-crossing velocity or the velocity which would be measured through a small distance change; i. e. $V_{pm} = dx/dt$, then, through a total derivative of Eq. (8), one gets,

$$V_{pm} = \frac{dx}{dt} = \frac{\omega_0 + \partial Arg_s(t,x)/\partial t}{k_0 - \partial Arg_s(t,x)/\partial x} \tag{15a}$$

or $$V_{pm} = \frac{dx}{dt} = \frac{\omega_0 - \partial Arg_t(t,x)/\partial t}{k_0 + \partial Arg_t(t,x)/\partial x} \quad . \tag{15b}$$

It is conceivable that the modifying terms $\partial Arg/\partial t$ and $\partial Arg/\partial x$ are in general small comparing to ω_0 and k_0 respectively. Therefore Eq. (15) can be approximated to

$$V_{pm} = \frac{\omega_0}{k_0}\left(1 \pm \frac{1}{\omega_0}\frac{\partial Arg_{s,t}(t,x)}{\partial t} \pm \frac{1}{k_0}\frac{\partial Arg_{s,t}(t,x)}{\partial x}\right) \tag{16}$$

where the plus sign corresponds to the space model and the minus sign corresponds to the time model.

Recall that τ_s is a function of time and τ_t is a function of distance only, we have

$$\frac{\partial Arg_s(t,x)}{\partial x} = \frac{V_g t - x}{B_s^2(1+\tau_s^2)}\tau_s \quad \text{and} \quad \frac{\partial Arg_t(t,x)}{\partial t} = -\frac{t - x/V_g}{B_t^2(1+\tau_t^2)}\tau_t. \tag{17}$$

Since within the wave packet, $\tan^{-1}\tau$ and $\tau/(1+\tau^2)$ are slowly varying functions comparing to $(V_g t - x)^2$, $\partial Arg_s(t,x)/\partial t$ and $\partial Arg_t(t,x)/\partial x$ can be expressed as

$$\frac{\partial Arg_s(t,x)}{\partial t} \approx -\frac{V_g t - x}{B_s^2(1+\tau_s^2)}V_g\tau_s \quad \text{and} \quad \frac{\partial Arg_t(t,x)}{\partial x} \approx \frac{t - x/V_g}{B_t^2(1+\tau_t^2)}\frac{\tau_t}{V_g}. \tag{18}$$

Then Eq. (16) becomes

$$V_{pm} = V_p\left(1 + (1 - \frac{V_g}{V_p})\frac{1}{k_0}\frac{(V_g t - x)}{B_s^2(1+\tau_s^2)}\tau_s\right) \tag{19a}$$

and $$V_{pm} = V_p\left(1 - (1 - \frac{V_g}{V_p})\frac{1}{k_0}\frac{(V_g t - x)}{B_t^2(1+\tau_t^2)}\frac{\tau_t}{V_g^2}\right) \tag{19b}$$

where V_p is the phase velocity as determined from ω_0/k_0 (center phase velocity). And the velocity change, dV_{pm}/dt, within the wave packet becomes:

$$\frac{dV_{pm}}{dt} \approx V_p(1 - \frac{V_g}{V_p})\frac{1}{k_0}\frac{V_g\tau_s}{B_s^2(1+\tau_s^2)} \tag{20a}$$

and $$\frac{dV_{pm}}{dt} \approx -V_p\left(1-\frac{V_g}{V_p}\right)\frac{1}{k_0}\frac{\tau_t / V_g}{B_t^2\,(1+\tau_t^2)}. \qquad (20b)$$

Because $\tau/(1+\tau^2)$ is monotonic, dV_{pm}/dt is a monotonic function too. Whether V_{pm} increases or decreases monotonically depends on the sign of ω_0'' or k_0'' as well as the sign of (V_p-V_g). Note that because of the relation $\omega_0''=-V_g^3k_0''$, Eqs. (19) and (20) give consistent predictions for both the time and the space models, unless, of course, the group velocity is negative or infinity.

For the space model, at $t = t_C = x/V_g$, $\partial Arg_s(t,x)/\partial t = \omega_0''/|2B_s^2(1+\tau_s^2)|$ and $\partial Arg_s(t,x)/\partial x=0$. At $t=t_D > x/V_g$, $\partial Arg_s(t,x)/\partial t = 0$ and $\partial Arg_s(t,x)/\partial x$ is related to ω_0'' by the first equation of Eq. (17). Using Eq. (15a), one concludes that at both t_C and t_D, $V_{pm} > V_p$ when $\omega_0'' > 0$ and $V_{pm} < V_p$ when $\omega_0'' < 0$.

For the time model, at $t = t_p = t_D = x/V_g$, $\partial Arg_t(t,x)/\partial x = k_0''/|2B_t^2(1+\tau_t^2)|$ and $\partial Arg_t(t,x)/\partial t=0$. From Eq. (15b), one finds that, assuming positive group velocity, $V_{pm} > V_p$ when $k_0'' < 0$ or $\omega_0'' > 0$ and $V_{pm} < V_p$ when $k_0'' > 0$ or $\omega_0'' < 0$.

The V_{pm} and V_p relation within the wave packet is summarized in Table II for the space model.

E. General Comments

The features presented and discussed so far are for the Gaussian shaped pulses. Depending on the model chosen, the predicted outcomes in different aspects can be similar or different. Both models predict a monotonic change in the period variation and measured phase velocity variation within the pulse envelope. The two models however, disagree on the pulse envelope shape variation in time and frequency domain as well as in space. Experiments to be presented in the next section will be used to evaluate the performance of the two models.

Real pulses are never Gaussians. Many of them are not even symmetric. There will be inevitably errors involved if one uses the two pulse models without discretion. Fortunately, many pulses in real application are

close to Gaussians at the beginning of propagation. If one imagines a non-Gaussian pulse as having many Gaussian components (similar to expressing a periodic function as a sum of many sinusoidal functions), the pulse may be expressed as a series of Gaussians, hopefully a convergent one. For a fast convergent series, one may conceive the first Gaussian term will provide a good approximation to the non-Gaussian pulse. In this case, some trends for the features discussed for the Gaussian should still be valid, and the pulse models should be able to provide some reasonable guidance. The bad news is that it is often mathematically impossible or impractical to determine the expansion coefficients associated with the Gaussian series.

As one may have already noticed, the models presented here have not attenuation or absorption factors included. If one wishes to include these factors in the models, the integrals in Eq. (3) may not be solvable analytically except for some special forms. Through out this paper, we recognize the existence of these factors but assume they are negligible in the analysis.

EXPERIMENTS

To evaluate the pulse propagation models presented in section II, experiments using ultrasonic dispersive waves have been performed. The experiments were all done on a 2.2 mm (0.0873") thick Al plate. This plate is smooth on both surfaces with no significant thickness and property inhomogeneity. Pulses of dispersive plate waves were applied to the Al plate. Some experiments were done using EMATs (electro-magnetic acoustic transducers), others using conventional PZT transducers. For the experiments using EMATs, the S_0 and the SH_1 plate modes were excited. The spatial periods of the S_0 and the SH_1 EMATs are 5.1 mm and 5.4 mm respectively. The operating frequencies for the two plate modes were about 0.8~0.9 MHz. For the experiments using PZT transducers, the S_0 and the A_1 modes were applied. The PZT transducers are 1 inch diameter Panametrics broadband transducers with center frequency of 1 MHz. In the PZT experiments, pulses were transmitted into the Al sample through local water couplings at appropriate angles. In both EMAT and PZT experiments, pulses were launched by a transmitter and picked up by a receiver, which was separated from the transmitter by distances of 100 mm to 200 mm. The S_0 and the SH_1 modes were chosen in the EMAT experiments because they have opposite signs for ω_0'' at the operation points, providing an ideal model evaluation environment. For the same reason, the S_0 and the A_1 modes were chosen in the PZT experiments.

A detailed texture study of the plate was first performed by ultrasonic techniques [8,9]. The texture parameters have been found to be $W_{400}=6.0\times10^{-3}$, $W_{420}=8.6\times10^{-4}$, and $W_{440}=5.6\times10^{-4}$ [8,10, and 11]. The elastic constants (stiffnesses) corresponding to this set of texture parameters in Al are listed in Table III [12]. It was found that the anisotropy introduced by the presence of texture has significant influence on the dispersion characteristics of the Al

plate, particularly in the region near the Lamé point where our EMATs operated. This can be seen from Fig. 1 which shows dispersion curves for the wave propagating in the rolling direction of the Al sheet [13]. In Fig. 1, two experimentally determined dispersion curves of the S_0 and the SH_1 modes are plotted along with their theoretical dispersion curves which used the elastic constants given in Table III. The apparent good agreement between the experimental and the theoretical results in Fig. 1 indicates a proper inclusion of anisotropic (or texture) effects. Note that the two modes do not touch each other tangentially at bk/π, the Lamé point where the two modes would have if the Al plate were isotropic [14, 15]. For the convenience of discussion later on the waveforms acquired using PZT transducers, a wider spectrum of dispersion curves of Lamb modes (excluding SH modes) are also given here in Fig. 2 for the propagation in the rolling direction. Incidentally, all the propagations discussed hereafter are for the propagation in the rolling direction, unless otherwise specified.

Figures 3~6 are the experimental waveforms for the S_0 and the SH_1 modes as obtained from the EMAT experiments. Figures 3 and 4 are the experimental S_0 mode waveforms for transducer separation distances of 110 mm and 165 mm respectively. Figures 5 and 6 are responses of the SH_1 mode with separations of 120 mm and 220 mm. They were acquired after an average of 500 repetitions. The instrument settings for Figs. 3 and 4 were identical, so were the settings for Figs. 5 and 6. However, the settings for Figs. 3 and 4 are necessarily different from those for Figs. 5 and 6 due to the tuning requirement for the EMAT system. This is primarily because the exciting signal is a narrow-banded toneburst and the EMATs have a narrow-banded filter characteristics. The toneburst usually has about 4~6 cycles and the EMATs have a two and half spatial periods in winding. The pulses excited in the Al plate have envelopes that are close to triangles which may be considered as approximations of Gaussians. These pulses should be symmetric initially both in time and in space. Table IV lists parameters of

the S_0 and the SH_1 waves at the points of operation. In Table IV, $K = bk/\pi$, $W = 2bf/V_t$, $W' = V_g/V_t$, and $W'' = \pi V_g \omega_0''/b$, where b is the plate total thickness and V_t is the bulk shear wave velocity of the corresponding isotropic media; these quantities are, respectively, dimensionless wave number, dimensionless frequency, dimensionless group velocity, and dimensionless curvature for $\omega=\omega(k)$.

From the S_0 waveforms in Figs. 3 and 4, one sees that the pulse width has increased significantly and at the same time the pulse magnitude decreased noticeably for the propagation distance of 110 mm to 165 mm. Similar comments can be made for the SH_1 waveforms in Figs. 5 and 6 where pulse broadening is accompanied by a reduction in amplitude. This pulse broadening phenomenon is well known and predicted by both of the pulse models presented in the previous section. A close look of the waveforms in Figs. 3~6 reveals another feature: all the pulses shown have some degrees of asymmetry. This feature was predicted by the space model but not the time model. In particular, the waveform in Fig. 4 has more asymmetry than that in Fig. 3; so does Fig. 6 than Fig. 5. In other words, the degree of asymmetry develops as the propagation distance increases. This is consistent with the prediction by the space model. The fact that the space model successfully predicts the development of the asymmetry of the pulses is an indication that the space model may be a better model than the time model.

Recall that both pulse models predict that there will be a period variation for the individual cycles within the pulse envelope and the variation pattern, period increase or decrease from the leading edge to the trailing edge, depends on the sign of ω_0'' or k_0''. A careful examination of the waveforms in Figs. 3 and 6, where a peak of a cycle near the center of the pulse is aligned with one of the background grids in each figure (see the pointers), proves that indeed there is a clear period variation within the pulses. In Fig. 4, one can count exactly nine cycles within two vertical divisions to the left of the pointer grid while two divisions to the right of the

pointer more than nine (close to nine and half) cycles can be realized. This means that the higher frequency components move slower than the lower ones and the period variation within the pulse envelope is decrease from the leading edge to the trailing edge, which indicates $\omega_0'' < 0$ or $k_0'' > 0$ at the point of pulse operation. This conclusion is in agreement with the shape of the S_0 dispersion curve in Fig. 1. Similarly, in Fig. 6, one finds a little more than nine and half cycles within two divisions to the left of the pointer and about exactly nine cycles within the same number of divisions to the right of the pointer. This implies that higher frequency components travel faster and the pulse is operated at the point where $\omega_0'' > 0$ or $k_0'' < 0$. This is also readily confirmed by the concavity of the SH_1 dispersion curve in Fig. 1.

One should not try to make any quantitative comparison between the S_0 waveforms and the SH_1 waveforms. The major problem of doing so is due to the fact the transducers used to obtain these two sets of waveforms were not identical and the instrument settings were not the same. This translates into different pulse width parameters B. Quantitative comparisons of these waveforms and period variations will be made in section IV along with some simulation results.

Now let us study the waveforms produced by using the conventional PZT transducers. Figures 7 and 8 show the pulses of the S_0 mode and Figs. 9 and 10 show the pulses of the A_1 mode. The center frequencies of the pulses are 0.82 MHz for the S_0 mode and 1.0 MHz for the A_1 mode. The propagation distances for Figs. 7 and 9 are about 150 mm. The exact propagation distances are unclear due to certain measurement difficulty, but the distance shifts from Figs. 7 to 8 and from Figs. 9 to 10 are both 100 mm. All these waveforms were obtained using the same pair of transducers except the angles of pulse incidence are different.

Unlike the pulses by EMATs, the pulses produced by PZT transducers are generally broadbanded; i.e., the pulse width (parameter B) is small,

typically corresponding to 1~3 cycles in time. At the time pulses enter the Al plate at an angle, the pulses are likely to be asymmetric. The extend of initial asymmetry of the pulses depends on many factors such as the transducer design, the electrical pulses applied on the piezoelectric disk in the transducer, the aperture of the transducer, the angle at which the pulses are launched, and the diffraction of the pulses in the water before they enter the plate. In this study, we neglect the asymmetry and assume the initial pulses are good approximations of Gaussians.

From the S_0 waveforms in Figs. 7 and 8, one sees clearly the distinguished asymmetry and broadening of the pulse envelopes. The rate of the development of the asymmetry and the broadening is apparently faster than that for the EMAT experiments, even though the operation point of these waveforms is close to the one in the EMAT experiments. This phenomenon is again consistent with the predictions by the space model (not with the time model) in that the rate of pulse broadening and skewing is closely associated with the initial pulse width: the smaller the initial pulse width, the faster the pulse spreads and skews (because of larger τ_s). The fast pulse spreading and skewing phenomenon can also be observed in the A_1 waveforms in Figs. 9 and 10. The envelope of these experimental waveforms show, once again, that the space model performs better than the time model, at least for the waveforms obtained in this study.

To see how the periods vary within the pulses of the PZT waveforms, we have obtained two additional waveforms, Figs. 11 and 12. These two waveforms, one for the S_0 mode and the other for the A_1 mode, were similarly obtained as those of Figs. 7 and 9 except that small shifts in space (transducer separation distances) were purposely made to align a peak of a cycle in each waveform to the background grids to help observe the period variation within the pulses. From Figs. 11 and 12, one sees clearly that the period decreases with time for the S_0 mode and increases for the A_1 mode, indicating that $\omega_0'' < 0$ or $k_0'' > 0$ for the S_0 mode and $\omega_0'' > 0$ or $k_0'' < 0$ for the A_1

mode. As a matter of fact, this feature can sometimes be used to identify the mode. This is especially helpful when the dispersion curves of two modes are close. Such situations are not uncommon when making measurements with Lamb modes. Dispersion curves of these modes frequently approach and repel each other. When this occurs, the two dispersion curves in that vicinity have opposite signs for ω_0'' (see Fig. 1).

SIMULATIONS

As discussed before in the previous section, the space model performs more realistically than the time model. In this section, a more quantitative comparison will be made between the experimental results and the simulated results based on the space model.

Using the parameters listed in Table IV, simulated waveforms have been generated for both the S_0 and the SH_1 modes. Figures 13 and 14 are the simulated waveforms for the S_0 mode with the pulse width parameter B being 16.0 mm and Figs. 15 and 16 are the simulated waveforms for the SH_1 mode with B being 10.0 mm. The two pulse width values were selected by trial-and-error to have the best visual fits between Figs. 4 and 13 for the S_0 mode and between Figs. 6 and 15 for the SH_1 mode.

Comparisons between the experimental waveforms (Figs. 3~6) and the simulated waveforms (Figs. 13~16) illustrate some common characteristic features. Overall, the shapes of the simulated waveforms are in very good agreement with the experimental ones. The space model reproduces very well both the pulse spreading and the pulse skewing phenomena, even though the pulses in the experiments cannot be true Gaussians. One may notice the disagreement in magnitudes between the experimental and the simulated waveforms. This disagreement is due to the attenuation and absorption factors not included in the pulse propagation model. One may also notice the time delay differences between the experimental and the simulated waveforms. The reason for this is that, for the simulated waveforms, the time starts at the center of a wave packet before it propagates. For the experimental waveforms, the time starts when the oscilloscope is trigged, which is at the beginning of a pulse; the time differences here roughly correspond to the half width of pulses in time.

Quantitative comparisons of the period variations within the pulses

have also been made between the experimental and the simulated waveforms. The period variation comparison for the S_0 mode is shown in Fig. 17. The experimental waveform were obtained for a travel distance of 165 mm. The time measurement error is about ±1 ns and the noise induced error is about ±5 ns in the central region of the pulse. In producing the experimental part of Fig. 17, the times of all the zero-crossings within the experimental waveforms were first recorded. The periods corresponding to consecutive two zero-crossings were then computed from the recorded times. There were about 40 cycles within the experimental waveform, of which about 30 cycles gave stable time values. The theoretical part of Fig. 17 was produced based on the pulse propagation model (the space model) with a computation rounding error of ±1 ns. Figure 18 is the period variation comparison for the SH_1 mode. The procedure for obtaining the data in Fig. 18 is the same as for the S_0 mode except that the waveform was for a propagation distance of 200 mm. The experimental waveform for the SH_1 mode was generally less noise contaminated.

The comparisons in Figs. 17 and 18 show a reasonable agreement overall. The period change pattern predicted by the space model have been clearly confirmed--higher frequency components move slower when $\omega'' < 0$ and faster when $\omega'' > 0$. The disagreement in details between the experiment and the theory in Figs. 17 and 18 can be accounted for by the following reasons. First of all, the experimental pulses are not Gaussian; there are many Gaussian components if one tries to expand the pulses in terms of a series of Gaussians. When we approximate the non-Gaussians with only one Gaussian component, the model should be valid for the first order approximation; i.e., showing up the trend. Indeed, the period variations from both the experimental and the simulated waveforms have the same trend. Secondly, there are experimental errors involved. EMATs are inductive in nature [16], the errors or noises associated with EMAT signals are generally larger than those of conventional PZT transducers. The error

for the S_0 mode for a specific zero-crossing is about ±5 ns at the central region and about ±10 ns at the half width when a repeatability test is conducted. The error for the SH_1 mode is a little less, about ±3 ns at the central region and ±5 ns at the half width. This is attributable to the structure of EMATs and will not be elaborated here. The third error source is the inaccuracy of the pulse width parameter B. Recall that this parameter was chosen through trial-and-error to have the best visual fit. It is unlikely that the found values are exact. The inaccuracy of parameter B alters the slope of the theoretical data. It should not, however, introduce local irregularities.

Of the three error sources mentioned above, the first one is believed to be the dominant, followed by the second one. Of course, the disagreement between the experiment and the theory may also be due to the pulse propagation model itself, since the development of the space model involves several approximations. However, it is our belief that these approximations do not significantly contribute to the disagreement shown in Figs. 17 and 18.

Recall that we have developed a relation for dV_{pm}/dt in Eqs. (20) and concluded that the change of phase velocity within a pulse is monotonic (increase or decrease). To see how the space model performs in this aspect, time changes for all the zero-crossings within a pulse were recorded when a small distance change were made. The change in distance for the S_0 mode was positive 2.6 mm (0.103") at 165 mm and the change for the SH_1 mode was 2.8 mm (0.109") at 200 mm. The local phase velocities ($\approx \Delta x/\Delta t$) within a pulse were then calculated from the time changes and the distance changes. The experimental data are plotted in Fig. 19 for the S_0 mode and Fig. 20 for the SH_1 mode, along with the results from the simulations. Although the comparisons are not excellent, the trends in phase velocity change within the pulse are the same for both the experimental and the simulated data. The disagreement is due to the error sources discussed in the previous paragraph.

CONCLUSIONS AND APPLICATIONS

Two models for pulse propagation of dispersive waves have been studied in this paper. Analytical solutions for some features associated with pulse propagation have been developed and discussed. The two models predict differently on the envelope shape of pulse propagation but similarly on the period variation within the pulse envelope. Experiments using various ultrasonic dispersive waves have been conducted to evaluate these two models. It has been found that the space model originally proposed by Thompson and Elsley gives more realistic outcomes than the time model. Quantitative comparison has also been done between the experimental waveforms and the simulated waveforms using the space model. Good agreement has been observed between the experimental and the simulated results. Certain minor disagreement is believed to be associated with the experimental errors as well as the non-Gaussian shaped pulses used in the experiments. In short, we have found that the space model works satisfactorily.

There are many possible applications of the pulse models. An obvious one is the determination of the concavity of the dispersion curve from shifts in local periods. Using the space model, one can also estimate or calculate the rate of pulse spreading and skewing when making or evaluating experimental and system design. The space model has been used to provide an error estimation model for phase velocity measurement based on tracking a zero-crossing as the transducer separation distance changes [17]. In addition, pulse models can provide a convenient tool to simulate pulse propagation without going through complicated Fourier transform analysis.

ACKNOWLEDGEMENT

Ames Laboratory is operated for the U. S. Department of Energy by the Iowa State University under contract No. W-7405-Eng-82. This work was supported by the Director for Energy Research, Office of Basic Energy Sciences.

REFERENCES

1. G. I. Terina. "On Distortion of Pulses in Ionospheric Plasma." Radio Eng. Electron. Phys. 12 (1967): 109-113.

2. G. I. Terina. "Propagation of Pulsed Signals in Media with Absorption and Dispersion." Radio Eng. Electron. Phys. 17 (1973): 611-13.

3. C. G. B. Garrett and D. E. McCumber. "Propagation of a Gaussian Light Pulse through an Anomalous Dispersion Medium." Phys. Rev. A 1 (1970): 305-13.

4. S. Chu and S. Wong. "Linear Pulse Propagation in an Absorbing Medium." Phys. Rev. Lett. 48 (1982): 738-741.

5. A. Katz and R. R. Alfano. "Pulse Propagation in an Absorbing Media." Phys. Rev. Lett. 49 (1982): 1292.

6. A. Puri and J. L. Birman. "Transient and Pulse Propagation in Linear Spatially Dispersive Media." In Semiconductors Probed by Ultrafast Laser Spectroscopy. Vol. II. Ed. R. R. Alfano. New York: Academic Press, 1984. 295-330.

7. R. B. Thompson and R. K. Elsley. "A Prototype EMAT System for Inspection of Steam Generator Tubing." Electric Power Research Institute, Palo Alto, California, Rept. S101-1, EPRI NP-2836, 1983.

8. R. B. Thompson, J. F. Smith, S. S. Lee, and G. C. Johnson. "A Comparison of Ultrasonic and X-ray Determinations of Texture in Thin Cu and Al Plates." Met. Trans. 20A (1989): 243147.

9. R. B. Thompson, S. S. Lee, and J. F. Smith. "Relative Anisotropies of Plane Waves and Guided Modes in Thin Orthorhombic Plates: Implication for Texture Characterization." Ultrasonics 25 (1987): 133-37.

10. R.-J. Roe. "Description of Crystallite Orientation in Polycrystalline Materials. III. General Solution to Pole Figure Inversion." J. Appl. Phys. 36 (1965): 2024-31.

11. R.-J. Roe. "Inversion of Pole Figures for Materials Having Cubic Crystal Symmetry." J. Appl. Phys. 37 (1966): 2069-72.

12. M. Hirao, K. Aoki, and H. Fukuoka. "Texture of Polycrystalline Metals Characterized by Ultrasonic Velocity Measurements." J. Acoust. Soc. Am. 81 (1987): 1434-40.

13. Y. Li and R. B. Thompson. "Influence of Anisotropy on the Dispersion Characteristics of Guided Ultrasonic Plate Modes." J. Acoust. Soc. Am. 87 (1990): 1911-31.

14. I. A. Viktorov. Rayleigh and Lamb Waves. New York: Plenum Press, 1967.

15. Y. Li and R. B. Thompson. "Use of the Velocity of Higher Order Lamb Modes in the Measurement of Texture." In Review of Progress in Quantitative Nondestructive Evaluation. Vol. 8B. Eds. D. O Thompson and D. E. Chimenti. New York: Plenum Press, 1989. 1863-70.

16. R. B. Thompson. "Physical Principles of Measurement with EMAT Transducers." In Physical Acoustics. Vol. XIX. Ed. W. P. Mason. New York: Academic Press, 1990. 157-200.

17. Y. Li and R. B. Thompson. "Effects of Dispersion on the Inference of Metal Texture from S_0 Plate Mode Measurements: Part II.Influence of Pulse Distortion on Velocity Measurements." To be submitted to IEEE Transactions on Ultrasonics, Ferroelectricity, and Frequency Control.

Table I. Relations between ω_0 and other relevant quantities for the space model

ω''	Arg(t,x)	∂Arg/∂t	∂^2Arg/∂t^2	D_0 - Δt	dΔt/dt
> 0	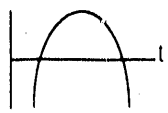	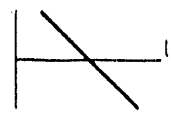	< 0	$> 0 \Longrightarrow < 0$	> 0
< 0	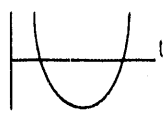	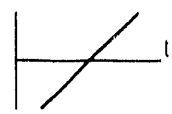	> 0	$< 0 \Longrightarrow > 0$	< 0

Table II. Relation between V_{pm} and V_p within wave packet for the space model

	$\omega_0'' > 0$		$\omega_0'' < 0$	
	$V_g > V_p$	$V_g < V_p$	$V_g > V_p$	$V_g < V_p$
$t < t_C$	$V_{pm} > V_p$	$V_{pm} < V_p$	$V_{pm} < V_p$	$V_{pm} > V_p$
$t = t_C$	$V_{pm} > V_p$	$V_{pm} > V_p$	$V_{pm} < V_p$	$V_{pm} < V_p$
$t = t_D$	$V_{pm} > V_p$	$V_{pm} > V_p$	$V_{pm} < V_p$	$V_{pm} < V_p$
$t > t_D$	$V_{pm} < V_p$	$V_{pm} > V_p$	$V_{pm} > V_p$	$V_{pm} < V_p$

Table III. Elastic constants (in GPa) of the textured Al plate

ij	11	22	33	23	13	12	44	55	66
C_{ij}	111.58	111.77	111.25	60.28	60.47	59.95	26.37	26.56	26.02

Table IV. Experimental parameters at the points of operation

Mode	D_0 mm	k_0 mm^{-1}	K	ω_0 μs^{-1}	W	ω_0' mm/μs	W'	ω_0'' $mm^2/\mu s$	W''
S_0	5.1	1.232	0.867	5.773	1.294	2.828	0.899	-4.097	-1.847
SH_1	5.4	1.164	0.819	5.789	1.297	1.985	0.631	1.029	0.464

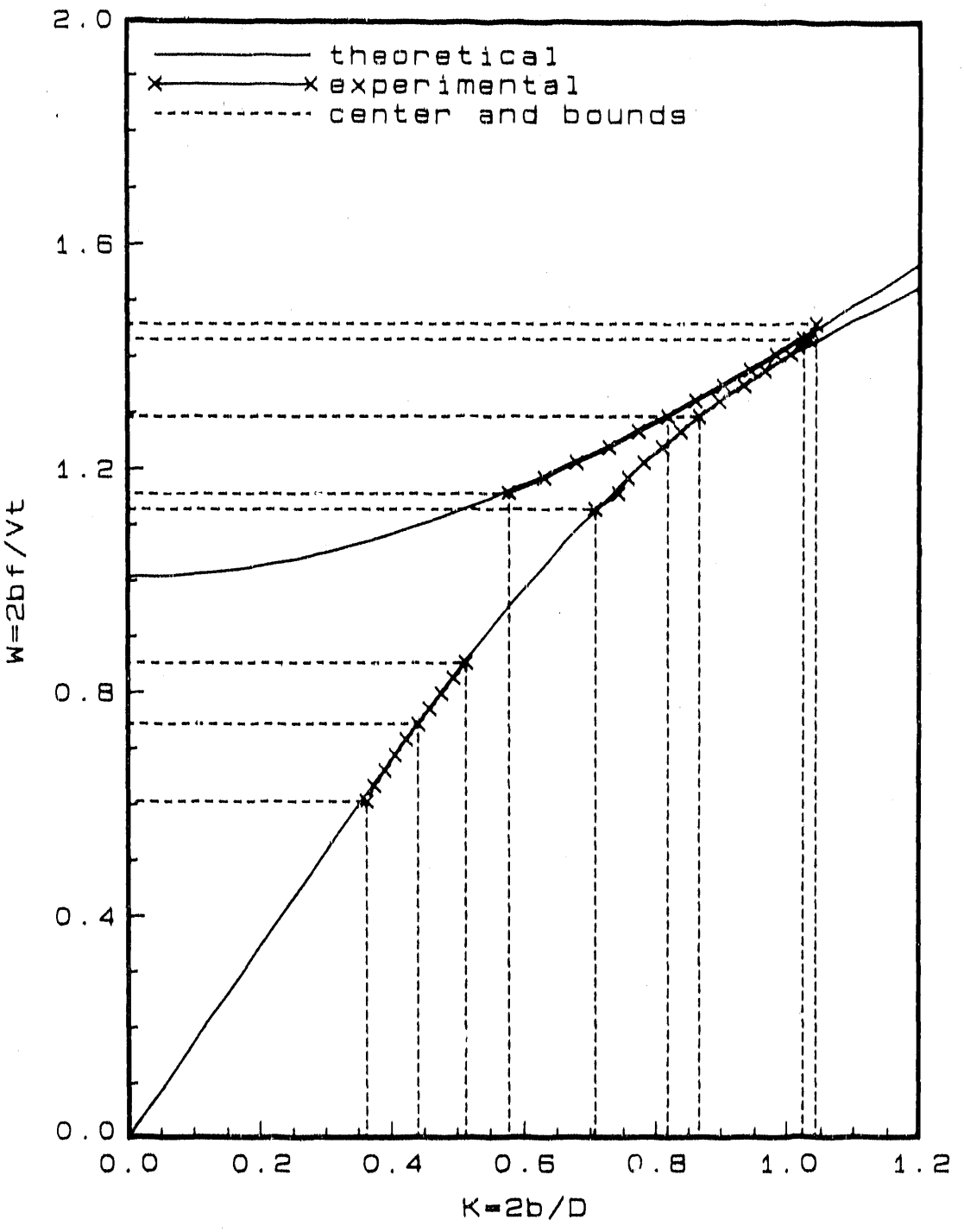

Fig. 1. Dispersion curves of S_0 and SH_1 modes

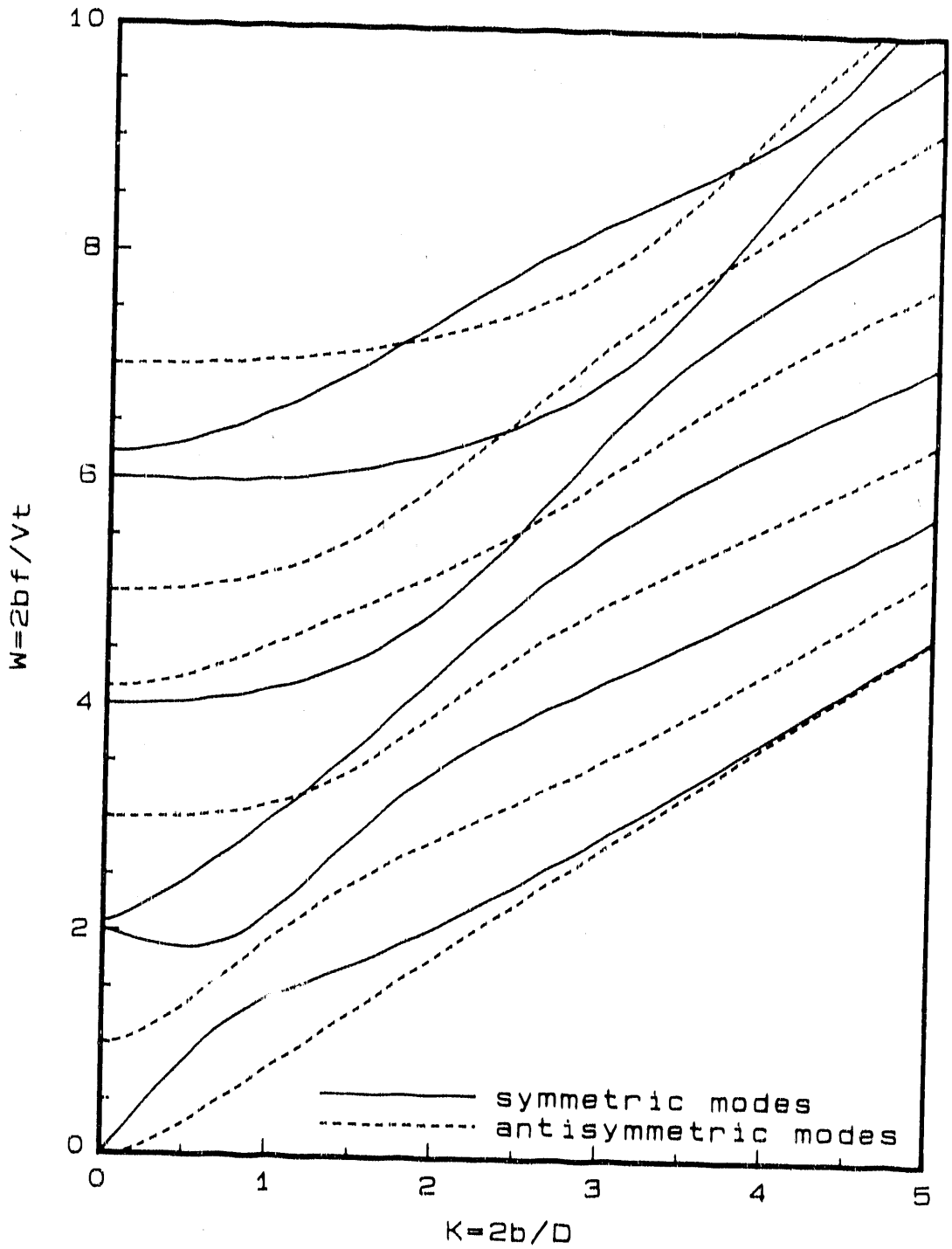

Fig. 2. Dispersion curves of a few lowest order Lamb modes

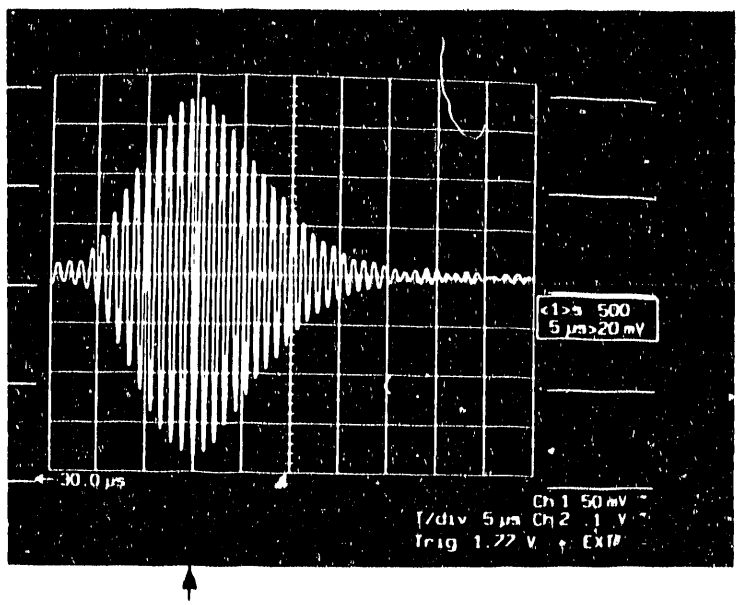

Fig. 3. Experimental waveform of S_0 mode (EMAT separation distance is 110 mm)

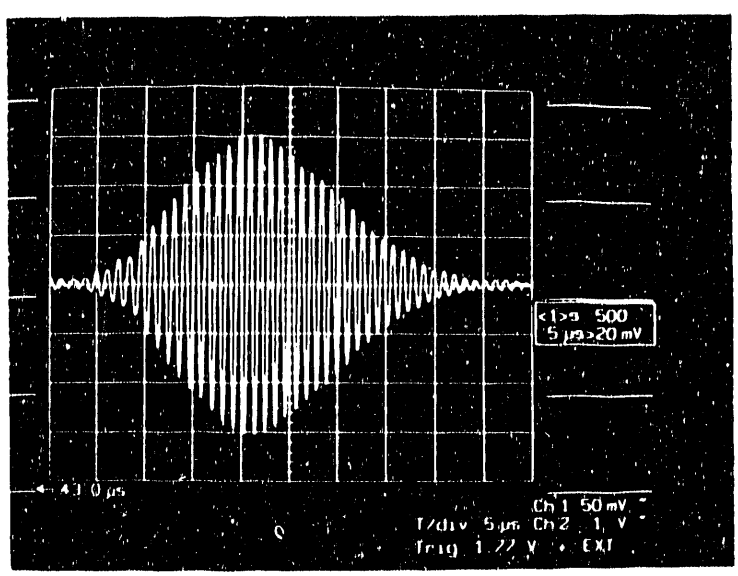

Fig. 4. Experimental waveform of S_0 mode (EMAT separation distance is 165 mm)

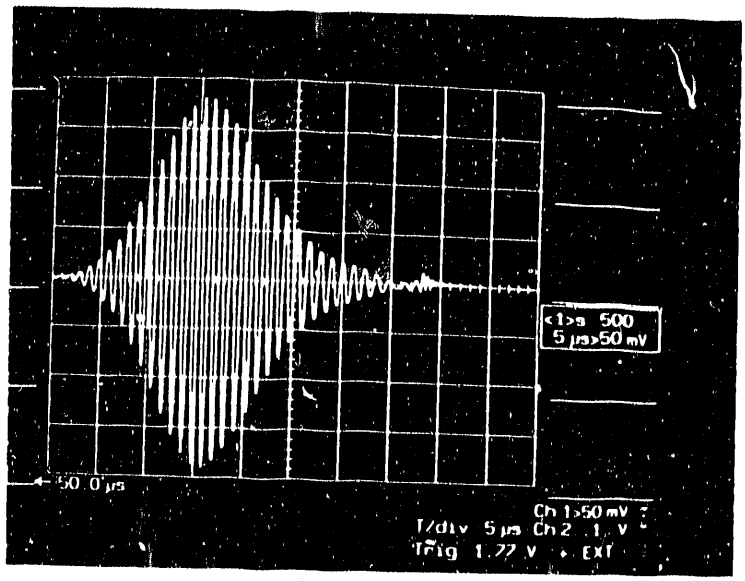

Fig. 5. Experimental waveform of SH_1 mode (EMAT separation distance is 120 mm)

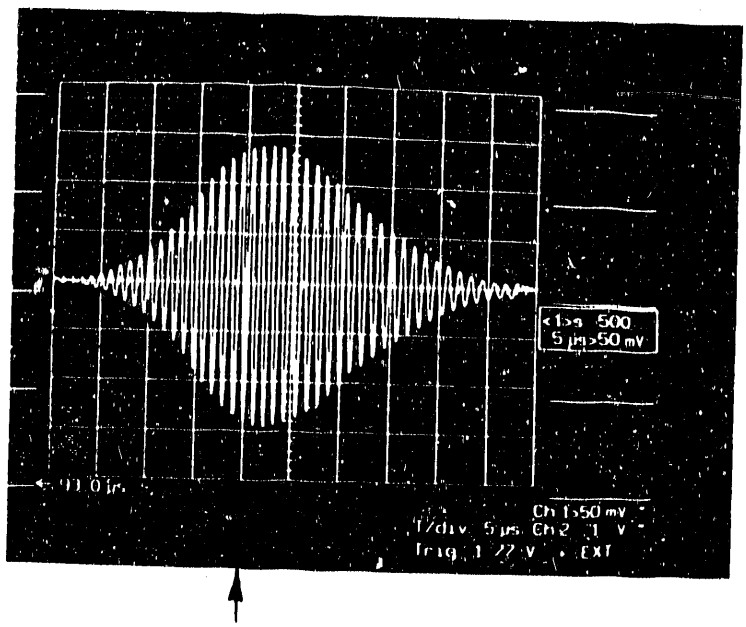

Fig. 6. Experimental waveform of SH_1 mode (EMAT separation distance is 220 mm)

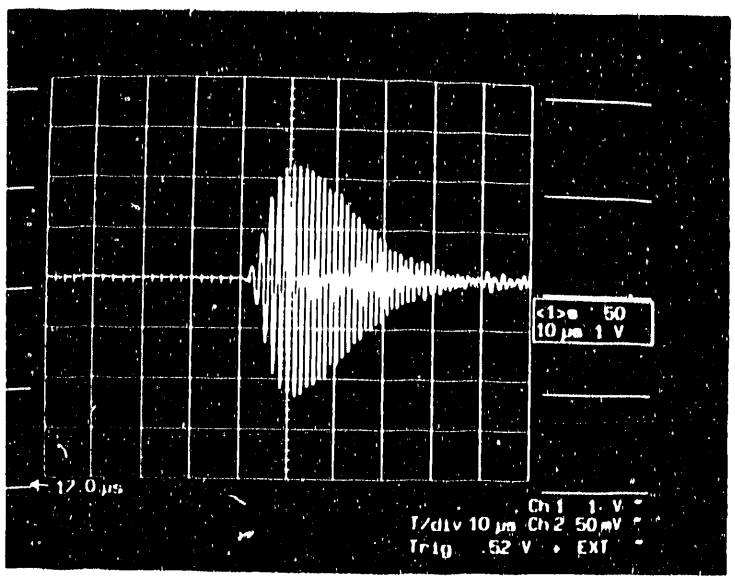

Fig. 7. S_0 mode waveform using PZT transducers (x≈150 mm)

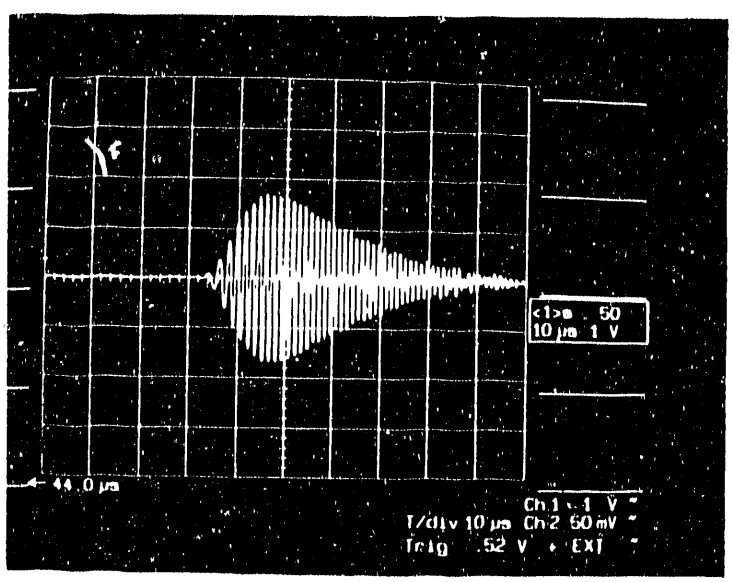

Fig. 8. S_0 mode waveform using PZT transducers (x≈250 mm)

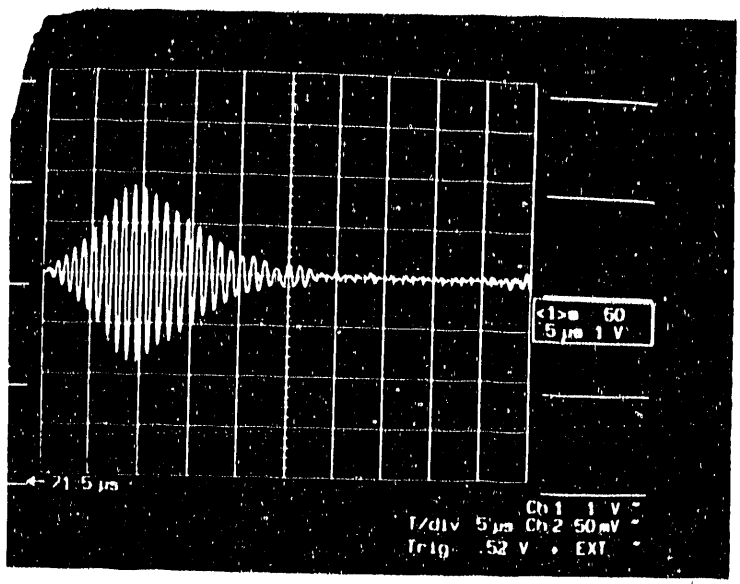

Fig. 9. A_1 mode waveform using PZT transducers (x≈150 mm)

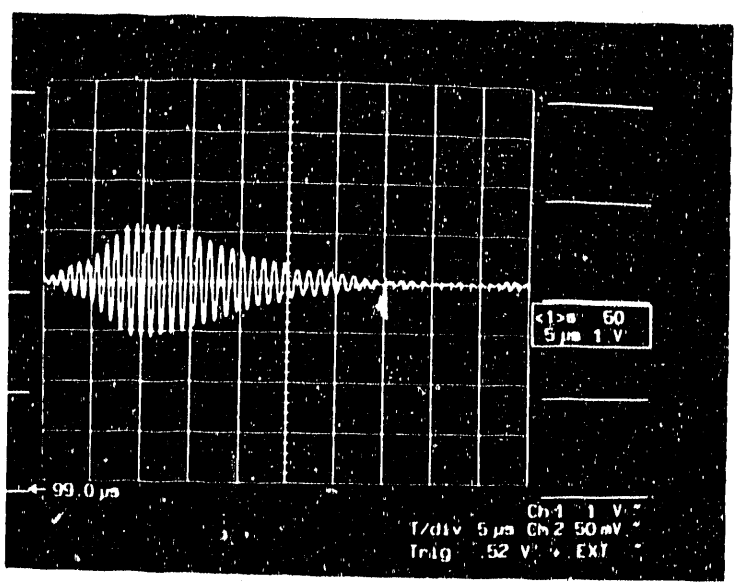

Fig. 10. A_1 mode waveform using PZT transducers (x≈250 mm)

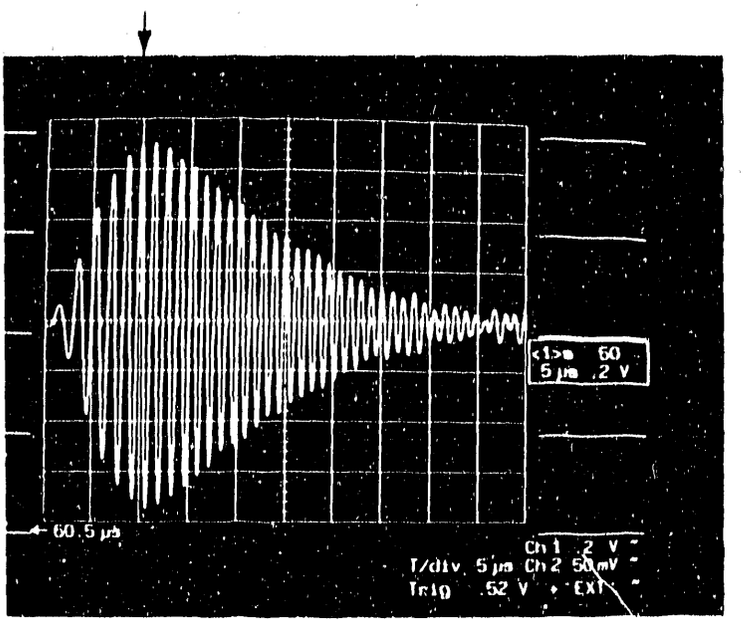

Fig. 11. S_0 mode waveform using PZT transducers where some peaks aligned with background grids

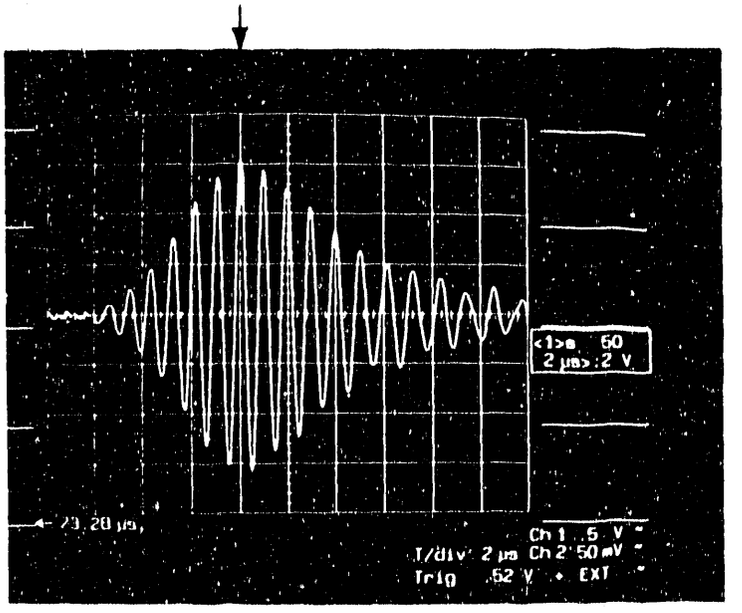

Fig. 12. A_1 mode waveform using PZT transducers where some peaks aligned with background grids

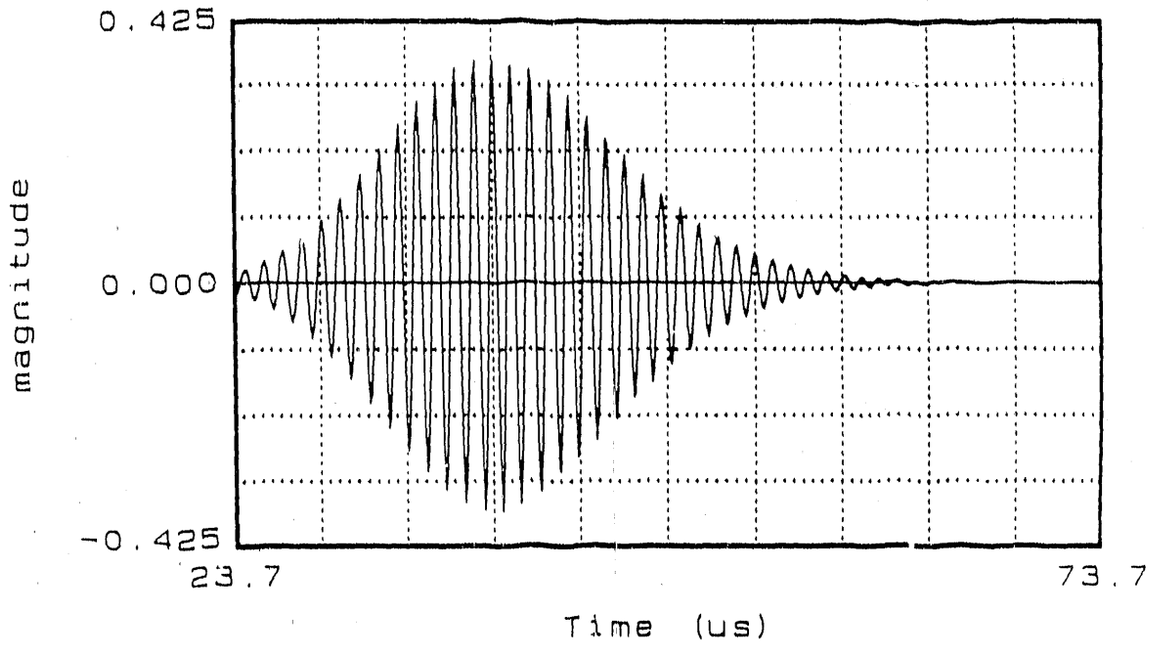

Fig. 13. Simulated waveform of S_0 mode (propagation distance is 110 mm)

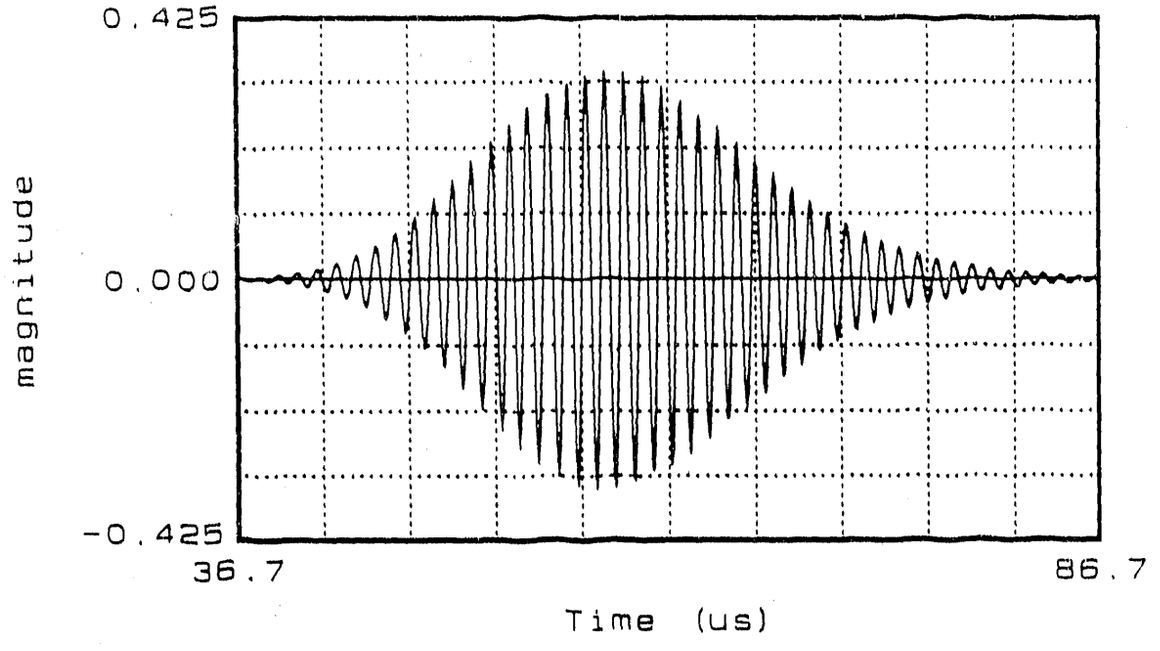

Fig. 14. Simulated waveform of S_0 mode (propagation distance is 165 mm)

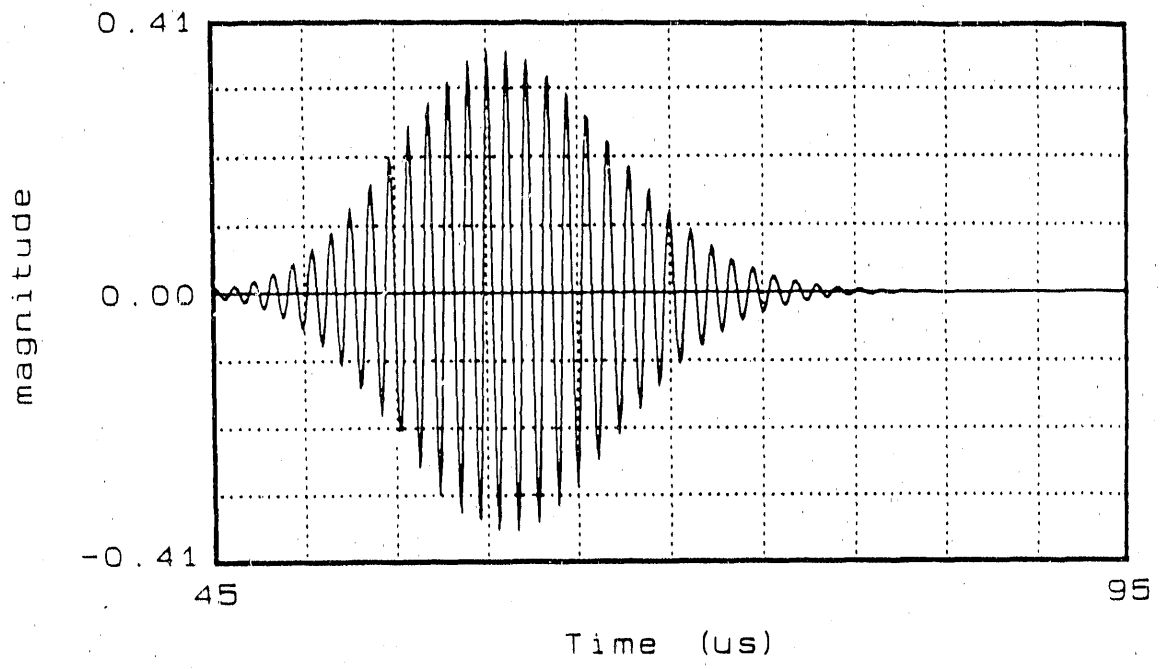

Fig. 15. Simulated waveform of SH_1 mode (propagation distance is 120 mm)

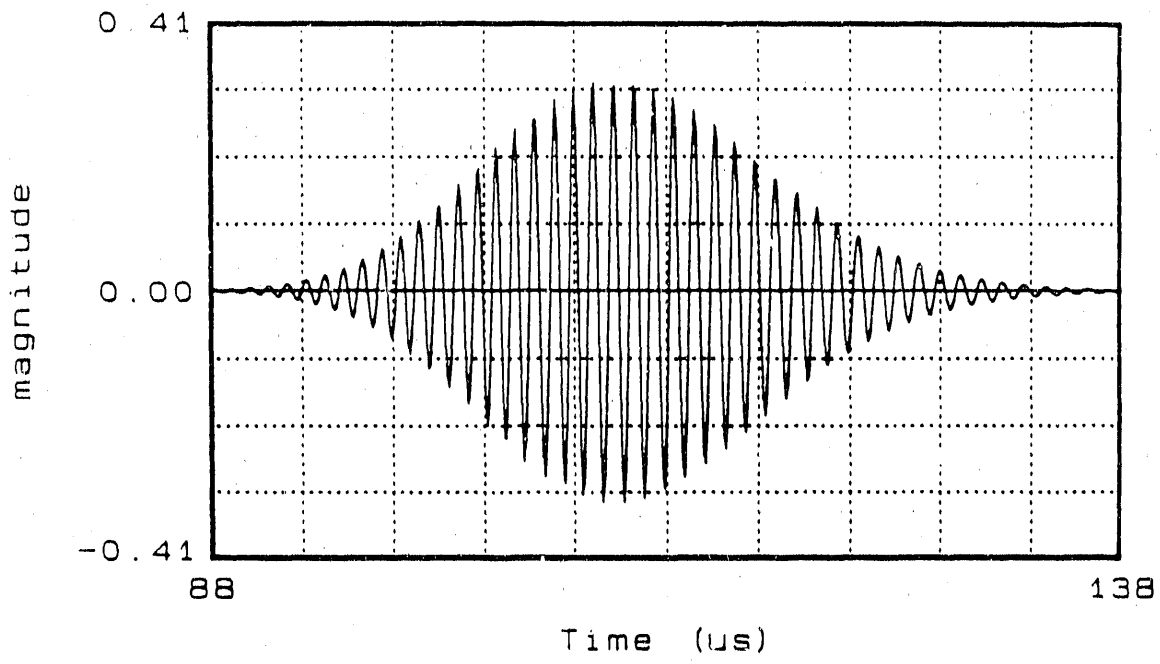

Fig. 16. Simulated waveform of SH_1 mode (propagation distance is 220 mm)

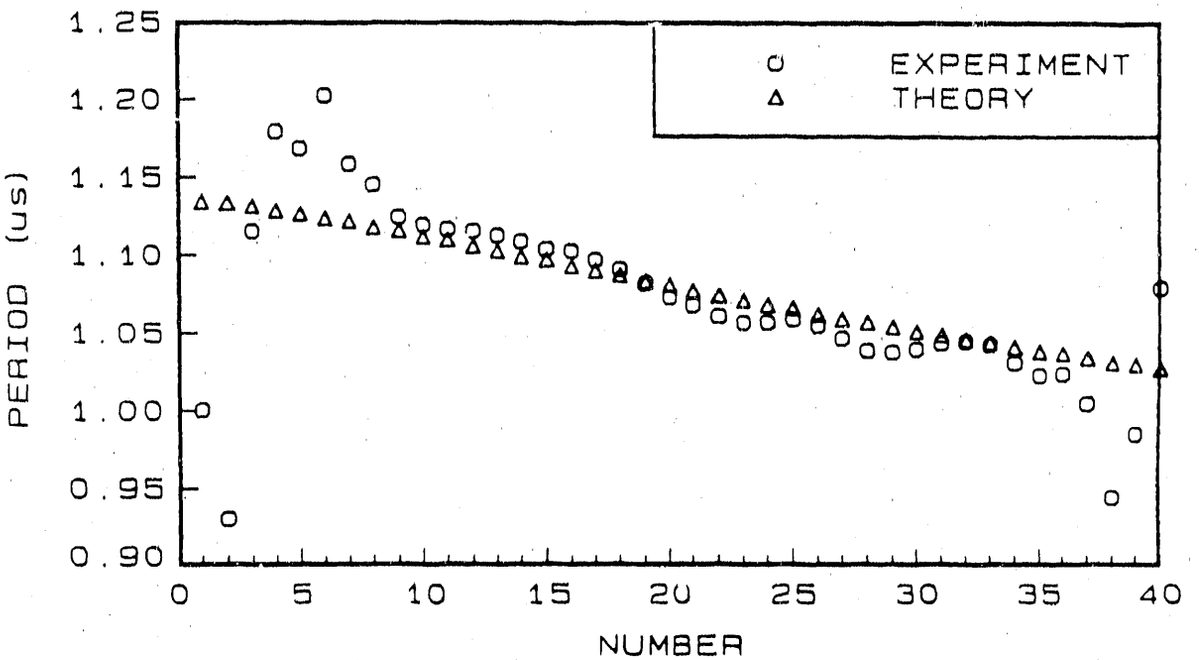

Fig. 17. Period variation within wave packet for the S_0 mode (x=165 mm)

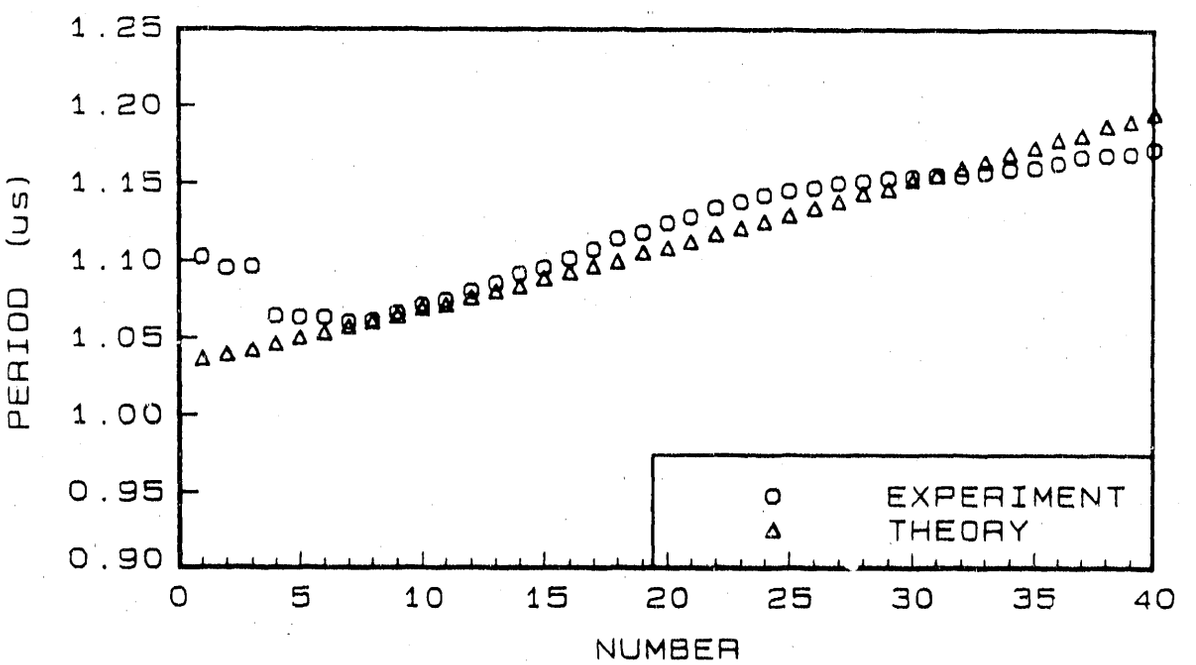

Fig. 18. Period variation within wave packet for the SH_1 mode (x=200 mm)

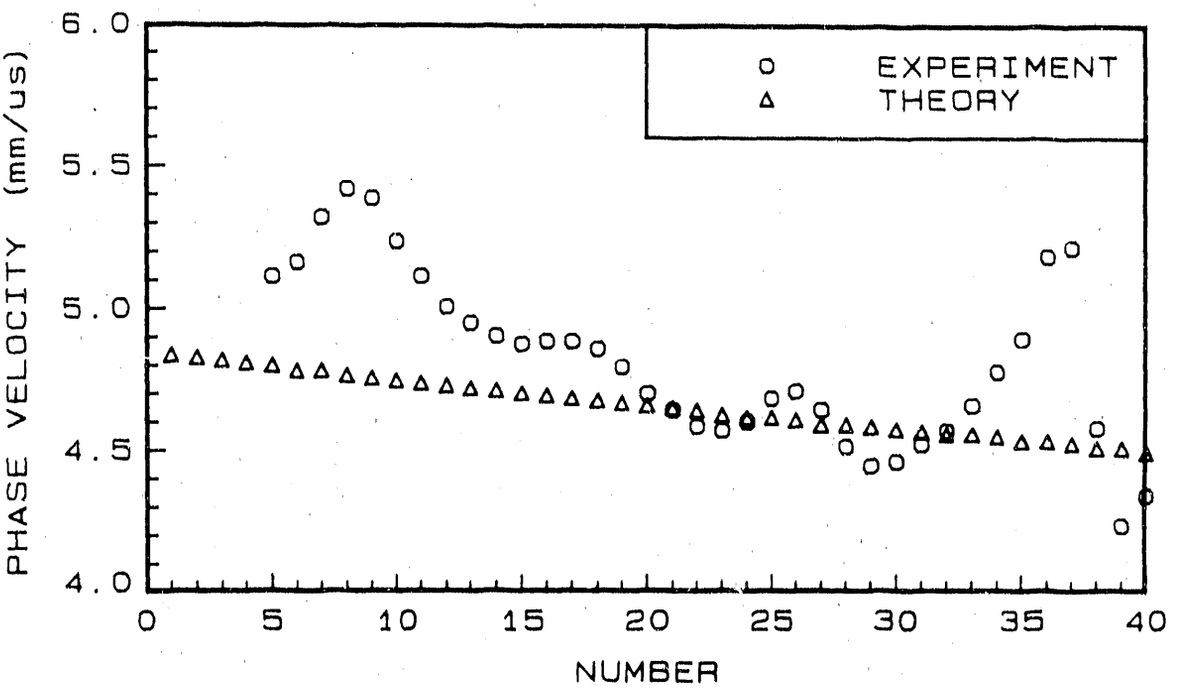

Fig. 19. Phase velocity variation within wave packet for the S_0 mode (x=165 mm)

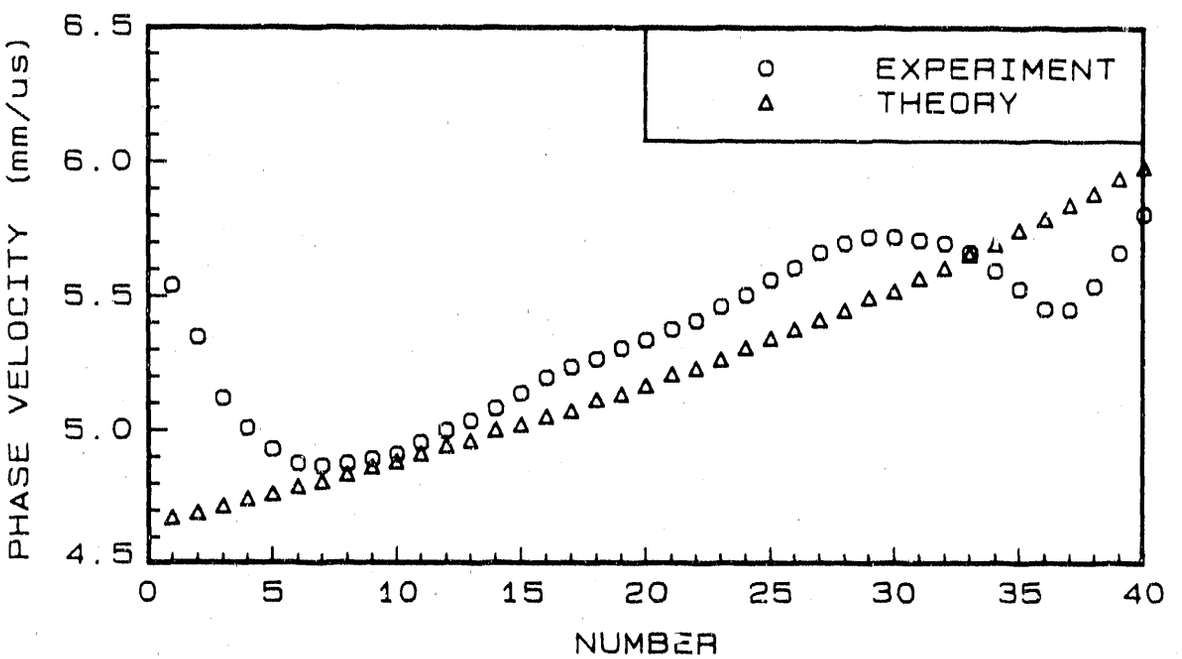

Fig. 20. Phase velocity variation within wave packet for the SH_1 mode (x=200 mm)

PART IV.

EFFECTS OF DISPERSION ON THE INFERENCE OF METAL TEXTURE FROM S_0 PLATE MODE MEASUREMENTS

PART I. EVALUATION OF DISPERSION CORRECTION METHODS

ABSTRACT

Ultrasonic S_0 waves (fundamental symmetric Lamb modes) are commonly used in nondestructive characterization of texture (preferred grain orientation) and formability in metal sheets and plates. In a typical experimental set up, the velocities of the S_0 waves are measured as a function of wave propagation angle with respect to the rolling direction of the plate. However, the S_0 waves are known to be dispersive, and that dispersion must be considered in order to isolate the small, texture induced shifts in the S_0 wave velocity. Currently, there are two approximate dispersion correction methods, one proposed by Thompson et al. and the other introduced by Hirao and Fukuoka. In this paper, these two methods will be evaluated using an exact theory for wave propagation in orthotropic plates. Through the evaluation, the limits of the current texture measurement techniques are established. It is found that when plate thickness to wavelength ratio is less than 0.15, both Thompson's and Hirao's methods work satisfactorily. When the thickness to wavelength ratio exceeds 0.3, neither Thompson's nor Hirao's dispersion correction method provides adequate corrections for the current texture measurement techniques. Within the range of 0.15-0.3, Thompson's method is recommended for weakly anisotropic sheets and plates and Hirao's method may be more appropriate for some strongly anisotropic cases.

INTRODUCTION

Texture is the non-random orientation of crystallites in a polycrystalline aggregate, often induced by manufacturing processes such as rolling and drawing. Knowledge of texture information is particularly important in making formability predictions. For materials made of cubic crystallites, such as Al (fcc), Cu (fcc), and Fe (bcc), texture is characterized by a set of dimensionless parameters W_{lmn}, called orientation distribution coefficients (ODCs). The detailed definition of these coefficients can be found in Refs. 1 and 2. The most important ODCs in formability analysis are W_{400}, W_{420}, and W_{440} for cubic polycrystals. Physically, W_{420} and W_{440} relate to the tendency of a metal sheet to form two and four ears respectively upon deep drawing. W_{400} relates to overall capacity to withstand deep drawing [3]. Traditionally, these ODC's are obtained through X-ray or neutron diffraction techniques. Typical values of these ODCs are on the order of 10^{-3}.

In recent years, ultrasonic waves have been utilized to provide a nondestructive estimation of the texture of cubic polycrystals [4-6]. The texture generally induces a weak elastic anisotropy which can be sensed by measurements of the velocity of waves propagating in different directions. When the sample is in the form of a sheet or plate, the waves take the form of guided modes with two types being commonly used in texture characterization, the zeroth order horizontally polarized shear waves (SH_0) and the fundamental symmetric Lamb waves (S_0). This paper deals with the latter ones only. S_0 waves are known to be dispersive, having frequency dependent propagation velocities. Because the texture induced velocity shifts are small, the dispersion effects must be considered if accurate estimation of texture is to be achieved.

There are two aspects to the influence of dispersion of the S_0 waves on the velocity measurements. First, both the phase velocity and the group

velocity are frequency dependent. Two dispersion correction methods have been proposed by Thompson et al. [7] and Hirao and Fukuoka [8] to remove the frequency dependency. In this paper, these two dispersion correction methods will be evaluated assuming perfect measurements of phase velocity. Another aspect of dispersion is the pulse distortion phenomenon; i.e., a pulse of a dispersive wave changes its shape and spreads out as it propagates. Part II of this paper discusses the influence of the pulse distortion on the accuracy of phase velocity measurements.

Several years ago, Thompson et al. [9] and Lee et al. [10] developed a theory which relates the aforementioned ODCs of textured sheets to the S_0 wave speeds in three different directions (0^0, 45^0, and 90^0) with respect to the rolling direction. This theory assumes the ratio of sheet thickness to wavelength to be small. In this limit, the velocity of the S_0 wave in a specific propagation direction asymptotically approaches a constant value, V_{lim}, and dispersion can be ignored. Upon comparison of experimental predictions of the ODCs based on this theory with the results from independent X-ray or neutron diffraction techniques, satisfactory agreement was found for W_{420} and W_{440}, but not for W_{400}. In those measurements, the ratio of thickness to wavelength was about 0.1. Recently, Thompson et al. [7] modified the theory and included dispersion correction in the calculation of the ODCs. In the modified theory, the dispersion correction is made on the basis of dispersion curves of the S_0 waves in the corresponding isotropic materials. It is assumed that the ratio V_p/V_{lim} is not altered significantly by the presence of texture (weak anisotropy), where V_p is the ultrasonic phase velocity measured at a specific frequency and V_{lim} is the long wavelength limit of the S_0 wave phase velocity. Hirao and Fukuoka [8] have proposed another method which takes dispersion effects into account by making a Taylor series expansion of the dispersion curves of the S_0 mode propagating in weakly orthotropic media. In the expansion, only the first order dispersion effects are retained.

The basis of our evaluation of the approximate dispersion correction methods is the exact theoretical equations recently developed for wave propagation in plates with orthotropic symmetry [11-14]. The equations which express the dependence of wave propagation velocity upon texture parameters are very complex and a simple technique has not been developed to compute the ODCs from given wave velocities on the basis of these exact equations. These equations, however, can serve as an exact reference solution. In this paper, we will use the exact solution for the S_0 wave propagation in orthotropic plates to simulate experimental data and then use those data to test the accuracy of the two approximate dispersion correction methods.

One semantic difficulty should be resolved before proceeding. In the metallurgical community, the terms "sheet" and "plate" have connotations of different thicknesses, with the former appropriate to thicknesses on the order of a millimeter to which the ultrasonic approach has been most extensively applied. In the ultrasonic literature, the term "plate" is generally used to describe a solid medium having parallel surfaces, independent of thickness. In the remainder of this paper, the latter convention will be employed. However, in considering metallurgical applications, the "sheets" should be understood to be included.

GENERAL THEORY FOR WAVE PROPAGATION IN ORTHOTROPIC FREE PLATES

The authors of the present paper [11,12] and Nayfeh and Chimenti [13,14] have recently developed and reported the analytical dispersion equations for wave propagation in orthotropic or monoclinic free plates. For detailed derivation and discussions, the readers are encouraged to refer to these references. Here only the equations necessary to make this paper self-contained will be presented.

Consider the coordinate system shown in Fig. 1. Let us first make the following dimensionless definitions:

$$K_1 = K\cos^2\alpha\,, \qquad K_2 = K\sin^2\alpha\,, \qquad K = \left(\frac{b}{\pi}k\right)^2\,,$$

$$W = \frac{\rho\omega^2}{C_{66}}\left(\frac{b}{\pi}\right)^2\,, \qquad R_i = \left(\frac{b}{\pi}r_i\right)^2\,, \qquad (i = 1, 2, 3)$$

where b is the plate thickness, ρ is the density, C_{ij} are the elastic constants of plate material, a is the wave propagation angle with respect to the rolling direction, k is the wave vector in the propagation direction, w is the angular frequency of the propagating wave, and r_i are the eigenvalues of the associated Christoffel equations for plane wave propagation.

For a general elastic, homogeneous orthotropic free plate whose rolling, transverse, and normal directions coincide with the X_1, X_2, and X_3 axes, as shown in Fig. 1, the dispersion equation for the S_0 wave propagating at 0^0 is

$$Q_1\left[\tan\left(\frac{\pi}{2}\sqrt{R_2}\right)\right]^{-1} - Q_2\left[\tan\left(\frac{\pi}{2}\sqrt{R_3}\right)\right]^{-1} = 0 \qquad (1)$$

where $Q_1 = Q(R_2,R_3)$, $Q_2 = Q(R_3,R_2)$;

and $Q(X, Y) = \sqrt{Y}\,(C_{13}X - C_{11}K + C_{66}W)\,[C_{11}C_{55}Y$

$$+ (C_{11}C_{33} - C_{13}C_{55} - C_{13}^2)K - C_{33}C_{66}W]$$

and R_2, R_3 are roots of the following equation for K_3:

$$(C_{11}K + C_{55}K_1 - C_{66}W)(C_{55}K + C_{33}K_1 - C_{66}W) - (C_{13} + C_{55})^2 K_1 K = 0 .$$

The dispersion equation for the S_0 wave propagating at 45^0 is (generalized Rayleigh-Lamb wave equation in orthotropic media):

$$P_1\left[\tan\left(\frac{\pi}{2}\sqrt{R_1}\right)\right]^{-1} + P_2\left[\tan\left(\frac{\pi}{2}\sqrt{R_2}\right)\right]^{-1} + P_3\left[\tan\left(\frac{\pi}{2}\sqrt{R_3}\right)\right]^{-1} = 0 \qquad (2)$$

where $P_1 = P(R_1,R_2,R_3)$, $P_2 = P(R_2,R_3,R_1)$, $P_3 = P(R_3,R_1,R_2)$,

$$P(X,Y,Z) = \sqrt{X}\,[C_{13}K_1N_x(x) + C_{23}K_2N_y(X) + C_{33}N_z(X)]\cdot \{[YN_x(Y) + N_z(Y)]\cdot[ZN_y(Z) + N_z(Z)] - [YN_y(Y) + N_z(Y)]\cdot[ZN_x(Z) + N_z(Z)]\},$$

$$N_x(X) = (C_{23} + C_{44})(C_{12} + C_{66})K_2 - (C_{13} + C_{55})(C_{66}K_1 + C_{22}K_2 + C_{44}X - C_{66}W),$$

$$N_y(X) = (C_{13} + C_{55})(C_{12} + C_{66})K_1 - (C_{23} + C_{44})(C_{11}K_1 + C_{66}K_2 + C_{55}X - C_{66}W),$$

$$N_z(X) = (C_{66}K_1 + C_{22}K_2 + C_{44}X - C_{66}W)(C_{11}K_1 + C_{66}K_2 + C_{55}X - C_{66}W) - (C_{12} + C_{66})^2 K_1 K_2 ,$$

and R_i are solutions to a cubic equation arising from the Christoffel equations [11,12].

The dispersion equation for the S_0 wave propagating at 90^0 has the same form as Eq. (1) except that the following changes must be made: C_{11}--> C_{22}, C_{13}--> C_{23}, C_{44}-->C_{55}, and C_{55}-->C_{44}.

In the absence of anisotropy, Eqs. (1) and (2) simplify to the well known Rayleigh-Lamb wave equation in isotropic media.

For an orthotropic material, there are in general nine independent elastic constants C_{ij}. When the plate is made of cubic crystallites, these elastic constants are not all independent. They are related to the elastic constants of single crystallites and texture parameters. The relations, published by Hirao et al. [15], are as follows:

$$C_{11} = \lambda+2\mu + (12\sqrt{2}c\pi^2/35)[W_{400} - (2\sqrt{10}/3)W_{420} + (\sqrt{70}/3)W_{440}] ,$$

$$C_{22} = \lambda+2\mu + (12\sqrt{2}c\pi^2/35)[W_{400} + (2\sqrt{10}/3)W_{420} + (\sqrt{70}/3)W_{440}] ,$$

$$C_{33} = \lambda+2\mu + (32\sqrt{2}c\pi^2/35)\,W_{400} ,$$

$$
\begin{aligned}
C_{44} &= \mu - (16\sqrt{2}c\pi^2/35)(W_{400}+\sqrt{5/2}\,W_{420}), \\
C_{55} &= \mu - (16\sqrt{2}c\pi^2/35)(W_{400}-\sqrt{5/2}\,W_{420}), \\
C_{66} &= \mu + (4\sqrt{2}c\pi^2/35)(W_{400}-\sqrt{70}\,W_{440}), \\
C_{23} &= \lambda - (16\sqrt{2}c\pi^2/35)(W_{400}+\sqrt{5/2}\,W_{420}), \\
C_{13} &= \lambda - (16\sqrt{2}c\pi^2/35)(W_{400}-\sqrt{5/2}\,W_{420}), \\
C_{12} &= \lambda + (4\sqrt{2}c\pi^2/35)(W_{400}-\sqrt{70}\,W_{440}),
\end{aligned}
\tag{3}
$$

where λ and μ are Lamé constants for the corresponding isotropic (texture free) material and c is a measure of the elastic anisotropy of the individual crystallites. The isotropic Lamé constants and the anisotropy constant can be obtained from single crystal elastic constants c_{ij} via different averaging methods. Voigt, Hill and Reuss averaging methods are commonly used in texture study owning to their simplicity. The Lamé constants for these averaging methods are given in Ref. 15 as:

$$
\begin{aligned}
&(\lambda+2\mu)_V = c_{11}-2c_V/5, \quad \mu_V = c_{11}+c_V/5, \\
&(\lambda+2\mu)_R = 2(s_{11}+s_{12}-s/5)/[(s_{11}+2s_{12})(s_{11}+4s/5)], \\
&\mu_R = (s_{44}+4s/5)^{-1}, \quad (\lambda+2\mu)_H = [(\lambda+2\mu)_V + (\lambda+2\mu)_R]/2, \\
&\mu_H = (\mu_V + \mu_R)/2, \quad c_V = c_{11}-c_{12}-2c_{44}, \quad c_R = -4\mu_R^2 s, \\
&c_H = (c_V + c_R)/2, \quad s = s_{11}-s_{12}-s_{44}/2,
\end{aligned}
\tag{4}
$$

where s_{ij} are elastic compliances for single crystallites.

From Eqs. (1)-(4), with a given set of ODCs, solutions for frequency w can be computed for each wave number k. Figure 2 shows an isotropic dispersion curve for the S_0 wave in an aluminum plate. References 11 and 12 include some examples of similar dispersion curve plots with wider ranges of k and w for different orthotropic materials. The phase velocities, defined as w/k, can then be calculated for different frequencies easily.

When propagating in the 0^0 and 90^0 directions, S_0 waves may be described as a superposition of plane longitudinal partial waves (L) and

vertically polarized shear partial waves (SV) only; they are decoupled from the horizontally polarized shear partial waves (SH). On the other hand, at 45^0 angle, all L, SV, and SH partial waves are coupled together to form the S_0 waves. Because of this, the dispersion equation for the S_0 wave propagating at the 45^0 angle is significantly more complicated, as can be seen in Eq. (2).

Although the dispersion relations given by Eqs. (1) and (2) can be used to compute ultrasonic wave speeds from given texture parameters, the inverse problem cannot be solved analytically. Therefore, the community has developed approximate procedures to obtain texture parameters from experimental data. In the following section, we will use the exact dispersion relations to evaluate the accuracy of the two dispersion correction methods which are currently in application.

APPROXIMATE THEORIES FOR DISPERSION CORRECTIONS

Thompson et al. [9] and Lee et al. [10] applied the theory of wave propagation to texture characterization of cubic polycrystalline aggregates in plates with infinitesimal thickness. Under that assumption, the propagating wave is not dispersive and the relation between its speed and the elastic constants of the plate [10] is (after dropping higher order texture and the stress related terms):

$$\rho V_{S_0}^2(\alpha) = \hat{C}_L + \frac{1}{2}\hat{\alpha}\hat{C}_L \cos 2\alpha - \frac{1}{2}\hat{\beta}\hat{C}_T(1-\cos 4\alpha) \tag{5}$$

where $\hat{C}_L = \left(\frac{C_{11}+C_{22}}{2}\right) - \left(\frac{C_{11}^2+C_{21}^2}{2C_{11}}\right)$, $\quad \hat{C}_T = C_{66}$

$$\hat{\alpha} = \left[(C_{11}-C_{22}) - \left(\frac{C_{11}^2 - C_{21}^2}{C_{11}}\right)\right]/\hat{C}_L$$

$$\hat{\beta} = \left\{\left[\left(\frac{C_{11}+C_{22}}{2}\right) - C_{12} - \frac{(C_{11}-C_{21})^2}{2C_{11}}\right]/2 - C_{66}\right\}/\hat{C}_T$$

To first order in anisotropy, the velocity is then given by [9]:

$$V_{S_0}(\alpha) = \left(\frac{\hat{C}_L}{\rho}\right)^{1/2}\left[1 + \frac{\hat{\alpha}}{4}\cos 2\alpha - \left(\frac{\hat{\beta}\hat{C}_T}{4\hat{C}_L}\right)(1-\cos 4\alpha)\right] \tag{6}$$

To express the velocity in terms of ODCs (using Eqs. (3) and (4)), after certain approximations involving moving the W_{400} terms in C_{33} in denominators to numerators by means of first order Taylor approximation, Eq. (5) can be reduced to:

$$\rho V^2(\alpha) = \left(1-\frac{P^2}{L^2}\right)L + \frac{4\pi^2 c}{35}\Big[\sqrt{2}\left(3+8\frac{P}{L}+8\frac{P^2}{L^2}\right)W_{400} - 4\sqrt{5}\left(1+2\frac{P}{L}\right)W_{420}\cos 2\alpha + 2\sqrt{35}W_{440}\cos 4\alpha\Big] \tag{7}$$

where $L \equiv l+2m$, $P \equiv l$ and c is an anisotropy constant also defined in Eqs. (4). Similar approximation to Eq. (6) leads to:

$$V(\alpha)=\sqrt{(1-P^2/L^2)L/\rho}+\frac{2\pi^2c}{35}\sqrt{\rho L/(L^2-P^2)}\left\{\sqrt{2}\left(3+8\frac{P}{L}+8\frac{P^2}{L^2}\right)W_{400}\right.$$
$$\left.-4\sqrt{5}\left(1+2\frac{P}{L}\right)W_{420}\cos 2\alpha+2\sqrt{35}\,W_{440}\cos 4\alpha\right\} \qquad (8)$$

From Eq. (7) or (8), linear combinations of velocities measured for a=0^0,45^0, and 90^0 can then be taken to obtain the values of W_{400}, W_{420} and W_{440}.

Since no plate is infinitesimally thick, wave propagation in a plate is always dispersive. Although this effect is small for thin plates, so is the effect of texture. Thus the experimental data must be corrected for dispersion if quantitative values of the texture parameters are to be obtained.

The S_0 waves used in texture studies are generally weakly dispersive, with a typical measurement frequency of 500 KHz and plate thickness of a few millimeters. In order to reduce the error introduced by the dispersion, Thompson et al. [7] suggested a simple dispersion correction approach. Starting from the measured phase velocity V_p, the data were corrected to estimate the long wavelength limit of that velocity, V_{lim}, by assuming the ratio V_p/V_{lim} to be the same in the weakly anisotropic plate as it would be in an isotropic plate of the same thickness. The corrected velocities (long wavelength limits) were then used in Eq. (7) or (8). In our experimental work, the dispersion correction normally amounts to less than 10% of the measured velocities, and the dispersion correction method described above was intuitively believed to be reasonable. This correction improved the accuracy of estimates of the ODCs, particularly on W_{400}, as expected. However, no rigorous evaluation of the range of accuracy of this approach was made.

Hirao and Fukuoka [8] have proposed another dispersion correction method. They have developed a dispersion equation for wave propagation in orthotropic plates under a perturbation frame which neglects the involvement of SH partial waves for wave propagation in nonsymmetry directions. The dispersion equation has a form which resembles Eq. (1) and

reduces to it when the wave propagation direction is in a symmetry direction. To develop an explicit relation between ODCs and wave speeds in different propagation directions, they then made a Taylor series expansion at zero frequency and included one higher order term to approximate dispersion effects at low frequencies. After dropping higher order terms in W_{lmn}, the equation for the square of the velocity is[1]

$$V_{S_0}^2(\alpha) = V_0^2\,(1-\Delta) + (2c/\rho)[(s_0 + d_0\Delta)W_{400} + (s_2 + d_2\Delta)W_{420}\cos(2\alpha) + s_4 W_{440}\cos(4\alpha)] \qquad (9)$$

After a further approximation, the final equation is

$$V_{S_0}(\alpha) = V_0\sqrt{(1-\Delta)} + (c/\rho V_0)[(s_0 + d_0\Delta)W_{400} + (s_2 + d_2\Delta)W_{420}\cos(2\alpha) + s_4 W_{440}\cos(4\alpha)] \qquad (10)$$

where $s_0=(2\sqrt{2}\pi^2/35)[3 + 16\lambda(\lambda+\mu)/(\lambda+2\mu)^2]$, $s_2=-(8\sqrt{5}\pi^2/35)(3\lambda+2\mu)/(\lambda+2\mu)$, $s_4=4\pi^2/\sqrt{35}$, and $d_0=(16\sqrt{2}\pi^2\rho V_0^2)(3\lambda+2\mu)/[35\lambda(\lambda+2\mu)]$, $d_2=-16\sqrt{5}\pi^2\rho V_0^2/35\lambda$, with $V_0=\sqrt{4\mu(\lambda+\mu)/\rho(\lambda+2\mu)}$ being the isotropic velocity at kb=0 and $\Delta=[\lambda/(\lambda+2\mu)]^2(kb/2)^2/3$ describing the dispersion. For either of these expressions, solution for the W_{lmn} in terms of the velocities at 0^0, 45^0, and 90^0 is straightforward.

Since Eq. (9) was derived via a Taylor expansion in wave vector, it is expected to be valid (or provide good approximation) for small kb. This is confirmed by comparing Eqs. (7) and (9), which reveals that they are identical for plates of zero thickness. The approximation made in the derivation of Eq. (10) involved a second Taylor series, in the small variables W_{lmn}, to eliminate the squares in velocities, an approximation similar to that made in going from Eq. (5) to Eq. (6) or from Eq. (7) to Eq. (8). Thus, Eq. (10) reduces to Eq. (8), but not Eq. (9), for zero thickness. However, Eqs. (7)-(10) are identical in the absence of anisotropy (texture free) in the long wavelength limit. The effects of this further approximation will be discussed in the next section.

[1]This equation was not published in Ref. 8, but is an intermediate step.

For the convenience of discussion later on, we shall call the Thompson's dispersion correction method applied to Eqs. (7) and (8) and the Hirao's dispersion correction method using Eqs. (9) and (10) as Thompson's-A, Thompson's-B, Hirao's-A, and Hirao's-B schemes respectively.

In summary, Thompson's schemes neglect the small deviation of the S_0 dispersion curves of textured plates from that of the isotropic ones and Hirao's schemes use a parabolic approximation to the anisotropic dispersion curves to replace the exact ones that are not suitable for the estimation of texture parameters.

EVALUATION OF DISPERSION CORRECTION SCHEMES

To evaluate the performance of the dispersion correction schemes mentioned above, we calculated the S_0 wave speeds for four selected groups of ODCs as a function of plate thickness to wavelength ratio using the exact dispersion relations presented earlier. These speeds were then used as input to the dispersion correction schemes to get estimates of the ODCs. The first step can be considered as a forward problem while the second step is an inverse problem. The initial values for the ODCs are listed in Table I. The values of the ODCs chosen here for the simulations are realistic representations of values encountered in textured plates. Groups I and II correspond to relatively strong textures and Groups III and IV correspond to relatively weak textures. Simulations have been run for the three commonly used cubic materials, Al, Cu, and Fe. The densities and the single crystal elastic constants for the three materials are given in Table II. For all the simulation runs, the Hill averaging method was employed because it is known to be more accurate than either the Voigt or Reuss averaging method, which respectively provides upper or lower bounds to the isotropic moduli. The isotropic and anisotropic elastic constants and Poisson ratios for the polycrystalline materials are listed in Table III for the Hill averaging method. For the purpose of this paper, we neglect any errors in the Hill approximation. Note that the anisotropy constant to isotropic shear modulus ratio c/m in Table III for Cu or Fe is about 4 to 5 times larger than that for Al. Since the anisotropy of a polycrystal aggregate arises from the anisotropy within the single crystals and W_{lmn} are the only orientation description parameters of the aggregate,the same set of W_{lmn} represents different degrees of anisotropy for different materials. For the four groups of ODCs we used in our study, Groups I and II for Cu and Fe exhibit the strongest anisotropy. All the rest are more weakly anisotropic, even though Groups I

and II for Al have same texture values as for the strongly anisotropic Cu and Fe cases. A feeling of the strength of the anisotropy for the four sets of ODCs in the simulation can be obtained from the elastic constants given in Table IV.

Figures 3-5 show the results from the inversion step. Here the values of the ODCs that would be predicted on the basis of different dispersion correction schemes are plotted as functions of plate thickness to wavelength ratio or b/D, where D denotes the wavelength. Please note the scales for the ordinates are different for the predictions of each of the three ODCs. For the current texture measurement configuration [16,17], the wavelength of the S_0 waves is about 10 mm; the range 0-0.5 for b/D represents a plate thickness of 0-5 mm.

In addition to the four curves representing the predictions from Thompson's and Hirao's schemes described in the previous section, there are three horizontal straight lines in each figure, identifying the value of the ODCs assumed in the forward calculations and the target error bounds (to be discussed shortly). To see how dispersion correction schemes influence the prediction of ODCs, the results calculated directly from Eq. (7) without any dispersion corrections are also included in Figs. 3-5. These results are represented by an extra dash-dotted curve in the W_{400} and W_{420} figures of Figs. 3-5. In the W_{440} figures of Figs. 3-5, this extra curve is not plotted; it would fall on top of the curve representing the response from the Hirao's-A scheme which uses Eq. (9). A comparison between Eq. (7) and Eq. (9) shows that in Hirao's-A scheme, dispersion correction plays no role in the prediction of W_{440}; therefore, the responses for W_{440} using Eqs. (7) and (9) are identical.

Consider first the performance of the predictions of W_{440} (figures (c), (f), (i), and (l) of Figs. 3-5). For the weakly anisotropic cases (figures (c), (f), (i), and (l) of Fig. 3, and figures (i) and (l) of Figs. 4 and 5), the performances of Thompson's schemes are practically equivalent, and Hirao's-B scheme is

found to be better than Hirao's-A scheme, providing wider range of reliable predictions. When the anisotropy becomes strong (figures (c) and (f) of Figs. 4 and 5), both Thompson's-B and Hirao's-B schemes may produce predictions of W_{440} with relatively large errors for small thickness to wavelength ratio. This is especially true for Thompson's-B scheme, although it may sometimes give good predictions at some large thickness to wavelength ratio. This error is the consequence of the approximations made in going from Eq. (5) to Eq. (8) and from Eq. (9) to Eq. (10), which suggests that Eqs. (8) and (10) are not favorable for such cases. Over the range of thickness to wavelength ratio plotted, Thompson's-A scheme has a longer flat region and is generally better than Hirao's-A scheme for the cases studied. In fact, in the region b/D = 0-0.25, the errors associated with the prediction by Thompson's-A scheme are very small. Since in Hirao's schemes W_{440} is not corrected for dispersion, when compared to Thompson's schemes, one finds that improvement can be made with the inclusion of the dispersion effect, although this effect is not as strong as that for W_{400}. (See discussions on W_{400}.)

Now consider the performance of the predictions of W_{420}. As can be seen in figures (b), (e), (h), and (k) of Figs. 3-5, Thompson's and Hirao's schemes influence the prediction of W_{420} in opposite directions in all the cases studied, although the amount of influence are about the same in the range of b/D = 0-0.25. Except for the strongly anisotropic cases, Hirao's-B scheme generally gives better predictions than Thompson's schemes and Hirao's-A scheme. Similar to the predictions of W_{440}, Thompson's-B and Hirao's-B schemes may give unacceptable errors to the prediction of W_{420} when the anisotropy of the plate gets strong. However, when compared to the predictions without dispersion correction, one finds that neither Thompson's nor Hirao's schemes are as good as the uncorrected predictions for all the cases studied. This clearly indicates that dispersion correction is really not necessary for W_{420}. As a matter of fact, the curves representing the predictions of W_{420} without dispersion correction in general have a very flat

region for b/D = 0-0.25. These results are not fully understood. It can be argued that, since W_{420} is known to be a measure of in-plane anisotropy, having little to do with the plate thickness which strongly influences the dispersion characteristics, no correction is needed. However, this same argument would apply to predictions of W_{440}. Since Hirao's-A scheme, corresponding to no correction, gives the poorest results for W_{440}, further factors must be involved.

The situation is somewhat different for the prediction of W_{400}, which is rather sensitive to the way in which correction is made for dispersion. A glance of figures (a), (d), (g), and (j) of Figs. 3-5 reveals that both Hirao's and Thompson's schemes improve the estimation of W_{400} significantly. Noting the compressed scale of these plots we see that the errors are considerably greater than in the predictions of W_{420} and W_{440}. Hirao's-A and Hirao's-B schemes generally exhibit similar performance, with the former being somewhat more accurate. Thompson's schemes also exhibit similar performance, particularly when the anisotropy is not strong. Depending on the sign of W_{400}, Thompson's and Hirao's schemes may affect the prediction of W_{400} in either same or opposite direction. For weakly anisotropic textured plates, Thompson's schemes generally predict W_{400} with smaller errors. When the anisotropy becomes stronger, Hirao's schemes can be superior than Thompson's schemes. This fact is due to the nature of the approximations made in the Thompson's and Hirao's schemes. For Hirao's schemes, the accuracy of the prediction is closely related to the value of b/D; it is relatively insensitive to the degree of anisotropy. The performance of Thompson's schemes, on the other hand, depend on the smallness of the difference between the isotropic and anisotropic dispersion curves. For most of rolling and annealing textures, particularly on Al plates, where the anisotropy is not very strong, this difference is indeed small. In this case, Thompson's schemes may be more appropriate for b/D > 0.15. The greater sensitivity of the predictions of W_{400} to the details of the dispersion correction

occurs because W_{400} depends on the absolute, rather than relative values of measured velocities [7].

To see how Thompson's and Hirao's schemes correct for the dispersion quantitatively, we set up the following target error bounds for each group: $|\delta W_{400}| \sim 0.001$, $|\delta W_{420}|$ and $|\delta W_{440}| \sim 0.0005$. These error bounds are chosen from a practical point of view, as they represent the experimentally observed differences between ultrasonic and diffraction (X-ray or neutron) predictions of the ODCs [7]. Table V shows the acceptable limits of thickness to wavelength ratio for Thompson's-A and Hirao's-A schemes as well as from the uncorrected equation if one wishes to stay within these bounds for the cases studied. It gives a guide line for the validity range of the current experimental configuration and dispersion correction schemes. For most metal sheets of interest in texture and formability prediction, the plate thickness is less than 2.5 mm. This thickness is about the limit of the present techniques if the wavelength is around the typical 10 mm value. From Table V, it is readily seen that, for the prediction of W_{400}, Hirao's-A scheme is not favorable for Al when the plate thickness to wavelength ratio is larger than 0.17. With the exception of Group II in Cu and Fe, Thompson's scheme provides a wider range of valid dispersion corrections for W_{400}. Both Thompson's-A and Hirao's-A scheme, however, significantly improve the prediction of W_{400}. On the other hand, the valid ranges for both Thompson's-A and Hirao's-A schemes for the prediction of W_{420} are narrower than that from the equation without dispersion correction. It also can be seen from Table V that the valid range of b/D for Thompson's-A scheme for the prediction of W_{440} is from 0 up to about 0.35-0.4. The corresponding range for Hirao's-A scheme (equivalent to no correction) is 0.23-0.3.

From Figs. 3-5, one cannot fail to see that even when the plate thickness approaches zero, where the dispersion corrections are zero for all schemes, the results from the inverse process do not give the right answers. This is not surprising. The errors for Thompson's-A and Hirao's-A schemes are

due to the approximations made when developing Eqs. (5), (7), and (9). These errors, however, are in general tolerable as they are well within the target error bounds. These errors are given in Table VI for all groups. For Thompson's-B and Hirao's--B schemes, the errors in predictions of W_{420} and W_{440} at zero thickness for Cu and Fe can be large, exceeding the target error bounds. Table VII lists the errors from these two schemes. A comparison of the values in Table VI to those in Table VII clearly indicates that, with few exceptions, Thompson's-A and Hirao's-A schemes are better than Thompson's-B and Hirao's-B schemes for thin plates.

CONCLUSIONS

We have evaluated the two available dispersion correction methods using numerical simulations to estimate the range of validity of each correction scheme. In general, both Thompson's-A and Hirao's-A schemes work well for plates with thickness to wavelength ratio less than 0.15. Thompson's-B and Hirao's-B schemes also lead to satisfactory results in this region, except for problems at small thickness to wavelength ratios of highly textured plates of Fe and Cu. Depending on the details of texture, preference may be given to a particular scheme. For thickness to wavelength ratios larger than 0.15, each technique begins to breakdown. Thompson's schemes usually have a greater range of validity for W_{400} for weakly anisotropic materials while Hirao's schemes may be superior in the prediction when the materials anisotropy is strong. None of these schemes, however, provides adequate corrections for W_{400} when the ratio exceeds 0.3. Therefore, one should be very cautious when applying the current experiment configuration to plates that give thickness to wavelength ratio larger than 0.3. For the prediction of W_{420}, the use of neither Thompson's schemes nor Hirao's schemes is encouraged as they all reduce the valid range for the prediction. For W_{440}, Thompson's-A and Hirao's-A schemes are practically equivalent for plates with thickness to wavelength ratio less than 0.2. When this ratio exceeds 0.2, Thompson's-A scheme is recommended. In either case, the dispersion correction effects are not as dominant as for W_{400}. Finally, Thompson's-B and Hirao's-B schemes should be avoided when the plate anisotropy is very strong, due to the relative large errors at small thickness to wavelength ratio.

ACKNOWLEDGEMENT

Ames Laboratory is operated for the U. S. Department of Energy by the Iowa State University under contract No. W-7405-Eng-82. This work was supported by the Director for Energy Research, Office of Basic Energy Sciences.

REFERENCES:

1. R.-J. Roe. "Description of Crystallite Orientation in Polycrystalline Materials. III. General Solution to Pole Figure Inversion." J. Appl. Phys. 36 (1965): 2024-31

2. R.-J. Roe. "Inversion of Pole Figures for Materials Having Cubic Crystal Symmetry." J. Appl. Phys. 37 (1966): 2069-72.

3. G. J. Davies, D. J. Goodwill, and J. S. Kallend. "Elastic and Plastic Anisotropy in Sheets of Cubic Metals." Met. Trans. 3 (1972): 1627-31.

4. C. M. Sayers. "Angular Dependent Ultrasonic Wave Velocities in Aggregates of Hexagonal Crystals." Ultrasonics 24 (1986): 289-91.

5. R. B. Thompson, S. S. Lee, and J. F. Smith. "Angular Dependence of Ultrasonic Wave Propagation in a Stressed Orthorhombic Continuum: Theory and Application to the Measurement of Stress and Texture." J. Acoust. Soc. Am. 80 (1986): 921-31.

6. A. V. Clark, Jr., R. C. Reno, R. B. Thompson, J. F. Smith, G. V. Blessing, R. J. Fields, P. P. Delsanto, and R. B. Mignogna. "Texture Monitoring in Aluminium Alloys: A Comparison of Ultrasonic and Neutron Diffraction Measurement." Ultrasonics 26 (1988): 189-97.

7. R. B. Thompson, J. F. Smith, S. S. Lee, and G. C. Johnson. "A Comparison of Ultrasonic and X-ray Determinations of Texture in Thin Cu and Al Plates." Met. Trans. 20A (1989): 2431-2447.

8. M. Hirao and H. Fukuoka. "Dispersion Relations of Plate Modes in Anisotropic Polycrystalline Sheets." J. Acoust. Soc. Am. 85 (1989): 2311-15.

9. R. B. Thompson, S. S. Lee and J. F. Smith. "Relative Anisotropies of Plane Waves and Guided Modes in Thin Orthorhombic Plates: Implication for Texture Characterization." Ultrasonics 25 (1987): 133-37.

10. S. S. Lee, J. F. Smith, R. B. Thompson. "Inference of Crystallite Orientation Distribution Function from the Velocity of Ultrasonic Plate Modes." In Nondestructive Characterization of Materials. Vol. 2. Ed. J. F. Bussiere. New York: Plenum Press, 1988. 555-62.

11. Y. Li and R. B. Thompson. "Propagation of Guided Elastic Waves in Orthotropic Plates." In Review of Progress in Quantitative Nondestructive Evaluation. Vol. 8A. Eds. D. O. Thompson and D. E. Chimenti. New York: Plenum Press, 1989. 189-96.

12. Y. Li and R. B. Thompson. "Influence of Anisotropy on the Dispersion Characteristics of Guided Ultrasonic Plate Modes." J. Acoust. Soc. Am. 87 (1990): 1911-31.

13. A. H. Nayfeh and D. E. Chimenti. "Free Wave Propagation in Plates of General Anisotropic Media." In Review of Progress in Quantitative Nondestructive Evaluation. Vol. 8A. Eds. D. O. Thompson and D. E. Chimenti. New York: Plenum Press, 1989. 181-88.

14. A. H. Nayfeh and D. E. Chimenti. "Free Wave Propagation in Plates of General Anisotropic Media." J. Appl. Mech. 56 (1989): 881-86.

15. M. Hirao, K. Aoki, and H. Fukuoka. "Texture of Polycrystalline Metals Characterized by Ultrasonic Velocity Measurements." J. Acoust. Soc. Am. 81 (1987): 1434-40.

16. S. J. Wormley, R. B. Thompson, and Y. Li. "Analysis of Semi-Automatic System for the Ultrasonic Measurement of Texture." In Review of Progress in Quantitative Nondestructive Evaluation. Vol. 7B. Eds. D. O. Thompson and D. E. Chimenti. New York: Plenum Press, 1988. 1639-46.

17. A. V. Clark, Jr., R. B. Thompson, G. V. Blessing, and D. Matlock. "Ultrasonic Measurement of Formability in Thin Ferritic Steel Sheet." In Review of Progress in Quantitative Nondestructive Evaluation. Vol. 8A. Eds. D. O. Thompson and D. E. Chimenti. New York: Plenum Press, 1989. 1031-38.

Table I. Initial ODCs for computer simulations

	Group I	Group II	Group III	Group IV
W_{400}	-0.01	0.01	-0.005	0.005
W_{420}	-0.005	-0.005	0.003	0.003
W_{440}	0.0075	0.0075	-0.004	-0.004

Table II. Densities and elastic constants of materials for single crystals

	C_{11}(GPa)	C_{12}(GPa)	C_{44}(GPa)	ρ(g/cm^3)
Al	108.0	62.0	28.3	2.71
Cu	169.0	122.0	75.3	8.9
Fe	229.0	134.0	144.0	7.8

Table III. Isotropic and anisotropic elastic constants and Poisson ratios of polycrystalline materials using the Hill averaging method

	$L=\lambda+2\mu$ (GPa)	$P=\lambda$ (GPa)	$T=\mu$ (GPa)	c (GPa)	c/μ	υ
Al	112.06	59.97	26.05	-10.77	-0.41	0.3486
Cu	200.73	106.13	47.30	-97.68	-2.07	0.3459
Fe	272.65	112.17	80.24	-132.08	-1.65	0.2915

Table IV. Elastic constants of the textured plates for the W_{mn} given in Table I (in GPa)

Mat'l	Group	C_{11}	C_{22}	C_{33}	C_{23}	C_{13}	C_{12}	C_{44}	C_{55}	C_{66}
Al	I	110.96	112.04	113.44	58.74	59.83	61.22	24.82	25.90	27.30
	II	109.93	111.01	110.69	60.11	61.20	60.88	26.19	27.28	26.95
	III	113.22	112.57	112.75	59.95	59.30	59.48	26.03	25.38	25.56
	IV	112.70	112.05	111.37	60.64	59.99	59.31	26.72	26.06	25.39
Cu	I	190.60	200.55	213.32	94.86	104.82	117.59	36.02	45.98	58.75
	II	181.15	191.11	188.14	107.45	117.41	114.44	48.62	58.57	55.60
	III	211.35	205.37	207.03	105.97	100.00	101.65	47.14	41.16	42.82
	IV	206.62	200.65	194.44	112.27	106.30	100.08	53.43	47.46	41.24
Fe	I	259.09	272.41	289.51	97.08	110.41	127.50	65.15	78.47	95.57
	II	246.45	259.77	255.80	113.94	127.26	123.29	82.00	95.33	91.35
	III	286.86	278.87	281.08	111.96	103.96	106.18	80.02	72.03	74.24
	IV	280.54	272.54	264.22	120.39	112.39	104.07	88.45	80.45	72.13

Table V. Acceptable limits of thickness to wavelength ratio for the error bounds: $|\delta W_{400}| \sim 0.001$, $|\delta W_{420}|$ and $|\delta W_{440}| \sim 0.0005$
(N--No dispersion correction,T--Thompson's-A scheme, H--Hirao's-A scheme)

		Group I			Group II			Group III			Group IV		
		N	T	H	N	T	H	N	T	H	N	T	H
Al	W_{400}	0.041	0.212	0.154	0.038	0.194	0.173	0.043	0.281	0.161	0.042	0.276	0.171
	W_{420}	0.394	0.307	0.278	0.395	0.281	0.293	0.438	0.500	0.344	0.438	0.500	0.347
	W_{440}	0.237	0.361	0.237	0.230	0.346	0.230	0.289	0.406	0.289	0.284	0.400	0.284
Cu	W_{400}	0.075	0.244	0.180	0.063	0.141	0.271	0.101	0.289	0.231	0.094	0.266	0.270
	W_{420}	0.393	0.348	0.220	0.400	0.193	0.311	0.441	0.500	0.344	0.437	0.500	0.354
	W_{440}	0.268	0.406	0.268	0.236	0.334	0.236	0.290	0.407	0.290	0.265	0.366	0.265
Fe	W_{400}	0.085	0.242	0.192	0.065	0.137	0.218	0.108	0.281	0.231	0.099	0.254	0.243
	W_{420}	0.472	0.330	0.286	0.464	0.170	0.365	0.494	0.490	0.403	0.489	0.471	0.406
	W_{440}	0.305	0.402	0.305	0.264	0.333	0.264	0.325	0.407	0.325	0.304	0.372	0.304

Table VI. Errors for zero thickness plates (x 0.01)
(For Thompson's-A and Hirao's-A schemes)

	$\|\delta W_{400}\|$			$\|\delta W_{420}\|$			$\|\delta W_{440}\|$		
	Al	Cu	Fe	Al	Cu	Fe	Al	Cu	Fe
Group I	0.009	0.050	0.050	0.006	0.029	0.029	0.003	0.012	0.010
Group II	0.019	0.054	0.054	0.007	0.033	0.034	0.003	0.017	0.013
Group III	0.002	0.012	0.012	0.002	0.009	0.008	0.001	0.005	0.005
Group IV	0.001	0.011	0.012	0.002	0.010	0.009	0.001	0.007	0.005

Table VII. Errors for zero thickness plates (x 0.01)
(For Thompson's-B and Hirao's--B schemes)

	$\|\delta W_{400}\|$			$\|\delta W_{420}\|$			$\|\delta W_{440}\|$		
	Al	Cu	Fe	Al	Cu	Fe	Al	Cu	Fe
Group I	0.014	0.087	0.081	0.007	0.035	0.030	0.003	0.017	0.011
Group II	0.015	0.108	0.095	0.016	0.089	0.074	0.013	0.072	0.050
Group III	0.001	0.022	0.020	0.005	0.021	0.018	0.003	0.016	0.013
Group IV	0.001	0.024	0.021	0.002	0.012	0.010	0.001	0.002	0.000

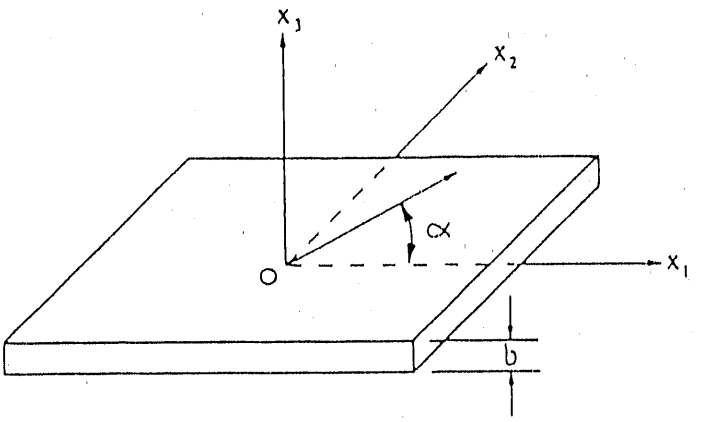

Fig. 1. Definition of coordinates

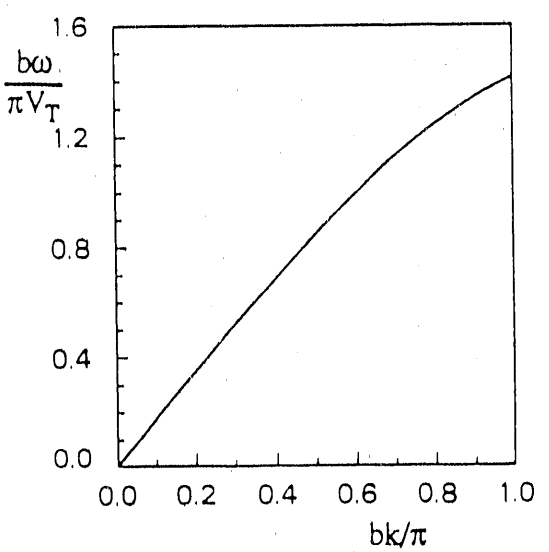

Fig. 2. Isotropic dispersion curve for the S_0 mode in aluminum

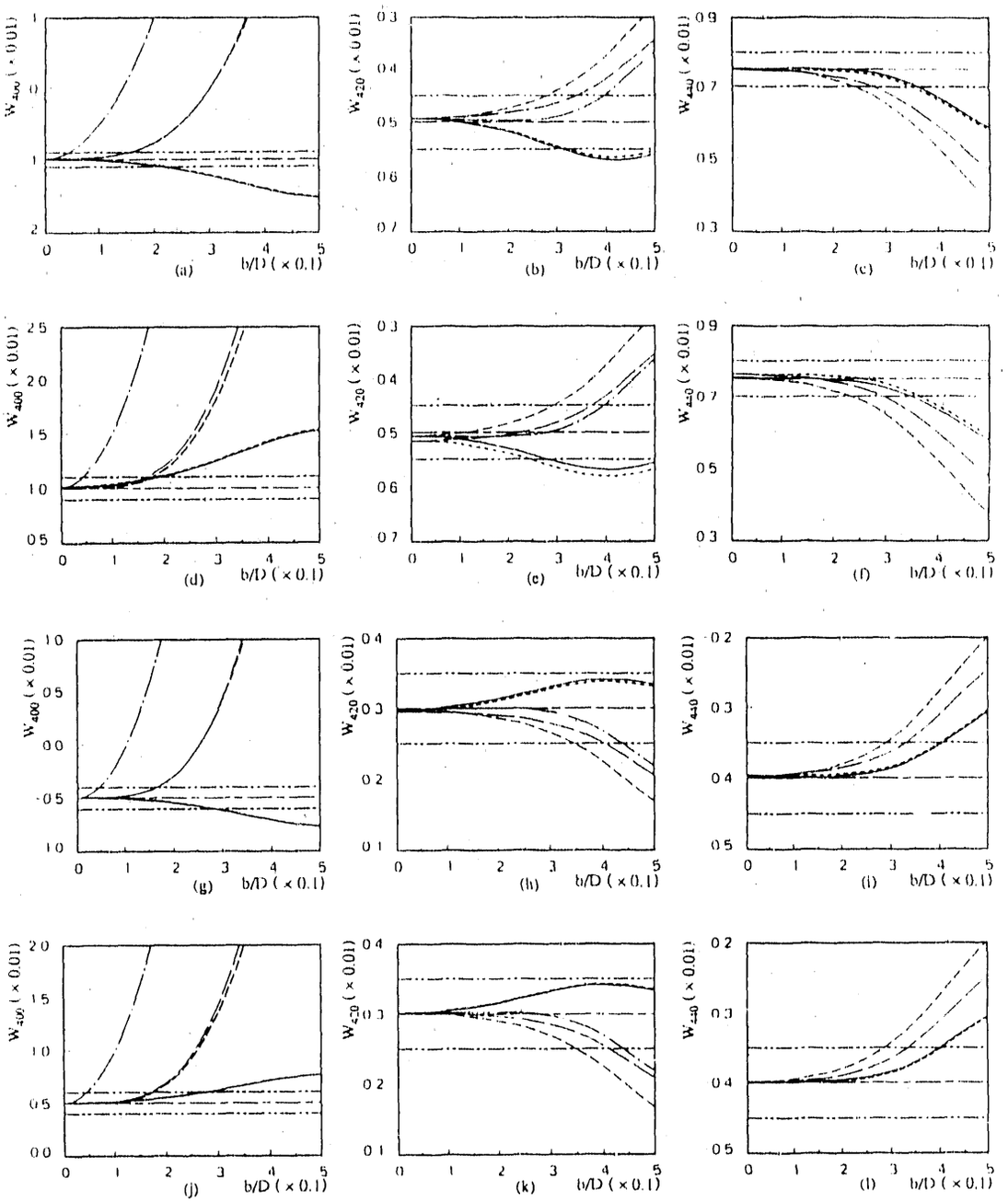

Fig. 3. Comparison of dispersion correction schemes in predicting ODCs for Al. (a)-(c): Group I; (d)-(f): Group II; (g)-(i): Group III; (j)-(l): Group IV. ———— Thompson's-A scheme, ---------- Thompson's-B scheme, - - - - - - - Hirao's-A scheme, — — — — — — — — Hirao's-B scheme, —·—·—·—·—·— no dispersion correction, ———————— exact value, ———————— target error bounds. The target errors are 0.001, 0.0005, and 0.0005 for W_{400}, W_{420}, and W_{440}

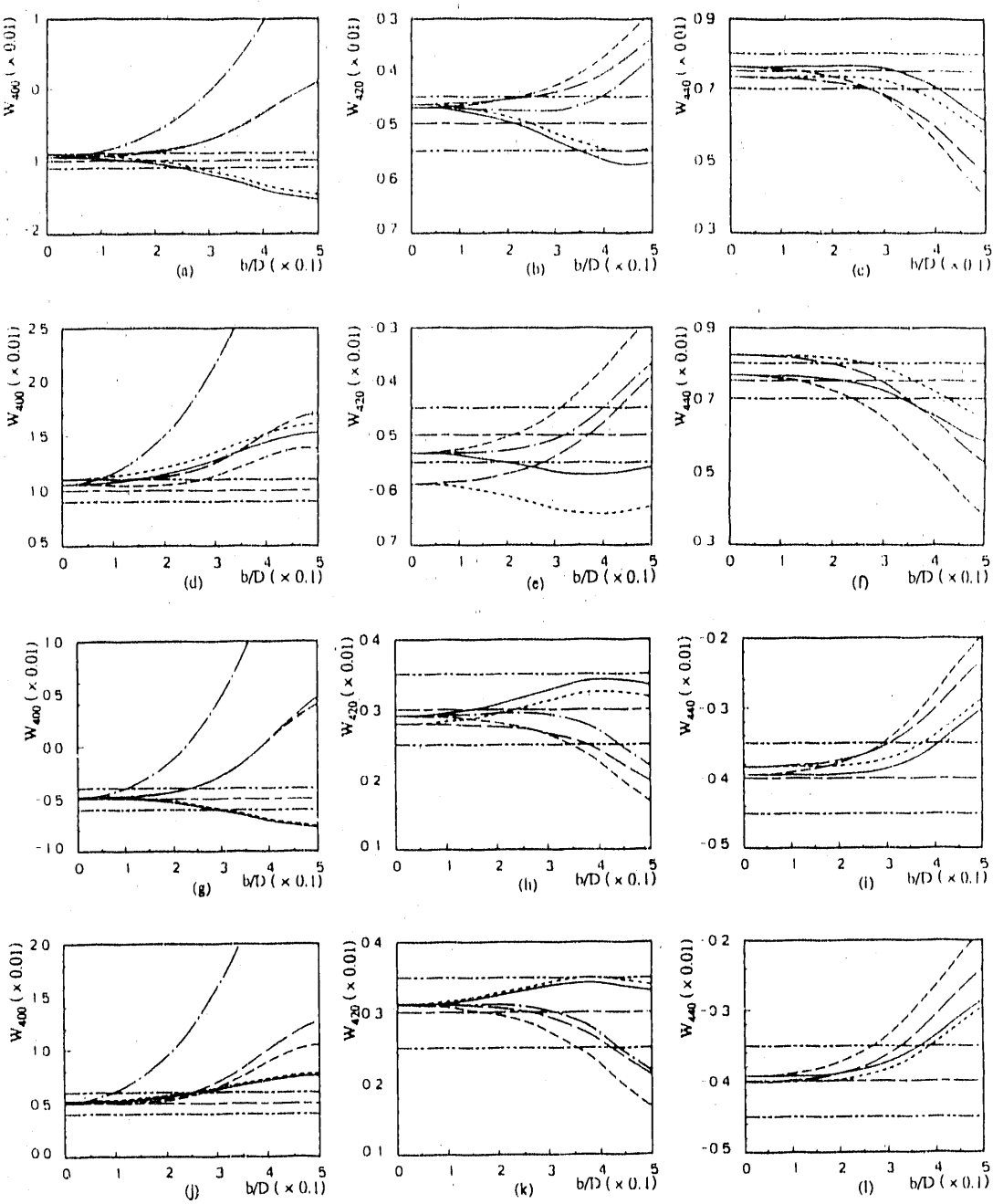

Fig. 4. Comparison of dispersion correction schemes in predicting ODCs for Cu. (a)-(c): Group I; (d)-(f): Group II; (g)-(i): Group III; (j)-(l): Group IV. ---------- Thompson's-A scheme, ---------- Thompson's-B scheme, - - - - - - - Hirao's-A scheme, — — — — — — — — Hirao's-B scheme, ——————— no dispersion correction, ——————— exact value, ——————— target error bounds. The target errors are 0.001, 0.0005, and 0.0005 for W_{400}, W_{420}, and W_{440}

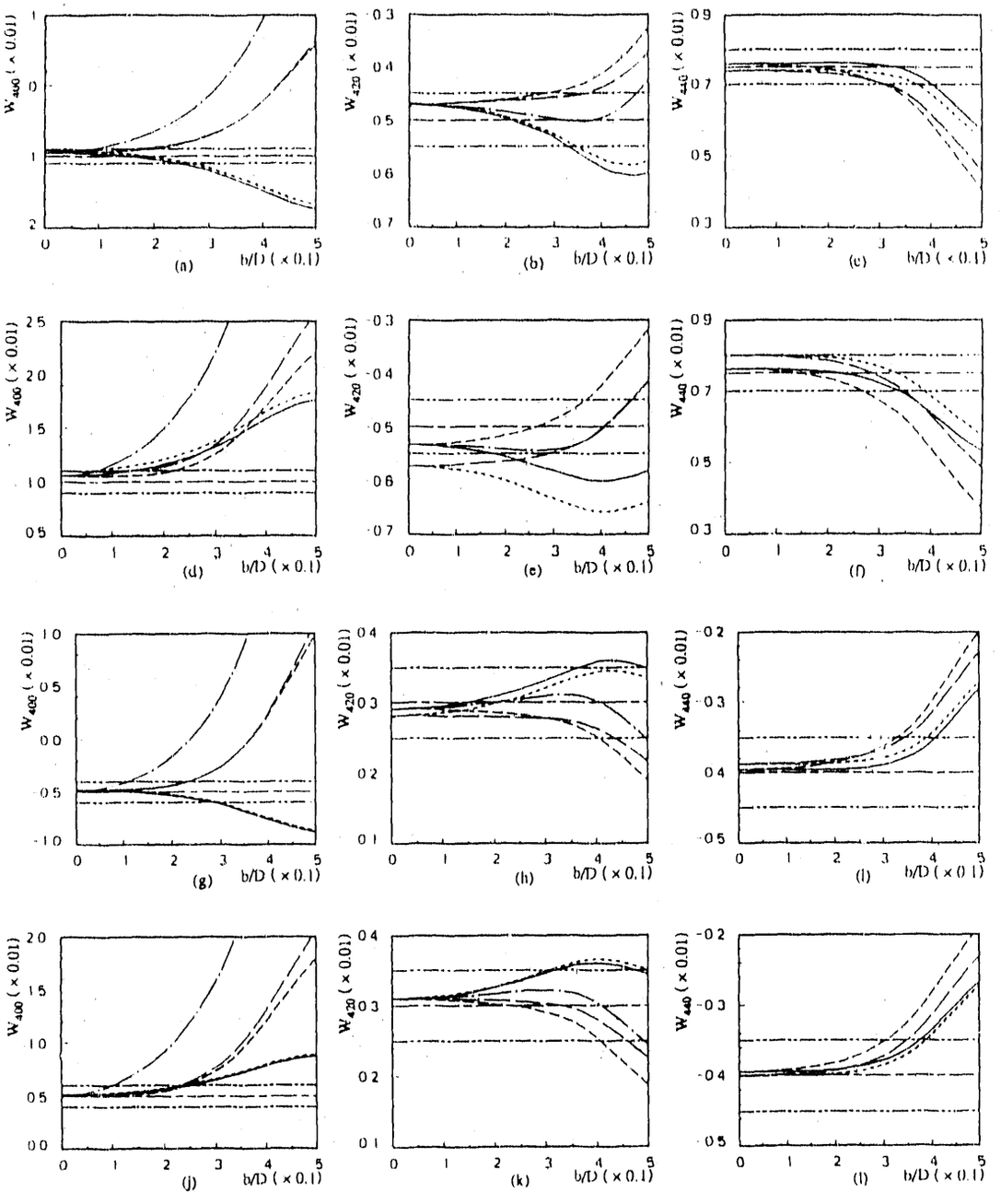

Fig. 5. Comparison of dispersion correction schemes in predicting ODCs for Fe. (a)-(c): Group I; (d)-(f): Group II; (g)-(i): Group III; (j)-(l): Group IV. ---------- Thompson's-A scheme, ---------- Thompson's-B scheme, - - - - - - - - Hirao's-A scheme, — — — — — — — — Hirao's-B scheme, ——·——·—— no dispersion correction, —————— exact value, —·—·—·—·— target error bounds. The target errors are 0.001, 0.0005, and 0.0005 for W_{400}, W_{420}, and W_{440}

PART V.

EFFECTS OF DISPERSION ON THE INFERENCE OF METAL TEXTURE FROM S_0 PLATE MODE MEASUREMENTS

PART II. INFLUENCE OF PULSE DISTORTION ON VELOCITY MEASUREMENTS

ABSTRACT

Metal texture (preferred grain orientation) can be studied by measurements of the anisotropy of the propagation speeds of guided elastic modes in rolled sheets or plates. In the most common experimental configuration, the phase velocity of the fundamental symmetric Lamb wave is inferred from measurements of the times of waveform zero-crossings as a function of propagation distance and angle. This paper analyzes the effects of dispersion on the accuracy of that technique. Using a general pulse distortion model to analyze the propagation of Gaussian shaped pulses, computer simulations of the effects of a variety of experimental parameters are studied. It is concluded that pulse distortion does not introduce an intolerable error in a typical experimental configuration.

INTRODUCTION

Measurements of the anisotropy of the velocities of ultrasonic guided modes are presently being utilized to study the texture (preferred grain orientation) in polycrystalline metal plates [1,2]. This information is of considerable interest to the manufacturing community, since it influences the ability of sheets or plates to be formed into complex shapes [3,4]. The guided mode which has been used most extensively is the S_0, or fundamental symmetric Lamb mode [5]. At long wave length limit, the velocity of this mode approaches a constant which can be interpreted in terms of texture parameters [1,2]. However, at any finite measurement frequency, some dispersion exists whose effects must be taken into account in the interpretation of experimental data. Assuming that the experimental technique precisely measures the phase velocity, part I of this paper evaluates two recently proposed techniques for extrapolating to the long wavelength asymptote of the velocity [6]. In this second part of the paper, the effects of dispersion on a commonly employed technique for estimating the phase velocity are discussed.

A technique that is commonly used in the measurement of phase velocities of elastic waves is the zero-crossing shift technique. A pulsed waveform is first excited by a transmitting transducer. One then measures the time delay (usually with a time interval counter) of a specific zero-crossing of the received waveform for a number of different separation distances between transmitting and receiving transducers. The phase velocity V_p is then computed as the slope of the distance-delay plot. For nondispersive waves, such an approach is quite rigorous. For dispersive waves, however, things are more complicated because of pulse distortion. First of all, because the group velocity V_g , with which the envelope propagates, and the phase velocity V_p , with which the zero-crossings

propagate, are unequal; the position of a selected zero-crossing may move out of the pulse envelope when the change of transducer separation is large. This limits the range of distances at which data can be obtained and hence the accuracy of the phase velocity measurement. Secondly, the pulse has many frequency components, and each frequency travels at a different phase velocity. The behavior of a particular zero crossing may not be characteristic of the phase velocity at a single frequency.

In the applications of the zero-crossing shift technique to the characterization of texture of metal plates, the texture induced anisotropy of plates is generally quite small, being on the order of a percent. To obtain good estimations of the texture parameters, the accuracy of the phase velocity measurement must be high. The commonly used transducers in texture characterization are electro-magnetic acoustic transducers (EMATs) [7] which launch and pick up narrowband toneburst. At a typical frequency of 500 KHz in plates of millimeter thickness, the dispersion of the S_0 mode is also on the order of a few percent [2]. Hence careful attention to its effects is required in order to isolate the texture effects.

To understand and assess the effects of pulse distortion on zero-crossing phase velocity measurements, we will first present a general pulse distortion model and use it to analyze the propagation of a Gaussian shaped pulse. Simulations of the behavior of wave forms similar to those employed in texture measurement will then be made using the model as a basis . Then, the accuracy of both absolute and relative velocity measurements using the zero-crossing technique will be analyzed and discussed based on computer simulations. Finally, a short summary concludes this paper.

THEORY AND MODEL

To investigate the pulse distortion phenomenon, a model introduced by Thompson and Elsley [8] and further analyzed by Li and Thompson [9] is applied here. For detailed study of this model, the reader is encouraged to refer to Ref. 9. Here, only the information relevant to this study is included.

Let us assume that only a single mode of propagation is present. Then a propagating wave may be described by the form

$$u(t,x) = \frac{1}{2\pi}\int_{-\infty}^{\infty} A(k)\, e^{j(\omega t - kx)}\, dk \qquad (1)$$

where A(k) is a function defining the spatial frequencies excited by the transducer, and the angular frequency ω is related to k by a dispersion relation.

The dispersion relation can be simplified by making a Taylor expansion at $k=k_0$:

$$\omega = \omega(k_0) + \omega'(k_0)(k-k_0) + \frac{1}{2}\omega''(k_0)(k-k_0)^2 + \ldots \qquad (2)$$

where (k_0, ω_0) is the point of operation (center wave number and frequency) and $\omega'(k_0) = V_g = \left.\frac{d\omega}{dk}\right|_{k=k_0}$ and $\omega''(k_0) = \left.\frac{d^2\omega}{dk^2}\right|_{k=k_0}$.

For an arbitrary A(k), numerical integration is usually required to evaluate u(t,x). When A(k) is a Gaussian function, however, integration can be carried out analytically, leading to useful physical insight.

Let

$$A(k) = B \exp\left\{-\frac{1}{2}(k-k_0)^2 B^2\right\} \qquad (3)$$

Substituting this expression into Eq. (1) and carrying out the integration, leads to the relation

$$u(t,x) = |U(t,x)| \exp\{j[\omega_0 t - k_0 x + \mathrm{Arg}(t,x)]\} \qquad (4a)$$

$$\text{with} \quad |U(t,x)| = \frac{\exp\left\{-\dfrac{(V_g(t-x)^2}{2B^2(1+\tau^2}\right\}}{\sqrt{2\pi}\,(1+\tau^2)^{1/4}} \tag{4b}$$

$$\text{and} \quad \text{Arg}\,(t,x) = \frac{1}{2}\tan^{-1}\tau - \frac{(V_g(t-x)^2\tau}{2B^2(1+\tau^2)} \tag{4c}$$

where $\tau = \omega''(k_0)\, t/B^2$.

There are many interesting features one can deduce from Eqs. (4). These features are discussed in details in Ref. 9. Briefly, when $\omega''(k_0)$ is not zero, the pulse spreads out as it propagates and the extra term Arg(t,x) in the exponent introduces an extra phase shift, which can be equivalently considered as a frequency modulation, such that linear relation between t and x no longer exists. The study of this pulse propagation model in Ref. 9 has shown that the model agrees well with experimental measurements such as those used in the characterization of texture.

Since the zero-crossing measurement technique relies on the linearity of the t--x relation, ignorance of dispersion effects may lead to erroneous estimation of phase velocity. In next section, we will investigate in-depth the effects the extra phase shifting (frequency modulation) has on the reliability of velocity measurement from the zero-crossing technique.

SIMULATION

The model presented in the above section is applicable to a general dispersion. Next, this model will be specialized to study quantitatively the influence of dispersion induced phase shifts on zero-crossing measurements of the velocity of the S_0 Lamb mode. We will use the experimental configuration at our laboratory [2] as a simulation basis. Since texture characterization is performed in the low frequency region, the dispersion of the S_0 mode is relatively weak [2].

To perform the computer simulation, the functions $\omega(k_0)$, $\omega'(k_0)$, and $\omega''(k_0)$ must be obtained first. One approach would involve numerically solving the Rayleigh-Lamb dispersion equation [5] and evaluating the derivatives numerically. The computations required could be very extensive. In an alternative approach, numerical studies in this section are based on a polynomial expression which closely approximates the corresponding isotropic dispersive equation. It is then possible to evaluate the derivatives analytically.

The approximate dispersion relation to be used here is

$$W = \sqrt{2}K\left[\sqrt{\frac{1}{1-\upsilon}}\,(1-4K^3+3K^4)+\frac{1}{2}K^3(1+K)+4K^3(1-K)\right] \qquad (5)$$

where $W=\frac{b}{\pi}\frac{\omega}{V_t}$, $K=\frac{b}{\pi}k$, υ is the Poisson's ratio of the plate material, b is the plate thickness, and V_t is the transverse plane wave velocity.

Equation (5) was developed by forcing a fifth degree polynomial satisfying the following boundary conditions:

$W=0$, $W' = dW/dK = \sqrt{2/(1-\upsilon)}$, $W''=W'''=0$ at $K=0$

$W=\sqrt{2}$, $W' = 1/\sqrt{2}$ at $K=1$,

These are conditions that all S_0 mode isotropic dispersion equations satisfy.

The performance of this approximation for isotropic aluminum is

illustrated in Figs. 1. It can be seen that in the range K=0~1, the approximation does a very good job for W and W', and is reasonable for W", especially in the range K=0~0.5 within which the error study in next section concentrates. Similar agreements were observed for isotropic copper and steel. With the approximate dispersion equation, $d\omega/dk$ and $d^2\omega/dk^2$ can be easily obtained, i.e., $V_g=d\omega/dk=V_t\, dW/dK$ and $\omega''= d^2\omega/dk^2 = (b/\pi)\, V_t\, d^2W/dK^2$.

Figures 2 and 3 show some experimental wave forms as well as simulated wave forms. The wave forms in Figs. 2 are obtained using two S_0 mode EMATs with a period of 5.1 mm excited at around 850 KHz on a 2.2 mm thick Al plate. The S_0 mode responses shown are for separations of approximately 150 mm and 250 mm between the transmitting and receiving EMATs and the plate is weakly anisotropic. The simulated wave forms are obtained from Eqs. (4) and Eq. (5). The parameters used are; thickness b=2.2 mm; Poisson's ratio υ=0.345; plane shear wave velocity V_t=3.15 mm/μs; wave length or EMAT period D=5.1 mm; and initial pulse width B=14.0 mm. Again, propagation distances of 150 mm and 250 mm are considered. These waves are not from current texture experiment; they have been selected to show the characteristics of dispersive waves. As will be shown later, the S_0 wave under investigation is less dispersive and the pulse distortion is less severe.

Comparison of Figs. 2 and 3 illustrates a number of common features. In each case, the high frequency components have moved to the trailing edge of the pulse ($\omega''<0$) and the pulse width increases substantially as the pulse propagates from 150 mm to 250 mm. Here the model reproduces the dominant features of the experiment. Further, the shapes of simulated wave forms are in good agreement with those of experimentally obtained wave forms, even though the experimental wave forms are not Gaussian shaped. Note that the delay times for the experimental wave forms are longer than those of simulated wave forms, although the relative difference in time delay for Figs. 2 and 3 are identical. This is because the oscilloscope's trigger time

is not the time at which the center of pulses enter the plate. A close examination of Figs. 2 and 3 reveals that the envelope peak locations for x=250 mm are slightly different. This discrepancy is originated from two sources. First, the Al plate possesses texture; it is weakly anisotropic. This weak anisotropy alters the dispersion characteristics of the plate leading to a slight deviation in group velocity from the isotropic model that our simulation is based on. Secondly, the EMAT separation distances for the experimental wave forms are not precise; a measurement error of ±2 mm is possible since they were not exactly measured. It has been found that the second error source contributes more than the first one in this specific case. One may also note that the relative magnitudes for simulated and experimental wave forms are different, which is due to the frequency dependent attenuation effects not included in the pulse propagation model. More detailed and quantitative comparisons of experimental and simulated waveforms can be found in Ref. 9.

Using Eqs. (4) and (5), computer simulations were made to determine the detailed effects of dispersion on phase shift and velocity measurements. Let us define the relative dispersion induced error as $(V_m-V_p)/V_p$, where V_m is the velocity as measured by the zero-crossing technique and V_p is the true phase velocity. In addition to the plate thickness, this error is determined by the following variables: x, the transducer separation distances; D, the EMAT period; υ, the Poisson's ratio; and B, the pulse width at the beginning of propagation.

Figures 4~7 are simulations of the relative error when one tracks the zero- crossing initially having zero excess phase ($\phi=\omega_0 t-kx+Arg(t,x)=0$ in Eq. (4a)) at x=0. This cycle is initially at the center of the packet but moves towards the leading edge as the pulse propagates since V_g is less than V_p for the S_0 mode. In (a) of Figs. 4~7, relative errors are plotted vs. thickness b of the plate. In (b) of Figs. 4~7, relative amplitudes $(A_g-A_m)/A_g$ of the envelope magnitude at the time of the measured zero-crossing are plotted. Thus A_m is

the magnitude (usually in volts) of the signal envelope at the measured zero-crossing time, and A_g is the magnitude of the maximum signal (peak voltage) or envelope magnitude at the time of $t=x/V_g$. Keep in mind that the relative amplitude plots give an indication regarding whether the zero-crossing is in the pulse envelope.

In practice, the selected zero-crossing is the one which stays near the envelope peak over the propagation distances utilized. This may not be the cycle with zero excess phase at the beginning of propagation. This difference will be discussed more fully in the next section. In experiments, when $(A_g-A_m)/A_g$ exceeds 0.3, the measured time delay is usually not reliable because of poor signal to noise ratio..

Table I shows the fixed and varied parameters which are used in Figs. 4~7. The fixed values selected here for simulation are based on the set-up at our laboratory. Figure 8 is a typical experimentally obtained wave form of the S_0 mode for a separation of 250 mm between transmitting and receiving EMATs. Figure 9 is the simulated wave form using the fixed parameters as those of Figs. 4 and a separation of 250 mm. It is clear that the shapes of Figs. 8 and 9 are remarkably similar, indicating that the performance of the simulations is reliable.

From Figs. 4, one sees that the error is generally less than $1x10^{-3}$ for $b <$ 2 mm. For thicker plates, the dispersion effects become stronger and the errors increase rapidly after a flat region. As the separation of transducers becomes larger, the flat region of small error becomes shorter. Notice that, however, when the error begins to increase rapidly, the corresponding zero-crossing also begins to move out of the pulse envelope. From Figs. 5, one sees how pulse width influences the relative error. The narrower the pulse width, the smaller the plate thickness must be to avoid introduction of large error in the measurement process. Figures 6 display the effects of Poisson's ratio on the measurement error. It is seen that Poisson's ratio has a very limited influence on the error curves, even though the range of Poisson's

ratio in the figures covers a wide range of engineering materials. Figures 7 show the effects of another parameter D, the EMAT's period on the measurement error. It is demonstrated that the period of EMATs (hence the central wave number k_0) has a very important role in the pulse distortion. This of course can be interpreted from the S_0 dispersion curve. For small k_0b or b/D, the dispersion is not severe. As k_0b increases (due to decrease in D), the dispersion becomes strong, thus introducing more error.

ERROR ESTIMATION FOR ABSOLUTE AND RELATIVE VELOCITY MEASUREMENTS

There are basically two velocity measurement procedures which are used in texture characterization: absolute and relative velocity measurements [2]. In the absolute velocity measurement, the separation distance between the transmitting and receiving transducers is varied, typically over a distance of 10 cm. The time arrival of a selected zero-crossing is recorded, usually through a counter, as a function of separation distance. The absolute velocity is then computed, through linear regression, as the slope of the distance-time relation. In the relative velocity measurement, the transmitter and receiver are held apart by a rigid frame; the change in time of a specific zero-crossing is recorded as a function of propagation direction. The relative velocity or $\Delta V/\bar{V}$ is then determined from $\Delta t/\bar{t}$, with $\bar{t}$ being the average arrival time of the zero-crossing and $\bar{V}$ the average wave speed. For plates of cubic polycrystallites, W_{400}, W_{420} and W_{440} are dimensionless texture parameters which can be determined ultrasonically [1, 2]. These three parameters are called orientation distribution coefficients (ODCs) whose definition and physical meanings can be found in Refs. 10~12. Generally speaking, W_{420} and W_{440} are most accurately determined through relative measurement of the S_0 wave velocities while W_{400} requires absolute velocity measurement [2]. The values of these ODCs are typically in the order of 10^{-3}. To obtain estimates of ODCs within tolerance and to be consistent with the experiment accuracy, we choose target error bounds for the absolute and relative velocity measurements (to be defined shortly) to be 2×10^{-3} and 1×10^{-3} for plates of thickness less than 4 mm. A detailed error propagation study can be found in [2]. Briefly, the 2×10^{-3} absolute velocity measurement error contributes about 1×10^{-3}, 0.3×10^{-3}, and 0.3×10^{-3} errors in W_{400} for Al, Cu, and Fe textured plates. The 1×10^{-3} error in relative velocity measurement leads to

errors of $4x10^{-4}$, $1x10^{-4}$, and $1x10^{-4}$ in W_{420} and $6x10^{-4}$, $1.5x10^{-4}$, and $1.5x10^{-4}$ in W_{440} for Al, Cu, and Fe materials respectively. These errors are compatible to or less than the overall accuracy of the ultrasonic technique as inferred from comparisons to neutron or X-ray diffraction measurements.

To ascertain how much error is introduced if the velocity is determined by the slope of the time-distance plot for zero-crossings, we plotted the absolute velocity measurement error $(V_r-V_p)/V_p$ vs. thickness in Fig. 10(a), where V_r is the velocity obtained through linear regression of time delay and transducer separation distance. Each velocity is computed from simulated wave forms at eleven separations (200~300 mm in steps of 10 mm). In Fig. 10(b), the average relative amplitude, which is defined as the mean of relative amplitudes at the eleven separations, are also included. The parameters used here are D=10.0 mm, υ=0.345, and B=20.0 mm. There are ten curves in Figs. 10, corresponding to tracking the times of ten zero-crossings. The ten zero-crossings have phase $\phi=2n\pi$ (n=0~9) at x=0 and t=0. As mentioned before, the zero-crossing selected for time measurement, which is usually the one that stays nearest to the envelope peak over the selected range of propagation distances, does not necessarily have zero initial phase (ϕ=0). If one uses the average relative amplitude as a discriminant, one can see that for plates of thickness less than 1.5 mm, the zero-crossing with zero initial phase (n=0) is most likely to be selected for the time measurement; for plates of thickness b=1.5~2.0 mm, the zero-crossing with phase $\phi=2\pi$ (n=1) is most likely to be selected, etc.

To illustrate how much error is produced when the zero-crossing is selected in accordance with the above criteria, we plotted only the parts of Figs. 10 that would have been selected in Figs. 11 with different vertical scales. Figure 11(a) shows only the error curve for the zero-crossings with minimum average relative amplitudes which is plotted in Fig. 11(b). It can be readily seen from Fig. 11(a) that the velocity error is generally bounded within $\pm 2.0x10^{-3}$, the acceptable error for the absolute velocity measurement.

Note the error fluctuates when thickness goes over 2 mm, which indicates that the exact error may be difficult to predict for thicker plates. These fluctuations occur when the optimum value of n changes.

Now consider the error from the relative velocity measurement. Due to the presence of texture, which introduces weak anisotropy in plates, the dispersion characteristics of the S_0 waves propagating at different directions with respect to the rolling direction are slightly different. Here the change in dispersion characteristics is modeled by the change of Poisson's ratio in Eq. (5) for the purpose of simplicity. This modeling is justifiable from the results in Part I of this paper [6]. Figure 12(a) shows the relative velocity measurement error plotted against plate thickness, where the relative velocity measurement error is defined as $(t_{m1}-t_{m0})/t_m-(t_{p1}-t_{p0})/t_p$, which is zero for the zero thickness plate. The parameters used in the simulation are D=10 mm, B=20 mm, x=300 mm, υ_0=0.345, and υ_1=0.300. The two Poisson's ratios are chosen to represent fairly strong texture (corresponding to $\Delta V_p/V_p$ of 0.03 at long wave length limit). Here t_{m1}, t_{m0}, t_m, t_{p1}, t_{p0}, and t_p are, respectively, the measured time for υ_1, the measured time for υ_0, the average of t_{m1} and t_{m0}, the time from the true phase velocity for υ_1, the time from the true phase velocity for υ_0, and the average of t_{p1} and t_{p0}. Figure 12(b) gives the associated average relative amplitude, being the mean of the relative amplitudes for the two different Poisson's ratios. The ten curves in Figs. 12, as those in Figs. 10, represent the errors for the ten zero-crossings having initial phase $\phi=2n\pi$ (n=0~9) at x=0 and t=0.

Again, similar to the error analysis for the absolute velocity measurement in Figs. 11, the parts of Figs. 12 that correspond to minimum average relative amplitude are plotted in Figs. 13. Figure 13(a) clearly shows that the errors for the relative velocity measurement are very small and well within the $\pm 1 \times 10^{-3}$ bound.

CONCLUSION

A model for pulse propagation in a dispersive media has been utilized to study the effects of pulse distortion and phase shift on the phase velocity as determined by the zero-crossing measurement technique. Assumptions employed in the velocity computations include a Gaussian spatial envelope and an analytic approximation to the S_0 mode dispersion curve with a Taylor series expansion about the operating point. Simulations have been made on the pulse distortion and phase shift effects as they would occur in a typical system for monitoring metal texture and the consequent errors in velocity measurements have been assessed. It is found that the influence of dispersion on the zero-crossing measurement technique does not induce severe discrepancy in either absolute or relative measurements of the velocity of the S_0 mode for the selected configuration when the plate thickness is less than 4 mm; thus, tracking zero-crossings is judged to be an appropriate experimental technique. However, for a different experimental configuration such as when EMAT's with a shorter period are used, this conclusion may not be valid.

ACKNOWLEDGEMENT

Ames Laboratory is operated for the U. S. Department of Energy by the Iowa State University under contract No. W-7405-Eng-82. This work was supported by the Director for Energy Research, Office of Basic Energy Sciences.

REFERENCES

1. R. B. Thompson, S. S. Lee, and J. F. Smith. "Relative Anisotropies of Plane Waves and Guided Modes in Thin Orthorhombic Plates: Implication for Texture Characterization." Ultrasonics 25 (1987): 133-37.

2. R. B. Thompson, J. F. Smith, S. S. Lee, and G. C. Johnson. "A Comparison of Ultrasonic and X-ray determinations of Texture in Thin Cu and Al plates." Met. Trans. 20A (1989): 2431-47.

3. A. V. Clark, Jr., R. C. Reno, R. B. Thompson, J. F. Smith, G. V. Blessing, R. J. Fields, P. P. Delsanto, and R. B. Mignogna. "Texture Monitoring in Aluminum Alloys: A Comparison of Ultrasonic and Neutron Diffraction Measurement." Ultrasonics 26 (1988): 189-97.

4 A. V. Clark, Jr., et al. "Ultrasonic Measurement of Sheet Steel Texture and Formability: Comparison With Neutron Diffraction and Mechanical Measurements." To be published in Research in Nondestructive Evaluation.

5. T. R. Meeker and A. H. Meitzler. "Guided Wave Propagation in Elongated Cylinders and Plates." In Physical Acoustics. Ed. W. P. Mason. New York: Academic, 1965. 112-119.

6 Y. Li and R. B. Thompson. "Effects of Dispersion on the Inference of Metal Texture from S_0 Plate Mode Measurements: Part I. Evaluation of Dispersion Correction Schemes." Submitted to Journal of Acoustical Society of America.

7. R. B. Thompson. "Physical Principles of Measurement with EMAT Transducers." In Physical Acoustics. Vol. XIX. Ed. W. P. Mason. New York: Academic Press, 1990. 157-200.

8. R. B. Thompson and R. K. Elsley. "A Prototype EMAT System for Inspection of Steam Generator Tubing." Electric Power Research Institute, Palo Alto, California, Rept. S101-1, EPRI NP-2836, 1983.

9. Y. Li and R. B. Thompson. "Pulse Propagation Analysis of Dispersive Waves." To be submitted to J. Acoust. Soc. Am.

10. R.-J. Roe. "Description of Crystallite Orientation in Polycrystalline Materials. III. General Solution to Pole Figure Inversion." J. Appl. Phys. 36 (1965): 2024-31.

11. R.-J. Roe. "Inversion of Pole Figures for Materials Having Cubic Crystal Symmetry." J. Appl. Phys. 37 (1966): 2069-72.

12. G. J. Davies, D. J. Goodwill, and J. S. Kallend. "Elastic and Plastic Anisotropy in Sheets of Cubic Metals." Met. Trans. 3 (1972): 1627-31.

Table 1. Fixed and variable parameters in Figs. 4-7.

Fig.	s(mm)	B(mm)	υ	D(mm)
4	vary	20.0	0.345	10.0
5	150.0	vary	0.345	10.0
6	150.0	20.0	vary	10.0
7	150.0	20.0	0.345	vary

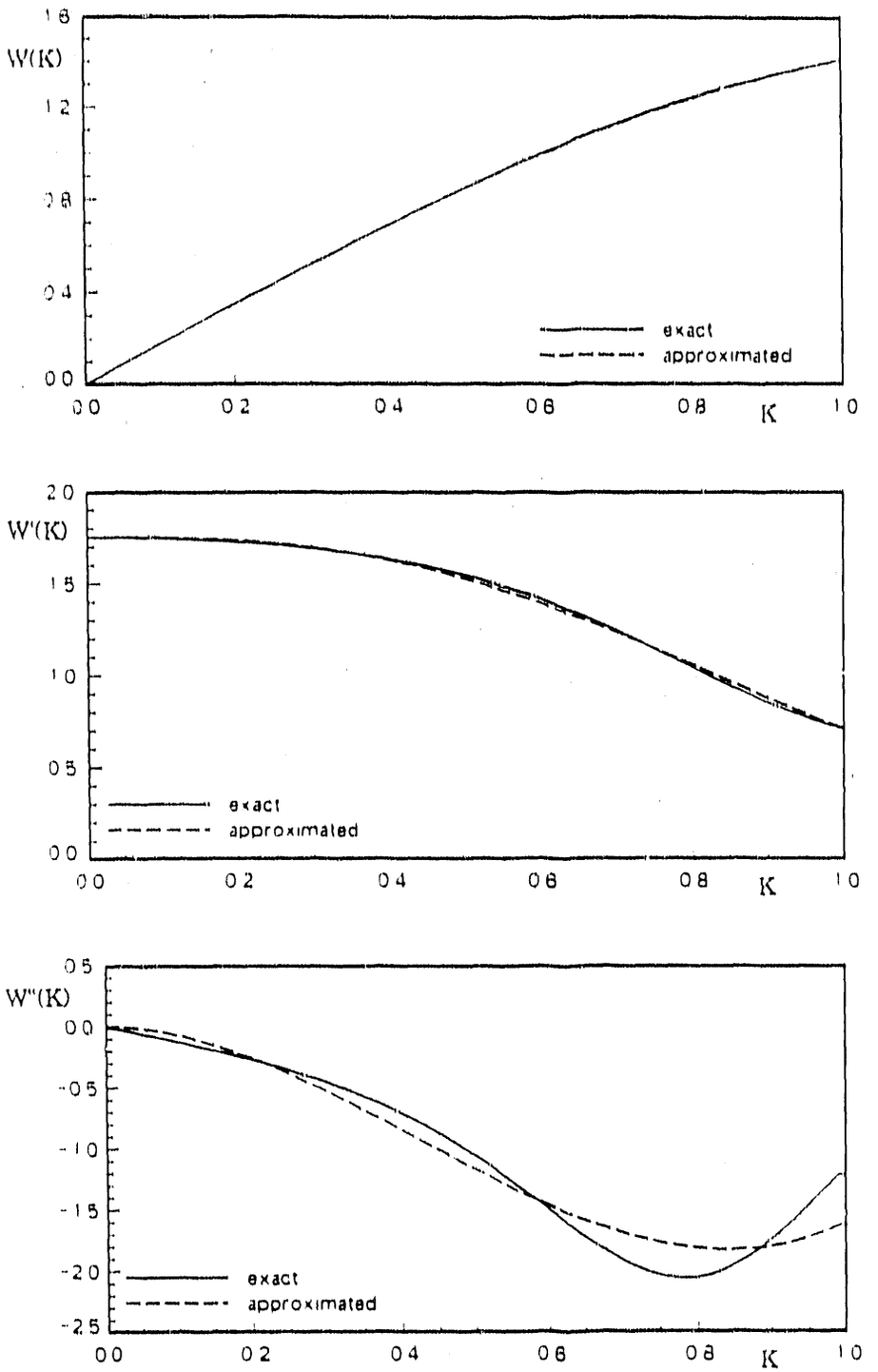

Fig. 1. Approximation of dispersion curves (a) W(K), (b) W'(K), (c) W''(K), (—— exact, ----- approximated)

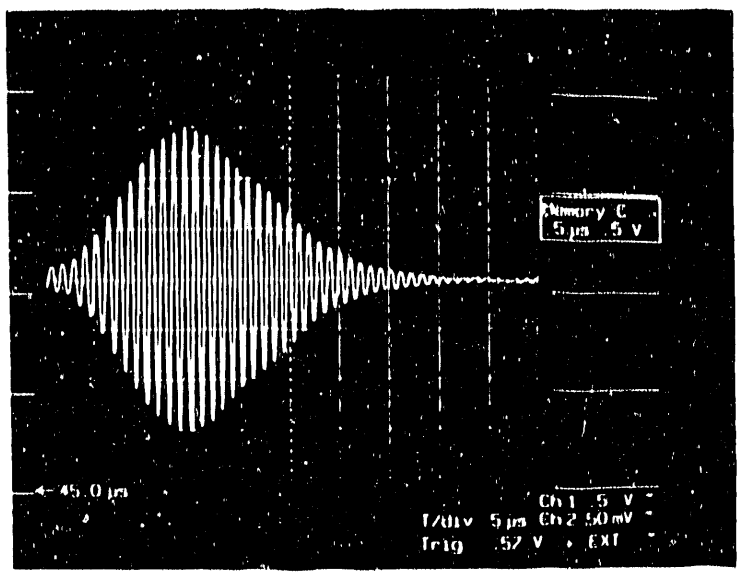

(a)

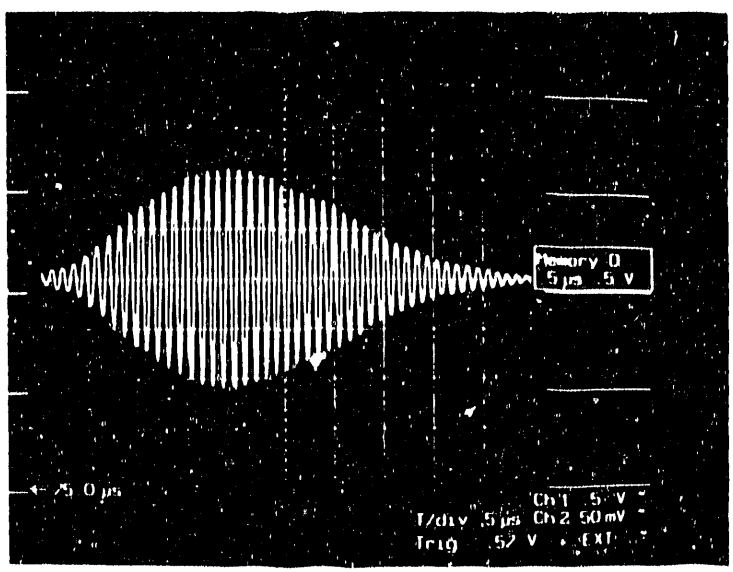

(b)

Fig. 2. Experimental waveforms (a) x=150 mm, (b) x=250 mm

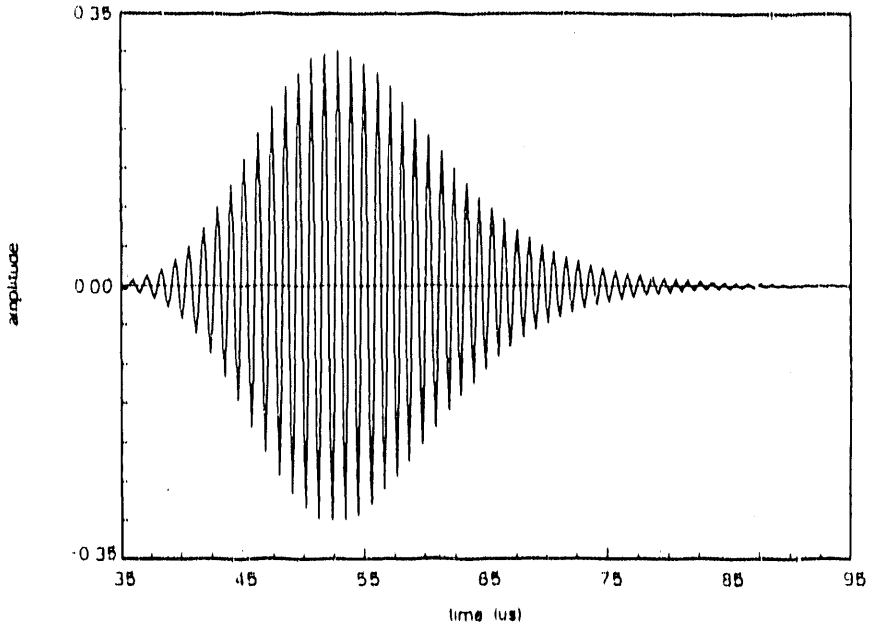

(a)

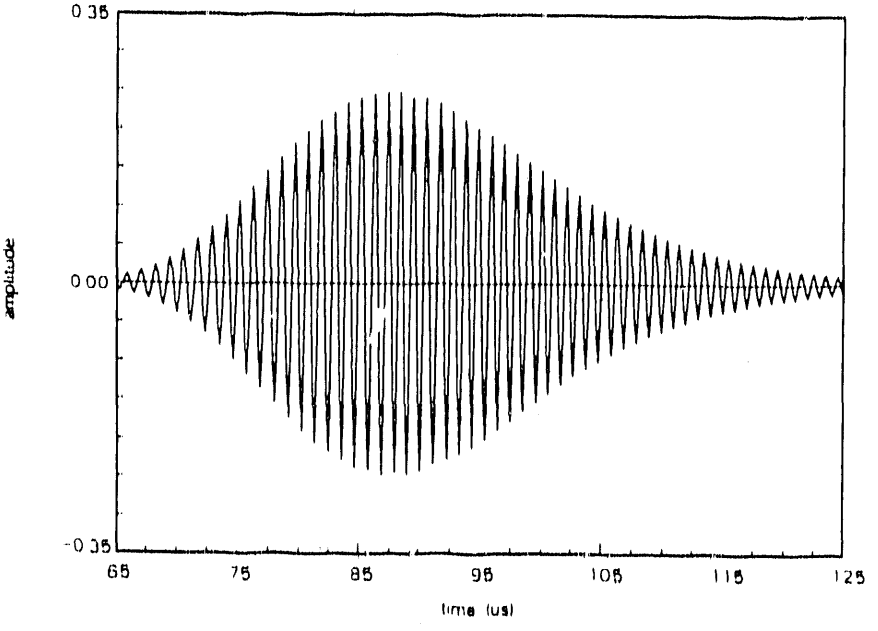

(b)

Fig. 3. Simulated waveforms (a) x=150 mm, (b) x=250 mm

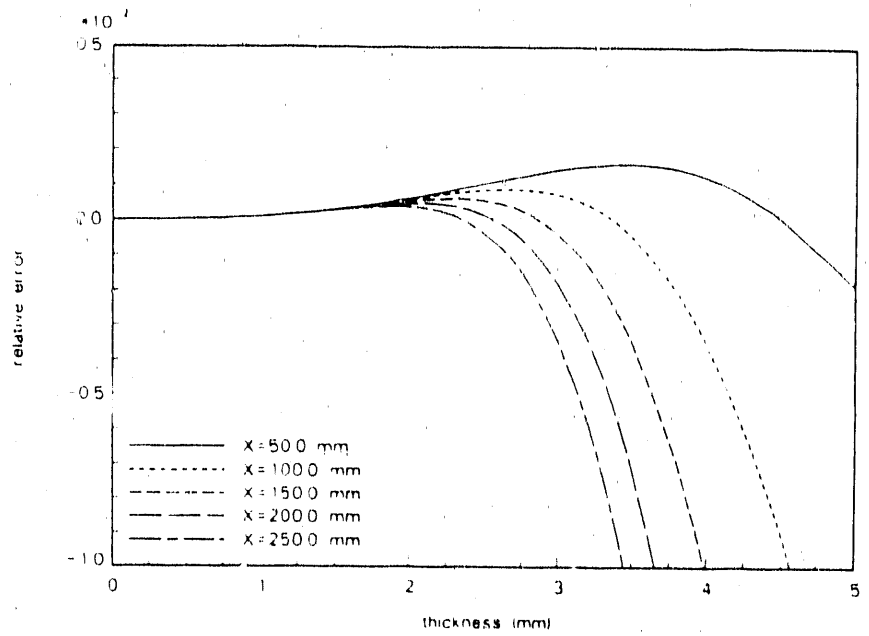

(a)

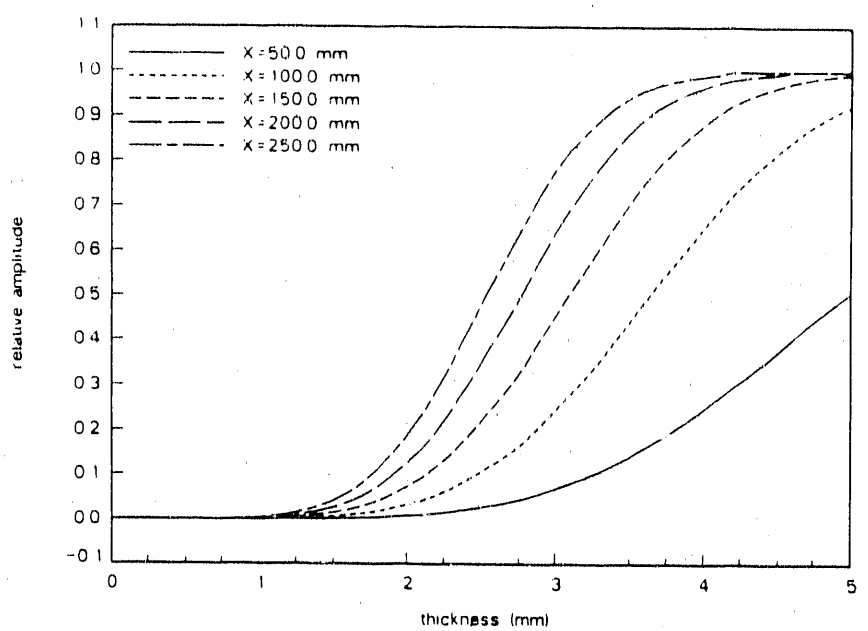

(b)

Fig. 4. Effects of transducer separation distance (a) relative error vs. thickness, (b) relative amplitude vs. thickness

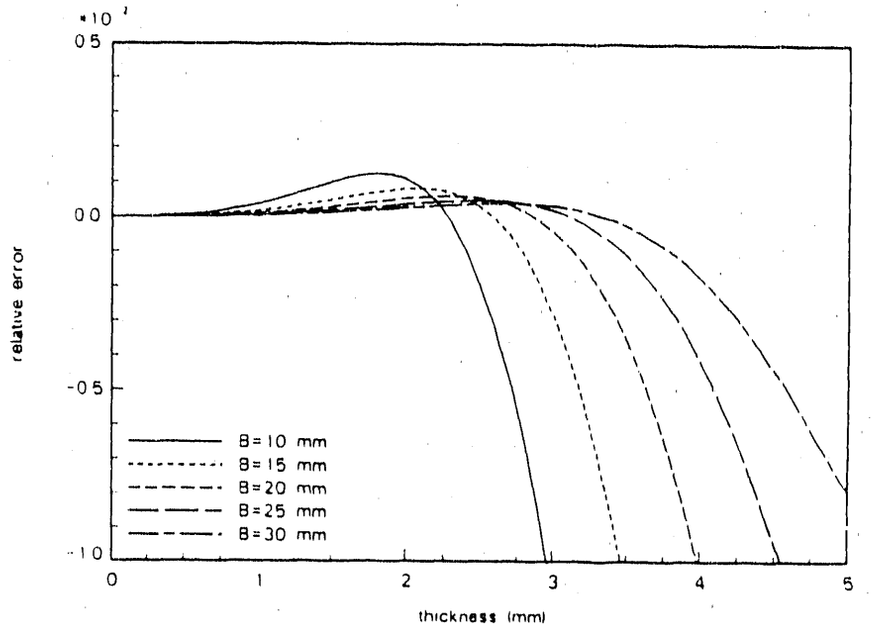

(a)

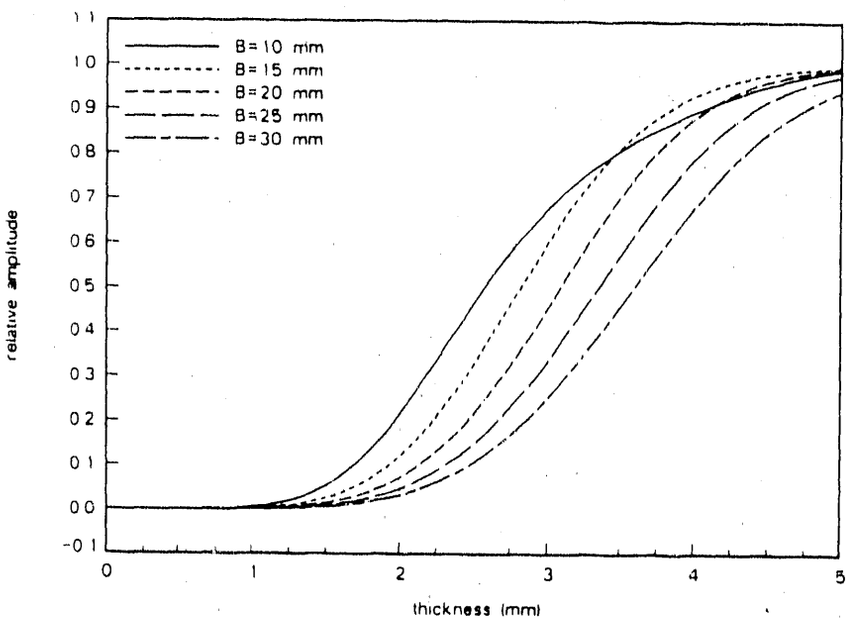

(b)

Fig. 5. Effects of pulse width of wave (a) relative error vs. thickness, (b) relative amplitude vs. thickness

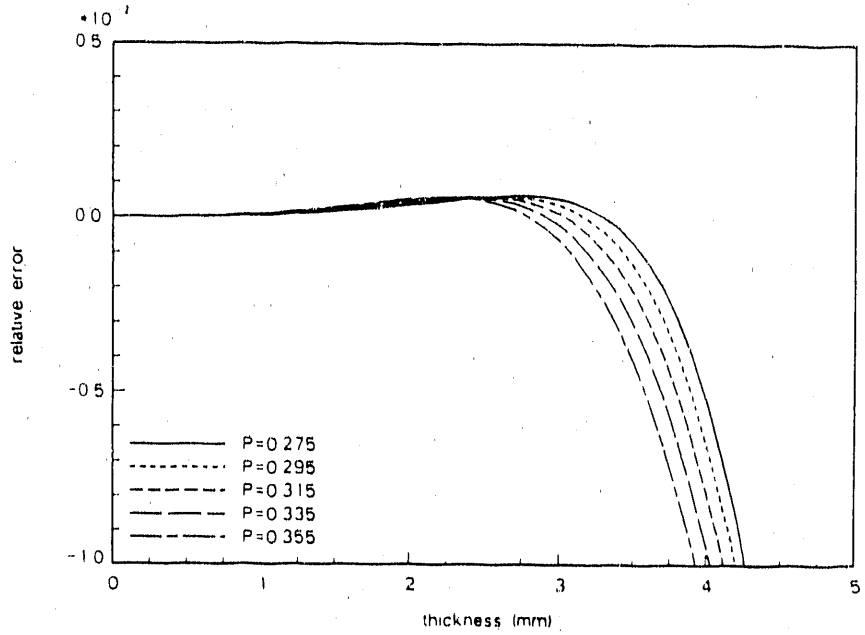

(a)

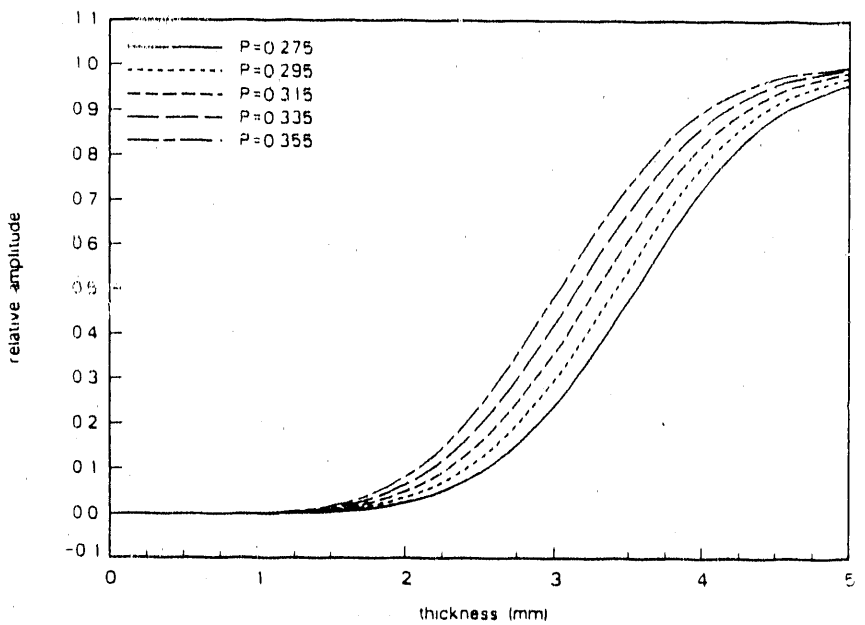

(b)

Fig. 6. Effects of Poisson's ratio of material (a) relative error vs. thickness, (b) relative amplitude vs. thickness

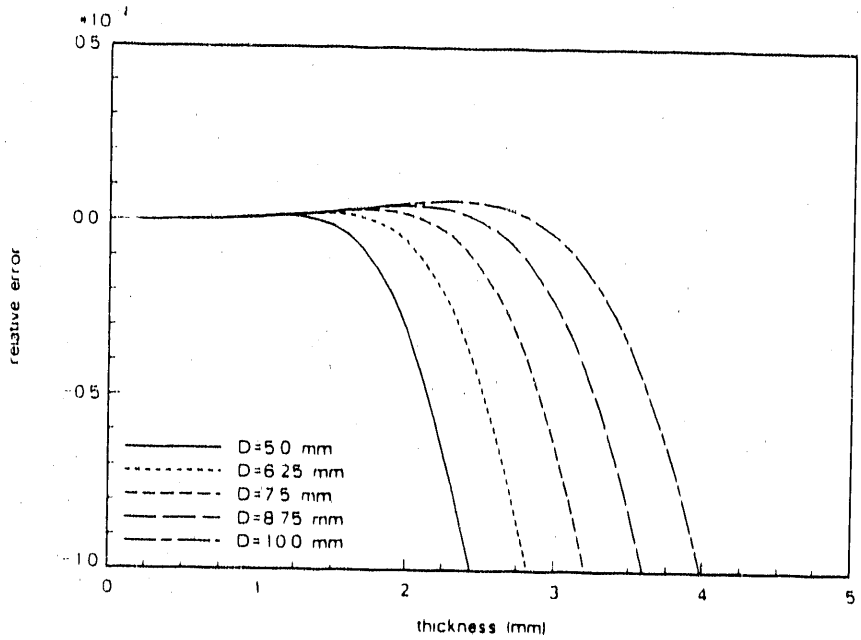

(a)

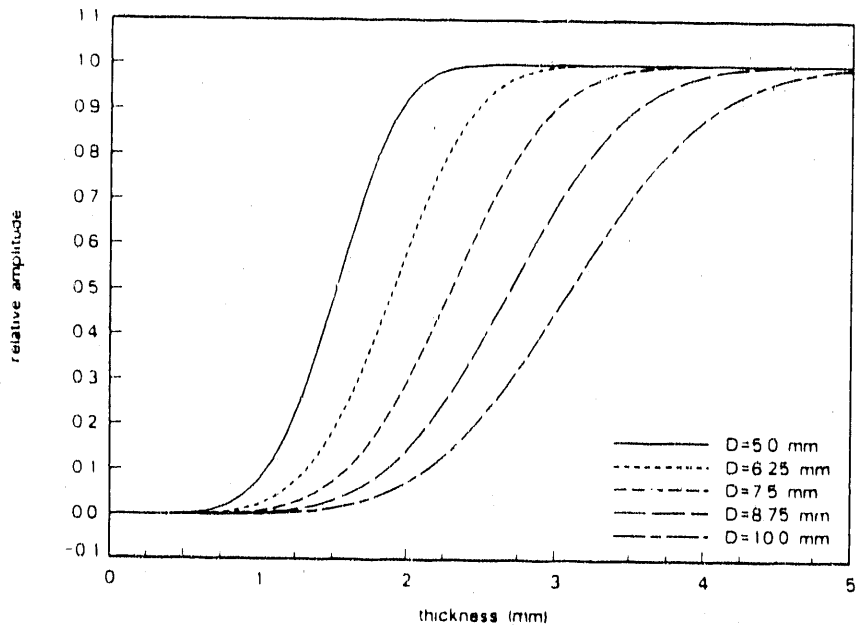

(b)

Fig. 7. Effects of transducer period, (a) relative error vs. thickness, (b) relative amplitude vs. thickness

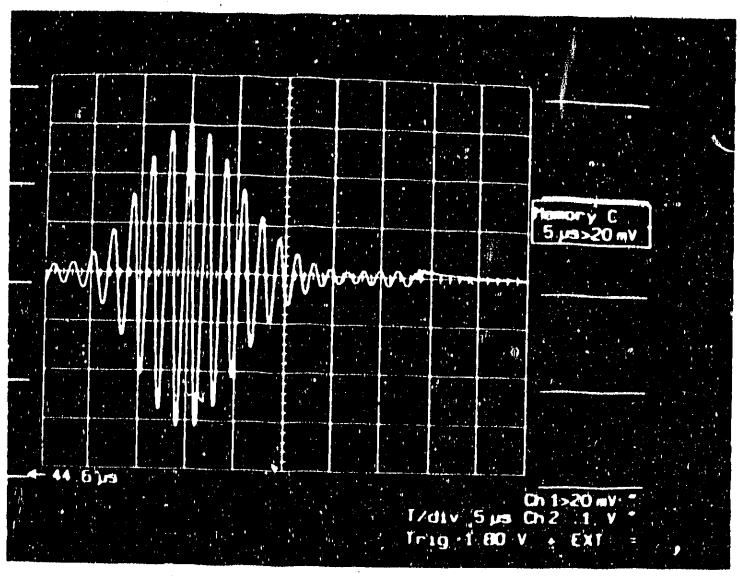

Fig. 8. A typical experimental wave form of S_0 mode in a typical texture measurement configuration. (EMATs are held 250 mm apart)

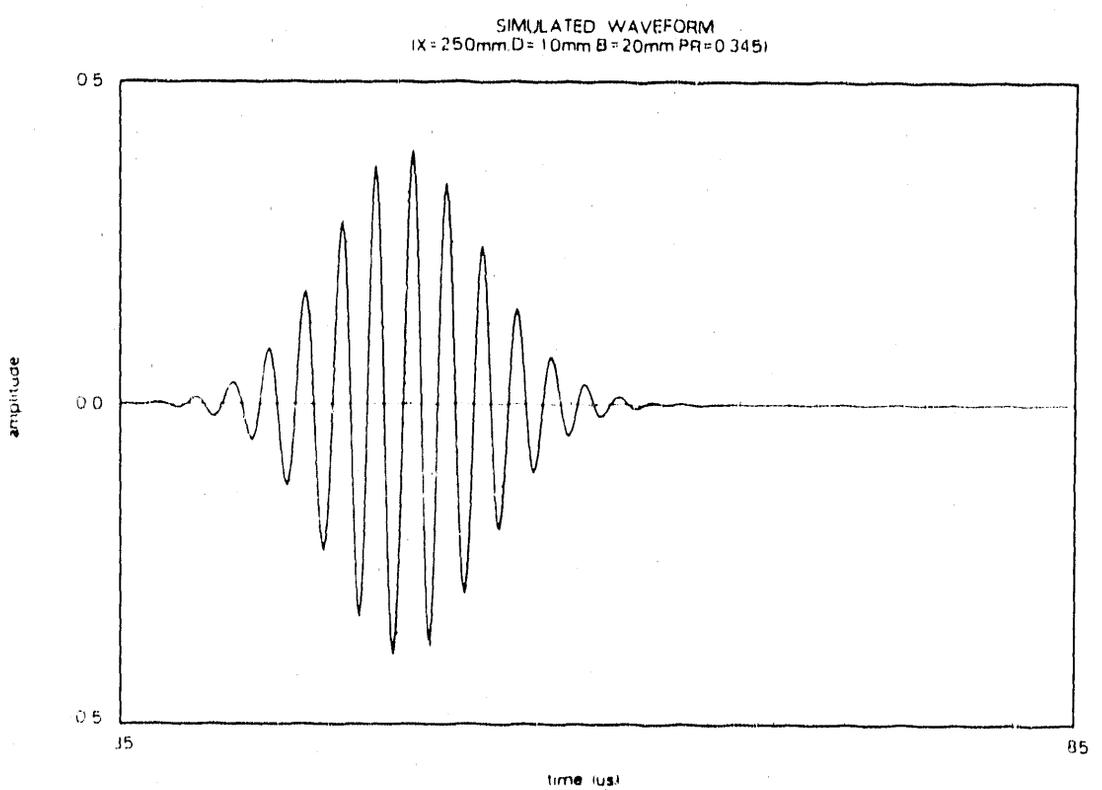

Fig. 9. Simulated wave form with following fixed parameters: x=250mm, B=20mm, υ=0.345, D=10.0mm, and b=2.2mm.

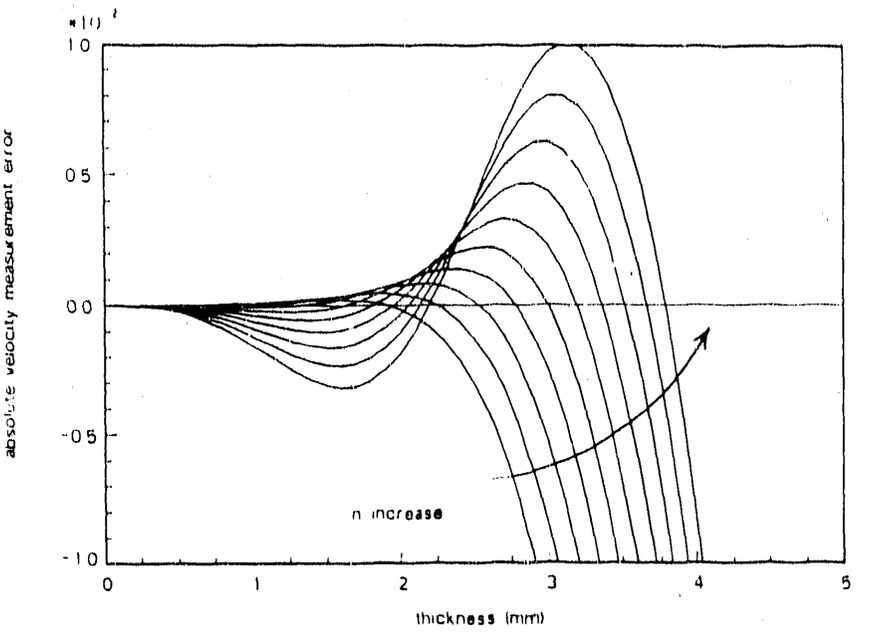

(a)

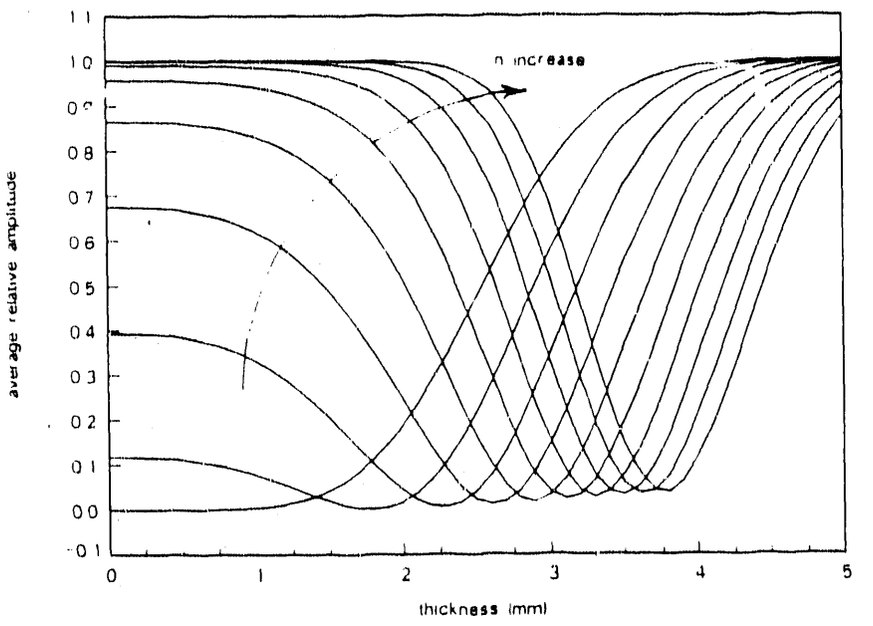

(b)

Fig. 10. Absolute velocity measurement error (a) error vs. thickness, (b) relative amplitude vs. thickness

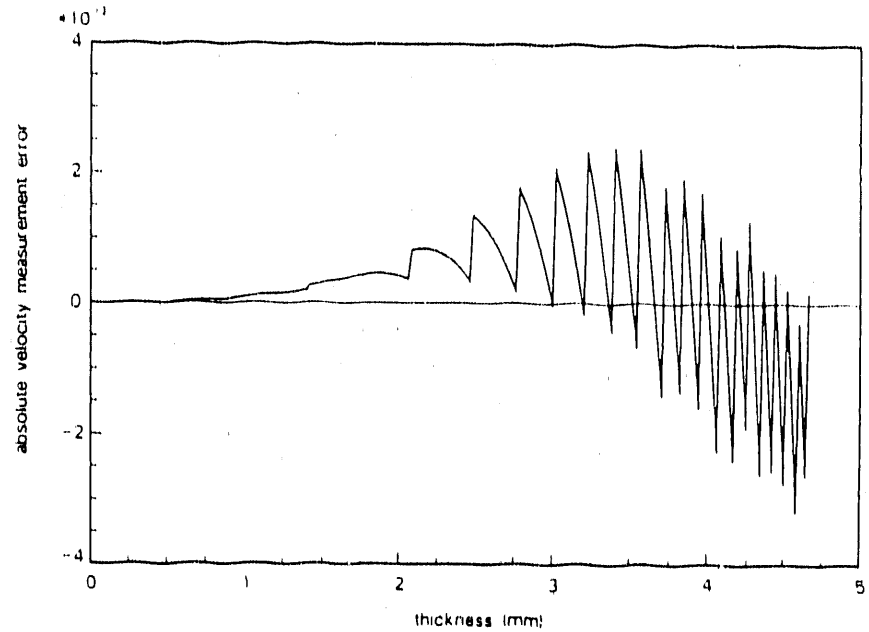

(a)

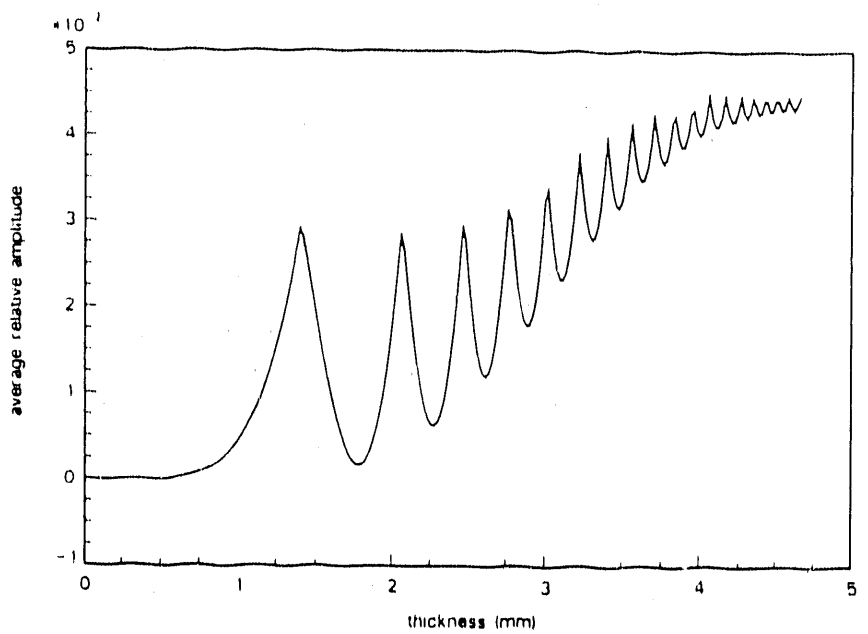

(b)

Fig. 11. The parts of Fig. 10 which bear practical significance

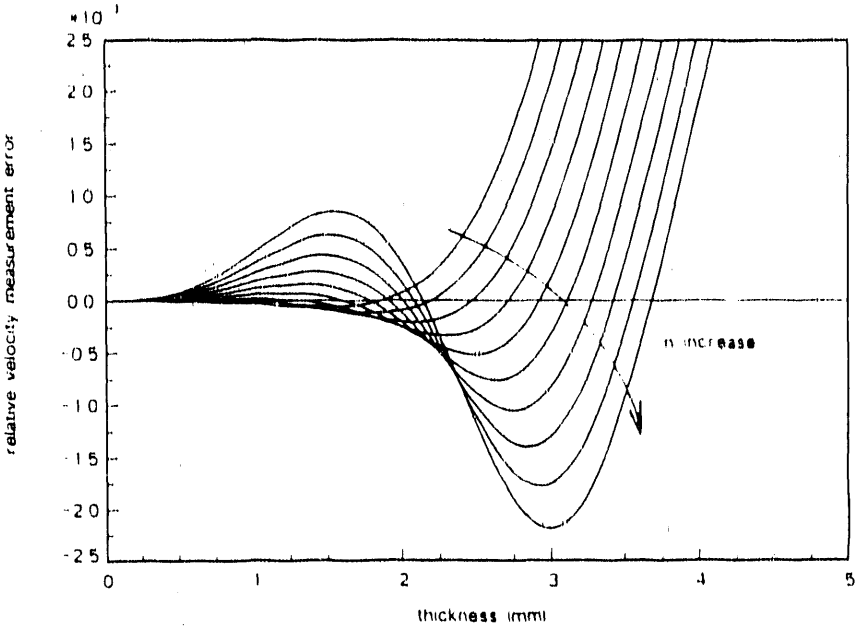

(a)

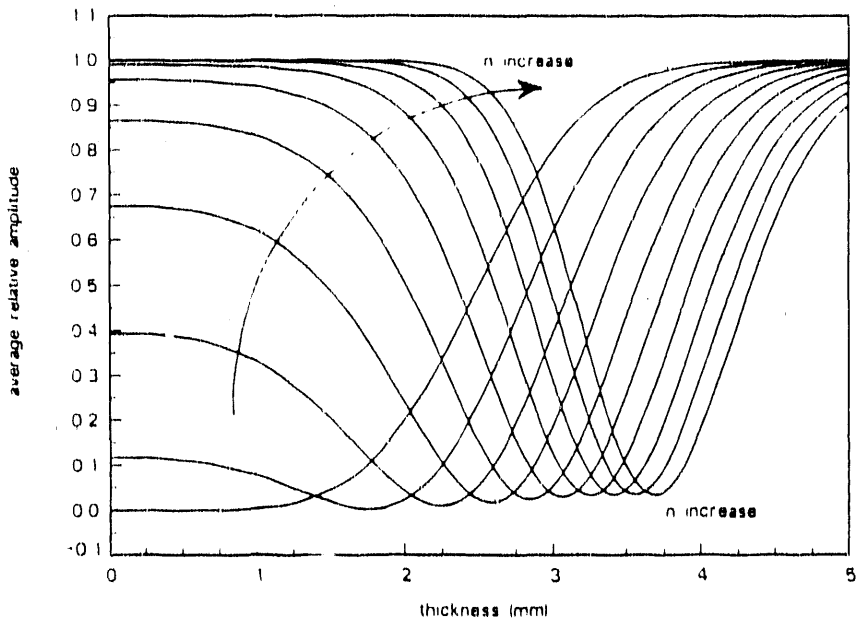

(b)

Fig. 12. Relative velocity measurement error (a) error vs. thickness, (b) relative amplitude vs. thickness

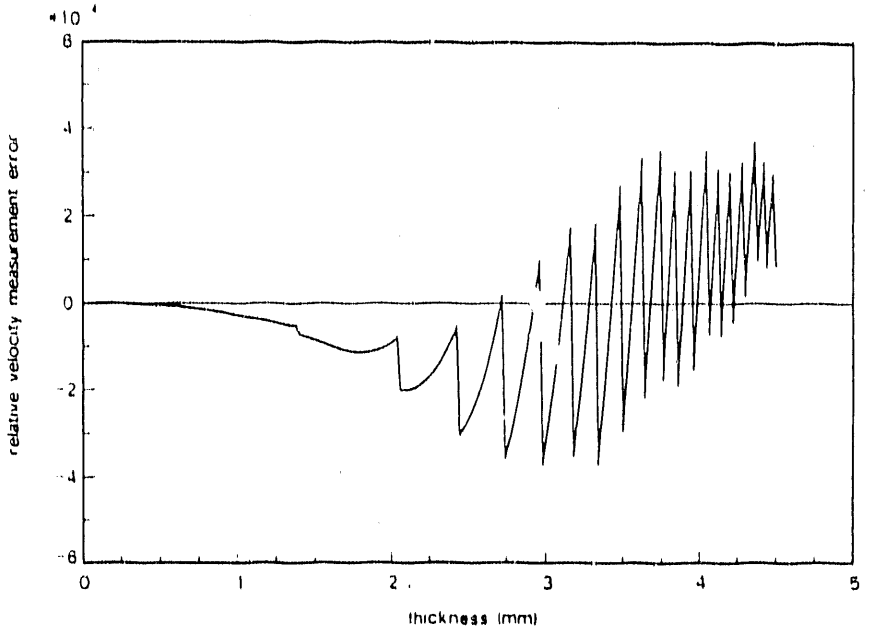

(a)

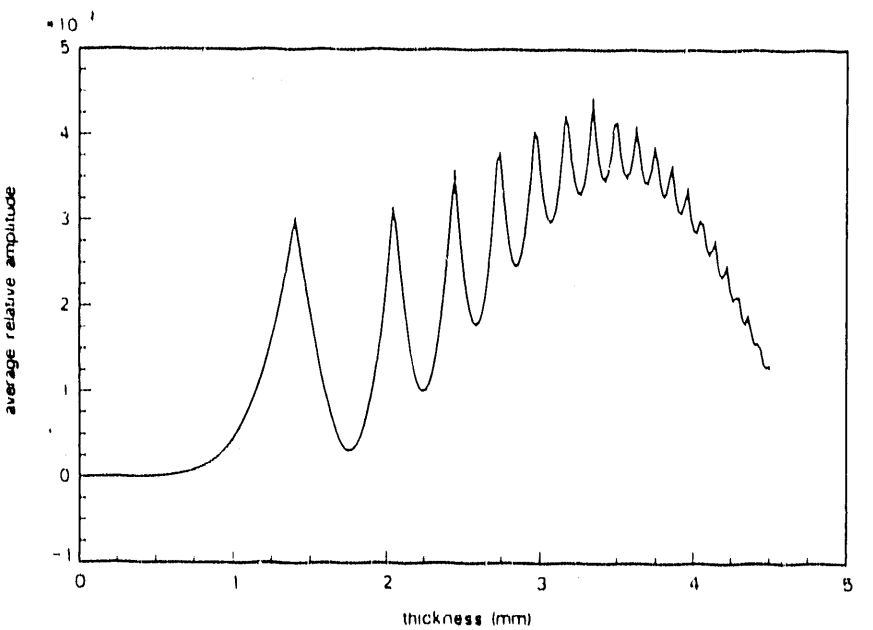

(b)

Fig. 13. The parts of Fig. 12 which bear practical significance

PART VI.

USE OF THE VELOCITY OF HIGHER ORDER LAMB MODES IN THE MEASUREMENT OF TEXTURE

ABSTRACT

Techniques for inferring texture orientation distribution coefficients (ODCs) from velocities of SH_0 (Fundamental horizontally polarized shear) and S_0 (fundamental symmetric Lamb) guided modes of plates are well known. For plates of cubic crystallites, W_{400} and W_{420} can be determined from relative variations of velocity as a function of angle. However, the remaining independent coeffient, W_{000}, requires an absolute measurement. Furthermore, the predicted value depends critically on theoretical estimates of average polycrystalline elastic constants. This paper discusses an alternative procedure to determine W_{000} which makes use of special properties of higher order guided waves. Attention is focused on a special point at which the S_0 and SH_1 (first order horizontally polarized shear) dispersion curves are tangent in isotopic materials. It is shown that the presence of anisotropy breaks the phase velocity degeneracy at this special position and that the degree of dispersion curves are overlay or separation provides a quantitative measure of W_{000}. Furthermore, the result does not require precise, independent knowledge of the plate thickness. The results are supported by both a perturbation theory and exact solution for wave propagation in anisotropic plate.

INTRODUCTION

The use of ultrasonic velocity measurements to determine the texture (preferred grain orientation) of metal plates has been the subject of considerable recent interest. The foundation for these procedures lies in the mathematical description of texture, in which the crystallite orientation distribution function (CODF) is expanded as a series of spherical harmonics. In the notation of Roe [1, 2], the expansion of the CODF takes the form

$$W(\xi,\psi,\phi) = \sum_{l=0}^{\infty} \sum_{m=-l}^{l} \sum_{n=-l}^{l} W_{lmn} Z_{lmn}(\xi)\, e^{-im\psi}\, e^{-in\phi} \qquad (1)$$

where θ, ϕ, and ψ are Euler angles describing the orientation of a particular crystallite with respect to the sample axes, $\xi=\cos\theta$, the Z_{lmn} are the Generalized Legendre functions, and W_{lmn} are the orientation distribution coefficients (ODC's). A similar relation has been developed by Bunge [3], using the expansion coefficient C_l^{mn}. Knowledge of either set of ODC's fully specifies the CODF, and hence the texture.

Ultrasonic measurements of texture are based on the fact that preferred grain orientations produce an anisotropy in the ultrasonic wave speed. Theoretical models have been developed relating the ODC's to the anisotropic elastic constants, C_{ij}, and ultimately to wave speeds. Because of the fourth rank nature of the elastic constants, only the ODC's of order $l \leq 4$ influence these wave speeds. For the case of cubic crystallites, the only nonvanishing, independent coefficients are W_{400}, W_{420} and W_{440}.

One of the most promising schemes for measurement of the ODC's has been based on measurements of the velocities of guided modes propagating in the plane of the plate, as shown schematically in Figure 1. In a promising configuration, use is made of the angular variation of the velocities of the SH_0 and S_0 modes [4]. Figure 2 presents the dispersion curves and deformation profiles of these modes for an isotropic plate. It should be noted that the long

wavelength limit of the S_0 mode velocity is required, which rigorously entails correction for dispersion. However these corrections are small as long as the wavelength is large with respect to the plate thickness. By measuring the velocities at 0°, 45° and 90° with respect to the rolling direction, it has been shown that all three ODC's can be deduced from S_0 mode data, while W_{400} and W_{440} can be deduced from SH_0 mode data [4, 5]. For either mode, relative measurements of the angular dependence of velocities can be used to predict W_{420} and W_{440}. However absolute velocity measurements are required to predict W_{400}. This fundamental consequence of the fact that the basis function having the coefficient W_{400} varies only with the polar angle θ, as can be seen from Eq. (1). When the polar axis is chosen normal to the plate, this contribution is independent of rotations of crystallites in the plane of the plate. Consequently, no information regarding W_{400} can be obtained from angular variations of a particular mode velocity in the plane of the plate. The formulae for predicting W_{400} follow [4]:

$$W_{400} = \frac{35\sqrt{2}}{16\pi^2 C^o}\left[\rho V^2_{SH_0}(0°) + \rho V^2_{SH_0}(45°) - 2C^o_{44}\right] \tag{2}$$

$$W_{400} = \frac{35\sqrt{2}}{32\pi^2[3+8(c^o_{12}/c^o_{11})+8(c^o_{12}/c^o_{11})^2]C^o}\left\{\rho V^2_{S_0}(0°) + 2\rho V^2_{S_0}(45°) + \rho V^2_{S_0}(90°) - 4C^o_{11}[1-(c^o_{12}/c^o_{11})]^2\right\}. \tag{3}$$

Here, C^o_{11}, C^o_{12} and C^o_{44} are moduli of an isotropic polycrystallite, C^o is a measure of the elastic anisotropy, ρ is the density, and the phase velocities are shown as a function of angle with respect to the rolling direction. Comparison of ODC's obtained by ultrasonics to those obtained by X-ray and neutron diffraction have shown good agreement for the cases of W_{420} and W_{440}, as illustrated in Fig. 3a [5, 6]. Note that scatter of W values is on the order of 10^{-3}. However, similar comparisons for W_{400} have shown a much more erratic behavior (Fig. 3b). It has been found that for both steel and copper, the agreement between ultrasonic measurements are excellent for the S_0 mode with the SH_0 mode valued being consistently lower. However, for the aluminum samples, there are serious differences between the ultrasonic

and diffraction predictions of W_{400}. The fact that the range of the abscissa and ordinate is an order of magnitude greater than that in Fig. 3a makes this disagreement even more severe. Although not fully understood, this greater apparent difficulty in predicting W_{400} in aluminum may arise from the small value of the elastic anisotropy, C', which makes the predictions particularly sensitive to errors. Sources of these errors may include the greater difficulty of absolute (as compared to relative) velocity measurements, possible errors in estimates of the isotropic polycrystal moduli (including alloying and second phase effects), and the need for dispersion correction for the S_0 mode which becomes more severe as plate thickness increases [6].

IMPROVED TECHNIQUE

Ideally, one would like to infer W_{400} from relative measurements. However, as noted above, measurements of the variation of velocities in the plane of the plate can not be used to determine W_{400}, which is the coefficient of a basis function which only varies with polar angle. One must then seek a different experimental configuration in which a wave parameter is varied in a cross-section of the plate. This can be accomplished by taking advantage of the properties of higher order Lamb modes. Since these can be viewed as the superposition of partial waves reflecting between the plate surfaces [7, 8], and since the angle of these partial waves with respect to the normal depends upon the point of operation on the dispersion curves, measurement of various features of the dispersion can be used to study the angular dependence of wave velocities in the cross-section of the plate. One such scheme based on the dispersion of SH modes has been demonstrated by Smith et al. [9] and Armstrong et al. [10]. However, that technique generally depends on a precise knowledge of the plate thickness. Although such knowledge is easily obtained in the laboratory, it may not be as accessible in production environments. Hence, alternate procedures are needed.

One technique which appears particularly attractive makes use of the properties of guided Lamé modes, operating at the point at which the isotropic S_0 mode and SH_1 mode dispersion curves are tangential, as shown in Fig. 2. Both modes consist of shear waves propagating at 45° with respect to the plate normal. However, the partial waves in the SH_1 mode are polarized parallel to the plane of the plate, while those in the S_0 mode are polarized in the sagittal plane. Because of this 90° polarization rotation, one would expect their relative velocities to depend on W_{400}. Furthermore, since the partial waves propagate through the same path at the same angle, one would expect measurement of their relative velocities to be insensitive to

small uncertainties in the plate thickness. Thus we expect the presence of W_{400} to split the tangency of the SH_1 and S_0 modes at the Lamé point, producing either a mode crossing or a mode separation depending on sign.

NUMERICAL EVALUATION

In order to evaluate this expectation, an exact theory has been used to calculate the dispersion curves of Lamb waves in an anisotropic plate [11]. Fig. 4 presents dispersion curves for waves propagating along the rolling direction of a plate. In each case, one of the ODC's (W_{400}, W_{420} or W_{440}) has been varied between ±0.005 with the other two held constant at 0.001, and the Hill averaging scheme was employed. As expected, introduction of texture causes the tangency to be broken, with either mode splitting or crossing occurring depending on the sign of W. The coefficients W_{400} and W_{440} are seen to have an influence of comparable magnitude, somewhat greater than that of W_{420}.

INVERSION

Having established the sensitivity of this special feature of the dispersion curves, it is necessary to seek an inversion algorithm that will allow the three ODC's to be separately determined from experimental data. Fig. 5 presents the strategy. Let (ω_0, k_0) define the point of Lamé mode propagation in the isotropic medium. When anisotropy is introduced, the dispersion curves will be shifted. Define

$$\Delta k \equiv \Delta k_{SH_1} - \Delta k_{S_0} \tag{3}$$

to be the relative shift in wave vector at the frequency ω_0. From perturbation theory, one can compute $\Delta k(\theta)$, Where θ is the angle of propagation with respect to the rolling direction. Explicitly examining the results at θ=0°, 45° and 90°, one obtains a set of linear equations in the ODC's which can be solved with the result,

$$W_{400} = \frac{7\sqrt{2}\ C_{44}^{o}}{40\ \pi^2 C^{o} k_0}\left[\Delta k(0°) + \Delta k(90°) + \Delta k(45°)\right] \tag{4a}$$

$$W_{420} = \frac{7\sqrt{2}\ C_{44}^{o}}{8\ \pi^2 C^{o} k_0}\left[\Delta k(90°) - \Delta k(0°)\right] \tag{4b}$$

$$W_{440} = \frac{7\sqrt{2}\ C_{44}^{o}}{24\ \pi^2 C^{o} k_0}\left[\Delta k(0°) + \Delta k(90°) - 2\Delta k(45°)\right] \tag{4c}$$

where C_{44}^{o} is the shear modulus.

The stability of this inversion scheme has been numerically evaluated by using the exact theory to calculate Δk and then inverting to obtain the ODC's by Eqs. (4). To test the sensitivity to small fluctuations in moduli, Hill's averaging procedure was used to compute the isotropic moduli in the exact calculation of dispersion and the Voigt, Hill and Reuss procedures were each used in the data inversion. The material was assumed to be polycrystalline copper, having W_{400}=W_{420}=W_{440}=1×10^{-3}. Table I presents the results of the inversion.

CONCLUSIONS

Previously proposed techniques have shown the ability to determine W_{420} and W_{440} from the angular dependence of the velocities of SH_0 and S_0 guided elastic modes of plates. Those procedures require absolute velocities for the prediction of W_{400}, and difficulties have been encountered under conditions of weak anisotropy (aluminum) or thick plates. An improved technique has been proposed based on the texture induced splitting of the tangency of the S_0 and SH_1 Lamé modes. Numerical calculations and perturbation theory have been used to verify the procedure. Experimental evaluations are in progress, utilizing EMATs to excite these special modes [12].

ACKNOWLEDGEMENT

Ames Laboratory is operated for the U. S. Department of Energy by Iowa State University under contract No. W-7405-Eng-82. This work was supported by the Director for Energy Research, Office of Basic Energy Sciences.

REFERENCES

1. R. -J. Roe. "Description of Crystallite Orientation in Polycrystalline Materials. III. General Solution to Pole Figure Inversion." J. Appl. Phys. 36 (1965): 2024-31.

2. R. -J. Roe. "Inversion of Pole Figures for Materials Having Cubic Crystal Symmetrv." J. Appl. Phys. 37 (1966): 2069-72.

3. H. J. Bunge. Texture Analysis in Materials Science. London: Butterworths, 1982.

4. R. B. Thompson, S. S. Lee, and J. F. Smith. "Relative Anisotropies of Plane Waves and Guided Modes in Thin Orthorhombic Plates: Implication for Texture Characterization." Ultrasonics 25 (1987): 133-37.

5. R. B. Thompson, J. F. Smith, and Y. Li. "Ultrasonic Measurement of Rolling Texture in Non-ferrous Plates." Presented at 8th International Conference on Texture of Materials, Santa Fe, New Mexico, 1987.

6. R. B. Thompson, J. F. Smith, S. S. Lee, and G. C. Johnson. "A Comparison of Ultrasonic and X-ray Determinations of Texture in Thin Cu and Al Plates." Metall. Trans. 20A (1989): 2431-47.

7. R. D. Mindlin. "Waves and Vibrations in Isotropic, Elastic Plates." Structural Mechanics. New York: Pergamon, 1960. 199-232.

8. B.A. Auld. Acoustic Fields and Waves in Solids. Vol.II. New York: Wiley, 1973.

9. J. F. Smith, G. A. Alers, P. E. Armstrong, and D. T. Eash. "Separation and Characterization of Stress Levels and Texture in Metal Sheet and Plate: I. Principles and Preliminary Experiment." J. Nondes. Eval. 4 (1984): 157-163.

10. P. E. Armstrong, D. T. Eash, J. A. O'Rourke, and J. F. Smith. "Separation and Characterization of Stress Levels and Texture in Metal Sheet and Plate: II. Rolled Copper Sheet Experiment" J. Nondes. Eval. 6 (1987): 33-45.

11. Y. Li and R. B. Thompson. "Propagation of Guided Elastic Waves in Orthotropic Plates." In Review of Progress in Quantitative Nondestructive Evaluation. Vol. 8A. Eds. D. O. Thompson and D. E. Chimenti. New York: Plenum Press, 1989. 189-96.

12. R. B. Thompson and C. F. Vasile. "An Elastic-wave Ellipsometer for Measurement of Material Property Variations." Appl. Phys. Lett. 34 (1979): 128-30.

Table I. Test of inversion ($\times 10^{-3}$)

	Voigt	Hill	Reuss
W_{400}	1.12	1.02	0.91
W_{420}	1.33	1.21	1.08
W_{440}	1.13	1.03	0.91

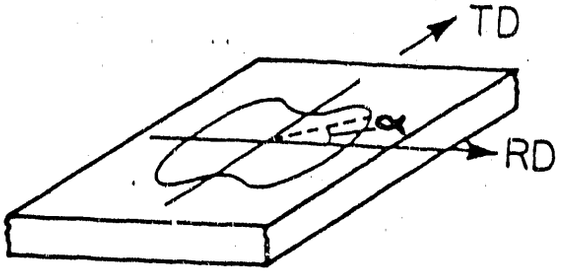

Fig. 1. Angular variation of ultrasonic velocity

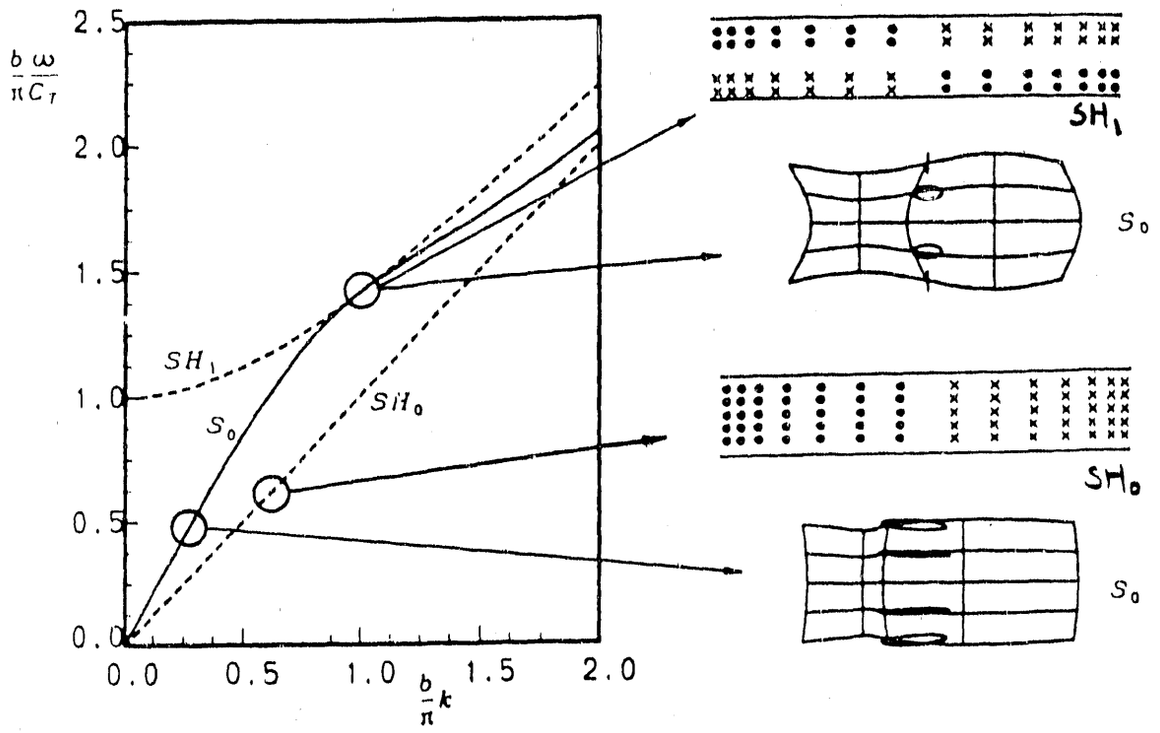

Fig. 2. Isotropic dispersion curves and displacement profiles of SH_0, SH_1, and S_0 modes

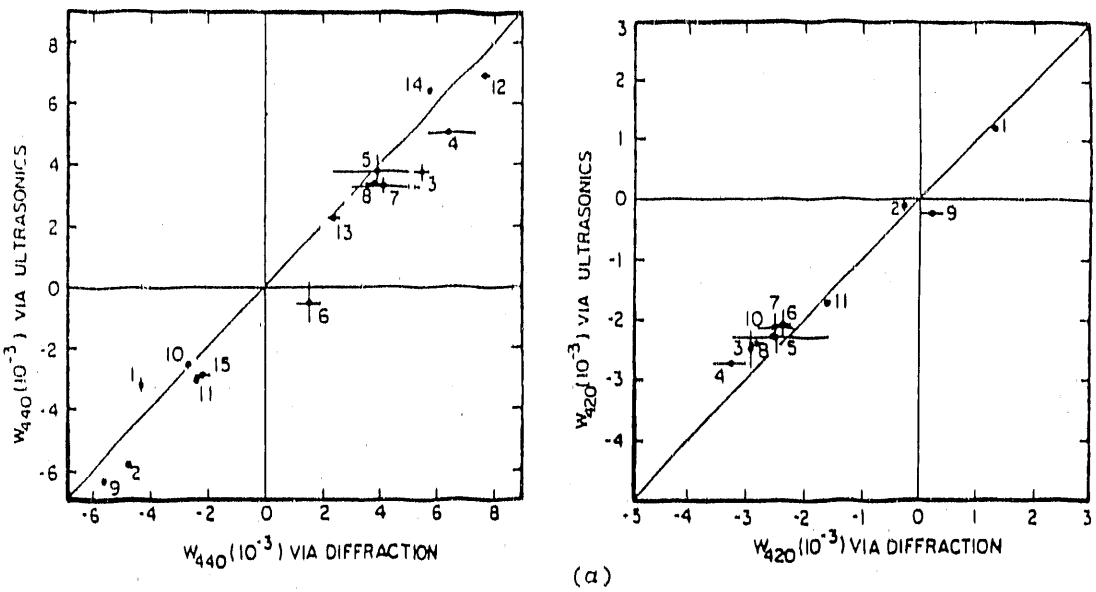

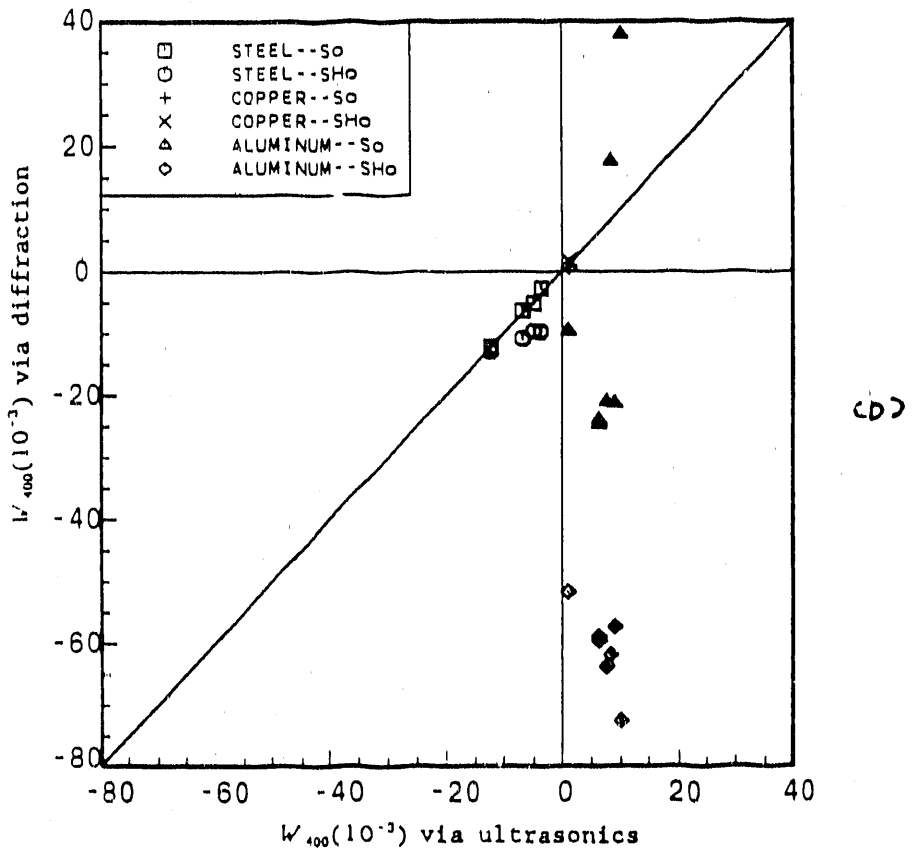

Fig. 3. Predictions of ODCs via ultrasonics. (a) good correlations for W_{420} and W_{440}. (b) erratic predictions for W_{400}

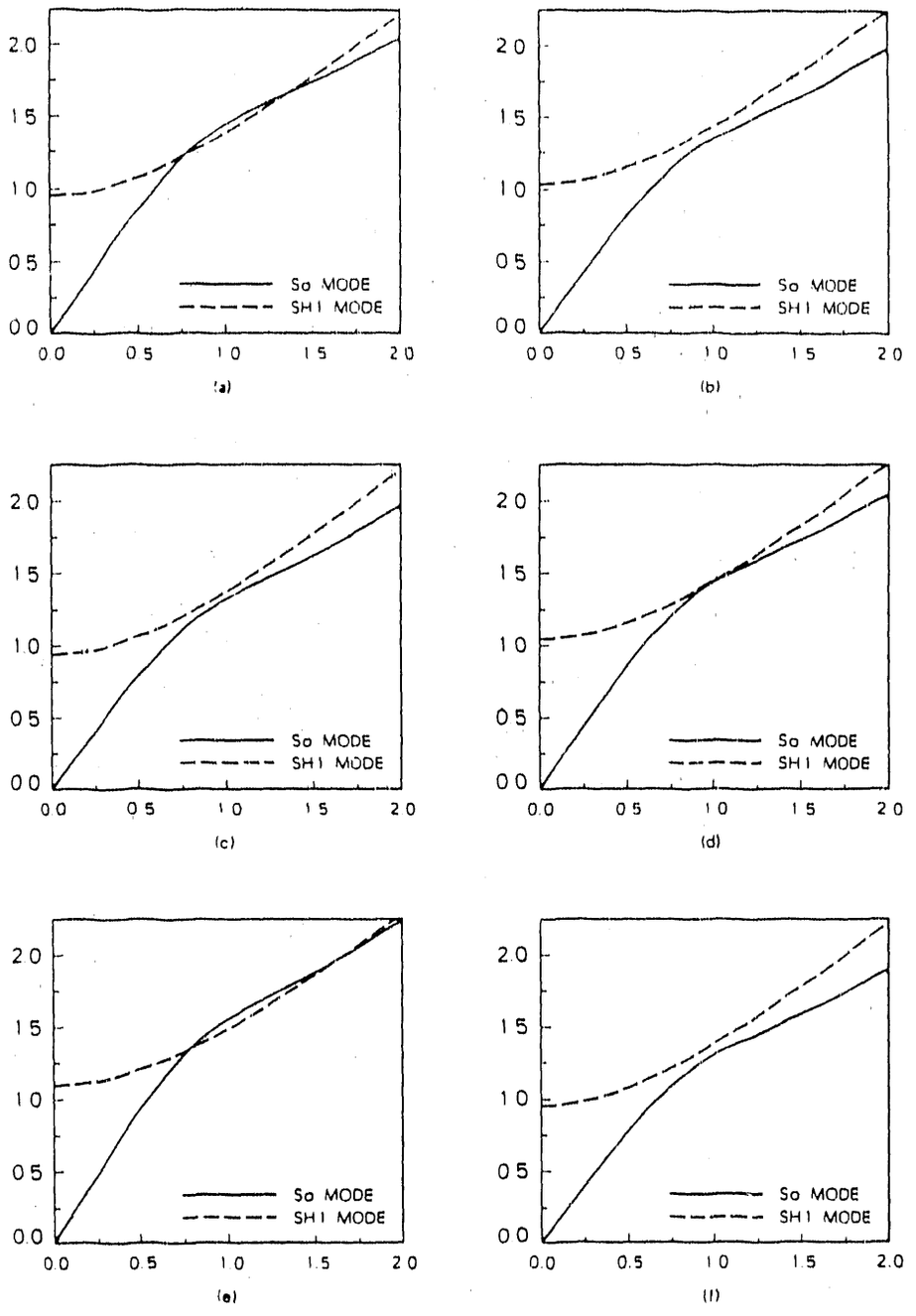

Fig. 4. Dispersion curves for wave propagation in rolling direction
(a) W_{400}=-0.005, W_{420}=W_{440}=0.001, (b) W_{400}=0.005, W_{420}=W_{440}=0.001,
(c) W_{420}=-0.005, W_{400}=W_{440}=0.001, (d) W_{420}=0.005, W_{400}=W_{440}=0.001,
(e) W_{440}=-0.005, W_{420}=W_{400}=0.001, (f) W_{440}=0.005, W_{420}=W_{400}=0.001.
All abscissae are in bk/π, and all ordinates are in $b\omega/\pi C_t$, where C_t is the through-thickness shear wave velocity and b is the plate thickness

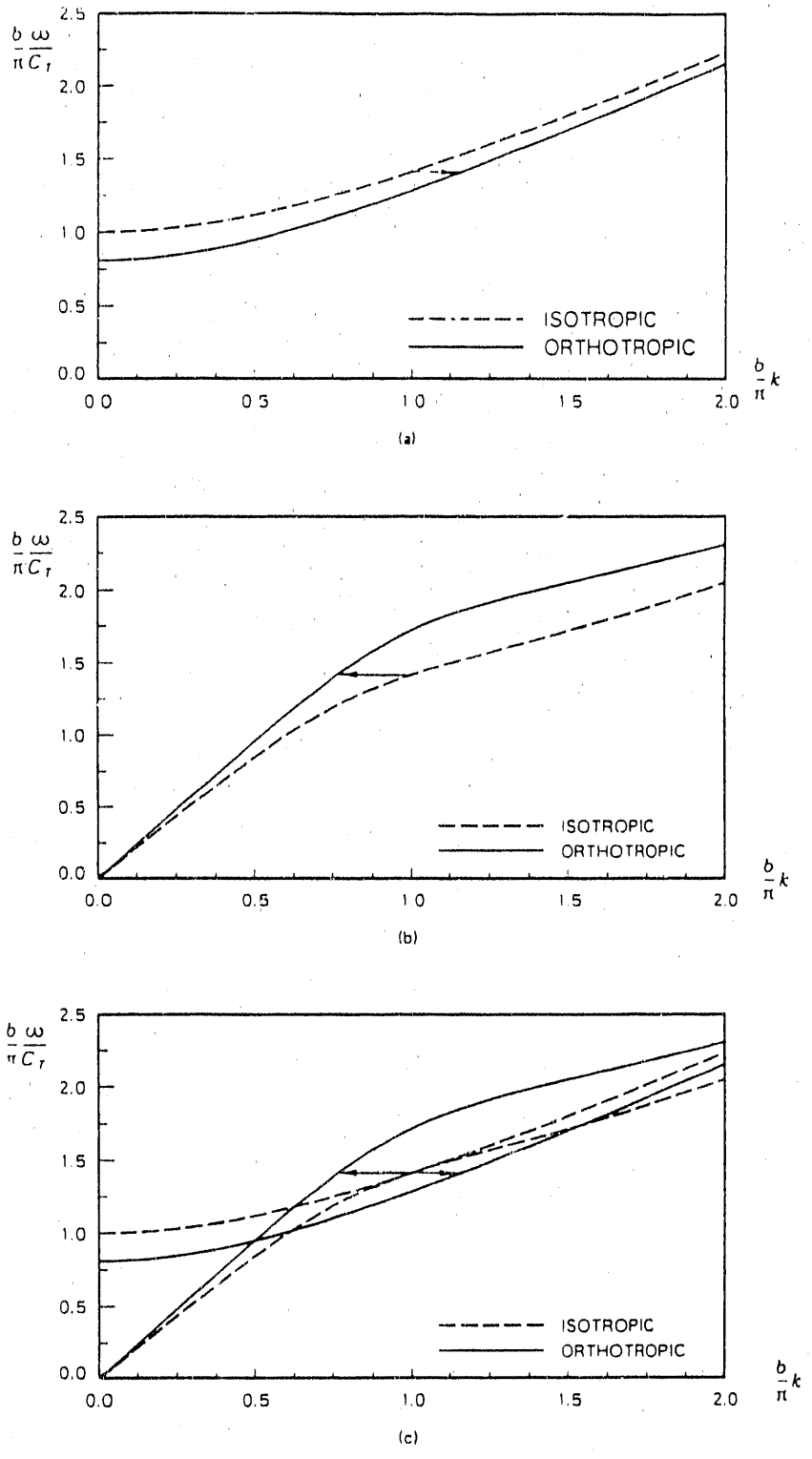

Fig. 5. Inversion algorithm strategy. (a) Shift in k for SH_1 mode, (b) shift in k for S_1 mode, (c) total shift in k for SH_1 and S_1 modes

PART VII.

DETERMINATION OF TEXTURE IN PLATES OF HCP METALS ZIRCONIUM AND TITANIUM BY ULTRASOUND AND NEUTRON DIFFRACTION

ABSTRACT

The demand for nondestructive characterization of texture in hexagonal close packed (hcp) materials has been increasing rapidly in the last few years. The texture of polycrystalline materials is typically described by coefficients, W_{lmn} by Roe's notations, of a harmonic expansion of the crystallite orientation distribution function (CODF). Recently, we described ultrasonic techniques for the determination of texture in hcp metal sheets. In principle five coefficients may be inferred ultrasonically but techniques conventionally applied to cubic materials do not yield all five in hcp materials. This paper presents experimental results in which higher order modes are include ! to determine all five coefficients for plates of zirconium and titanium. Values of W_{lmn} determined by ultrasonics and neutron diffraction will be compared and errors associated with the ultrasonic method will be discussed.

INTRODUCTION

The demand for nondestructive characterization of texture in hexagonal close packed (hcp) materials has been increasing rapidly in the last few years, particularly in aerospace and nuclear industries for quality control purposes. Texture study has traditionally been done by X-ray or neutron diffraction techniques. These diffraction techniques are generally slow or destructive. Recent advances in ultrasonics have shown that texture can also be determined by fast and nondestructive ultrasonic techniques [1,2,3]. An ultrasonic texture measurement instrument is currently being built at Iowa State University which can calculate texture parameters of cubic polycrystallites in a few seconds[4].

The texture of a polycrystalline material is generally described by a set of orientation distribution coefficients (ODCs) or W_{lmn} in Roe's notation. The detailed definitions of these coefficients can be found in Refs. 5 and 6. In principle, only W_{lmn} for l up to 4 can be inferred ultrasonically. For materials of cubic polycrystallites, there are only three nonzero and independent coefficients: W_{400}, W_{420}, and W_{440}. For materials of hexagonal polycrystallites, there are two extra independent coefficients: W_{200} and W_{220}.

Until recently, most of the study in ultrasonic characterization of texture has been concentrated on polycrystals of cubic crystallites. In the determination of texture in plates of cubic materials, long wave length limit of S_0 Lamb waves and SH_0 waves are generally used and the velocities are measured for propagation directions of 0°, 45°, and 90° with respect to the rolling direction [1,2,3]. These conventional techniques are sufficient and have been proved to be successful for cubic polycrystallites. Typically, EMATs (electro-magnetic acoustic transducers) are used in texture study because their couplant free operation enhances the potential for industrial applications.

ULTRASONIC TECHNIQUES AND SAMPLES

The key to the extension of the conventional techniques to texture characterization in hexagonal materials is the relations between the elastic constants and the texture parameters W_{lmn}. These relations have been established and published recently in Ref. 7. Once we have the relations, the following equations, describing the information provided by the conventional ultrasonic techniques, can be obtained:

$$
\begin{aligned}
&BW_{400} - \sqrt{5}A_3W_{200} = \frac{105\sqrt{2}}{16\pi^2}\rho\left[V^2_{SH_0}(0^0) + V^2_{SH_0}(45^0) - 2C^0_{44}/\rho\right]\\
&W_{440} = \frac{3\sqrt{35}}{16\pi^2 B}\rho\left[V^2_{SH_0}(45^0) - V^2_{SH_0}(0^0)\right]\\
&\left[3+8(C^0_{12}/C^0_{11})+8(C^0_{12}/C^0_{11})^2\right]BW_{400} + 2\sqrt{5}\left\{\left[1-2(C^0_{12}/C^0_{11})^2\right]A_1\right.\\
&\qquad\left. - (C^0_{12}/C^0_{11})A_2\right\}W_{200} = \frac{105\sqrt{2}}{32\pi^2}\rho\left[V^2_{S_0}(0^0) + V^2_{S_0}(90^0)\right.\\
&\qquad\qquad\left. + 2V^2_{S_0}(45^0) - 4(C^0_{11} - C^{0^2}_{12}/C^0_{11})/\rho\right] \qquad (1)\\
&(1+2C^0_{12}/C^0_{11})BW_{420} + \sqrt{3}\left[A_1+(C^0_{12}/C^0_{11})A_2\right]W_{220} = \frac{21\sqrt{5}}{32\pi^2}\rho\left[V^2_{S_0}(90^0) - V^2_{S_0}(0^0)\right]\\
&W_{440} = \frac{3\sqrt{35}}{32\pi^2 B}\rho\left[V^2_{S_0}(0^0) + V^2_{S_0}(90^0) - 2V^2_{S_0}(45^0)\right]
\end{aligned}
$$

where A_1, A_2, A_3, and B are elastic anisotropy constants and C^0_{ij} are isotropic elastic constants of the materials. These constants are related to the elastic constants of single crystals [7] and they are averaging method dependent. The elastic constants for Voigt, Hill, and Reuss averaging method and material densities of Ti and Zr are listed in Table I. Throughout this paper, we will use the Hill averaging method, unless otherwise specified.

In Eqs. (1), one sees clearly that W_{200} and W_{400} are coupled in the first and the third equations and W_{120} and W_{220} are coupled in the fourth equation. These couplings are due to the nonzero terms W_{200} and W_{220} in the hexagonal

class. W_{440} is still uncoupled, computable directly from the second or the fifth equations.

Obviously, the conventional techniques cannot solve for all five Ws. New ultrasonic techniques need to be developed. The one technique that we are going to discuss in this paper utilizes SH_1 modes. The dispersion equations for SH_1 waves are:

$$\begin{aligned} &\text{Propagating at 0 degrees:} && C^o_{11}W = C_{66}K + C_{44} \\ &\text{Propagating at 45 degrees:} && C^o_{11}W = \tfrac{1}{4}(C_{11}-2C_{12}+C_{22})K + \tfrac{1}{2}(C_{44}+C_{55}) \qquad (2) \\ &\text{Propagating at 90 degrees:} && C^o_{11}W = C_{66}K + C_{55} \end{aligned}$$

where $K=(\frac{b}{\pi}k)^2$ is the square of dimensionless wave number with b being the plate thickness,and $W=(\frac{2bf}{V_t})^2$ is the square of dimensionless frequency with $V_t=\sqrt{C^o_{44}/\rho}$ being the normalization shear wave velocity.

Note that all three equations in Eqs. (2) are linear equations. The slopes of the solutions for 0° and 90° propagation are identical, indicating a constant separation distance between the two solutions, and the intercept of 45° propagation solution is exactly half way between the other two. Using the relations in Ref. 7, Eqs. (2) can be expressed in terms of ODCs.

There are two measurement methods that are used in our texture study: zero-crossing method for determining phase velocity and Fourier-phase method for obtaining wave vectors. Each method can be further subdivided into two measurement schemes: absolute and relative measurements.

In the zero-crossing absolute velocity measurement, one changes the transducer separation distance and keeps track of the time delays of a specific zero crossing within the waveform. In the zero-crossing relative measurement, one fixes transducer separation distance but changes the wave propagation direction and keeps track of the time delays of a specific zero crossing within the waveform. The phase velocity is associated with the shifts of the arrival time with angle or distance.

In the Fourier-phase absolute measurement, one takes waveforms at two different transducer separation distances and uses the deconvolution technique to obtain the wave number information. In the Fourier-phase relative measurement, one takes waveforms at different propagation directions for a fixed transducer separation distance and uses the deconvolution technique to obtain the information on the change of wave numbers.

When using the zero-crossing method, one generally measures the propagation velocity of a nondispersive or weakly dispersive wave. When using the Fourier-phase method, one can measure either the propagation velocity or the wave number of a wave which can be either nondispersive or strongly dispersive. In real applications, the Fourier-phase method is favorable because it can be easily automated.

We used two samples in our study. The first one is a 1.86 mm thick titanium sample and the second one is a 0.89 mm thick zirconium plate. Both samples were purchased at a local vender. These samples are of commercial purity although it is unclear if second phase exists in either of these samples. We did notice some apparent thickness variations within the zirconium sample.

EXPERIMENTAL DATA

Five sets of neutron pole figures have been obtained for the Ti and the Zr samples. $W_{l\,mn}$ for l up to 10 have been computed based on these pole figures. The $(10\bar{1}0)$ and (0002) pole figures are shown in Figs. 1 and 2 and the $W_{l\,mn}$ for l up to 4 for the two samples are given in Table II. The errors in Table II correspond to the last two digits of $W_{l\,mn}$.

The measured ultrasonic data for the two samples are given in Table III and Table IV. In these tables, the zero-crossing measurements are a combination of absolute measurements at 0° and relative measurements at other angles. The relative measurements in these tables are given with respect to the rolling direction (0°). Each entry in these two tables is the mean value averaged from three repetitions of independent measurements. For the Ti sample, measurements were made using S_{0lim}, SH_0 and SH_1 modes. The values for the S_{0lim} and SH_0 modes are velocities and the values for the SH_1 modes are wave numbers. We were not successful in obtaining useful SH_1 waveforms for the Zr plate hence the values in Table IV are all velocities. The errors for the absolute velocity measurements are about ±0.005 mm/ms for S_{0lim} and ±0.003 mm/ms for SH_0. The errors for the relative measurements are about an order of magnitude smaller. The measurement errors for the dimensionless wave numbers are about ±0.003 in Table III.

Theoretically, when the plate is orthotropic, the velocities or wave numbers for propagation in 45° and 135° directions are identical. The entries in the 45° and 135° columns are generally very close and can be considered to be the same if the measurement error is taken into account. Further, SH_0 velocities for propagation in 0° and 90° directions should also be the same for orthotropic media. This is affirmed by the data in Tables III and IV.

FORWARD COMPARISONS

Using the $W_{l\,mn}$ obtained from neutron diffraction, we can calculate the elastic constants from the relations given in Ref. 7. Then dispersion curves for wave propagating in the two samples can be generated using the generalized Rayleigh-Lamb equations of anisotropic plates [8,9]. On the other hand, using Fourier phase absolute measurement method, experimental dispersion curves can be reconstructed. The comparison of the theoretical dispersion curves and the ultrasonically reconstructed dispersion curves are shown in Fig. 3 for the Ti sample for wave propagation in the rolling direction. In Fig. 3 the continuous curves are the theoretical curves and the curves with crosses are experimental dispersion curves. There are four experimental dispersion curves: low wave number S_0 mode, high wave number S_0 mode, SH_0 mode, and SH_1 mode. In this paper, the information pertaining to the high wave number S_0 mode will not be discussed.

Generally good agreement can be observed from Fig. 3 between the theoretical and experimental dispersion curves. There is, however, one acute problem associated with the Fourier phase method: an ambiguity of a multiple of 2p in determining the relative phase of the two signals being deconvolved. When using Fourier phase method, the phase computation involves an inverse tangent function. The returned value of the inversion is always within the $-\pi$ to π range while the true phase does not have such a limit. In other words, the true phase is the computed phase plus/minus $2n\pi$. Physically, this corresponds to an n cycle misalignment in time domain. To choose the correct value n, we have utilized an algorithm that will be discussed elsewhere because of the page limitation here.

To make sure that we have selected the right multiple, we have plotted the experimental dispersion curves with a positive and a negative offset of 2p phase in Fig. 4. The comparison between the theoretical and experimental

curves shows beyond doubt that we have chosen the right multiple in ou fitting. Fig. 4 also demonstrates that if we do not have the prior knowledge of neutron diffraction results, it can be very difficult to identify the correct multiple of 2p for relatively strongly dispersive waves.

Table V gives a data analysis and comparison example. In this case, the conventional S_{0lim} velocity data are used to obtain a linear combination of W_{220} and W_{420} using the fourth equation in Eqs. (1). The equation at the beginning of the table expresses a simplified relation between W_{220} and W_{420} and ultrasonic velocities. The coefficients $C_4^{\%}$ and $C_3^{\%}$ given at the bottom of the table are constants computed based on the fourth equation in Eqs. (1) and the elastic isotropy and anisotropy constants listed in Table I. The values of these coefficients are for the Hill averaging method while the bounds of the values correspond to the Voigt and the Reuss averaging methods. On the left hand side of Table IV, the values are computed based on neutron diffraction data and the errors correspond to the standard deviation in W_{220} and W_{420}. On the right hand side of Table IV, results calculated from ultrasonic velocity measurements are listed along with the standard deviations based on the three repetitions of the experiment for each of the different measurement methods.

From Table V, one can see that there is a good agreement between ultrasonic data and neutron diffraction results for the Ti sample, but the comparison for the Zr plate is not so good, even though consistent results are obtained from different ultrasonic techniques and measurement methods. We do not have a good explanation for this discrepancy at this stage.

Table VI is another data analysis example. In this example, information of the SH_1 mode measurements is used to obtain another linear combination of W_{220} and W_{420}. Here only the analysis for the Ti sample is presented since we did not get reliable waveforms for the Zr because of the nonuniform thickness of the plate. The analysis in this table is presented in the same fashion as in Table V, except that the squares of dimensionless

wave numbers, rather than velocities, are used on the ultrasound side. The zero-crossing measurements are missing from this table because the SH_1 waves are strongly dispersive and the zero-crossing measurement method is unsuitable for such a situation. Again, a very good agreement between diffraction and ultrasonic data can be observed.

INVERSION AND CONCLUSIONS

We have calculated the predictions of $W_{l\,mn}$ based on ultrasonic data for different combinations of techniques and measurement methods discussed in this paper. Comparisons of neutron diffraction data to the best and the worst estimates by ultrasound are given in Table VII. For the Ti sample, except for W_{400}, the best estimates by ultrasound are in very good agreement with those by neutron diffraction. We currently do not have a good explanation on why the estimate of W_{400} by ultrasound is so much different from neutron data. The worst estimates for the Ti are sometimes considerably off from the neutron results except for W_{220} and W_{420} where the differences are relatively small. For the Zr sample, W_{220} and W_{420} remain coupled since reliable ultrasonic data were unavailable for the SH_1. For other ODCs, the best estimates are very close to the neutron estimates. On the other hand, the worst estimate for W_{400} is again far off from the neutron data, even the sign has changed.

In conclusion, we have shown that ultrasonic techniques can be used to characterize texture in plates of hexagonal polycrystallites. The distinguishing aspect of texture characterization in hexagonal materials is the coupling of W_{220} with W_{420} and W_{200} with W_{400}. Conventional ultrasonic techniques that have been used for texture determination of cubic polycrystals cannot alone determine all five ODCs for hexagonal materials; therefore other ultrasonic technique or techn'ques must be used or developed. This paper addresses one of the techniques we are using: the SH_1 mode technique. Other techniques may also be used [10]. When using the SH_1 mode technique, along with the conventional techniques, all five $W_{l\,mn}$ for l up to 4 can be determined. The results presented in this paper has shown a promising future of ultrasonic determination of texture, but more work

needs to be done on the issue of ambiguity of multiple of 2π before transferring the technology to industry.

ACKNOWLEDGEMENT

Ames Laboratory is operated for the U. S. Department of Energy by the Iowa State University under contract No. W-7405-Eng-82. This work was supported by the Director for Energy Research, Office of Basic Energy Sciences.

REFERENCES

1. R. B. Thompson, S. S. Lee, and J. F. Smith. "Relative Anisotropies of Plane Waves and Guided Modes in Thin Orthorhombic Plates: Implication for Texture Characterization." Ultrasonics 25 (1987): 133-37.

2. R. B. Thompson, J. F. Smith, S. S. Lee, and G. C. Johnson. "A Comparison of Ultrasonic and X-ray Determinations of Texture in Thin Cu and Al Plates." Met.Trans. 20A (1989): 2431-2447.

3. Y. Li, J. F. Smith, and R. B. Thompson. "Characterization of Textures in Plates by Ultrasonic Plate Wave Velocities." In Nondestructive Characterization of Materials. Vol. 3. Eds. P. Höller, V. Hauk, G. Dobmann, C. Ruud, and R. Green. New York: Springer-Verlag, 1989. 312-19.

4. E. P. Papadakis, et al. "An Automatic Instrument For The Ultrasonic Measurement Of Texture." In Nondestructive Characterization of Materials. Vol. 4. Eds. C. Ruud and R. Green. New York: Plenum Press, in press.

5. R.-J. Roe. "Description of Crystallite Orientation in Polycrystalline Materials. III. General Solution to Pole Figure Inversion." J. Appl. Phys. 36 (1965): 2024-31.

6. R.-J. Roe. "Inversion of Pole Figures for Materials Having Cubic Crystal Symmetry." J. Appl. Phys. 37 (1966): 2069-72.

7. Y. Li and R. B. Thompson. "Relations between Elastic Constants C_{ij} and ODCs for Hexagonal Materials." J. Appl. Phys. 67 (1990): 2663-65.

8. Y. Li and R. B. Thompson. "Propagation of Guided Elastic Waves in Orthotropic Plates." In Review of Progress in Quantitative Nondestructive Evaluation. Vol. 8A. Eds. D. O. Thompson and D. Chimenti. New York: Plenum Press, 1989. 189-96.

9. Y. Li and R. B. Thompson. "Influence of Anisotropy on the Dispersion Characteristics of Guided Ultrasonic Plate Modes." J. Acoust. Soc. Am. 87 (1990): 1911-31.

10. Y. Li, R. B. Thompson, and S. S. Lee. "Ultrasonic Measurement of Texture of Cubic and Hexagonal Materials." In Review of Progress in Quantitative Nondestructive Evaluation. Vol. 9B. Eds. D. O. Thompson and D. E. Chimenti. New York: Plenum Press, 1990. 1781-88.

Table I. Elastic isotropy and anisotropy constants in GPa and densities in g/cm^3

Mat'l	method	C^o_{11}	C^o_{12}	C^o_{44}	A_1	A_2	A_3	B	ρ
Ti	Voigt	163.93	75.53	44.20	-62.00	-145.00	207.00	23.00	4.510
	Hill	162.86	76.07	43.40	-61.80	-141.81	203.61	16.69	
	Reuss	161.78	76.60	42.59	-61.60	-138.61	200.21	10.38	
Zr	Voigt	145.68	72.16	36.76	-55.80	-6.60	62.40	42.40	6.505
	Hill	145.18	72.28	36.45	-49.05	-5.22	54.27	38.99	
	Reuss	144.68	72.39	36.14	-42.30	-3.85	46.14	35.59	

Table II. ODCs calculated from neutron pole figures

l	m	$W_{l\,m0}$ (error) -- Ti	$W_{l\,m0}$ (error) -- Zr
2	0	0.01709 (59)	0.01300 (40)
2	2	-0.00545 (17)	-0.00575 (34)
4	0	0.00574 (24)	0.00088 (18)
4	2	-0.00687 (20)	-0.00497 (06)
4	4	0.00217 (06)	0.00236 (16)

Table III. Measured ultrasonic velocities and wave numbers for the Ti

Measurement method		mode	(unit)	0°	45°	90°	135°
zero-crossing	Abs + Rel	S_{0lim}	(mm/μs)	5.3236	5.3778	5.4506	5.3830
		SH_0	(mm/μs)	2.9540	2.9582	2.9523	2.9611
Fourier-phase	Abs	S_{0lim}	(mm/μs)	5.3191	5.3791	5.4646	5.3846
		SH_0	(mm/μs)	2.9511	2.9575	2.9510	2.9572
		SH_1	(bk/π)	0.6367	0.6757	0.7011	0.6796
	Rel	S_{0lim}	(mm/μs)	0.0000	-0.0655	-0.1508	-0.0741
		SH_0	(mm/μs)	0.0000	-0.0070	0.0008	-0.0072
		SH_1	(bk/π)	0.0000	-0.0410	-0.0685	-0.0405

Table IV. Measured ultrasonic velocities for the Zr

Measurement method	mode			0°	45°	90°	135°
zero-crossing	Abs + Rel	S_{0lim}	(mm/μs)	4.0941	4.0805	4.0987	4.0811
		SH_0	(mm/μs)	2.3309	2.3594	2.3309	2.3605
Fourier-phase	Abs	S_{0lim}	(mm/μs)	4.0862	4.0648	4.0901	4.0579
		SH_0	(mm/μs)	2.3286	2.3584	2.3239	2.3560
	Rel	S_{0lim}	(mm/μs)	0.0000	0.0143	-0.0073	0.0155
		SH_0	(mm/μs)	0.0000	-0.0309	0.0015	-0.0305

Table V. Data analysis for W_{220} and W_{420} using S_{0lim} modes

$C^{S_0}_{220} W_{220}$ + $C^{S_0}_{420} W_{420}$ =			$\rho[V^2_{S_0}(90°) - V^2_{S_0}(0°)]$		
Ti:	6.6375	±0.2573	6.1712	±0.1875	(zero-crossing)
			7.0763	±0.2577	(Fourier phase absolute)
			7.3273	±0.0863	(Fourier phase relative)
Zr:	0.8586	±0.2070	0.2452	±0.1191	(zero-crossing)
			0.2074	±0.1846	(Fourier phase absolute)
			0.3871	±0.3022	(Fourier phase relative)

Based on	neutron	ultrasound (measurement method)
Ti:	$C^{S_0}_{220} = -1491.6^{+5.1}_{-5.2}$;	$C^{S_0}_{420} = 217.1^{+80.1}_{80.2}$
Zr:	$C^{S_0}_{220} = -601.7^{+5.5}_{-5.5}$;	$C^{S_0}_{420} = 523.4^{+44.3}_{44.5}$

Table VI. Data analysis for W_{220} and W_{120} using SH_1 modes

$C^{SH_1}_{220}$ W220 + $C^{SH_1}_{420}$ W420 =			[K(90) - K(0)]		
Ti:	0.0922	±0.0024	0.0861	±0.0036	(Fourier phase absolute)
			0.0923	±0.0243	(Fourier phase relative)

Based on	neutron	ultrasound (measurement method)
Ti:	$C^{SH_1}_{220} = -13.66^{+0.02}_{-0.03}$;	$C^{SH_1}_{420} = -2.59^{-0.91}_{+0.95}$

Table VII. Comparisons of neutron diffraction data to the best and the worst estimates by ultrasonic techniques

		W_{200}	W_{220}	W_{100}	W_{420}	W_{440}
Ti	Neutron	0.01709	-0.00545	0.00574	-0.00687	0.00217
	Best	0.01746	-0.00542	0.02787	-0.00646	0.00231
	Worst	0.00672	-0.00571	0.04263	-0.00415	-0.00696
Zr	Neutron	0.01300	-0.00575	0.00088	-0.00497	0.00236
	Best	0.01092		0.00060	*	0.00239
	Worst	0.01040		-0.00320	*	0.00410

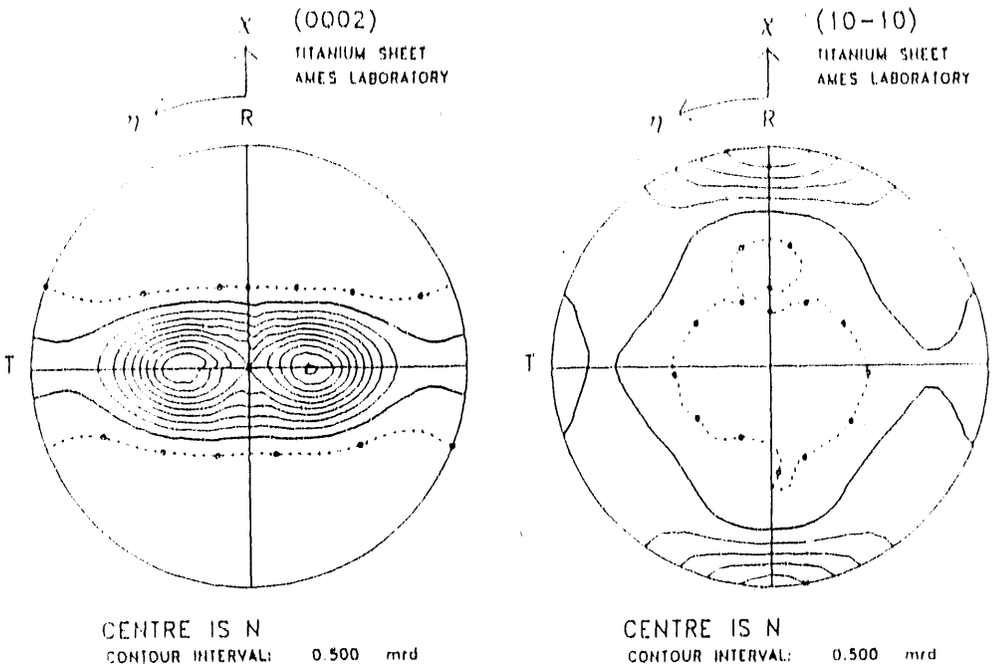

Fig. 1. Pole figures for the Ti samples

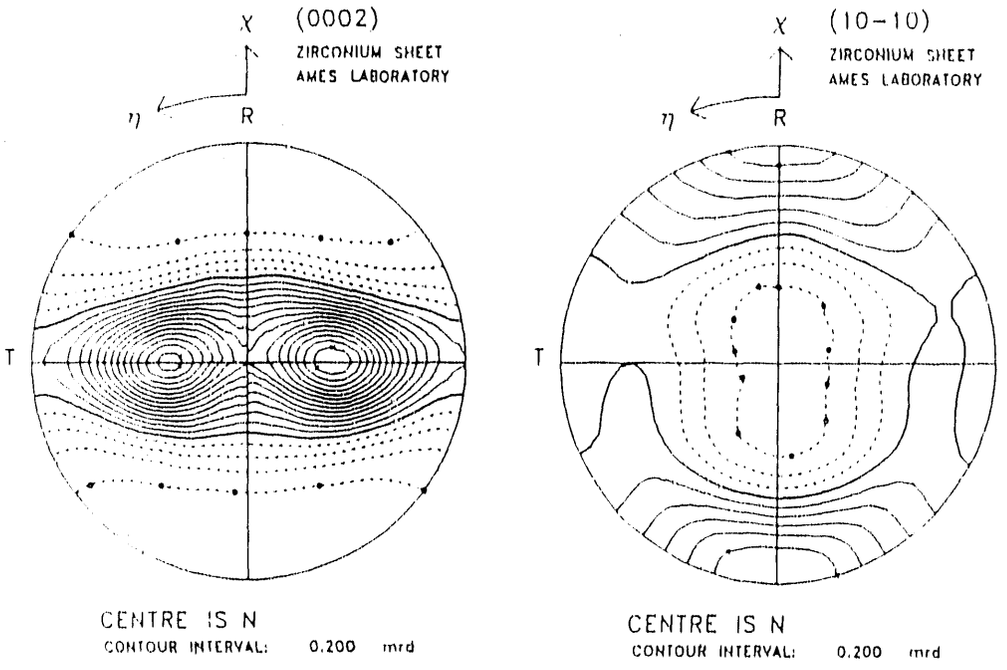

Fig. 2. Pole figures for the Zr sample

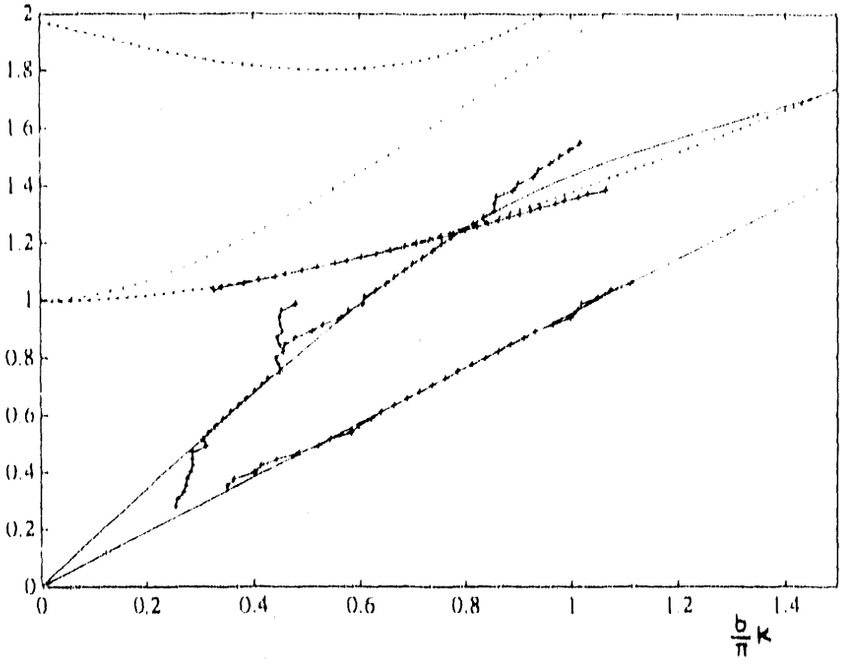

Fig. 3. Some dispersion curves for the Ti sample

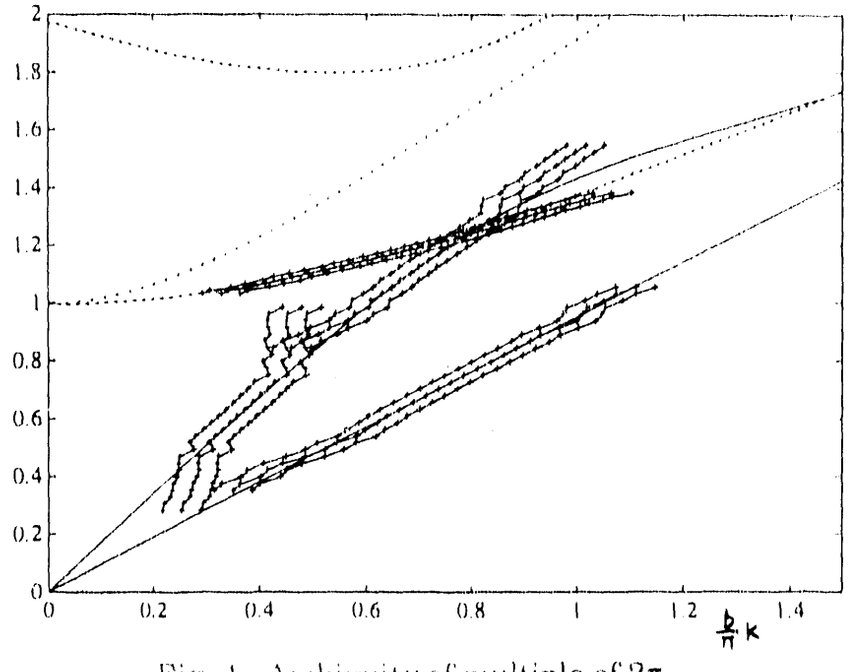

Fig. 4. Ambiguity of multiple of 2π

PART VIII.

USE OF LAMÉ MODE PROPERTIES IN THE DETERMINATION OF TEXTURE PARAMETERS ON AL PLATES

ABSTRACT

We have recently proposed an ultrasonic technique which utilizes Lamé mode properties to characterize texture of cubic and hexagonal polycrystalline aggregates. It is known that when a plate is isotropic, there is always a point where S_0 and SH_1 modes touch each other tangentially at $k=\pi/b$. When the plate is anisotropic, S_0 and SH_1 modes may cross over or split at the Lamé point. The amount of cross-over and splitting is found to be sensitive to the weak anisotropy induced by the texture in the metal sheets. In this paper, we will report the experimental results on ten Al plates. We will compare the estimations of texture parameters Wlmn obtained using the Lamé mode technique and the conventional ultrasonic techniques. We will also compare our ultrasonic predictions to those obtained independently from neutron and X-ray diffraction techniques. The advantages and disadvantages of the Lamé mode technique and errors associated with the measurement will also be discussed.

INTRODUCTION

Texture (preferred grain orientation) characterization of polycrystalline aggregates has traditionally been done by X-ray or neutron diffraction techniques. These techniques are generally slow and destructive. Advances in ultrasonics over the last decade have made it possible to determine texture of cubic polycrystalline aggregates quickly and nondestructively [1-3]. It is known that all polycrystalline materials have some degrees of texture or not, when texture is present, the materials are anisotropic, usually weakly orthotropic for rolled plates or sheets. The principle of ultrasonic characterization of texture is to infer texture by sensing and determining the material anisotropy.

The mathematical description of texture was developed over 20 years ago by Roe [4,5] and Bunge [6]. Texture is quantitatively described by the orientation distribution coefficients (ODC's) or $W_{l\,mn}$ in Roe's notations. These ODCs are dimensionless parameters. Theoretically, diffraction techniques can determine $W_{l\,mn}$ for l up to infinity, though in practice $W_{l\,mn}$ is determined for l up to no more than 20 or 30. In principle, only $W_{l\,mn}$ for l up to 4 can be determined ultrasonically. It is very fortunate that these $W_{l\,mn}$ are often the most important texture parameters for formability study for cubic metals [7,8]. For these materials, there are only three independent and nonzero $W_{l\,mn}$ for l up to 4; these are W_{400}, W_{420}, and W_{440}. Typical values of these $W_{l\,mn}$ are on the order of 10^{-3}. These $W_{l\,mn}$ are related to deep drawability and earing in the manufacturing process [8].

The key to the ultrasonic determination of texture is the set of relations between the texture parameters $W_{l\,mn}$ and the elastic constants C_{ij} of the material. For rolled plates or sheets of cubic crystallites, these relations are linear and can be expressed as [9]:

$$C_{ij}=C_{ij}^{m}+C_{ij}^{c}\sum_{l\,mn} a_{l\,mn}W_{l\,mn} \qquad (m\ 0,2,4) \tag{1}$$

where $C_{11}^{(0)}$ and $C^{(0)}$ are isotropic elastic constants and an anisotropy measure, and a_{i00} are constant coefficients. In Eq. (1), $C_{11}^{(0)}$ and $C^{(0)}$ can be calculated from the elastic constants of single crystals c_{ij} via different averaging methods. The values of c_{ij}, $C_{11}^{(0)}$ and $C^{(0)}$ for Al, Cu, and Fe are tabulated in Table I. The values for $C_{11}^{(0)}$ and $C^{(0)}$ in the table are obtained by the Hill averaging method with the bounds corresponding to the Voigt and Reuss averaging results.

The conventional techniques for texture determination on rolled plates or sheets are the long wavelength S_0 (symmetric Lamb) and the SH_0 (shear horizontal) plate mode techniques (see Fig. 1). Using these techniques, one measures phase velocities of these two modes at 0, 45, and 90 degrees with respect to the rolling direction. The equations which calculate W_{420} and W_{440} from the S_0 or the SH_0 mode velocities can be found in Refs. 2 and 10. These equations use the angular variation in velocity, V(a), hence do not require absolute velocity measurements. The equations for the calculation of W_{400} are given below:

$$W_{400} = \frac{35\sqrt{2}}{16\pi^2 C^{(0)}} [\rho V_{SH_0}^2(0°) + \rho V_{SH}^2(45°) - 2C_{11}^{(0)}] \tag{2}$$

$$W_{400} = \frac{35\sqrt{2}}{32\pi^2 [3+8(c_{12}^{(0)}/c_{11}^{(0)})+8(c_{12}^{(0)}/c_{11}^{(0)})^2] C^{(0)}} [\rho V_{S_0}^2(0°) + 2\rho V_{S_0}^2(45°) + \rho V_{S_0}^2(90°) - 4C_{11}^{(0)}[1+(c_{12}^{(0)}/c_{11}^{(0)})]^2] \tag{3}$$

where ρ is the density of the material.

The conventional techniques work satisfactorily overall except for the determination of W_{400} on Al plates, whose prediction is often found to be inconsistent with independent diffraction measurements. This discrepancy is believed to be caused primarily by the following reasons. (a) The accuracy of the prediction of W_{400} relies on the accurate measurement of phase velocities in all three different directions. The typical measurement error in velocity is about ±0.005 mm ns for manual absolute measurement. This may be improved to ±0.0005 mm ns or better for automated measurement. (b) Existence of second phase or alloying elements in Al samples alters the isotropic elastic moduli. The influence of second phase material or alloying

elements is still unclear. Up to 5% of difference in isotropic moduli for the alloyed aluminum can be found in the literature. A paper presented recently has shown that for pure Al plates, the ultrasonic predictions and X-ray diffraction results are reasonably consistent [11]. Table II shows how each of these two reasons contributes to the errors in the prediction of W_{400}. From this table one can see clearly why Al is particularly vulnerable to the errors and uncertainty in the measurement and calculation.

The objective of this paper is to explore or develop a different ultrasonic method that does not rely on very precise absolute measurements or precise knowledge of the isotropic elastic moduli and density to predict W_{400}.

THEORY OF LAMÉ MODE TECHNIQUE

We have recently proposed an ultrasonic technique which utilizes Lamé mode properties to characterize texture of cubic and hexagonal polycrystalline aggregates [11,12]. It is known that, when a plate is isotropic, there is always a Lamé point where dispersion curves of the S_0 and the SH_1 modes touch each other tangentially at the wavevector $k=\pi/b$ (see Fig. 1), where b is the plate thickness. At this point, both modes have the dimensionless frequency $2bf/V_t = \sqrt{2}$, the phase velocity $V_p = \sqrt{2}V_t$, and the group velocity $V_g = V_t/\sqrt{2}$, where V_t is the plane shear wave velocity, $\sqrt{C_{44}^o/\rho}$. The S_0 Lamb mode at the Lamé point has only vertically polarized shear wave components (the longitudinal wave component is absent); the wave bounces back and fourth from the two surfaces at 45 degree angles. The SH_0 mode has only horizontally polarized shear wave components, also propagating at $\pm 45^\circ$ with respect to the plate surfaces.

When the plate is anisotropic, Lamé modes do not exist any more. Instead, the S_0 and the SH_1 modes may cross over or split in the vicinity of the Lamé point. The amount of cross-over and splitting, which is sensitive to the weak anisotropy induced by the texture in the metal sheets, is related to the texture parameters by:

$$\Delta k = \frac{k\pi^2 C^o}{35 C_{44}^o}(25\sqrt{2}W_{400} - 4\sqrt{5}W_{420}\cos 2\alpha + 6\sqrt{35}W_{440}\cos 4\alpha) \qquad (4)$$

where $\Delta k \equiv k(SH_1) - k(S_0)$, $k(SH_1)$ and $k(S_0)$ are the wave numbers of the SH_1 and the S_0 modes of the anisotropic materials at the Lamé frequency ($f=V_t/\sqrt{2}b$), $k=\pi/b$ is the wave number at the Lamé point, and a is the wave propagation angle. By measuring Δk at 0, 45, and 90 degree directions, estimates of all three Ws can be made based on this equation.

SAMPLES AND EXPERIMENT

We have used ten Al sheets in this study. All the samples are about 0.1" (2.5 mm) thick. One of these samples is a pure Al sample (99.99%) and all of the others are alloys with different heat treatments and rolling histories. Neutron diffraction measurements have been made on six samples and results of five samples have been reported [13]. X-ray diffraction has also been done on the pure Al sample on the top and the bottom surfaces as well as in the middle plane [14]. Of all the samples, none of them are fully flat -- local curvature exists irregularly on all the plates.

The experiments have been done using EMATs. The Lamé mode transducers have 5.1 mm period for the S_0 mode and 5.4 mm for the SH_1 mode. These enable the waves to be excited close to the Lamé point. For comparison purpose, we have also made measurements using the conventional S_0 technique.

The measurement method used in this study is the Fourier-phase method. Because both the S_0 and the SH_1 modes are strongly dispersive near the Lamé point, the commonly used zero-crossing velocity measurement method is not suitable. Using the Fourier-phase method, one takes waveforms at two different transducer separation distances and uses deconvolution technique to obtain the wave number information or phase velocity information. The typical change of separation distance is about 100 mm in this study. For each measurement, there are three repetitions and the averaged value is used in the final computation.

RESULTS AND DISCUSSIONS

Using the Fourier-phase measurement method, we can construct dispersion curves from the experiments. Because the ultrasonic pulses are bandlimited, the constructed dispersion curves are also bandlimited. Figure 2 shows the experimentally constructed dispersion curves and the dispersion curves generated theoretically based on the ODCs obtained from the conventional ultrasonic technique (the long wavelength S_0 mode). These dispersion curves are for one set of measurements only. They are obtained for wave propagation in the rolling direction on one specific sample. One can see from this figure that the dispersion curves from experiments are in very good agreement with the theoretical ones, indicating a mathematical consistency in the computations.

Unfortunately, the ultrasonic results are different from the neutron diffraction results. To see this, we enlarged the portion of Fig. 2 near the Lamé point. Figure 3 shows the zoomed-in portion with two added curves. The two additional curves are the S_0 and the SH_1 dispersion curves produced using the ODCs from the neutron diffraction analysis. One sees clearly from this figure that the S_0 and the SH_1 mode dispersion curves from the ultrasonic techniques cross over near the Lamé point while those from neutron diffraction split there. The reason for this is that the values for W_{400} are significantly different between ultrasound and neutron diffraction. As will be seen later, of the six samples for which we have neutron diffraction data, all exhibit such kind of disagreement.

When using the Fourier-phase method, there exists an ambiguity of a multiple of 2π in the phase computation. Figure 4 shows how much of shift in the dispersion curves may occur if a plus/minus 2π phase error is introduced in the dispersion curve construction process. We have paid very careful attention to this problem and convinced ourselves that we have selected correct multiples of 2π in our study.

Figures 5~7 show the comparisons between the ODC values inferred from ultrasonic techniques (both the conventional S_0 and the Lamé mode techniques) and neutron diffraction. Six sets of data for each of the six samples on which neutron measurements were made are shown in each of the figures. Separate symbols are used to denote the correlations between the conventional S_0 and the Lamé mode ultrasonic measurements and the neutron diffraction with the straight lines being the loci of perfect agreement. Figure 5 is the comparison for W_{420} and Fig. 6 is the comparison for W_{440}. Agreements are generally to within $\pm 1 \cdot 10^{-3}$, with two exceptions. This is the order of accuracy obtained in previous studies [10]. Considering the nonsmooth surfaces on all the samples, the correlations in Figs. 5 and 6 are satisfactory. Figure 7, however, shows very poor agreement between the ultrasonic and neutron predictions of W_{400}. We do not understand this major disagreement at this stage.

We have also made a comparison for the two different ultrasonic techniques. Figure 8 shows how the Lamé mode results on W_{400} compare to those obtained by the conventional S_0 technique. Relatively good agreement can be observed in this figure.

Despite the poor agreement between the ultrasonic and neutron diffraction predictions of W_{400} on the alloys, reasonably good agreement was obtained on the pure Al sample, which was studied by X-ray rather than neutron diffraction. This sheet was studied before with the conventional S_0 technique using the zero-crossing method and the comparison between the results from ultrasound and X-ray was found satisfactory [11]. Figure 9 shows, in addition to the results from the previous study, the comparison of X-ray results with the Lamé mode and the S_0 mode results from the current study. One can see from this figure that W_{400}'s estimated from both the Lamé mode and the S_0 mode methods fall within the range given by X-ray results on the surfaces and mid-plane. The estimates for W_{420} and W_{440} are not bad either, even though they are not always within the X-ray limits.

SUMMARY AND CONCLUSION

We have shown in this paper that the Lamé mode properties can be utilized to determine texture in plates (sheets) of cubic polycrystalline aggregates. In principle, this method has the advantage of requiring relative rather than absolute measurements in the determination of W_{400} and being not sensitive to the measurement error or the error in isotropic moduli. Experimental results on the pure Al samples have shown that estimates by the Lamé mode technique are in good agreement with estimates by the X-ray diffraction method. On the other nine alloy samples, we have found that the results from the conventional techniques are consistent with those from the Lamé mode technique. However, for the six samples on which we have neutron diffraction data, ultrasonic results for W_{400} are significantly different from those obtained by the diffraction method. Further work is needed to understand this disagreement.

ACKNOWLEDGEMENT

Ames Laboratory is operated for the U. S. Department of Energy by the Iowa State University under contract No. W-7405-Eng-82. This work was supported by the Director for Energy Research, Office of Basic Energy Sciences.

REFERENCES

1. C. M. Sayers. "Angular Dependent Ultrasonic Wave Velocities in Aggregates of Hexagonal Crystals." Ultrasonics 24 (1986): 289-91.

2. R. B. Thompson, S. S. Lee and J. F. Smith. "Relative Anisotropies of Plane Waves and Guided Modes in Thin Orthorhombic Plates: Implication for Texture Characterization." Ultrasonics 25 (1987): 133-37.

3. A. V. Clark, Jr., R. C. Reno, R. B. Thompson, J. F. Smith, G. V. Blessing, R. J. Fields, P. P. Delsanto, and R. B. Mignogna. "Texture Monitoring in Aluminum Alloys: A Comparison of Ultrasonic and Neutron Diffraction Measurement." Ultrasonics 26 (1988): 189-97.

4. R.-J. Roe. "Description of Crystallite Orientation in Polycrystalline Materials. III. General Solution to Pole Figure Inversion." J. Appl. Phys. 36 (1965): 2024-31.

5. R.-J. Roe. "Inversion of Pole Figures for Materials Having Cubic Crystal Symmetry." J. Appl. Phys. 37 (1966): 2069-72.

6. H. -J. Bunge. Texture Analysis in Materials Science. Trans. P. R. Morris. Berlin: Butterworths, 1982.

7. C. A. Stickles and P. R. Mould. "The Use of Young's Modulus for Predicting the Plastic-strain Ration of Low-carbon Steel Sheets." Met. Trans. 1 (1970): 1303-12.

8. G. J. Davies, D. J. Goodwill, and J. S. Kallend. "Elastic and Plastic Anisotropy in Sheets of Cubic Metals." Met. Trans. 3 (1972): 1627-31.

9. M. Hirao, K. Aoki, and H. Fukuoka. "Texture of Polycrystalline Metals Characterized by Ultrasonic Velocity Measurements." J. Acoust. Soc. Am. 81 (1987): 1434-40.

10. R. B. Thompson, J. F. Smith, S. S. Lee, and G. C. Johnson. "A Comparison of Ultrasonic and X-ray Determinations of Texture in Thin Cu and Al Plates." Met. Trans. 20A (1989): 2431-47.

11. Y. Li, R. B. Thompson and S. S. Lee. "Ultrasonic Measurement of Texture of Cubic and Hexagonal Materials." In Review of Progress in Quantitative Nondestructive Evaluation. Vol. 9B. Eds. D. O. Thompson and D. E. Chimenti. New York: Plenum Press, 1990. 1781-88.

12. Y. Li and R. B. Thompson. "Use of the Velocity of Higher Order Lamb Modes in the Measurement of Texture." In Review of Progress in Quantitative Nondestructive Evaluation, Vol. 8B. Eds. D. O. Thompson and D. E. Chimenti. New York: Plenum Press, 1989. 1863-70.

13. R. C. Reno, R. J. Fields, and A. V. Clark, Jr. "Crystallographic Texture in Rolled Aluminum Plates: Neutron Pole Figure Measurements." In Review of Progress in Quantitative Nondestructive Evaluation, Vol. 7B. Eds. D. O. Thompson and D. E. Chimenti. New York: Plenum Press, 1989. 1439-45.

14. S. Panchanadeeswaran and B. Schabel, ALCOA Center, PA, private communication, 1989.

Table I. Elastic constants of cubic materials (in GPa)

	c_{11}	c_{12}	c_{44}	C^{o}_{11}	C^{o}_{12}	C^{o}_{44}	C^{o}
Al	108.0	62.0	28.3	112.1±0.2	60.0±0.1	26.0±0.1	-10.8±0.2
Cu	169.0	122.0	75.3	200.7±9.7	106.1±4.9	47.3±7.3	-98.7±4.9
Fe	229.0	134.0	114.0	272.7±9.6	112.2±4.7	80.2±7.2	-132.1±0.9

Table II. Error in determination of W_{100} by the conventional ultrasonic techniques

error source	error	mode	Al	Cu	Fe
Velocity	0.005 mm/us	SII_0	0.004	0.0014	0.0009
Velocity	0.005 mm/us	S_0	0.001	0.0003	0.0002
Isotropic moduli	1%	SII_0	0.015	0.003	0.004
Isotropic moduli	1%	S_0	0.0015	0.0003	0.0003

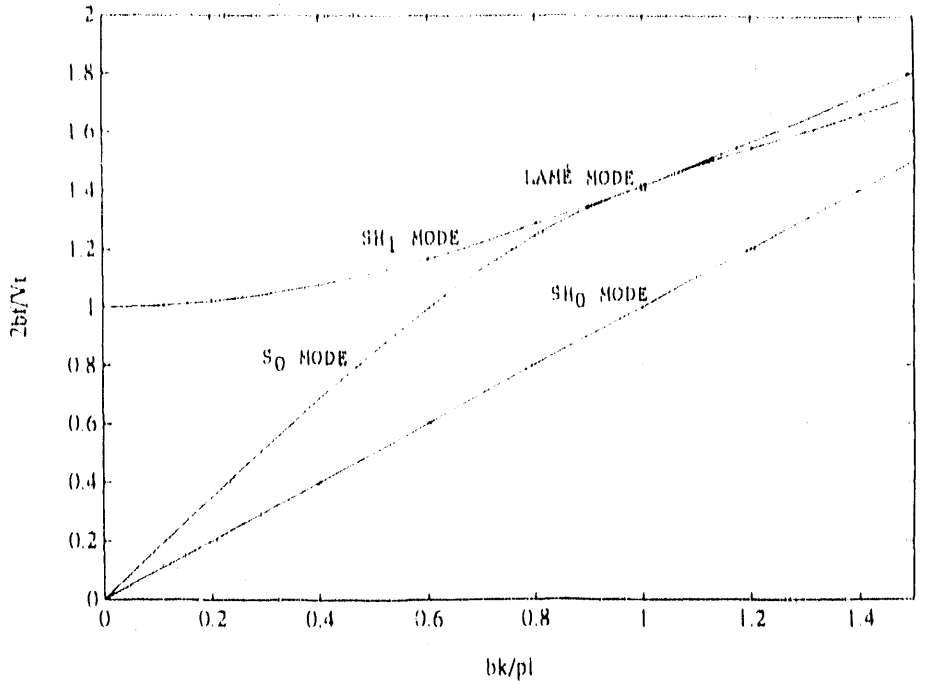

Fig. 1. Dispersion curves for the Lamb waves that are used in ultrasonic characterization of texture

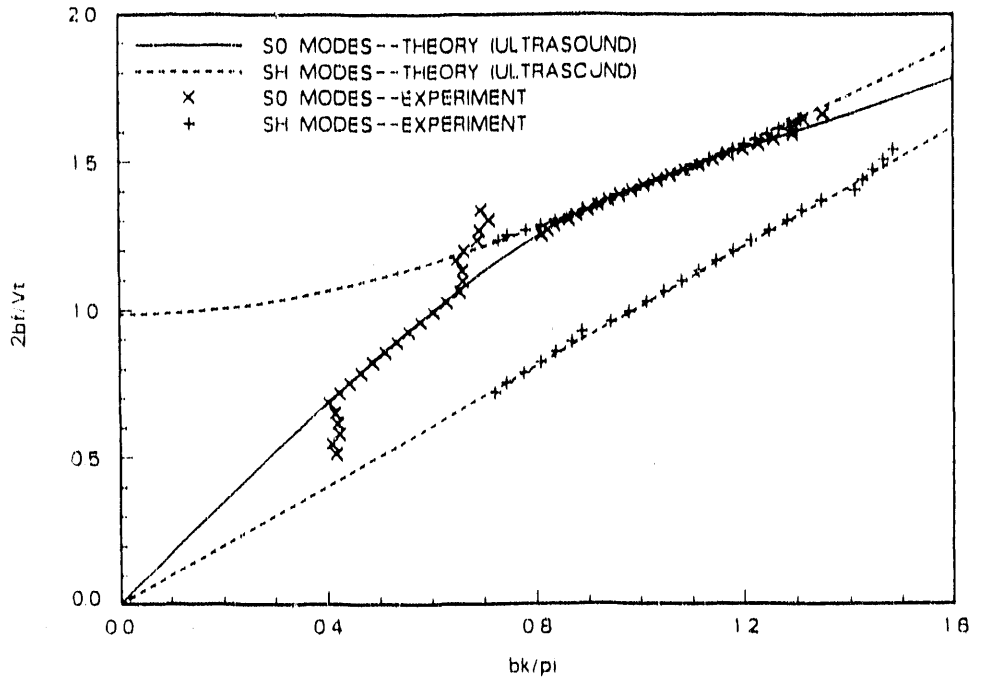

Fig. 2. Theoretical and experimental dispersion curves

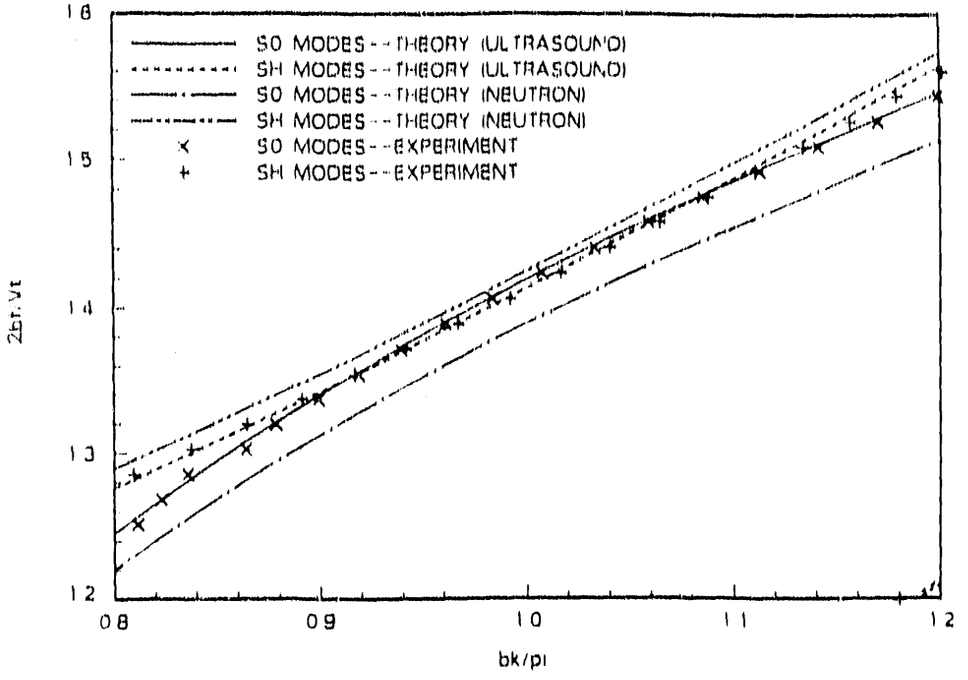

Fig. 3. Dispersion curves obtained from ultrasonic and neutron diffraction data

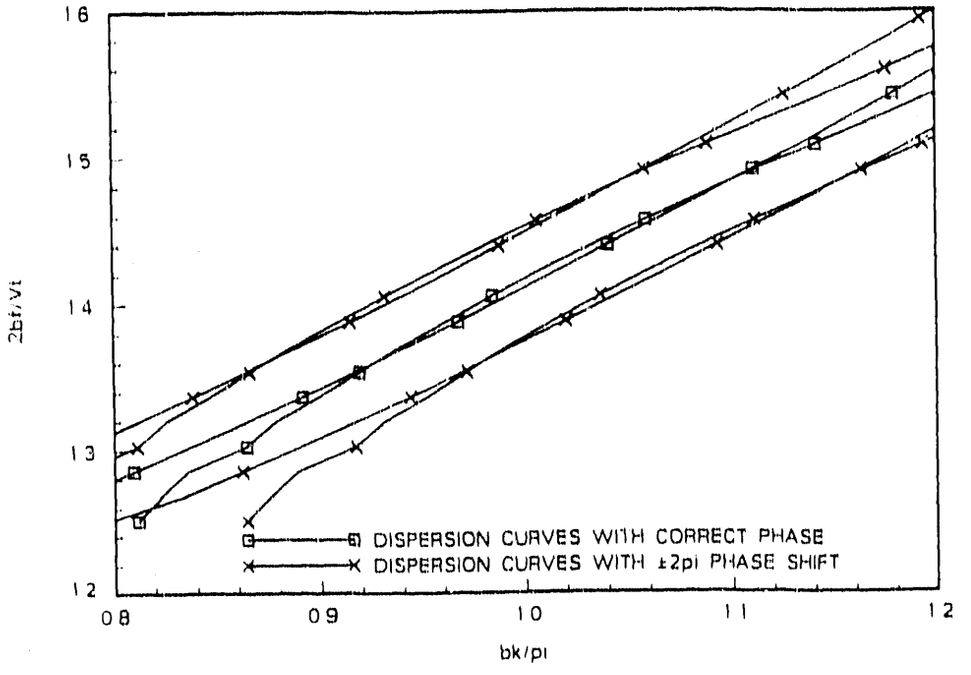

Fig. 4. Shifts due to the ambiguity in the choice of multiple of 2π

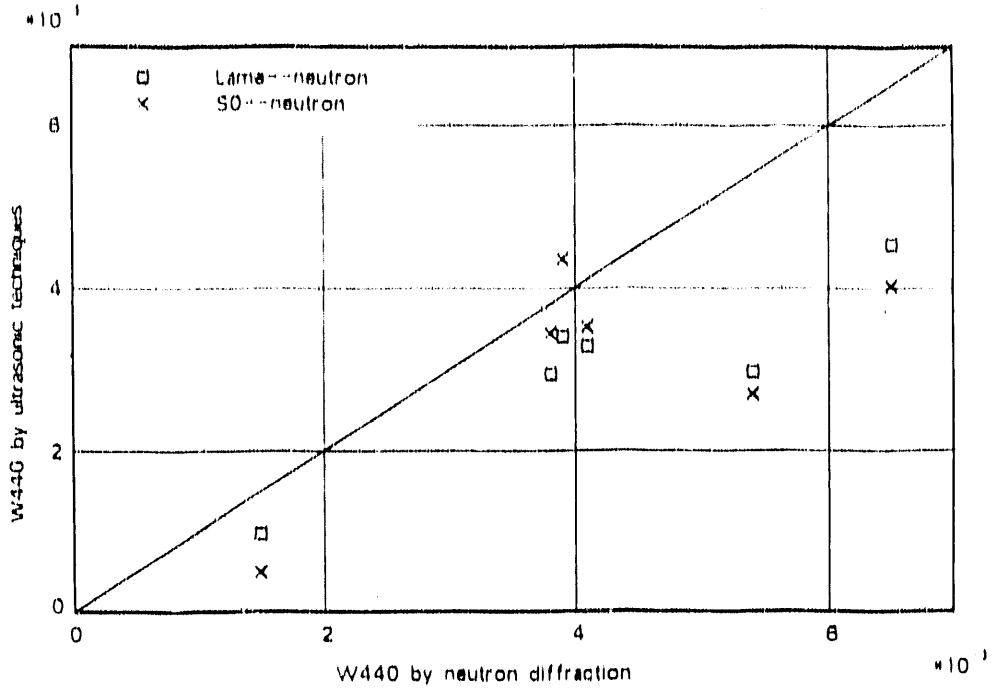

Fig. 5. Correlation between ultrasonic and neutron diffraction results (W_{440})

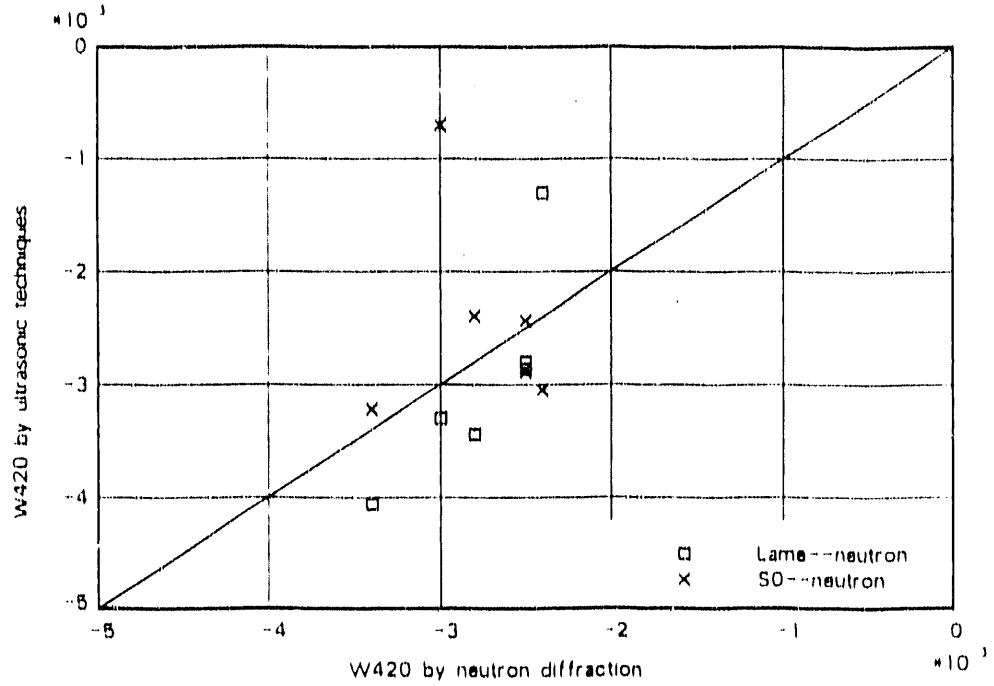

Fig. 6. Correlation between ultrasonic and neutron diffraction results (W_{420})

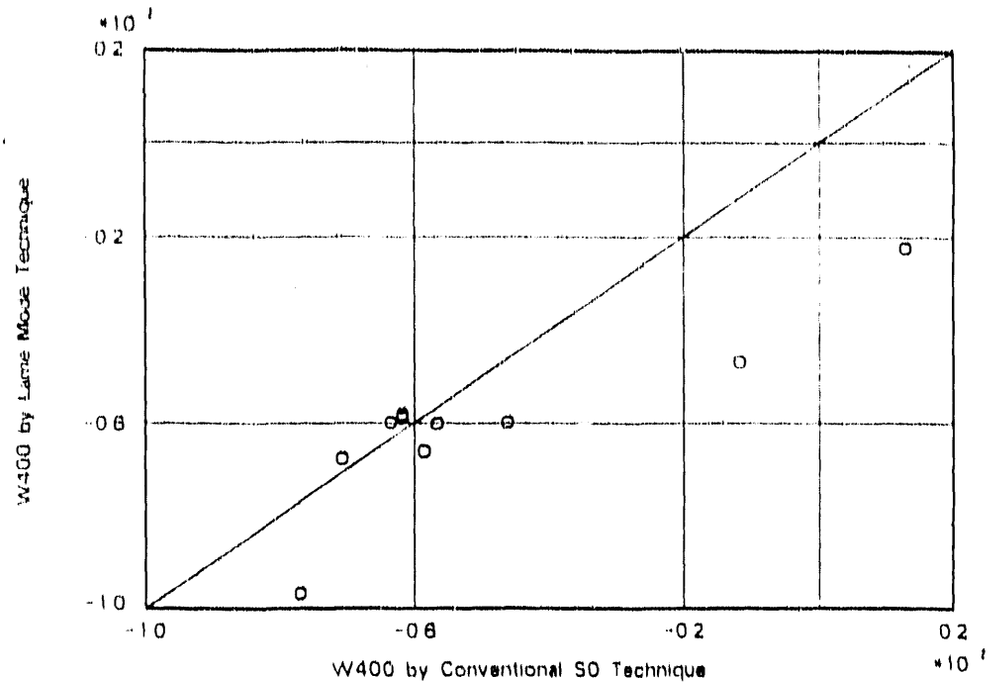

Fig. 7. Correlation between ultrasonic and neutron diffraction results (W_{400})

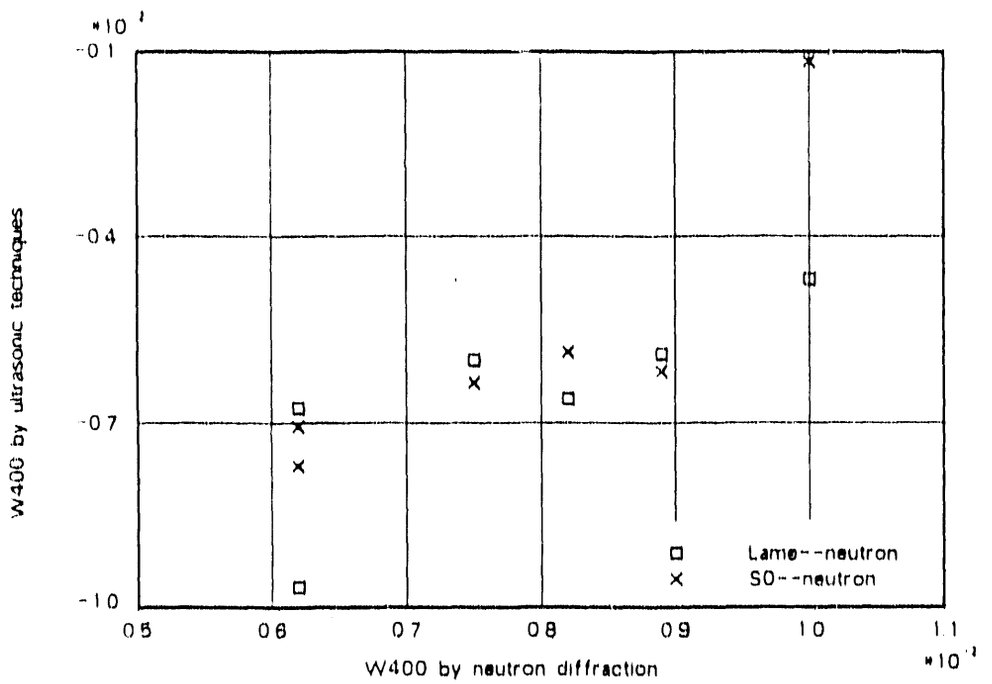

Fig. 8. Comparison of two different ultrasonic techniques (W_{400})

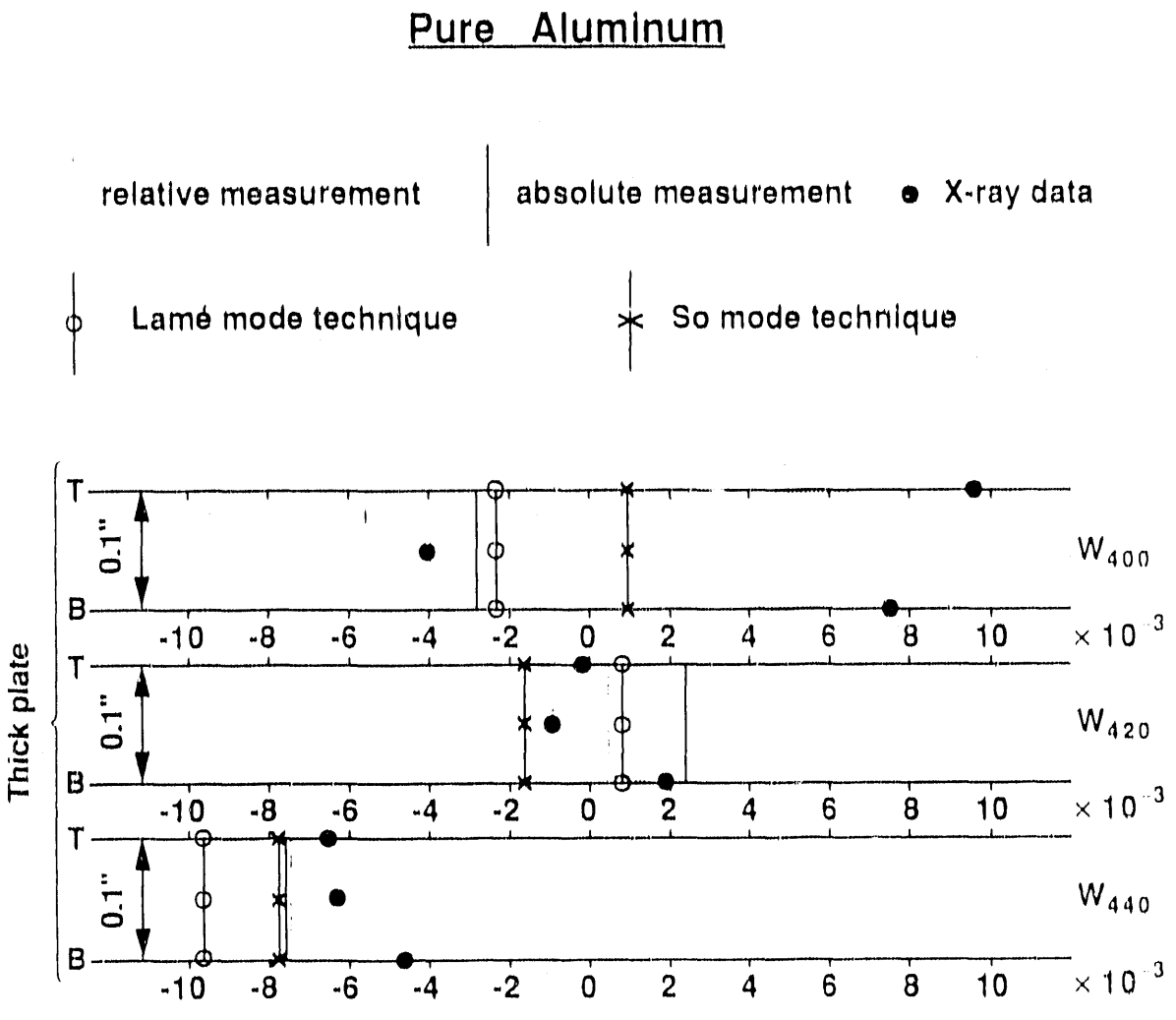

Fig. 9. Comparison of ultrasonic predictions with those obtained from X-ray diffraction measurement on the pure Al sample (see Ref. 11 for definition of previously used relative and absolute measurements)

GENERAL SUMMARY AND CONCLUSIONS

In Part I of this dissertation, relations between elastic constants and texture parameters for hexagonal crystallites have been developed. These relations are the bridge between texture and anisotropy. Ultrasonic measurements determine the material anisotropy which implies texture through these relations. The relations are relatively simple: the elastic constants are linear functions of isotropic moduli and texture parameters ($W_{l\,mn}$ for l up to 4). With these relations, ultrasonic characterization of texture of polycrystalline aggregates of hexagonal crystallites becomes possible.

In Part II, the influence of the material anisotropy on the dispersion characteristics of guided plate waves has been investigated and discussed. This part provides a theoretical foundation for wave propagation analysis in anisotropic plates. Included are analytical expressions for dispersion equations along with a few analytical solutions for some dispersion characteristics. Through some numerical examples with different degrees of anisotropy, many interesting features associated with wave propagation in anisotropic plates have been explored. The analytical equations presented in this part have been frequently used in the rest of the dissertation.

In Part III, two pulse propagation models for dispersive waves have been analyzed. Using these models, some important dispersion characteristics can be obtained without going through complicated Fourier analysis. Comparisons have been made between the predictions by the models and the experimental waveforms obtained using several plate modes with the EMATs and the conventional piezoelectric transducers. It is found that one of the two models is favorable in our study and this model is used in Part V as a tool in the analysis.

In Parts IV and V, the effects of dispersion on the texture

characterization have been studied. These effects had long been suspected to play important roles in texture measurements but were not studied quantitatively. With the development of the analytical equations and models in Parts II and III, it is now possible to make in-depth investigations.

Part IV has shown how to obtain long wavelength limits of the S_0 wave from the finite wavelength measurements. Two available approximate methods have been evaluated for some representative texture. Through the evaluation process, the importance of dispersion correction has been demonstrated and the limit of the conventional S_0 mode technique has been established. The dispersion studied in this part is under the assumption that the phase velocities of the finite wavelength S_0 mode are correctly measured.

Part V has studied the influence of dispersion on a popular but approximate measurement technique. It analyzes one of the commonly employed velocity measurement methods: the zero-crossing measurement method in which the phase velocity of a propagating wave is calculated from the variation of the time delay of a zero-crossing of a particular cycle within a pulse as the transducer separation distance changes. This method is rigorously correct only for nondispersive waves. By using one of the pulse propagation models presented in Part III, it has been shown that the measurement errors, which are introduced by treating the weakly dispersive waves as nondispersive waves, do not really influence significantly the accuracy of the estimates of ODCs, providing that the plate thickness is less than 4 mm and a linear regression approach is used in the velocity calculations.

Part VI has introduced the newly proposed Lamé mode technique. This technique utilizes the unique features of a special point, the Lamé point, on the dispersion curves of the SH_1 and S_0 modes. In particular, texture free plates always have such a point, at which the dispersion curves of the two modes touch each other tangentially. When texture is present, the dispersion curves split or cross over in the vicinity of the Lamé point. The

amount of this splitting or cross over is related to the texture parameters, and a quantitative relation has been developed using the perturbation method. Numerical evaluation of the accuracy of the perturbation formula has also been carried out and the results of the evaluation are satisfactory.

Part VII has extended the conventional ultrasonic techniques to the texture characterization of hexagonal materials. It also includes the theory and applications of a newly proposed SH_1 mode technique. The texture of two hexagonal samples has been measured using both the nondestructive ultrasonic method and the destructive neutron diffraction method. Values of the ODCs from these two methods have been compared and encouraging results have been demonstrated. However, some disagreements still exist between the predictions by the ultrasonic and neutron diffraction measurements.

Part VIII has reported experimental results on ten Al samples using the conventional S_0 mode technique and the Lamé mode technique proposed in Part VI. Although the theory presented in Part VI indicates that the Lamé mode technique predictions of the ODCs should be better than the conventional ones, it has been found that the results from the Lamé mode technique do not have a good correlation with the neutron diffraction results for W_{400} for the Al alloys. They are, however, consistent with the results of the conventional techniques. In spite of this discrepancy, relative good agreements on the ODCs have been found for the results from the ultrasonic measurements and the X-ray diffraction measurements on a pure Al sample. This point has not been clearly understood. Further work is needed before this technique can be widely used.

Although the work presented in this dissertation was motivated by the ultrasonic characterization of texture of polycrystalline aggregates of cubic and hexagonal crystallites, many of the equations, analysis, and discussions can be readily applied to characterization of other materials such as texture, elastic anisotropy and moduli of composite materials. The dispersion

equations and Rayleigh wave velocity calculations presented in Part II can be employed in the study of wave propagation in many anisotropic plates. The pulse propagation models analyzed in Part III are applicable to any types of dispersion, not just limited to that of textured plate waves. The analysis method presented in Part V can be similarly adopted to any zero-crossing velocity measurement system when dealing with pulses of dispersive waves. The principles and methods of using orientation distribution function to compute the effective elastic constants of the aggregates of anisotropic crystallites can also be used in multi-phased materials, including composites.

In addition to the work included in this dissertation, there are still many interesting problems left unsolved in the area of ultrasonic characterization of texture. These problems can generally be divided into three categories: (a) texture description and formability analysis; (b) ultrasonic techniques and measurement methods; and (c) the relations between texture parameters and elastic constants.

In the first category, there is an urgent need for quantitative studies on the influence of alloying elements or second phase materials within the polycrystalline aggregates on the determination of the texture of the aggregates, since most of industrial materials are not pure or single phased. In addition, more works are needed to understand the relations between texture parameters (an elastic property) and the formability (a plastic property) of cubic and hexagonal polycrystalline aggregates.

In the second category, better understanding and applications of the Lamé mode technique are important. Application of this technique to other cubic and hexagonal materials may also be of interest to see if similar discrepancy as shown in Part VIII remains. Other ultrasonic techniques may also need to be developed, particularly for the hexagonal materials. In the area of signal processing of dispersive waves, a solution is needed to determine the correct multiple of 2π in the phase deconvolution computation.

The relations between elastic constants and texture parameters established in some literature and in this dissertation are approximate ones. The approximations are made to make the development of analytical relations possible. These relations are correct to the first order of approximation. It may be the time to develop and evaluate some sophisticated methods such as the energy method [3] through numerical analysis to improve the existing relations.

It would certainly be of future interest to apply the methodology developed for the texture characterization of polycrystalline aggregates to composite materials as they become more and more important these days.

ACKNOWLEDGEMENTS

I would like to especially thank Dr. R. Bruce Thompson, my major professor, for his guidance, inspiration, patience and understanding throughout this program. The last four years have been the most creative, productive and enjoyable time in my life, and I owe it to him. I am also much indebted for his generous advice and help outside my academic area.

I would also like to thank Samuel J. Wormley for his help in solving technical problems and for letting me "mess up" his office, Dr. Otto Buck for providing financial support that allowed me to participate in many academic conferences, and Dr. David Hsu for many interesting and eye-opening conversations on various subjects.

Thanks are also due to Drs. D. O. Thompson, L. W. Schmerr, W. A. Spitzig and J. P. Basart for serving on my committee.

Finally, on a personal level, I thank my wife, Yunling Ma, who has shared the joy and the frustration I had during the course of work on my Ph. D. degree. I thank her for the help, understanding, and encouragement she has given me in the last few years. I also thank my parents, Jilin Li and Zhenlian Chen, whose support has been invaluable.

This work was performed at Ames Laboratory under contract no. W-7405-eng-82 with the U. S. Department of Energy. The United State government has assigned the DOE Report number IS-T 1515 to this thesis.

REFERENCES

1. R. -J. Roe. "Description of Crystallite Orientation in Polycrystalline Materials. III. General Solution to Pole Figure Inversion." J. Appl. Phys. 36 (1965): 2024-31.

2. R. -J. Roe. "Inversion of Pole Figures for Materials Having Cubic Crystal Symmetry." J. Appl. Phys. 37 (1966): 2069-72.

3. H. J. Bunge. Texture Analysis in Materials Science. London: Butterworths, 1982.

4. S. Matthies, G. W. Vinel, and K. Helming. Standard Distributions in Texture Analysis. Vol. 1. Berlin: Akademie-Verlag, 1987.

5. P. R. Morris. "Averaging Fourth-Rank Tensors with Weight Functions." J. Appl. Phys. 40 (1969): 447-48.

6. C. M. Sayers. "Ultrasonic Velocities in Anisotropic Polycrystalline Aggregates." J. Phys. D.: Appl. Phys. 15 (1982): 2157-67.

7. M. Hirao, K. Aoki, and H. Fukuoka. "Texture of Polycrystalline Metals Characterized by Ultrasonic Velocity Measurements." J. Acoust. Soc. Am. 81 (1987): 1434-40.

8. C. S. Barrett. Structure of Metals. 2nd ed. New York: McGraw-Hill, 1952.

9. R. Hill. "The Elastic Behaviour of a Crystalline Aggregate." Proc. Phys. Soc. A65 (1952): 349-354.

10. C. M. Sayers. "Angular Dependent Ultrasonic Wave Velocities in Aggregates of Hexagonal Crystals." Ultrasonics 24 (1986): 289-91.

11. C. M. Sayers. "The Elastic Anisotropy of Polycrystalline Aggregates of Zirconium and its Alloys." J. Nuclear Materials 144 (1987): 211-13.

12. Y. Li and R. B. Thompson. "Relations Between Elastic Constants Cij and ODCs for Hexagonal Materials." J. Appl. Phys. 67 (1990): 2663-65.

13. Y. Li, R. B. Thompson, and S. S. Lee. "Ultrasonic Measurement of Texture of Cubic and Hexagonal Materials." In Review of Progress in Quantitative Nondestructive Evaluation. Vol. 9B. Eds. D. O. Thompson and D. E. Chimenti. New York: Plenum Press, 1990. 1781-88.

14. R. B. Thompson, J. F. Smith, and S. S. Lee. "Inference of Stress and Texture from the Angular Dependence of Ultrasonic Plate Mode Velocities." In Nondestructive Evaluation of Microstructure for Process Control. Ed. H. N. G. Wadley. Metals Park, OH: ASM, 1985. 73-80.

15. S. S. Lee, J. F. Smith, and R. B. Thompson. "Ultrasonic Techniques for the Quantitative Characterization of Texture: A Survey." In Formability and Metalurgical Structures. Warrendale, PA: TMS, 1987. 177-90.

16. R. B. Thompson, S. S. Lee, and J. F. Smith. "Relative Anisotropies of Plane Waves and Guided Modes in Thin Orthorhombic Plates: Implication for Texture Characterization." Ultrasonics 25 (1987): 133-37.

17. S. S. Lee, J. F. Smith, and R. B. Thompson. "Inference of Crystallite Orientation Distribution Function from the Velocity of Ultrasonic Plate Modes." In Nondestructive Characterization of Materials. Vol. 2. Ed. J. F. Bussiere. New York: Plenum Press, 1988. 555-62.

18. M. Hirao, N. Hara, H. Fukuoka, and K. Fujisawa. "Ultrasonic Monitoring of Texture in Cold-rolled Steel Sheets." J. Acoust. Soc. Am. 84 (1988): 667-72.

19. A. V. Clark, Jr., G. V. Blessing, R. B. Thompson, and J. F. Smith. "Ultrasonic Methods of Texture Monitoring for Characterization of Formability of Rolled Aluminum Sheet." In Review of Progress in Quantitative Nondestructive Evaluation. Vol. 7B. Eds. D. O. Thompson and D. E. Chimenti. New York: Plenum Press, 1988. 1365-73.

20. A. V. Clark, Jr., R. C. Reno, R. B. Thompson, J. F. Smith, G. V. Blessing, R. J. Fields, P. P. Delsanto, and R. B. Mignogna. "Texture Monitoring in Aluminum Alloys: A Comparison of Ultrasonic and Neutron Diffraction Measurement." Ultrasonics 26 (1988): 189-97.

21. Y. Li and R. B. Thompson. "Propagation of Guided Elastic Waves in Orthotropic Plates." In Review of Progress in Quantitative Nondestructive Evaluation. Vol. 8A. Eds. D. O. Thompson and D. E. Chimenti. New York: Plenum Press, 1989. 189-96.

22. Y. Li, J. F. Smith, and R. B. Thompson. "Characterization of Textures in Plates by Ultrasonic Plate Wave Velocities." In Nondestructive Characterization of Materials. Vol. 3. Eds. P. Höller, V. Hauk, G. Dobmann, C. Ruud, and R. Green. New York: Springer-Verlag, 1989. 312-19.

23. R. B. Thompson, J. F. Smith, S. S. Lee, and G. C. Johnson. "A Comparison of Ultrasonic and X-ray Determinations of Texture in Thin Cu and Al Plates." Metall. Trans. 20A (1989): 2431-47.

24. J. F. Smith, R. B. Thompson, D. K. Rehbein, T. J. Nagel, P. E. Armstrong, and D. T. Eash. "Illustration of Texture with Ultrasonic Pole Figures." In Review of Progress in Quantitative NDE. Vol. 6B. Eds. D. O. Thompson and D. E. Chimenti. New York: Plenum Press, 1987. 1541-1548.

25. M. Hirao and N. Hara. "Ultrasonic Pole Figure for the Texture of Aluminum Alloy." Appl. Phys. Lett. 50 (1987): 1411-12.

26. D. Daniel, K. Sakata, J.J. Jonas, I. Makarow, and J. F. Bussiere. "Acoustoelastic Determination of the Fourth Order ODF Coefficients and Application to R-value Prediction." In Nondestructive Measurement of Materials Properties. Eds. J. Holbrook and J. Bussiere. Pittsburgh, PA: MRS, 1989. 77-82.

27. Manual of MODUL-r Drawability Testing System, manufactured by Tinius Olsen, Willow Grove, PA, 1985.

28. P. R. Mould and T. R. Johnson, Jr. "Rapid Assessment of Drawability of Cold-rolled Low-carbon Steel Sheets." Sheet Met. Ind. 50 (1973): 328-48.

29. C. A. Stickels and P. R. Mould. "The Use of Young's Modulus for Predicting the Plastic-strain Ration of Low-carbon Steel Sheets." Metall. Trans. 1 (1970): 1303-12.

30. G. J. Davies, D. J. Goodwill, and J. S. Kallend. "Elastic and Plastic Anisotropy in Sheets of Cubic Metals." Metall. Trans. 3 (1972): 1627-31.

31. A. V. Clark, R. B. Thompson, G. V. Blessing, and D. Matlock. "Ultrasonic Measurement of Formability in Thin Ferritic Steel Sheet." In Review of Progress in Quantitative Nondestructive Evaluation. Vol. 8A. Eds. D. O. Thompson and D. E. Chimenti. New York: Plenum Press, 1989. 1031-38.

32. O. Cassier, C. Donadille, and B. Bacroix. "Drawability Assessment of Steel Sheets by an Ultrasonic Method." In Review of Progress in Quantitative Nondestructive Evaluation. Vol. 8B. Eds. D. O. Thompson and D. E. Chimenti. New York: Plenum Press, 1989. 2189-96.

33. M. Spies and E. Schneider. "Nondestructive Analysis of the Deep-drawing Behaviour of Rolling Sheets with Ultrasonic Techniques." In Nondestructive Characterization of Materials. Vol. 3. Ed. P. Höller, V. Hauk, G. Dobmann, C. Ruud, and R. Green. New York: Springer-Verlag, 1989. 296-302.

34. M. J. Philippe, F. Wagner, and C. Esling. "Textures, Deformation Mechanisms and Mechanical Properties of Hexagonal Materials." Proc. 8th International Conference on Textures of Materials. Eds. J. S. Kallend and G. Gottstein. Warrendale, PA: The Metallurgical Society, 1988. 837-42.

35. T. M. Holden, R. R. Hosbons, J. H. Root, and E. F. Ibrahim. "Neutron Diffraction Measurements of Strain and Texture in Welded Zr 2.5 Nb Tube." Nondestructive Monitoring of Material Properties. Eds. J. Holbrook and J. Bussiere. Pittsburgh, PA: MRS, 1988. 59-64.

36. Y. Li and R. B. Thompson. "Ultrasonic Characterization of Texture." Nondestructive Monitoring of Material Properties. Eds. J. Holbrook and J. Bussiere. Pittsburgh, PA: MRS, 1988. 83-88.

37. S. S. Lee, et al. "Angular Dependent Ultrasonic Wave Velocities in Thin Zircaloy Plate." Nondestructive Characterization of Materials. Vol. 4. Eds. C. O. Ruud and R. E. Green. New York: Plenum Press, in press.

38. Y. Li, R. B. Thompson, J. H. Root, and T. M. Holden. "Determination of Texture in Plates of hcp Metals Zirconium and Titanium by Ultrasound and Neutron Diffration." Nondestructive Characterization of Materials. Vol. 4. Eds. C. O. Ruud and R. E. Green. New York: Plenum Press, in press.

39. Y. Li and R. B. Thompson. "Influence of Anisotropy on the Dispersion Characteristics of Guided Ultrasonic Plate Modes." J. Acoust. Soc. Am. 81 (1990):1911-31.

40. Y. Li and R. B. Thompson. "Use of the Velocity of Higher oder Lamb Modes in the Measurement of Texture."In Review of Progress in Quantitative Nondestructive Evaluation. Vol. 8B. Eds. D. O. Thompson and D. E. Chimenti. New York: Plenum Press, 1989. 1863-70.

41. E. P. Papadakis, et al. "An Automatic Instrument for the Ultrasonic Measurement of Texture." Nondestructive Characterization of Materials. Vol. 4. Eds. C. O. Ruud and R. E. Green. New York: Plenum Press, in press.

42. Manual of Ultra-Form Ultrasonic Formability Instrument, Manufactured by Iowa State University, Ames, IA, 1990.

APPENDIX. CALCULATION OF LONG WAVELENGTH LIMIT OF THE S_0 MODE USING FOURIER PHASE METHOD

A time signal detected as an ultrasonic pulse arrives at a specific location can be expressed as

$$f(t) = \int A(\omega) \exp[j(\omega t - kx)]\, d\omega \qquad (A.1)$$

where $A(\omega)$ is a function related to the bandwidth of the signal, and k, the wave number, is a function of frequency ω for dispersive waves.

The Fourier transform of this signal is then

$$F(\omega) = A(\omega) \exp[-j\, k(\omega)x] = M(\omega) \exp[j\Phi(\omega)] \qquad (A.2)$$

where $M(\omega)$ and $\Phi(\omega)$ are the magnitude and phase of the Fourier transform respectively, and $A(\omega)$ need not be a real function.

If two signals are obtained at two different locations x_1 and x_2 with respect to a common time frame, then the division of the Fourier transforms of these two signals becomes

$$\frac{F_2(\omega)}{F_1(\omega)} = \frac{A_2(\omega) \exp[-j\, k(\omega)x_2]}{A_1(\omega) \exp[-j\, k(\omega)x_1]} = \frac{M_2(\omega) \exp[j\Phi_2(\omega)]}{M_1(\omega) \exp[j\Phi_1(\omega)]} \qquad (A.3)$$

Thus, the phase difference, $\Delta\Phi(\omega)=\Phi_2(\omega)-\Phi_1(\omega)$ of the Fourier transforms of the two signals is

$$\Delta\Phi(\omega) = -k(\omega)(x_2 - x_1) \qquad \text{or} \qquad \Delta\Phi(\omega) = -k(\omega)\Delta x\,. \qquad (A.4)$$

Often the two signals are not recorded with respect to the same time frame (the trigger delays are different). In this case, Eq. (A.4) can be modified as

$$\Delta\Phi(\omega) = \omega \Delta t - k(\omega)\Delta x \qquad (A.5)$$

where $\Delta t = t_2 - t_1$, t_1 and t_2 are trigger delays of signals at x_1 and x_2 respectively.

When estimating the phase difference $\Delta\Phi$ from experimental data, there is always an ambiguity of a multiple of 2π. In other words, the true phase difference is the computed phase difference, $\Delta\Phi_c(\omega)$, plus $2n\pi$, where n is an integer. Thus Eq. (A.5) can be rewritten as

$$\Delta\Phi_c(\omega) + 2n\pi = \omega\,\Delta t - k(\omega)\,\Delta x \qquad (A.6)$$

For signals generated by an EMAT system, n can often be determined from the raw received data. When the EMAT system is tuned for maximum efficiency, the waves excited by the EMATs have a period that is very close to the EMAT period D; i.e., the wave number at the peak frequency f_{peak}, which corresponds to the frequency of peak power spectrum, should be close to $2\pi/D$. Using this principle, one can determine n as the nearest integer to the quantity an, where

$$an = f_{peak}\Delta t - \Delta x/D - \Delta\Phi_c(f_{peak})/2\pi. \qquad (A.7)$$

Once the n is determined, the dispersion curve in the operation area can be obtained as

$$k(\omega) = \frac{\omega\,\Delta t - \Delta\Phi_c(\omega) - 2n\pi}{\Delta x}. \qquad (A.8)$$

The resolution of the power spectrum Δf is governed by the sampling frequency f_s and number of sampling points N: $\Delta f = f_s/N$. Typical sampling frequency and sampling points in our study are 10 MHz and 1024 points. Thus $\Delta f \approx 0.01$ MHz. Often a better resolution is required to compute the f_{peak}. To do this, a parabola is fitted to the three points that have the highest magnitudes. f_{peak} is then the frequency where the maximum of the parabola occurs.

To find the wave number $k_{peak} = k(f_{peak})$, $\Delta\Phi_c(f_{peak})$ needs to be determined first. This is achieved by fitting a second order polynomial to $\Delta\Phi_c(\omega)$ using the magnitude of the averaged power spectrum as the weighting function. $\Delta\Phi_c(f_{peak})$ can be readily obtained once the polynomial equation is established. This $\Delta\Phi_c(f_{peak})$ should be used in Eq. (A.7) to determine the quantity an and the nearest integer n. Then k_{peak} can be calculated using Eq. (A.8).

Occasionally, due to the filtering effects of various electronic components, which pulls the peak power spectrum away from the point $2\pi/D$, the integer n determined from Eq. (A.7) is still off by one. In other words, if we denote the integer obtained from Eq. (A.7) as n_0, the true n can be n_0+1, n_0,

or n_0-1. The k_{peak} calculated from Eq. (A.8) then have three possibilities, denoted as k_+,k_0, and k_-. This ambiguity can be resolved by using the following method.

Most textured materials are weakly anisotropic. Because of this, the dispersion characteristics of a textured plate or sheet are close to that of an isotropic one. Using the approximate isotropic dispersion relation given in Eq. (5) of Part V, frequencies corresponding to k_+,k_0, and k_- can be computed as f_+,f_0, and f_-. Comparing these frequencies to f_{peak} obtained earlier, and under the assumption that the textured response should be close to the isotropic response, one of the three should be very close to f_{peak}. The correct choice of n should be the one corresponding to this frequency.

After the value n is selected, k becomes known and the phase velocity of the peak frequency is $V_{peak}=2pf_{peak}/k_{peak}$. Dispersion correction can now be performed using the Thompson's method described in Part IV and the ratio V_{llm}/V_{S_0} can be determined for $k=k_{peak}$. The long wavelength limit of the S_0 mode becomes $V_{llm} = V_{peak}(V_{llm}/V_{S_0})_{k_{peak}}$.

END

DATE FILMED

11/14/90